QUANTIFICATION OF POLYMETHYL METHACRYLATE (PMMA) SHOCK, STRESS, AND FRACTURE RESPONSE UNDER EXPLOSIVE LOADING

by

Sivana Mirhai Torres

Submitted in Partial Fulfillment
of the Requirements for the Degree of
Doctor of Philosophy in Mechanical Engineering
with Dissertation in Intelligent Energetic Systems

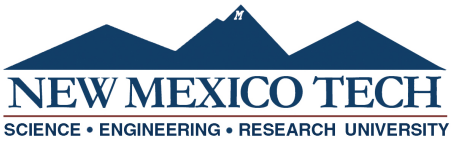

New Mexico Institute of Mining and Technology
Socorro, New Mexico
May, 2024

This thesis is dedicated to my parents, Tim and Michelle Torres, and my Nani.

Sivana Mirhai Torres
New Mexico Institute of Mining and Technology
May, 2024

ACKNOWLEDGMENTS

I would like to thank my family for all of their love and support throughout the past 5 years. I am also thankful for the past, current, and honorary SGDL members that have helped me run experiments and for their in-depth research discussions. I would like to thank my academic and research advisor, Dr. Michael Hargather, for always pushing me to reach my full potential and for creating an environment for me to meet some amazing scientist!

This dissertation was typeset with LaTeX[1] by the author.

[1]The LaTeX document preparation system was developed by Leslie Lamport as a special version of Donald Knuth's TeX program for computer typesetting. TeX is a trademark of the American Mathematical Society. The LaTeX macro package for the New Mexico Institute of Mining and Technology dissertation format was written by John W. Shipman.

ABSTRACT

The fracture response of geologic materials is of interest for multiple applications including geothermal energy harnessing, petroleum extraction, and containment of underground explosives. Polymethyl methacrylate (PMMA) is an optically transparent rock surrogate often used for shock and fracture studies to allow for visualization of internal processes. Quasi-static and dynamic experiments were performed here using PMMA to image shock waves and fractures. Quasi-static tests were used to develop an optical diagnostic analysis methodology and the dynamic explosive tests were used to quantify the explosively driven shock and fracture response. Quasi-static testing was performed on the small scale whereas explosive testing was explored on multiple scales. The small scale quasi-static experiments were used to validate stress gradients calculated using quantitative schlieren images against an analytical solution. Quantitative schlieren measurements of the stress field in a thin sample with a point load compared well to the analytical Flamant solution. The explosive induced response of PMMA was experimentally studied using high-speed schlieren and shadowgraphy to visualize the shock propagation and fracture growth in conjunction with Photon Doppler Velocimetry (PDV) to record surface velocity histories. Small scale experiments contained a single explosive source in prismatic samples less than 10 cm in length. The large scale experiment contained two explosive sources 50.8 mm apart in 30 cm x 30 cm x 30 cm cubes. RP-80 EBW detonators were used as the explosive sources for all experiments. Fracture experiments were subjected to 2 MPa of uni-axial stress in both the vertical direction and horizontal direction, 20 MPa of uni-axial stress in the vertical direction and a baseline test of no external stress to measure the fracture behavior under varied external stresses. The particle velocity histories were compared to the shock response recorded in the high-speed videos to determine the explosive induced shock Hugoniot for PMMA. The high-speed video records were analyzed to extract the shock and fracture fronts. Post-test images of the PMMA cubes aided in the determination of three-dimensional fracture effects. The small scale shock studies quantified the shock pressure decay as a function of shock radius. The large scale tests were compared to numerical simulations where it was found that the fractures are primarily driven by the high pressure gases produced by the explosive detonation.

Keywords: Polymethyl methacrylate (PMMA), stress gradients, explosive induced shock, explosive induced fracture, schlieren, shadowgraphy, high-speed imaging, Photron Doppler Velocimetry (PDV)

CONTENTS

LIST OF TABLES

LIST OF FIGURES

Figure **Page**

This dissertation is accepted on behalf of the faculty of the Institute by the following committee:

Micheal J. Hargather

Academic and Research Advisor

Jamie Kimberley

Andrei Zagrai

Thomas Engler

I release this document to the New Mexico Institute of Mining and Technology.

Sivana Mirhai Torres April 12th, 2024

NOMENCLATURE

$\bar{\omega}$	Radial phase difference
α	Wave form parameter
α, β, γ	Angles between the light vector and the three coordinate axis
$\mathbf{I}$	Second order identity tensor
$\mathbf{T}'$	Deviatoric part of the stress tensor
$\mathbf{T}$	Cauchy stress tensor
Δs, Δs_x, Δs_y	Optical path length change
Δ	Distance between the object plane and the image plane
$\dot{\epsilon}_0$	Reference strain rate
ϵ_R	Resultant refraction angle
ϵ_x, ϵ_y	Refraction angles in the x- and y-direction
Γ_0	Mie Gruneisen parameter
$\mathbf{\Pi}$	Total potential energy
$\mathbf{G_c}$	Critical energy release rate
$\mathbf{G}$	Energy release rate
ν	Poisson's ratio
Φ	Optical phase difference
ρ	Density
ρ_0	Reference density
σ_e	Von Mises effective stress
σ_1, σ_2, σ_3	Principal stresses
$\sigma_{\theta\theta}$	Hoop stress

σ_H Horizontal stress

$\sigma_{ij}^{(I)}, \sigma_{ij}^{(II)}, \sigma_{ij}^{(III)}$ Stress field for Mode I, Mode II, and Mode III loading

σ_{inf} Infinite body

σ_l Lateral stress

σ_{PDV} Stress calculated using the surface velocity history from PDV

σ_{rr} Radial stress

σ_{SD} Standard deviation

σ_V Vertical stress

σ_{xh} Hugoniot stress

$\sigma_{xx}, \sigma_{yy}, \sigma_{zz}$ Normal stresses

τ Shear stress

θ Fracture angle

$\vec{d}$ Light vector

A Area

A Crack area

a, b, c Direction cosines

A_c,B_c Stress optic coefficients

C_0 Reference bulk sound speed

C_h $U_s - u_p$ Hugoniot fitting parameter having units of velocity

C_L Longitudinal sound speed

C_σ Elasto-optic coefficient

d Magnitude of the light vector from the object plane and the image plane

D_c General stress optic coefficient

d_{eff} Sample thickness

E Total energy output of the explosive

e Explosive energy pre unit mass

E_y Young's modulus

F Force

f Focal length of calibration lens

$f_{ij}^{(I)}, f_{ij}^{(II)}, f_{ij}^{(III)}$ Dimensionless function of θ for Mode I, Mode II, and Mode III loading

h Explosive height

I_x, I_y Pixel intensity for the vertical cut-off and horizontal cut-off schlieren images

k Gladstone-Dale constant

K_{IC} Materials resistance to crack growth

K_I, K_{II}, K_{III} Stress intensity factor for Mode I, Mode II, and Mode III loading

L Schlieren object length

m Pressure hardening rate

n,n_0 Index of refraction

n_1, n_2, n_3 Refractive indices corresponding to the principal stresses for a temporary birefringent material under stress

n_x,n_y,n_z Refractive indices corresponding to the normal stresses for a temporary birefringent material under stress

n_{s0}, n_{s1},n_{s2} rate power - simulation parameter

P Pressure

p Volumetric part of the stress tensor

p_0 Peak over pressure at t = 0

p_I Instantaneous over pressure

r Radius

R_y, R_x Location of a pixel in the calibration lens

r_{act} Actual fracture radius

r_{PMMA} Location in the calibration lens of zero refraction

r_{proj} Projected fracture radius on to the imaging plane

r_{xy} Element in space

r_x, r_y Displacement in the x- and y- direction

$S(f)$ electrical signal in the frequency domain

$s(t)$ electrical signal in time domain

S_1, S_2, S_3 Shock Hugoniot parameters

t_d Pulse duration

t_{act} Uncorrected time

t_{ac} Time corrected for detonator function time

t_n Corrected time such that time zero was when the shock reached the free surface

u_p Particle velocity

U_s Shock velocity

u_{sf} Free surface velocity

w_t STFT window size for SIRHEN analysis

x_H Sample height

x_L Sample length

x_W Sample width

x_{exp} Explosive length

x_{pd} Propagation distance

Y Yield strength

Y_{c0} Unconfined compressive strength

C1, C2, C Camera

CL Corrector lens

EBW Electronic bridge-wire

EOS Equation of state

HEL Hugoniot Elastic Limit

HS2-2 PMMA block with two holes and 2 MPa of horizontal external stress

JWL Jones-Wilkins-Lee (EOS)

KE Knife edge cutoff

kfps, Mfps thousand frames per second, million frames per second

LS Light source

NS1 PMMA block with one hole and no external stress

NS2 PMMA block with two holes and no external stress

PDV Photon Doppler velocimetry

PETN Pentaerythritol tetranitrate

PM1, PM2 Plano-convex mirror

PMMA Poly(methyl methacrylate)

RDX Research Department Explosive, or 1,3,5-trinitroperhydro-1,3,5-triazine

s $U_s - u_p$ Unit-less Hugoniot fitting parameters

SIF, DSIF Stress Intensity Factor, Dynamic Stress Intensity Factor

SIRHEN Sandia InfraRed HEtrodyne aNalysis

SL1, SL2 Schlieren lens

SO Schlieren Object

SS Small-scale sample

STFT Short-time Fourier transform

VISAR Velocity Interferometry System for Any Reflector

VS2-2 PMMA block with two holes and 2 MPa of vertical external stress

VS2-20 PMMA block with two holes and 20 MPa of vertical external stress

CHAPTER 1

INTRODUCTION

1.1 Research Motivation

Explosives are one tool that can be utilized to fracture rock in mining, petroleum extraction, and geothermal well construction applications. Explosives are used to drive shock waves into the hard material producing stress states which fracture the material. The explosive gas production and the resulting high pressures can produce sustained fracture growth beyond the timescale of the shock wave pulse. The characteristics under which the shock wave induced versus the pressure driven fracture occurs are, however, not well understood especially when considering the stress state imparted by overburden rock. The in-situ stress field is dictated by the magnitude and direction of the force which impact and influence the fracture extent.

Performing experiments in geologic materials presents several challenges including non-homogenaities, anisotropies and difficulties for instrumentation. A common substitute for geologic materials has been polymethyl methacrylate (PMMA) [6, 7] which is an optically transparent polymer material which fractures similarly to geologic materials at deep depths. PMMA is a more ideal test material because it is homogeneous, isotropic, and optically transparent which enables a wider suite of instrumentation to be applied.

Here PMMA will be utilized as a rock substitute to explore conditions for explosively-induced fracture growth from embedded explosives. The goal is to develop an understanding of how the shock wave from an embedded explosive charge propagates through the material, produces a given stress field, and how the resulting fracture network grows. The shock wave and gas production will be explored for their contribution to the fracture production to understand how changing the external stress field impacts the fracture response. Experiments performed with externally applied stress on the PMMA will simulate explosions in deeply buried rock. The work here will enable better, and potentially more controlled, explosively driven fracture of materials.

1.2 Wave propagation in solids

Waves propagating through a medium consist of the rate at which the wave travels through the medium, known as the wave velocity, and the rate at which a particle in the medium oscillates in its fixed position, known as the particle velocity. In solids, the mechanical response of the material plays a significant role in how the particle motion moves relative to the wave propagating through the material. It also dictates any deformation caused by the wave or the application of external force which imparted the wave. Two classifications of wave propagation will be considered: elastic wave propagation, and plastic, or inelastic, wave propagation.

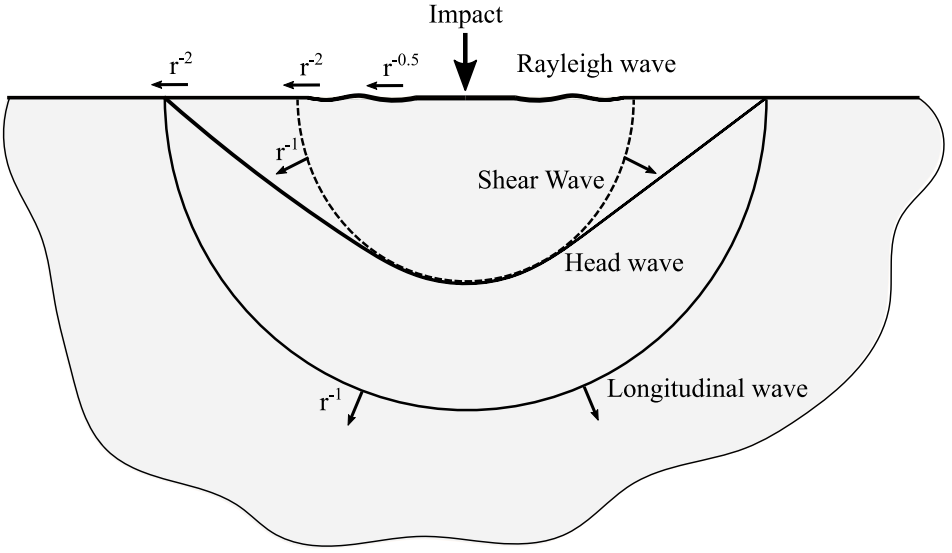

Figure 1.1: Schematic of an impact on a semi-infinite body showing the formation of Rayleigh, shear, and longitudinal waves. The head wave is an artifact of the longitudinal wave interacting with the free-surface.

The classification of elastic waves is governed by the particle motion relative to the wave motion. The elastic wave classifications to be discussed here are dilatational, shear, Rayleigh, interfacial, and bending waves [8]. For dilatational, or longitudinal, waves the particle motion moves parallel to the wave propagation direction. If the particle motion moves in the same direction as the wave propagation then the longitudinal wave is compressive. If the particle motion and wave motion are in opposing directions then the longitudinal wave is tensile. As for shear waves, the particle motion is perpendicular to the wave propagation direction. Longitudinal and shear waves propagate through the medium, however, on the surface other waves form including Rayleigh waves as shown in Figure 1.1. Since Rayleigh waves are surface waves that are composed of both transverse and longitudinal motion the particle motion mimics an elliptical path. If two surfaces are in contact then interfacial waves can also occur. Lastly, bending waves occur in one- and two- dimensional configurations consisting of the propagation of flexure.

Figure 1.1 schematically shows wave propagation through a semi-infinite body resulting from an impact on the surface. It is shown that the shear and longitudinal waves are propagating through the medium and the Rayleigh waves are occurring only on the surface. As the waves move further from the source there is a reduction in the particle and wave amplitude indicating a reduction in pressure or wave "strength". As the strength of the wave is reduced the wave asymptotically approaches the material sound speed regardless of the strength of the initial wave. The rate at which the strength of the wave decays is simply based on the radial location of the wave relative to the point of impact. Longitudinal and shear waves decay more rapidly close to the surface having a decay rate proportional to the radial distance from the impact, r, to the negative 2 power, r^{-2}. Far away from the surface the decay rate is proportional to r^{-1}. The decay behavior of the shear and longitudinal waves close to the surface should not be confused with surface wave decay, as surface waves decay slower at a rate of $r^{-1/2}$ [8]. The notional wave decay rates are shown schematically in Figure 1.1.

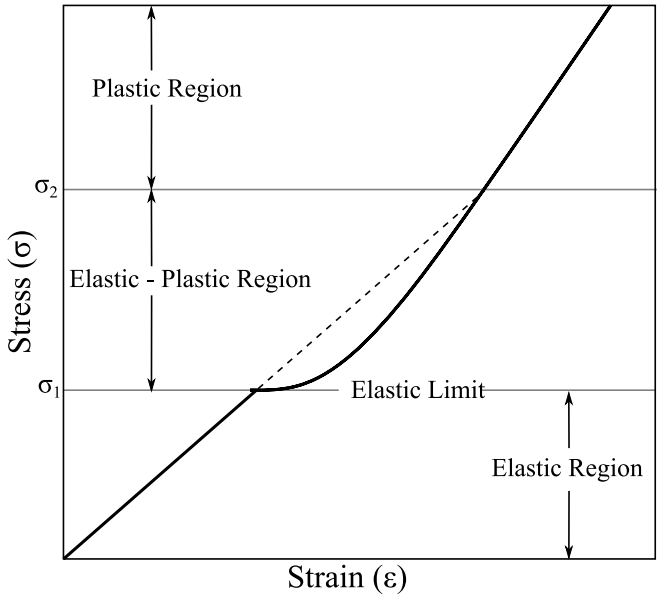

Figure 1.2: Stress-stain curve for large amounts of compressive stress on a notional solid material.

Elastic wave propagation indicates an elastic material response in which the material stress and strain are linearly related. After the elastic wave propagates through the material, the material will return to its original shape and will leave no residual effects. An example of this is a sound wave propagating through the material. The wave induces stress as it passes through the material but after the wave leaves there is no residual effects. If the material stress exceeds the elastic limit, σ_1 in Figure 1.2, the linear relationship no longer holds true. Beyond the elastic limit the material is permanently, or plastically, deformed. Here, the

stress-strain curve will be segmented into two regimes corresponding to the two classifications of wave propagation of interest.

The second classification to be discussed is when the external stress exceeds the elastic limit of the material thus plastic deformation sets in. Some materials, such as metals, will behave both elastically and plastically after the elastic limit is exceeded. For wave propagation, this limit is refereed to as the Hugoniot Elastic Limit (HEL) of a material. In this region it is theorized that distortional strain is plastic deformation and the volumetric strain is purely elastic [9]. With regard to the wave propagation in this regime, the wave is decomposed into two waves having different wave velocities; an elastic wave, also referred to as an elastic precursor, and a plastic wave [8, 10] as shown in Figure 1.3. In this region the elastic wave travels at the longitudinal sound speed of the material, $v_0 = C_L$, and the plastic wave, v_1, travels at the Rayleigh wave speed to be discussed later [10]. Once the material reaches a second stress amount, σ_2 in Figure 1.2, where $\sigma_2 >> \sigma_1$ then the material behaves like a fluid which is the regime where strong shock waves exist.

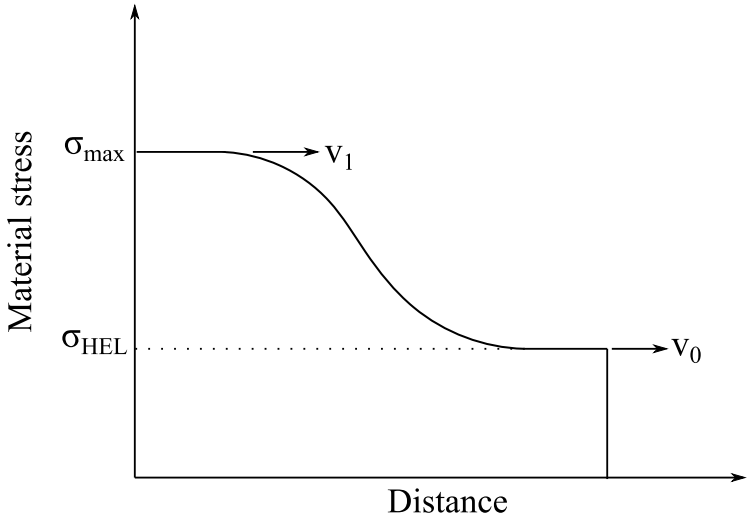

Figure 1.3: Schematic showing the two wave structure for elastic-plastic wave propagation.

Amorphous polymers, such as a polymethyl methacrylate (PMMA), exhibit a viscoelastic material response. Unlike linear elastic materials where the material returns to it's unstrained state with no memory of the deformation, viscoelastic materials remember the deformation history. Once the elastic limit is exceeded the decomposition of the wave into a plastic wave and the elastic precursor is expected. The elastic precursor, however, has yet to be experimentally observed in PMMA [11, 12]. There is also an implied rate-dependence associated with viscoelastic materials. The viscoelasticity of PMMA has been attributed to a nonlinear and rate-dependant shock response experimentally observed [4].

A shock wave is described as a discontinuity in pressure, temperature or internal energy, and density. A shock discontinuity is caused by a high-pressure input greatly exceeding the elastic limit of the material such that the deviatoric component of the stress state is negligible [8]. Only the hydrostatic component is considered, thus, the material is treated as a fluid. In treating the material as a fluid, conservation equations are used to determine the shocked state of the material. Conservation of mass, momentum, and energy equations are used to define pressure P, temperature T (or internal energy E), density ρ and particle velocity u_p in the "shocked" and "unshocked" region's of the material [8, 10] as shown schematically in Figure 1.4.

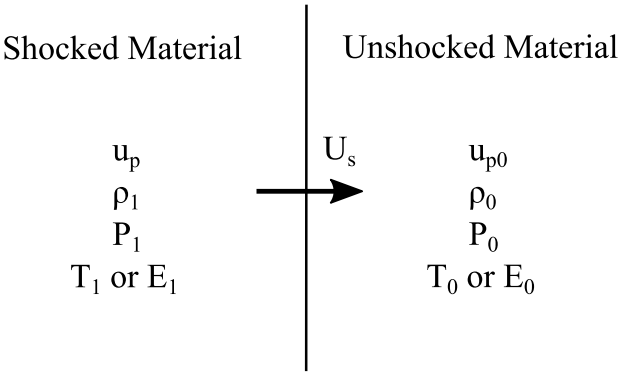

Figure 1.4: Parameters of a material after the shock wave, "shocked" material, and before the shock wave, "unshocked" material. The shock moves to the right at a velocity of U_s.

The Rankine-Hugoniot equations are derived from the following conservation equations [10].

$$\text{Conservation of Mass:} \quad \frac{\rho_1}{\rho_0} = \frac{U_s - u_{p0}}{U_s - u_p} = \frac{v_0}{v_1} \tag{1.1}$$

$$\text{Conservation of Momentum:} \quad P_1 - P_0 = \rho_0(u_p - u_{p0})(U_s - u_{p0}) \tag{1.2}$$

$$\text{Conservation of Energy:} \quad e_1 - e_0 = \frac{P_1 u_p - P_0 u_{p0}}{\rho_0(U_s - u_{p0})} - \frac{1}{2}(u_p^2 - u_{p0}^2) \tag{1.3}$$

Using a Lagrangian reference frame, equations 1.1, 1.2, and 1.3 are used to relate five unknowns, u_p, ρ_1, P_1, T_1, and U_s, for a shocked material. Introducing a material Equation Of State (EOS) in terms of internal energy, pressure, and volume, the Hugoniot equations are reduced to two equations: conservation of mass and momentum. Reducing the number of equations also reduces the number of unknowns to four variables. The solution to this system of equations generally requires additional knowledge of the shocked material which is the approach

typically implemented. However, a Rayleigh line equation or graph to solve for the state after the shock wave can also be utilized. The most common variable used to solve shock Hugoniots is the shock velocity since it is easily observed. For shock waves in solids the secondary variable easily observed is particle velocity and in air shocks it is pressure.

The Hugoniot relations are most commonly presented as 'Hugoniot Planes' which relate the four shock parameters and facilitate determination of final states from given initial conditions and shock jump interactions. The most common Hugoniot plane plotted relates shock velocity to particle velocity and is referred to as the $U_s - u_p$ Hugoniot. Shock velocity and particle velocity are frequently experimentally determined and plotted as U_s versus u_p. Most materials exhibit a linear relationship in this Hugoniot plane such that:

$$U_s = C_h + s \cdot u_p \tag{1.4}$$

Where C_h and s are fitting parameters. C_h has units of velocity and s is unitless. If the Hugoniot relationship is given as a quadratic equation that implies that there is likely material behaviors, such as phase change or a shift in crystal lattice, causing a change in slope or a transition region [10]. PMMA exhibits a non-linear $U_s - u_p$ shock Hugoniot behavior which is to be discussed later [4]. The best representation for such a material response is to fit linear equations to segments of the Hugoniot. The Hugoniot planes are not limited to $U_s - u_p$ Hugoniot. The other common Hugoniot planes are pressure-specific volume, where the Rayleigh line is plotted, and the pressure-particle velocity Hugoniot plane. Hugoniot planes are plotted or examined to understand other state variable variations for different shock conditions [10]. The Hugoniot equations are utilized to define the material state after a shock wave, so all of the planes represent the same states, but each allow different visualization and insight for the property relationships.

As such, the mechanism for a shock wave decaying to the acoustic sound speed of a material is best described in the pressure-volume, $P - v$, Hugoniot plane using the Rayleigh line slope change. Figure 1.5 shows the $P - v$ Hugoniot where the region below P_1 is the elastic region, P_1 to P_2 is the elastic-plastic region, and above P_2 is the plastic region where strong shocks occur. Since the Hugoniot is not the path a material takes when shocked, it represents all of the possible states to be reached after the shock. However, the Rayleigh line, the linear line connecting $P_1 v_1$ and $P_2 v_2$, represents the shock "jump" from the initial material state to the shock state [10]. As such the Rayleigh line is drawn connecting the initial and final states.

In the elastic region the wave velocity will be equal to the longitudinal sound speed of the material C_L. In the plastic region the plastic shock wave velocity is higher than the elastic sound speed, which can be calculated using the slope of the Rayleigh line. In the region between P_1 and P_2 the Rayleigh line still can be drawn but has a slope less than the elastic region of the material. This is the graphical representation of the elastic precursor. Two waves will exist, the elastic wave having a velocity of C_L and the slower plastic wave having a velocity given

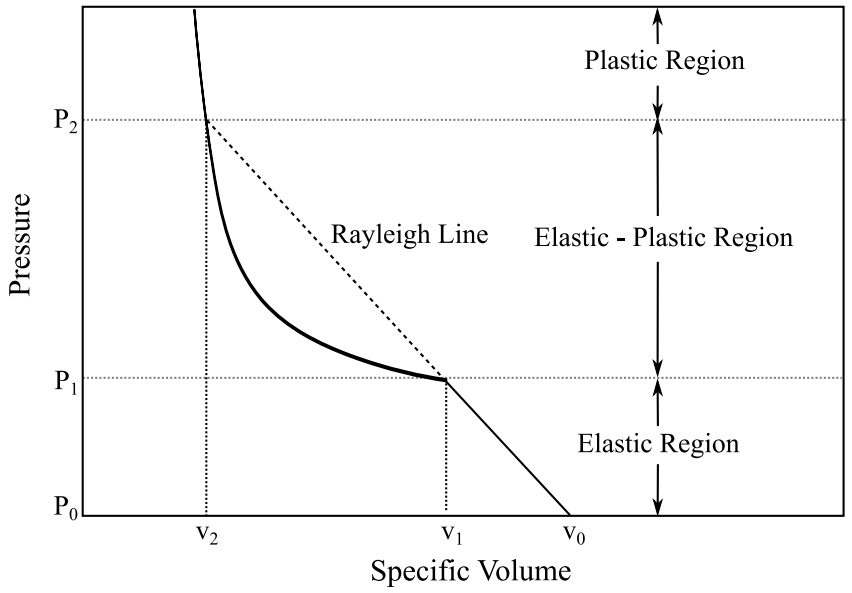

Figure 1.5: Pressure versus specific volume Hugoniot plane.

by the slope of the Rayleigh line indicating an elastic-plastic material response [10].

The last Hugoniot plane to be discussed here for completeness is the pressure-particle velocity, $P - u_p$, Hugoniot plane [10]. The $P - u_p$ is typically used for analyzing shock-shock interactions and impact problems. In this Hugoniot plane "left going" shocks and "right going" shocks are defined. Manipulation of the momentum equation leads to:

$$\text{Left going:} \quad P_L = \rho_0 C_0 (u_0 - u_1) + \rho_0 s (u_0 - u_1)^2 \tag{1.5}$$

$$\text{Right going:} \quad P_R = \rho_0 C_0 (u_1 - u_0) + \rho_0 s (u_1 - u_0)^2 \tag{1.6}$$

The definition of left going and right going shocks is based upon the Lagrangian reference frame. For planar impact problems the pressure between the two materials impacting is equal such that P_L=P_R. Graphical solutions in the $P - u_p$ also exist for impact problems.

The Rankine-Hugoniot equations are a useful set of equations which can be used to fully define the shock wave. The Hugoniot planes yield additional information. The $U_s - u_p$ Hugoniot can be used to determine the particle velocity if the shock velocity is known or visa versa. The $P - v$ Hugoniot can be used to calculate the shock velocity using the Rayleigh line slope and the $P - u_p$ Hugoniot describes shock-shock interactions and planar impact problems.

The shock front is discontinuous in nature, however, the unloading of the shock in which the material returns to its zero pressure state is a continuous

process [10]. The unloading process is often referred to as a rarefaction wave or a release wave [8, 10]. The source of the wave influences the shape of the pressure pulse, i.e., the compression and release wave shape. Impact experiments impart a square shock pulse with a duration proportional to the flyer plate thickness, Figure 1.6a. The shock imparted by an explosive point source yields shock with an instantaneous jump and a subsequent exponential decay, as shown in Figure 1.6b [1]. The geometry of the wave, one-dimensional (1D) planar wave versus a three-dimensional (3D) spherical wave, is of importance for the shock attenuation.

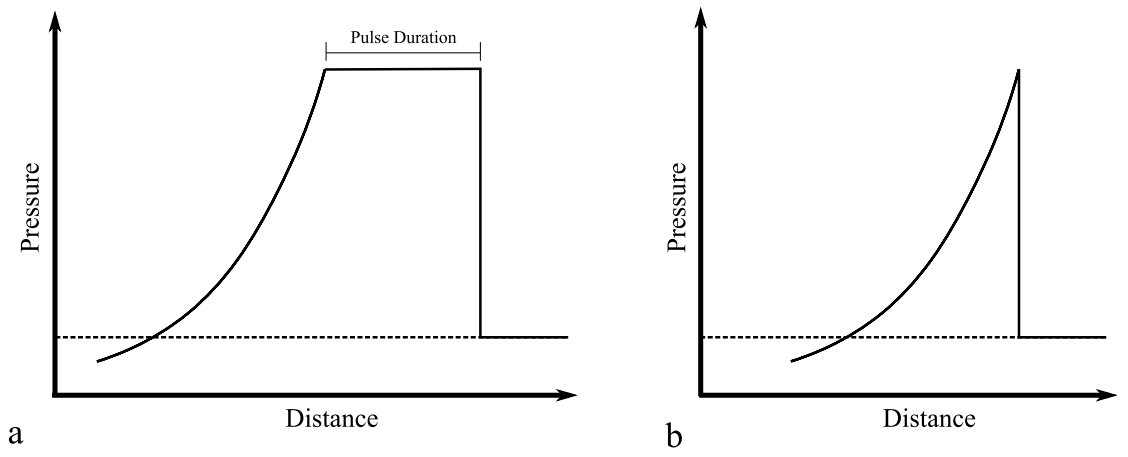

Figure 1.6: Schematic of an idealized (a) square shock pulse and (b) explosive shock pulse.

The attenuation of the shock wave occurs when the shock wave is overtaken by the release wave [13]. Shock wave attenuation is the pressure decay of the pulse as it propagates through the material. As shown schematically in Figure 1.7 if the pulse has a longer pulse duration, meaning it does not decay immediately after the peak pressure, then the wave propagates longer without being attenuated by the release wave. Once the release wave catches up with the compression wave front then the peak pressure begins to decay thus reducing the velocity the wave is traveling at. The concept of this decay behavior was explored by Duvall, where the shock pressure ultimately decays to an elastic wave at large distances from the source [14].

1.2.1 Experimental polymethyl methacrylate (PMMA) shock studies

PMMA is an amorphous glassy polymer that exhibits non-linearity and strain-rate dependence [4, 15]. Characterization of the shock response of PMMA has been carried out since the late 1960's with the rise of interferometry techniques [4, 11, 16–19]. Extensive research has been carried out to define the dynamic

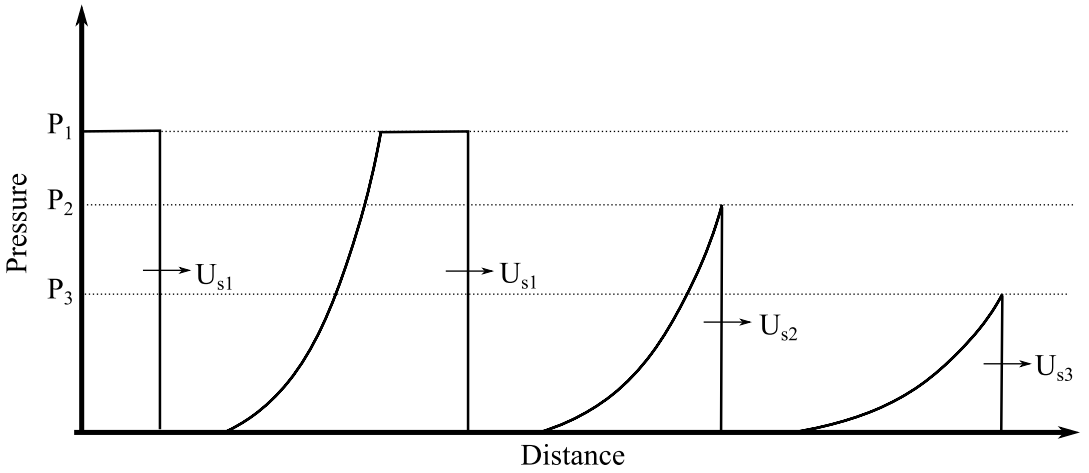

Figure 1.7: A Schematic of shock wave attenuation as a wave propagates through a material. As the wave propagates through the sample and the peak pressure decreases ($P_1 > P_2 > P_3$) the shock velocity also decreases ($U_{s1} > U_{s2} > U_{s3}$).

material response from the shock-wave evolution in PMMA [18] to the definition of the shock Hugoniot [2, 3, 20, 21], the viscoelastic/viscoplastic response [22, 23], shock response at elevated temperatures [12], window corrections and index of refraction variation [4, 24, 25], and even the comparison of manufactures [5]. The experiments typically observe one-dimensional wave profiles created using planar impact experiments or explosive plane-wave generators.

One-dimensional (1D) wave profiles from planar impact experiments began early on. A gradual rounding up to the peak particle velocity when measuring the particle velocity history was noted [4]. This behavior was the first indication of the viscoelastic response of PMMA. Viscoelastic materials are materials which exhibit a material response that is both elastic and viscous in nature [26]. Viscoelastic materials exhibit time- and load-dependence. Time-dependence is revealed as strain-rate sensitivity, stress relaxation, creep and hysteresis [26]. For viscoelatic materials the deformation history, such as the amount of force applied and how long the force was applied, plays a significant role in the material's response to additional loading. PMMA is viscoelastic by nature therefore the viscoelasticity is often attributed to strain-rate sensitivity and time-dependence experimentally observed during shock loading [4].

One of the most notable shock characteristics is the non-linear shock Hugoniot. The non-linear shock Hugoniot for PMMA has been validated using 1D wave profiles [2–5, 22]. The $U_s - u_p$ Hugoniot from previous works is presented in Figure 1.8 where it can been seen that there is a non-linearity up to a particle velocity of approximately 0.5 mm/μs which coincides with a pressure of approximately 2 GPa [27]. A rate-dependence, or a viscoelastic response, causes the non-linear region in the Hugoniot [4, 27]. By accounting for the inter-molecular

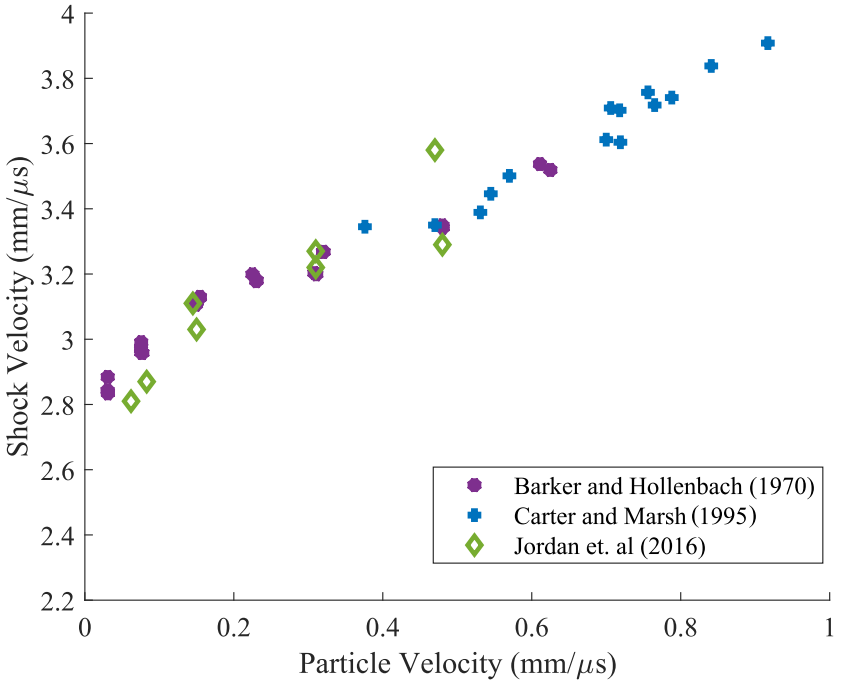

Figure 1.8: $U_s - u_p$ Hugoniot for PMMA for experimentally determined values of shock velocity and particle velocity collected by Barker and Hollenbach [4], Carter and Marsh [2], and Jordan et al. [5].

and inter-chain forces in a polymer it was found that the shape of the non-linear $U_s - u_p$ Hugoniot was achieved when predicting the shock Hugoniot [4]. This behavior is attributed to the magnitude of the forces along a polymer chain being much larger than the forces between polymer chains [5]. Due to the difference in force magnitude, during the early stages of compression, the non-linear $U_s - u_p$ region, the length along the polymer backbone will remain essentially unaffected while the distance between the polymer chains decrease. As the forces between the neighboring chains increase reaching the same order of magnitude as the polymer backbone the $U_s - u_p$ becomes linear [2, 5]. The validity of the use of Hugoniot equations could be in question since PMMA is strain-rate dependant. For a single shock velocity value there exists a region where two particle velocities could occur, however, in the linear region the material becomes rate-independent [4].

The viscoelastic response of PMMA has also been attributed to anomalies observed during shear strength experiments. The shear strength of PMMA was determined for increasing 1D planar impact experiments. Stress gages were aligned such that the lateral and longitudinal components of stress could be experimentally measured [5, 22]. The equation used to calculate the shear strength, τ, is a function of the Hugoniot stress, σ_{xh}, and lateral stress, σ_l [28, 29]:

$$2\tau = \sigma_{xh} - \sigma_l \tag{1.7}$$

For impact stresses in the range of 0.5 - 4.06 GPa the shear strength was found to increase with in increased impact stress [22]. A reduction in lateral stress, indicating material strengthening, relative to the increase in shear strength was attributed to the viscoelastic and/or viscoplastic response of PMMA [5, 22]. Jordan et al. [5] found that the reduction in lateral stress was only prevalent in the lower region of the shock Hugoniot whereas Millett and Bourne [22] measured the lateral stress reduction both above and below the PMMA Hugoniot elastic limit.

The Hugoniot elastic limit (HEL) of a material defines the upper limit for elastic wave propagation [4, 10, 30]. Above the HEL the two wave structure, shown in Figure 1.3, consisting of a faster low pressure elastic wave and a slower high pressure plastic wave can actually be experimentally observed [31]. The two wave structure can be observed via particle velocity history or stress measurements as a function of time. However, an elastic precursor is not observed in the particle velocity histories for PMMA requiring other methods for determining the HEL of PMMA [4, 11]. One method is to analyze loading-unloading stress-stain paths [4]. The method utilized the particle velocity histories (u_p) and the associated shock velocities (U_s) to calculate the change in stress σ and strain ϵ from the initial state to the final using:

$$\Delta\sigma = \rho_0 U_s (u_{pf} - u_{pi}) \tag{1.8}$$

$$\Delta\epsilon = (u_{pf} - u_{pi})/U_s \tag{1.9}$$

Through this method it was found that PMMA behaves like a nonlinear viscoelastic material below 0.7 GPa and above 0.7 GPa the behavior is elastic-plastic [4]. This indicated a Hugoniot elastic limit (HEL) of approximately 0.7 GPa. Uncertainty in this methodology stems from the rate-dependence of PMMA, for a single shock velocity more than one particle velocity exists. The accepted HEL for PMMA is 0.75 GPa [11, 12, 22] which was determined though shock-reshock experiments [11]. The particle velocity wave profiles indicated an elastic material response below 0.75 GPa and an inelastic material response above 0.75 GPa [11] which was the approximate value of the HEL determined by [4]. The non-linear shock Hugoniot reflects HEL of PMMA [12]. The first segment of the linear region of the shock Hugoniot exists up to a particle velocity of approximately 0.13 km/s where it terminates. The stress associated with this termination is approximately 0.75 GPa. The transition zone occurs from 0.75 GPa to 1.5 GPa, where the principal Hugoniot of PMMA begins.

Interferometry is widely used to record the particle velocity history of PMMA. Prior to interferometry, particle velocity was determined using the wave shape on the rear sample surface measured using a pressure sensitive transducer or measuring surface motion using displacement pins [16, 32]. Once the Doppler-shifted laser was developed interferometry gained popularity. Early on the Michelson interferometer in a heterodyne configuration was used to measure slow velocities

[33]. The record rate of the Michelson interferometer was not fast enough for shock studies due to rapid fringe development at high velocities. The solution to detecting rapid displacements was to incorporate a 'Delay-Leg' giving time for the fringe patterns to be recorded leading to the development of VISAR - Velocity Interferometry System for Any Reflector [4, 33]. This lead to the development of interferometers such as the Fabry – Pérot interferometer [33] and the Optically Recording Velocity Interferometer System (ORVIS) [34]. The advantages of interferometry are the accuracy, it is a non-intrusive measurement, and the full velocity history can be measured [4, 16]. Measuring the full velocity history means both the compressive wave and the rarefaction wave can be measured [4].

Photon Doppler Velocimetry (PDV) Photon-Doppler velocimetry (PDV), like VISAR and the Fabry – Pérot system, is an interferometry technique which utilizes the Doppler-effect to detect surface motion [35]. The Doppler-shifted light is mixed with a reference light creating an interference pattern. In its simplest form PDV is a fast fiber based Michelson interferometer [36, 37]. PDV can be arranged in a homodyne arrangement or a heterodyne arrangement. The homodyne system uses a single laser as both the reference laser and the detecting laser whereas the heterodyne system uses two separate lasers of different frequencies as the reference laser and the detecting laser [35]. A diagram of the heterodyne arrangement, which is the arrangement most often utilized, is shown in Figure 1.9.

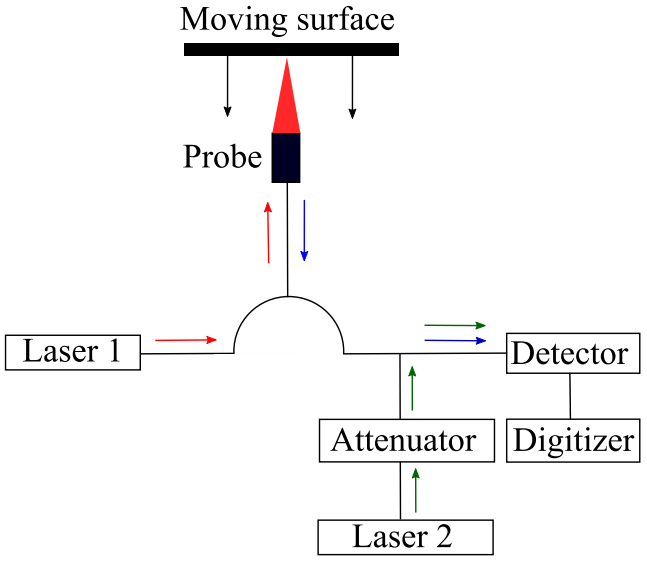

Figure 1.9: A diagram of the heterodyne PDV laser arrangement.

PDV is highly accurate and can measure a broad range of velocities from a few m/s up to approximately 50 km/s [36, 38]. PDV has been implemented on a broad range of experiments due to the ease of implementation. Some examples

of tests PDV has bee instrumented on are cylinder tests, projectile tests, ejecta, and bare high explosives [39]. Since its introduction, PDV has replaced VISAR for most shock studies [5, 39]. Novel measurements of the shock pressure decay of PMMA from a spherical explosive source have been recorded using PDV. The shock pressure decay was measured at distances of 0 to 10 mm from an explosive detonator [1], which yielded an initial rapid decay in peak shock pressure within the first 2 mm of shock propagation, followed by a slower decay in the next 8 mm.

For materials that are not optically transparent, PMMA is often used as a witness block material or as a window material for interferometry testing [5]. Witness blocks yield the advantage of visualizing the performance of the material. PMMA witness blocks have been used to characterize detonator performance using high-speed imaging and PDV [40, 41]. A window material is beneficial to reduce interface reflections when measuring shock compression- and release waves at an interface [4]. When using PMMA as a window material for interferometry based shock studies, a velocity correction is often required [4, 24, 25, 42]. This is because the shock wave propagating through the PMMA introduces temporary birefringence altering the refractive index of the material [9, 42, 43]. The refractive index change is associated with a change in density perturbing the measurement at the specimen/window interface [42]. Experiment have been preformed to characterize window material response of PMMA due to shock loading [24, 25, 27] where it has been found that the velocity measured from laser interferometry requires essentially no window correction [27]. Often it is useful to characterize the refractive index of a material using an empirical formula such as the Gladstone-Dale law:

$$n = 1 + k\rho \tag{1.10}$$

Where ρ is density, n is refractive index, and k is the Gladstone-Dale constant (k $\approx$ 0.415 cc/g for PMMA). It has been found that the relationship between refractive index and density are linearly related for shocked PMMA [27] satisfying the Gladstone-Dale law [24]. A modified Gladstone-Dale equation has been fit to PMMA [27]:

$$n = 1.01 + 0.413\rho \tag{1.11}$$

Where ρ has units of g/cc. The modified Gladstone-Dale law for PMMA and the formal equation only differ slightly. The agreement of the material response to the Gladstone-Dale relationship indicates that a window correction is not required for PMMA [27]. However, the stress induced change in optical properties from compression waves in PMMA makes visualization of the shock propagation possible.

Experimental methods for determining shock velocity The optical transparency and stress induced change in optical properties of PMMA makes high-speed imaging advantageous for the visualization of the material response [15, 44]. The instantaneous increase in density imparted by a shock wave allows for visualization of the wave and its propagation [21, 45]. Tracking the shock wave position as

a function of time is a direct measurement of the shock velocity. Streak imaging was used early on to determine the explosive shock velocity of PMMA in the high pressure range of 1.5 GPa to 59.9 GPa [2]. Experiments have recently been conducted where shock-position as a function of time was measured simultaneously with particle-velocity histories in PMMA [1, 46]. The experiments were achieved using high-speed schlieren imaging, a refractive imaging technique, in conjunction with PDV. High-speed schlieren imaging is used primarily in the gas phase, with extensive application to shock wave measurements including extracting quantitative air shock density profiles [47, 48], but has also been implemented to measure shock Hugoniots of optically transparent solid materials [21]. Further discussion of schlieren and shadowgraphy is in section 1.4.1.

High-speed imaging of the shock response of PMMA requires high frame rates due to strain rates on the order of 10^6 s^{-1}. Early high-speed imaging testing utilized streak imaging [2] where higher sweep speeds were achievable. The alternative to high-speed cameras is using gauges. Shock experiments in solids have utilized electromagnetic gauges [27] and most commonly piezoresistive Manganin gauges [5, 22, 49–51]. These gauges are either embedded in the solid directly during a casting operation or the material is cut to insert the gauge. Shock velocity is measured using the shock arrival time at a single gauge and a free surface measurement or the shock arrival time at two gauge locations.

Measuring shock velocity is not the primary measurement when implementing gauges. Depending on the gauge type and orientation the shock stresses of the material can be determined. Three piezoresistive deviatoric gauges in different planes have been used to determine mean and deviatoric shock stresses in PMMA [51]. Using piezoresistive gauges to measure the lateral component of stress (σ_l) [50] has allowed for shear strength (τ) to be calculated using two measured values (Equation 1.2.1) [22]. Gauge measurements are crucial in determining the stress state of a material. Extracting quantitative information about the stress state of a material due to shock loading from high-speed images has not been done.

1.2.2 Computational polymethyl methacrylate (PMMA) shock studies

Computations, or numerical simulations, model material behavior and are frequently compared to an experiment. Since extensive experiments have been conducted to understand the shock response of PMMA, similar efforts have been put into simulating the material response. Relative to shock experiments the key factor is having an Equation Of State (EOS) that accurately represents the shocked material response [52]. Computational shock studies consist of defining an EOS for the dynamic material response [52, 53], simulating density distributions [54], modeling the growth and decay of acceleration waves [23], and numerically investigating the influence of viscoelasticity [55, 56].

PMMA shock experiments allude to a viscoelastic response in the weak shock regime [4, 5, 22, 27] in which computations validate this response [55, 56]. The

rounding up to the peak particle velocities captured in experiments was accurately simulated for particle velocities of 64 m/s to 645 m/s when accounting for the viscoelasticity of PMMA [55]. The Maxwell model of viscoelastic matter with a constant relaxation time accurately models the shock wave front with less accuracy in the modeled release wave [55, 56].

In general, physically based polymer models are difficult due to their complex internal structure [57]. When accounting for the intermolecular forces and interchain forces it was found that the modeled $U_s - u_p$ Hugoniot trend matched the experimental Hugoniot trend, however, the model did not match the experiments exactly [4]. When modeling polymers especially in the low strain rate regime nonlinear rate sensitivity, nonlinear unloading, creep, and recovery have to be accounted for to accurately model the material [57]. When developing an EOS for a material undergoing shock compression it is of particular importance to understand the thermal response of the material [58, 59]. Experimental temperature measurements in shock loaded PMMA has been extensively researched in the low pressure, viscoelastic, regime [12, 60] and in the high pressure, strong shock, regime [53, 59]. In the strong shock regime, where $\sigma > \sim$1.5 GPa, the viscoelasticity is no longer a concern in which the principal Hugoniot is used when defining the EOS [52]. Due to the amount of experiments that have been conducted for shock compressed PMMA model validation can easily be achieved [61].

1.3 Dynamic fracture

Fracture mechanics is a relatively new field of mechanics which is important for reducing potential structural failures. Two approaches for quantifying a material's fracture response are: the energy criterion and the stress intensity approach [62]. The energy criterion, first explored by Griffith [63], was defined by an energy release rate **G**:

$$\mathbf{G} = \frac{\mathrm{d}\Pi}{\mathrm{d}A} \tag{1.12}$$

Where Π is the total potential energy and A is the crack area. Energy release rate is based on the Griffith energy balance in which the first law of thermodynamics was applied to the concept of crack growth [62]. In order for a crack to grow there must be a potential energy to overcome the surface energy to create a new surface. Crack growth is ultimately a rate process that occurs when the energy release rate is equal to the critical energy release rate, $\mathbf{G_c}$, which is a material property. In general, the energy release rate relates the net change in potential energy to crack extension.

The second approach for describing fracture growth employees a Stress Intensity Factor (SIF), K_I to quantify all components of stress, strain, and displacement

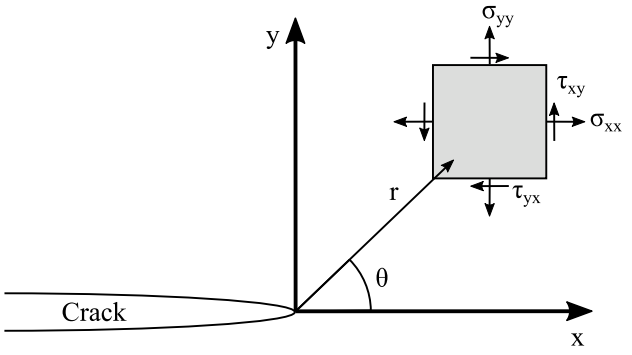

Figure 1.10: Coordinate axis for stresses near a crack tip.

near a crack tip. The stress intensity factor completely defines the crack tip conditions. K_I is not material dependant but rather is a function of sample geometry and far field load. There are three modes of loading that are considered, Mode I (opening), Mode II (in-plane shear) and Mode III (out-of-plane shear) which correspond with stress intensity factors of K_I, K_{II}, and K_{III}, respectively. For an linear elastic cracked body, the crack tip stress field is characterized in polar coordinates such that at the crack tip there is an $r^{-1/2}$ singularity. The stress fields can be expressed as:

$$\lim_{r\to 0} \sigma_{ij}^{(I)} = \frac{K_I}{\sqrt{2\pi r}} f_{ij}^{(I)}(\theta) \tag{1.13}$$

$$\lim_{r\to 0} \sigma_{ij}^{(II)} = \frac{K_{II}}{\sqrt{2\pi r}} f_{ij}^{(II)}(\theta) \tag{1.14}$$

$$\lim_{r\to 0} \sigma_{ij}^{(III)} = \frac{K_{III}}{\sqrt{2\pi r}} f_{ij}^{(III)}(\theta) \tag{1.15}$$

Where $f_{ij}(\theta)$ is a dimensionless function of θ where θ is defined in Figure 1.10. Crack growth occurs when the material's resistance to crack growth, K_{IC}, is overcome by the stress intensity factor, K_I.

In the case of explosively driven fracture the same force balance holds true, fracture occurs when the fracture driving force exceeds a materials resistance to crack extension. The explosive detonation process is a chemical reaction resulting in the production of a shock wave and high-pressure gases [7] which are the two mechanisms for driving explosive fracture growth. The detonation of energetic materials imparts a shock wave into the material causing a rapid increase in material strain [7, 10]. The area immediately near the explosive source is cracked and crushed due the stress from the strong shock greatly exceeding the compressive strength of the material [7, 64]. If the explosive gas pressure also exceeded the materials resisting compressive stress then the fractures will be driven further [65].

There are three distinct fracture regions when analyzing fracture patterns from contained explosions in geomaterials [7]. The strong shock region, the non-linear zone, and the elastic region. The fractures in the three zones are then extended due to cavity expansion. The three zones of the fracture pattern are imparted by the stress waves then extended by the confined explosive gases. The first region, which is the strong shock region, crushes the geomaterial because the strength of the wave significantly exceeds the compressive strength of the material. The non-linear zone is a transitional zone between the crushing fracture zone to the elastic region. In this region the strength of the wave is still above the yield strength of the material. The fractures in the elastic region are due to the tangential stress. In the elastic region the fracture are significantly longer than the first two regions. In the final step of explosive induced fracture, the existing fractures are driven by the pressurized cracked cavity. A full description of the fracture process is described in [7].

1.3.1 Experimental polymethyl methacrylate (PMMA) fracture studies

PMMA is an amorphous brittle material that is often used for fracture studies due to its optical transparency [66, 67] and because it exhibits fracture patterns similar to rock [6, 7]. Dynamic fracture in PMMA due to detonation and deflagration of energetic materials has been explored both theoretically and experimentally to establish driving mechanisms [7], compare various energetic sources [68], and to measure physical parameters used in theoretical models [6, 69]. The dynamic fracture response of PMMA has been explored for large scale blast experiments [6, 69, 70], small scale blasts [7, 71], impact testing [67, 72], and tensile testing [73].

Early research into the explosive induced fracture process began with small scale experiments to study the difference between explosive fracture and gas fracture separately [7]. In order to study the stress wave induced fracture separate from the explosive gases, an underwater spark discharge was used. The fracture pattern created by the stress wave in two-dimensional (2D) geomaterials were studied post-mortem. A qualitative analysis of the fractured samples revealed that two fracture zones appeared. It was found that the fractures in the first zone do not have sufficient time to grow since the shock wave is a short duration pulse, and the zone was sufficiently "crushed" due to the pressure greatly exceeding the yield strength of the material. In the second zone, the surface of the cracks were mirror like, indicating that they were running cracks. Increasing the peak input pressure extended the fracture lengths in both zones. Experiments using three-dimensional (3D) cylindrical PMMA samples to study the explosively fracture response found that the amount of explosives determined the extent of fracture growth [70].

Small-scale 2D explosive induced fracture experiments conducted by Kutter and Fairhurst [7] explored crack extension under uni-axial compression of the PMMA disks. Shock induced fracture experiments and gas driven fracture experiments were conducted separately. The experiments revealed separately that the preferred fracturing direction was in the direction of the maximum principal stress

for both the gas driven and shock driven fractures. The reason for the the fractures aligning with the direction of the maximum principal stress was hypothesised to occur because the fractures propagate in the direction with the highest tangential tension [7]. Studying the gas driven and shock driven fracture separately revealed that the pressurized gases are not very effective alone, however play a significant role in the blasting process [7].

The 3D blast-induced fracture response has been explored in cubes of PMMA for a sealed cylindrical charge, a stemmed cylindrical charge, a stemmed cylindrical charge with pre-fractures and uni-axial stress [6]. PMMA was used as the test specimen material because the fracture patterns of PMMA are similar to fracture patterns produced in rock with the only difference being in the length [6, 7]. High-speed imaging was implemented for visualization of the shock induced material response, however, the majority of the analysis was a comparison of the post-test fracture patterns. From the analysis it was found that containing the explosive gases significantly changed the fracture pattern when compared to the fracture pattern for the unconfined explosive gas experiment [6]. It was concluded that approximately 11% of the total fracture surface was from the stress wave, thus, the majority of the fracture was produced by confined explosive gases. Much like the small-scale experiments preformed by [7], it was found that the application of uni-axial compressive stress caused the fractures to align with the direction of the major principal stresses [6]. The high-speed imaging of the blast-induced fracture aided in analyzing the stress waves, but only a few images of the wave were recorded. Recent advancement in high-speed imaging technology has aided in the ability to record more of the event [74].

Three-dimensional explosive induced fracture experiments from two different detonators leveraged advancements in high-speed imaging to visualize the fracture event [70]. The explosive induced fracture response of cylindrical PMMA samples was visualized at 10 thousand frames per second in which the cylinder of PMMA for one of the fracture experiments was captured fracturing in half. For the sample which was still intact, post test analysis revealed two fracture zones, the shock driven fracture and gas driven fracture zones. As expected, the shock driven fracture zone was significantly smaller than the gas driven fracture zone to which the conclusion that gas driven fracture is more significant was made [70]. However, the three dimensional blast induced fracture radius as a function of time have not been reported until recently by Torres et al. [69]. The three dimensional effects introduce complexity associated with measuring fracture lengths or stress intensity factor. Furthermore, the rate at which the blast induced fracture occurs also impacts the ability to measure the blast induced stress intensity factor. One of the complexities associated with measuring Dynamic Stress Intensity Factor (DSIF) has been over come with high speed camera developments. Recent research has implemented high-speed imaging to analyze the dynamic fracture growth and extract fracture parameters such as resolved fracture length, and DSIF [75, 76].

The blast-induced DSIF in PMMA has been determined using the method of caustics [71, 76]. The optical method of caustics utilizes light deflection caused by the stress singularity near the crack tip to be concentrated, creating ”shadow”

spots with areas of bright light rings around the shadow, which are known as caustics [71]. The caustics method has been extensively used to determine both static and dynamic SIF [75, 76] with limited application for blast-induced fracture [71]. Calculating SIF using the caustics method requires the caustics to be circular, yet, blast wave experiments cause elliptical caustics [76]. To overcome the caustic shape numerical simulations were used to define a relationship between the blast induced DSIF and the caustic shape [76].

Often experimental results have been used in conjunction with numerical simulations to validate the simulation results for a simple geometry allowing for more complex geometries to be simulated. Inner fracture connectivity between two cylindrical holes in thin PMMA plates, 300mm x 400 mm x 5 mm, were explored both experimentally and numerically determining there is a critical distance for the fractures to coalesce [77]. Others have simulated similar geometries in thin PMMA plates yielding similar results [78, 79].

In the case of external confinement a material's fracture response is dependant on the compression direction and the material's in-situ stress [80]. Uni-axial compressive stress experiments have shown that fractures align with the direction of major principal stresses [6, 7]. If the compressive stress is bi-axial the fracture response is dependant on the ratio between the vertical and horizontal components of the compressive stress [80]. Experiments conducted in 300 mm x 300 mm x 5 mm plexiglass plates showed that bi-axial compression reduced the time to crack arrest while increasing SIF [81]. A material's fracture extent is based on the fracture driving force, shock pulse and gas pressure, and the material's resistance to crack growth. A material's resistance to fracture is dependent on the material properties and the in-situ stress.

1.3.2 Computational fracture studies

Experimental results are used to validate numerical simulations allowing for complex fracture geometries to be explored [82]. Simulation of the fracture response of geomaterials is of interest for hydraulic fracturing [65, 83] and simulation of blast induced fracture [69, 84–86]. Ultimately, the ability to simulate dynamic fracture propagation is of interest which requires high-fidelity constitutive models.

The process of hydraulic fracturing is a achieved by the fluid pressure wedging the fractures open. Simulation of this phenomenon is fairly well understood. Equilibrium equations for the geomaterial and fluid volume are used in conjunction with fluid flow equations and propagation conditions to simulate the propagation of planar fractures [65, 83]. In the simplest form, the fluid flow is assumed to be laminar, which can be an appropriate assumption in some cases. Recent advancements in hydraulic fracturing in low permeability reservoirs introduced advancements in the hydraulic fracturing methods to which the fluid flow borders turbulent flow. Simulation efforts have followed the need for simulating turbulent fluid driven fractures [83]. Since geomaterials are porous media with

granular structures, computations to better simulate the fluid driven fracture response of granular materials have also been studied [87, 88]. The method for simulating hydraulic fractures can be extend to blast induced fractures if the gas driven fractures are being analyzed independently [65].

The reason for transiting from hydraulic fracturing, which is a quasi-static process, to dynamic fracturing stems from in-situ stresses aligning the fractures in a preferential direction [89]. The preferential direction the fractures will grow aligns with the direction of the maximum principal stresses which is not always ideal. Dynamically fracturing the material such that the dynamic stress field is strong enough to overcome the static stress field creates radial fractures rather than the fractures alignment being dictated by the in-situ stresses [89]. Dynamic fracture can be achieved using high-energy gas fracturing (HEGF), high-pressure gas blasting (HPGB) [89], Instantaneous Expansion with a Single Fracture (IESF) [90], or by simply using explosive initiation [86] which was of interest for the present work.

Modeling of the explosive induced fracture response of a material is complex due to the multiple time scales in which the process occurs over and the in-situ stresses add another layer of complexity. There have been different approaches for simulating the fragmentation of geomaterials which are validated against experimental results. A numerical investigation of the fracture pattern produced by stress wave propagation was preformed in [85] which was compared to experiments conducted in granite samples. The numerical simulations accurately simulated the experimental fracture patterns. The blast induced fracture response for deep rock has also been explored numerically [86]. It was found that at deep enough depths the beneficial effects of explosive fracturing are limited. Ultimately, the ability to accurately model the material behavior of geomaterials due to explosive loading requires appropriate material models. As such, experiments have been conducted to compare commonly used hydro-codes under different stress conditions [82].

1.4 Optical experimental methods

Maxwell formulated a relationship between a materials refractive indices and the principal stresses [9]. The relation is the stress-optic law or "Brewster's law". It was found that materials which exhibit stress induced birefringence will temporary portray a direct relationship between the ellipsoid of stress and the index ellipsoid [9]. The stress-optic law is based on the proportionality of the indices of refraction and the principal stresses for temporarily birefringent materials, which is expressed as:

$$n_1 - n_0 = \Delta n_1 = A_c\sigma_1 + B_c(\sigma_2 + \sigma_2) \tag{1.16}$$

$$n_2 - n_0 = \Delta n_2 = A_c\sigma_2 + B_c(\sigma_1 + \sigma_3) \tag{1.17}$$

$$n_3 - n_0 = \Delta n_3 = A_c\sigma_3 + B_c(\sigma_1 + \sigma_2) \tag{1.18}$$

Where n_1, n_2 and n_3 are the refractive indices that coincide with directions of the principal stresses σ_1, σ_2, and σ_3. A_c and B_c are the stress-optic constants, and n_0 is the refractive index of the undisturbed material. The temporary birefingence of a material can thus be leveraged to visualize stresses and strains in a material. The refractive index change is indicative of an optical path length change. It is important to note that surface deformation, or change in thickness, also contributes to a change in optical path length of the transmitted light rays. Methods such as photoelasticity [9], the shadow optical method of caustics [71, 91], coherent gradients sensing (CGS) [92, 93], and digital gradient sensing [94, 95] are a few examples of methods which leverage Brewster's law to quantify the principal stresses of a material based on the stress induced change in optical properties. Photoelasticity is the only method in which birefringence is required for the optical method to work, the other methods utilize the stress optic law for both birefringent material and optically isotropic materials. These experimental methods are widely used in the study of fracture mechanics.

Photoelasticity is a non-destructive full-field optical method which is used to visualize stresses and strain fields in a structure and measures the principal stress differences [93, 96, 97]. This method is based on light interference to which the polarization of light is utilized to visualize isoclines and isochromes. The isoclines and isochromes are used to determine areas of stress concentration [96]. There are several methods to produce polarized light such as, Polaroid sheets, through scattering, reflection, or double refraction [9]. There are instruments such as a polariscope which consist of polarizers used to measure the relative phase difference. Photoelasticity has been used to experimentally measure stress distributions and fracture toughness in PMMA [96, 97].

Photoelasticity is ideal for full-field optical analysis, however, difficulties can arise with measurement of stress singularities [98]. For stress singularities, like crack tips and discontinuities, analysis of isocromatic fringe patterns is non-ideal. The introduction of the optical method of caustics introduced an alternative method for quantifying stress concentration problems [9, 98]. Unlike photoelasiticity, the optical arrangement is quite simple because the method is based on the law of refraction of geometric optics. All that is required is an illumination source and a reference screen [98]. The light from the illumination source propagating through, or reflecting off, a deformed specimen will be refracted from the original light path creating a shadow pattern as depicted in Figure 1.11. Evaluation of the shadow patterns then can be applied to solve stress concentration problems [9]. This method is typically implemented for determination of stress intensity factors around crack tips in which only the diameter of the caustic is needed [71]. However, the mapping equations utilized for the shadow optical method of caustics are general and have been utilized for other optical analysis methods such as coherent gradient sensing (CGS).

Coherent gradient sensing is a full-field optical technique developed by Tippur et al. [99] to measure surface slopes or in-plane stress gradients [93]. However, due to the similarity to the optical method of caustics it was extended to quantification of crack tip deformations [93, 100]. This method is a lateral shearing

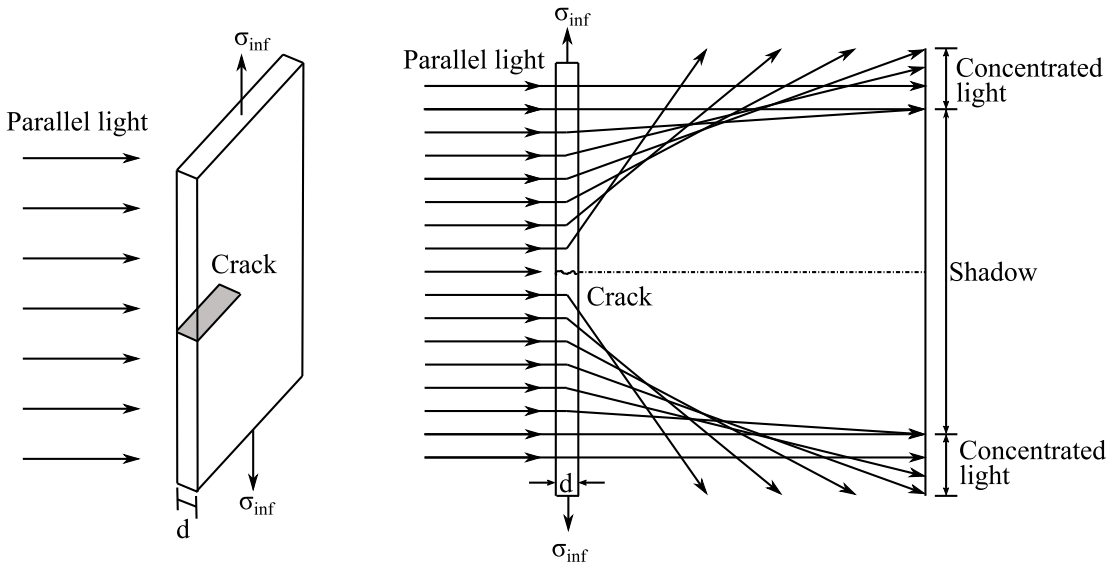

Figure 1.11: A schematic of the light rays producing the shadow pattern created using the optical method of caustics for a transparent material with a crack.

interferometry technique to which a first order diffraction analysis is used [99]. The optical arrangement consists of light propagating through, or reflecting off, of the specimen, two Ronchi gratings, a filtering lens, and and a camera. The Ronchi gratings and the filtering lens are what create the interference pattern. This method has been found to be more reliable than the method of caustics and is widely used for static and dynamic fracture analysis [92, 93, 101]. The mapping of the deflected light ray's angular deflection to the mechanical field used for CGS was then extended to Digital gradient sensing (DGS).

Digital gradient sensing (DGS) is a full-field method for measuring small light deflections due to local stresses in optically transparent materials [94]. This method is similar to background oriented schlieren (BOS) [102–104] in that both methods leverage a speckled background (BG) to detect changes caused by disturbances in the object plane (SO) as depicted in Figure 1.12. Both methods utilize Digital Image Correlation (DIC) to determine how much the speckles on the background appear to have been displaced. The displacement is then related to a refraction angle which can then be used to calculate optical properties of the disturbance. For schlieren, the refraction angles are used to calculate index of refraction which is then related to pressure, temperature, or density which is further discussed in the next section. Digital gradient sensing relates the refraction angles to the principal stress gradients based on the same relations used for CGS. DGS has been experimentally validated against an analytical solution [94]. The stress gradients parallel and perpendicular to a line load applied to sheet of PMMA were experimentally measured and compared to the Flamant solution [94]. The method was also extended to dynamic experiments, where a PMMA sample was

dynamically loaded with a line load and was again validated against the Flamant solution [95]. The solution to the Flamant problem yields an analytical solution for stresses and displacements for a body subjected to a line load in a half space. Both the static and dynamic experiments were in good agreement with the analytical solution. Due to the agreement, in the present work, the method for calculating the stress gradients from refraction angles was extended to schlieren imaging analysis.

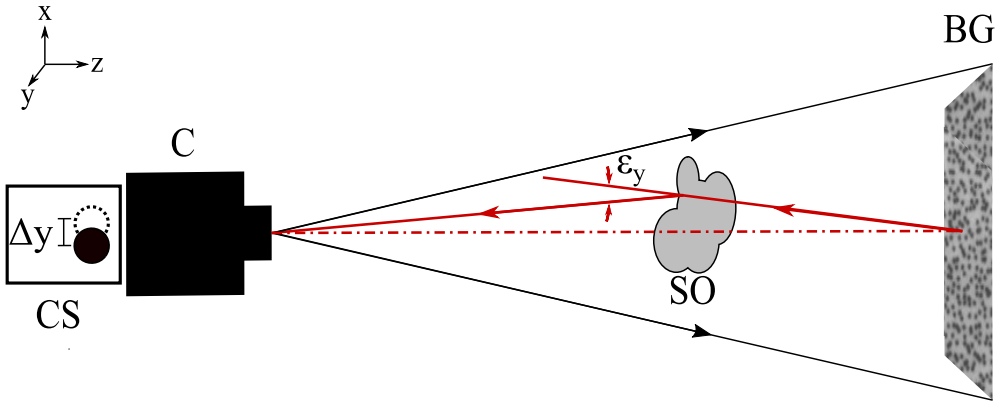

Figure 1.12: Schematic of the experimental set up for digital gradient sensing and background oriented schlieren.

The schlieren imaging method in the present work was lens based schlieren imaging, thus, DIC was not required. DIC correlates displacements over a user specified window size, yielding a value which is averaged over the size of the correlation window. The lens based quantitative schlieren imaging analysis allows for the refraction angle on a per-pixel basis to be determined.

1.4.1 Schlieren imaging

Schlieren imaging is a refractive imaging technique used to visualize the first spatial derivative of refractive index in optically transparent materials [45, 102]. The schlieren effect requires the implementation of a knife-edge cut-off. Without the cut-off the imaging technique visualizes the Laplacian of the refractive index referred to as focused shadowgraphy [45]. A schematic of a (a) lens-type and (b) z-type schlieren imaging system are shown in Figure 1.13. The lens based system utilizes achromatic doublets as the schlieren optics (SL) and the z-type system utilizes parabolic mirrors (PM). Light from a point light source is collected by a schlieren optic (SL1 or PM1) collimating the light. After the test section the collimated light is recollected and refocused using a second schlieren optic (SL2 or PM2). The refocused light creates a point, having a diameter equivalent to the original light source, one focal length from SL2 where the knife-edge cut-off

(KE) is placed for the schlieren effect. The light is then collected and imaged by a camera.

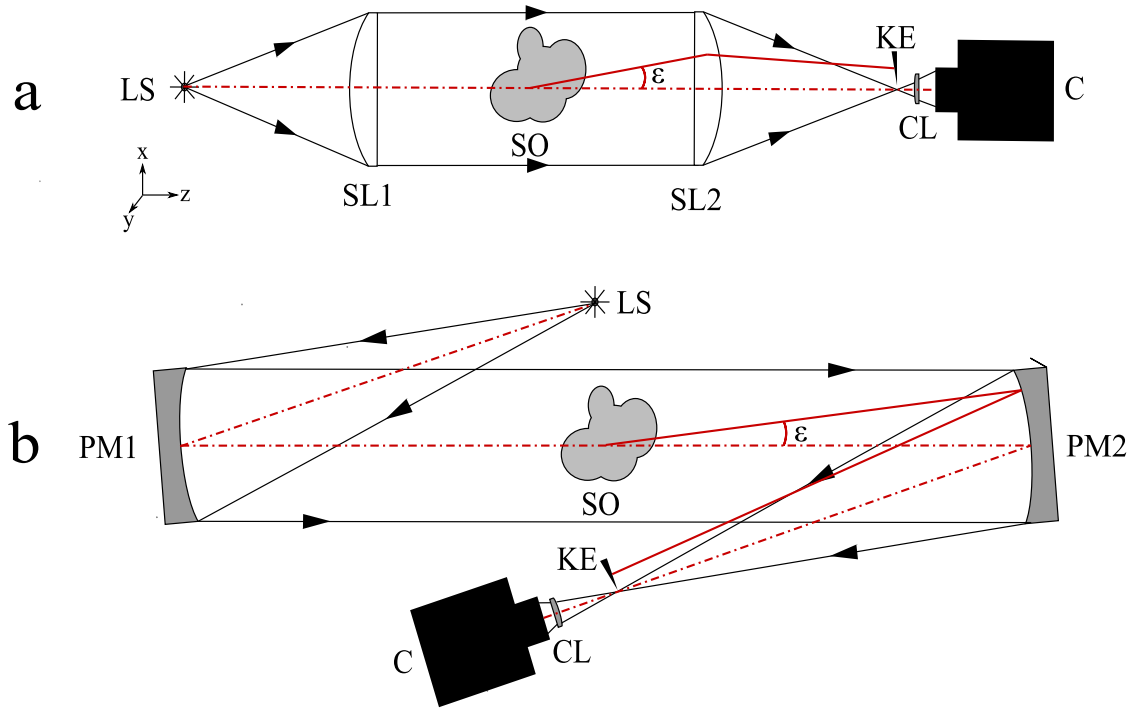

Figure 1.13: Schematics of (a) lens-type schlieren system and (b) z-type schlieren system.

Throughout the imaging test section (the area between the two schlieren optics) the light rays are parallel. Any refractive index change in the test section shifts the light path by an angle ϵ as depicted in Figure 1.13. In a schlieren imaging system the relationship between index of refraction and refraction angle is based on the gradient of the refractive index being proportional to the bent light rays [45]:

$$\frac{\partial^2 x}{\partial z^2} = \frac{1}{n}\frac{\partial n}{\partial x}, \quad \frac{\partial^2 y}{\partial z^2} = \frac{1}{n}\frac{\partial n}{\partial y} \tag{1.19}$$

Integrating the relationship:

$$\epsilon_x \cong \int \frac{1}{n}\frac{\partial n}{\partial x}\partial z, \quad \epsilon_y \cong \int \frac{1}{n}\frac{\partial n}{\partial y}\partial z \tag{1.20}$$

In a two-dimensional (2D) schlieren system, with a schlieren object having a fixed length L in the z-direction, the relation is further simplified:

$$\epsilon_x = \frac{L}{n_0}\frac{\partial n}{\partial x}, \quad \epsilon_y = \frac{L}{n_0}\frac{\partial n}{\partial y} \tag{1.21}$$

The bent light rays are visualized in the schlieren imaging system as a change in pixel intensity. Depending on the direction the ray is bent an individual pixel will either experience an increase or decrease in pixel intensity due to the interaction with the knife edge cutoff. An object with a known angle of refraction, ϵ, is used to calibrate the intensity change to a refraction angle. Knowing the angle of refraction allows for Eq. 1.21 to be implemented for determination of the material refractive index, n. Refractive index is then used to calculate density through the Gladstone-Dale relationship:

$$\rho = \frac{(n-1)}{k} \tag{1.22}$$

Where ρ is density, n is refractive index, and k is the Gladstone-Dale constant. There are limitations in the implementation of the Gladstone-Dale relationship as a material must portray a linear relationship between density and refractive index. The relationship between density and refractive index for PMMA satisfies this relationship as discussed in section 1.2.1.

Quantitative schlieren techniques have been achieved and validated for objects of a fixed length [48] and for spherically symmetric objects like shock waves using the Abel transform [47]. Pressure and temperature measurements using the calculated density have also been demonstrated [47, 48]. In the literature quantitative schlieren techniques have not been applied to PMMA.

1.5 Objectives of Present Research

The goal of the present work is to quantify the material response of explosively loaded PMMA. The explosively driven shock wave pulse and the confined explosive gas pressure will be investigated to identify the primary mechanisms driving fracture during explosive loading of PMMA. These two components of the explosive loading have opposite characteristics which are hypothesized to work together to initiate and then sustain fracture growth: the explosive shock pulse is a short duration high pressure pulse producing a limited fracture extent which then experiences sustained growth driven by the gas products which expand as the fracture cavity grows. This research will be accomplished through experimental research at multiple scales and supporting computational simulations with the following objectives:

- To measure the explosively-driven shock wave propagation in PMMA as a function of distance from an explosive source to quantify the shock-induced material response.
- To quantify the fracture length and propagation velocity as a function of time during the explosion process in PMMA.
- To determine the effect of externally applied force on the blast-induced material response of PMMA

- To develop optical techniques to provide quantification of the dynamic shock material response and stress state.

CHAPTER 2

EXPERIMENTAL METHODS FOR SHOCK AND FRACTURE STUDIES IN PMMA

Quantification of shock propagation and fracture growth in PMMA is a multi-timescale process requiring experiments at multiple scales. Small-scale experiments were used to define the shock state of the PMMA close to the spherical explosive source. Measurements were required close to the source due to the rapid attenuation of shock waves in PMMA. The shock state was quantified from the experimental shock and particle velocity then Hugoniot relations were used to define other shock parameters.

Large-scale experiments were used to quantify the explosively driven fracture response of the material. There are two fracture driving forces: the shock pulse and the confined explosive gases. The sample had to be large enough to allow for the confined explosive gases to drive the fractures without venting into the environment. PMMA configurations were classified here as small-scale and large-scale experiments based on the sample size and shock wave propagation distance. Small-scale experiments were made such that the shock would propagate approximately 0.97 mm to 74.15 mm through the PMMA whereas the large-scale experiments allowed for the shock propagation to be approximately 138.4 mm, maximum, which allowed for the fractures to grow without reaching the sample boundaries.

RP-80 electronic bridge-wire (EBW) detonators were used as the explosive source for all but one experiment. RP-80 EBW detonators are used here because of their high consistency of explosive material, explosive material press density, and their initiation. The EBW detonators contain 80 mg of PETN as the initiating explosive and 123 mg of RDX as the output explosive. The total explosive mass of the detonators was 203 mg, with a total energy output of about 1.14 kJ. The explosives were tamped into a plastic cup with a diameter of 7.5 mm and a length of 30.0 mm. Typically, the housing cup is aluminum with a density of 2.7 g/cc which was replaced here with Delrin having a density of about 1.41 g/cc. Replacing the aluminum allows for a better impedance match between the EBW detonator and the PMMA. The detonators were purchased from Teledyne Defense Electronics (part number 188-7072). The EBW detonators were detonated using an FS-17 fire set.

2.1 Sample Geometry

Various sample lengths were used to quantify the shock pressure decay from a spherical explosive source in PMMA. Free surface velocity was used to determine pressure as a function of propagation distance requiring a range of sample lengths. Short propagation distances were used because of the rapid attenuation of the explosively driven shock pressure in PMMA [1].

The large scale tests were conducted in 305 x 305 x 305 mm PMMA cubes to study the fracture response from an explosive source. Previous literature used 250 x 250 x 240 mm cubes of PMMA to study the explosively driven fracture response from 160 mg of lead azide [6] where the fractures did not reach the sample boundary which aided the size choice here. Simulations were also run with the sample size and the RP-80 EBW detonators to ensure the fractures would not reach the sample boundary.

2.1.1 Small-Scale Samples

The shock pressure decay of PMMA from a spherical explosive source was experimentally determined through the measurement of particle velocity history at the free surface opposite of the explosive source. Figure 2.1 shows the samples used for the small-scale tests. The height, x_H, and width, x_W, were the same for the small-scale (SS) tests, 76.2 mm and 25.4mm, respectively. The sample lengths tested are reported in Table 2.1. A 25.4 mm deep hole, x_{exp}, was drilled into the sample for the detonator. The RP-80 EBW detonators are approximately 20 mm in length, and were placed so that the output face was in contact with the PMMA at the bottom of the hole. The remaining space behind the detonator was filled with epoxy.

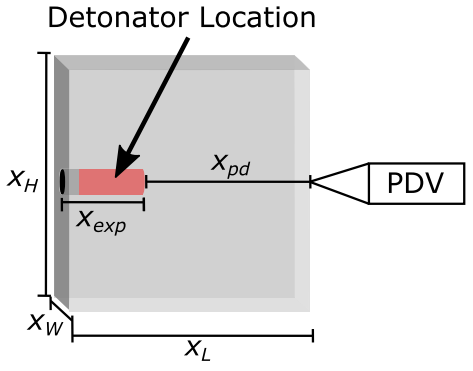

Figure 2.1: Small scale shock attenuation sample geometry.

Table 2.1 outlines all of the small scale sample lengths tested. The sample geometries indicate the sample thickness, x_W. SS, small-scale, indicates a sample thickness of 25.4 mm and cube indicates a sample thickness of 76.7 mm. The uncertainties in the propagation distances of 0.97 mm to 20.01 mm were based on the uncertainty in Vernier Caliper measurements. The uncertainty in the propagation distances from 21.91 mm to 74.15 mm was based on the uncertainty in the schlieren images which was determined using the distance calibration uncertainty. Discussion about distance calibration is in Section 2.4.1.

Table 2.1: Table of tested small-scale sample sizes

Sample Geometry	Propagation Distance x_{pd} (mm)	Sample Geometry	Propagation Distance x_{pd} (mm)
SS	0.97 ± 0.01	SS	22.74 ± 0.13
SS	1.92 ± 0.01	SS	23.25 ± 0.13
SS	3.01 ± 0.01	SS	47.77 ± 0.13
SS	3.03 ± 0.01	SS	47.77 ± 0.13
SS	3.97 ± 0.01	SS	48.02 ± 0.13
SS	5.94 ± 0.01	Cube	50.20 ± 0.12
SS	7.82 ± 0.01	Cube	50.45 ± 0.12
SS	10.06 ± 0.01	Cube	50.70 ± 0.12
SS	10.14 ± 0.01	Cube	50.80 ± 0.17
SS	15.16 ± 0.01	Cube	52.17 ± 0.17
SS	20.01 ± 0.01	Cube	52.52 ± 0.17
SS	21.91 ± 0.13	SS	73.06 ± 0.13
SS	22.07 ± 0.13	SS	73.59 ± 0.13
SS	22.22 ± 0.13	SS	73.59 ± 0.13
SS	22.48 ± 0.13	SS	74.15 ± 0.13

The sample thickness for the SS samples was selected to reduce schlieren system over-ranging. However, for the nominal propagation distances of 48.2 mm and 74.1 mm the sample thickness was shorter than the propagation distances. Such a configuration introduces free surface wave interactions with the sample boundaries parallel to the imaging plane. The boundary interactions had a potential to effect the results, therefore, cubes of PMMA ($x_L = x_H = x_W$ = 76.7 mm) were also tested. The cubic samples had the same hole assembly described above. The cube-like samples (denoted as "cube") had a nominal propagation distance of 51.3 mm. The machine drawings for the samples tested are in Appendix A.1.

2.1.2 Large Scale samples

The explosively driven fracture response of PMMA was quantified using the large-scale (LS) 305 x 305 x 305 mm PMMA cubes. The machine drawings for

the large-scale samples are in Appendix A.2. A specialized tool was used to drill the hole geometry with a bottom hole depth of 165.1 mm into which the RP-80 detonator was epoxied. The bottom hole diameter was approximately 8.0 mm. The remaining hole volume was filled with fracturing proppant (40/70 carboeconoprop). An aluminum plug consisting of two O-rings and a pass-through for the detonator wires was seated into the top of the hole after the proppant was added. This plug was intended to keep explosive gases from expanding out the top of the hole, allowing for the contained explosive gases to further drive the fracture.

A preliminary test was preformed in 305 x 305 x 305 mm PMMA cube with a single hole drilled in the center of the cube as show in Figure 2.2. The explosive source was 750 mg of PETN tamped to a density of 70% TMD. The explosives were detonated using an open faced RP-80 exploding bridge-wire. Due to the uncertainty associated with loading and tamping the PETN into the sample this method was abandoned and for subsequent experiments RP-80 EBW detonators were used as the explosive source.

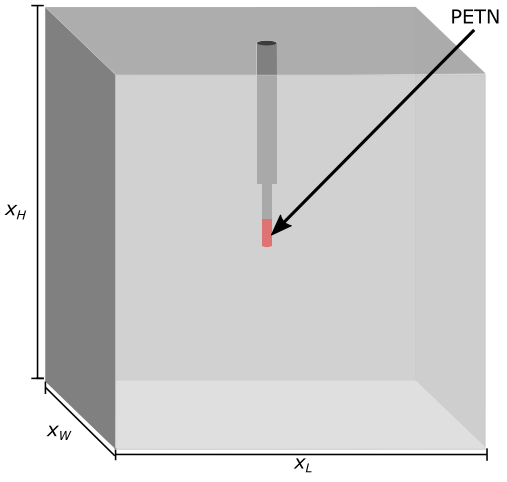

Figure 2.2: A schematic of the single hole PMMA cube. The machine drawing is in Appendix A.2.

Four tests were performed to explore changes in the fracture response due to shock wave interactions and the applied external stresses. To achieve shock wave interactions, two RP-80 EBW detonators were used as the explosive source. The centers of the detonators were 58.4 mm apart such that the holes were drilled 29.2 mm from the cube center-line as depicted in Figure 2.3. The detonators were wired in parallel and detonated using an FS-17 firing system.

The impact of external stress on the shock and fracture response was studied using the two explosive source sample configuration. Four stress arrangements were studied: No external Stress (NS2), 2 MPa uniaxial Horizontal Stress (HS2-2),

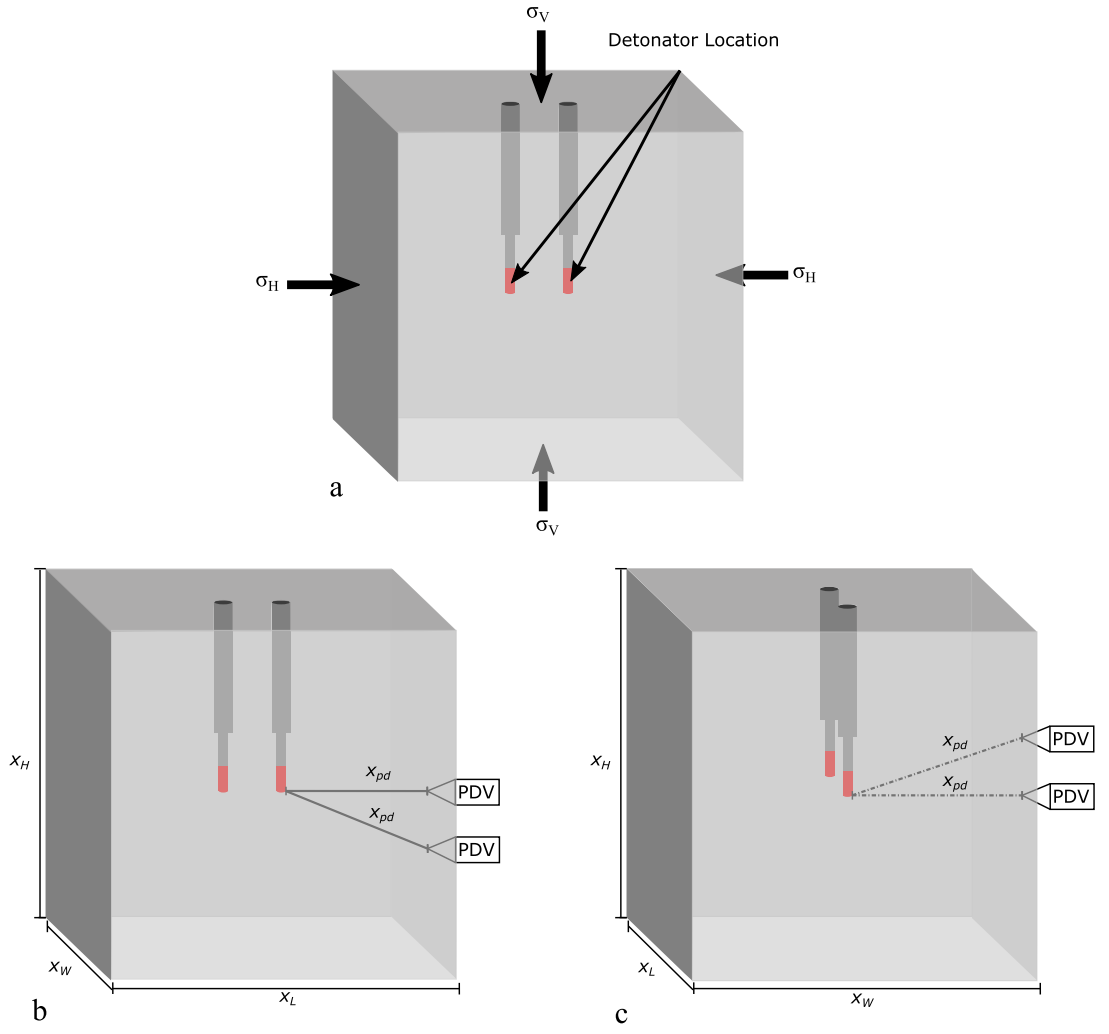

Figure 2.3: Schematic of PMMA cubes with two explosive sources. The direction of the external stress states is shown in (a). The location of the PDV probes for (b) the NS2, VS2-2, and VS2-20 test and (c) the PDV probe location for the HS2-2 test.

2 MPa uniaxial Vertical Stress (VS2-2), and 20 MPa uniaxial Vertical Stress (VS2-20). The stress direction is relative to the detonator axis where the external stress was applied parallel to the hole direction (vertical stress) and perpendicular to the hole direction (horizontal stress) as shown in Figure 2.3. For consistency, the HS2-2 test required the sample to be turned 90 degrees in order to use the top cylinder of the press for all tests. Since the PDV measurements for the NS2, VS2-2, and VS2-20 were take on the face perpendicular to the horizontal stress direction (Figure 2.3b) the PDV measurement had to be taken at a different location for the HS2-2 test (Figure 2.3c). Moving the PDV probe location resulted in a slightly longer propagation distance (x_{pd}) for the HS2-2 test.

2.2 Refractive Imaging Systems

High-speed schlieren and shadowgraphy were implemented to visualize the shock propagation and fracture growth in explosively loaded PMMA samples. Further quantification of shock parameters required the implementation of Photon Doppler Velocimetry (PDV) which was used to measure free surface velocity history.

Refractive imaging of the explosive event allows for the shock wave to be visualized due to the refractive index change imparted by the event. The refractive imaging system used parallel light through the test section allowing for a 2D imaging plane to be visualized without needing geometric corrections. The refractive index difference between the PMMA sample and surrounding air added additional complexity to the imaging arrangement requiring the implementation of both schlieren and shadowgraphy. Schlieren visualized the first derivative of the refractive index field whereas shadowgraphy visualized the Laplacian of the refractive index field.

2.2.1 Small Scale refractive imaging system

The lens-based schlieren imaging system used for the small-scale experiments is presented in Figure 2.4. The system consisted of a SI-LUX laser with a wavelength of 640 nm as the light source, 700-mm-diameter f/5 lenses, and a Shimadzu HPV-X2 high-speed camera. A "boombox" with optical glass windows was used to contain the explosive event. The distance between the two schlieren optics was about 0.35 m.

The SI-LUX laser light was refocused using a condensing lens. At the focal point of the condensing lens before passing through the first schlieren optic, an iris was placed to reduce the light diameter and overall light intensity. Refocusing the light source to a smaller point source allows for more crisp shadowgrams to be recorded. The iris was one focal length, 700 mm, from the first schlieren optic which collimates the light. The light was refocused to a point after the second schlieren lens. At this focal point, 700 mm from the second schlieren lens, a knife edge cut-off was placed. After the knife edge cut-off a band-pass filter, at the laser wavelength of 640 nm, was placed in front of the camera to reduce external illumination from the detonation. The minimum exposure achieved with the camera was 200 ns, thus, the laser was pulsed to provide 10 ns illumination to further reduce pixel blur.

Each test was recorded at a frame rate of 5 Million frames per second (fps). The camera was limited to 128 frames at full resolution or 256 frames at an interpolated resolution. The sensor size of the camera was 400 x 250 pixels, thus interpolation of pixels increases uncertainty. Full resolution at 5 Mfps was used to visualize the shock propagation for nominal propagation distances of 0.97 mm to 52.52 mm. The full event duration for the samples with a nominal propagation distance of 74.15

mm was not captured using the full resolution thus the interpolated resolution was required.

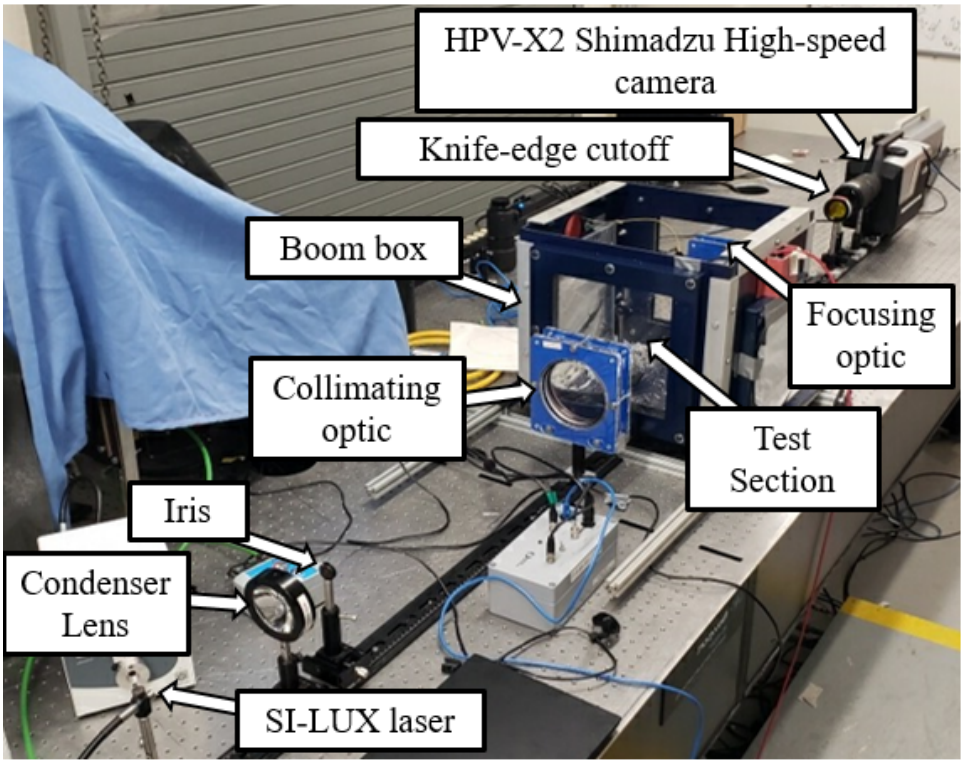

Figure 2.4: Image of the small-scale experimental set up inside the laboratory boombox.

2.2.2 Large Scale refractive imaging system

The large-scale experiments explored both the shock propagation and the fracture growth in the PMMA. These two processes occur on significantly different timescales, so two separate high-speed cameras were used to record the individual processes. The two high-speed cameras were used to image the same event along the same imaging plane where the imaging path was split into two cameras having different frame rates. A schematic of the the two camera refractive imaging system is presented Figure 2.5. The actual experimental setup is shown in Figure 2.6 and was constructed at the Energetic Material Research and Testing Center (EMRTC) Ballistic Science Lab (BSL).

The refractive imaging system was a shadowgraphy imaging system with two light sources, two 317-mm-diameter f/6 parabolic mirrors (Edmund optics part #32-276-533), and two high-speed cameras. Schlieren imaging enhances the distortion caused by stress waves in the PMMA adding complexity when

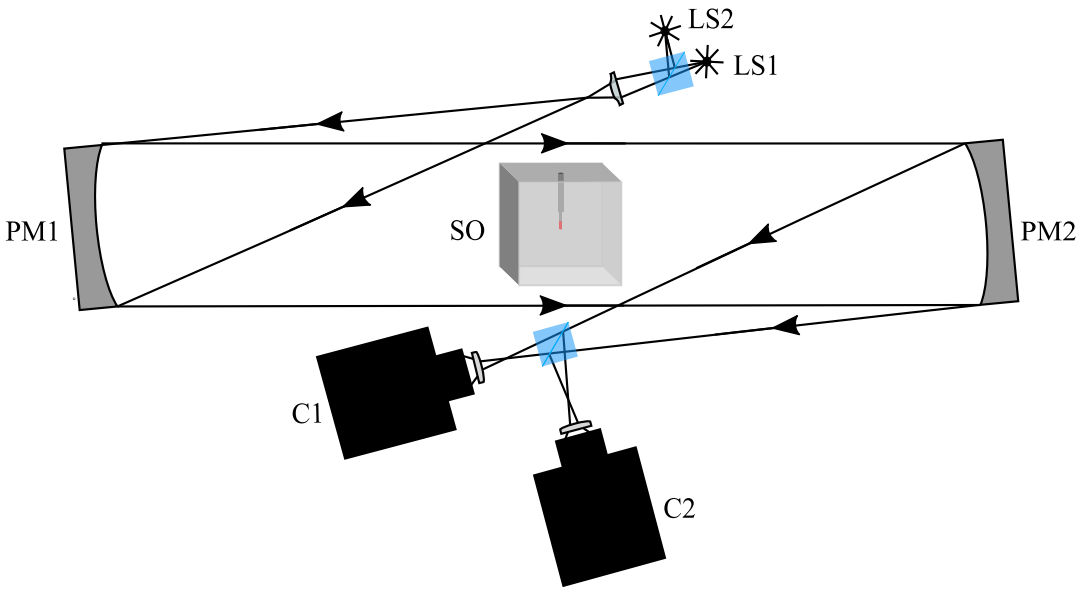

Figure 2.5: Schematic of the large scale z-type shadowgraphy imaging system used for visualization of shock propagation and fracture growth in PMMA.

visualizing fracture growth. To mitigate visualization of weak stress waves after the shock propagation, shadowgraphy was implemented, therefore the knife-edge cut-off was excluded. Two light sources were used because the SI-LUX laser (LS1) was the preferred light source, however, it has a limited on-time therefore it was not appropriate as the light source for the late time fracture measurments. In order to overcome the light source limitations, a beam splitter cube was used to combine the laser light with the light from a SUGARcube LED white light source (LS2) used as the second light source. The beam splitter cube allowed for the light from both sources to be on a common optical path. After the beam splitter cube the light was focused to a sharp point using a condenser lens. The combined light beam was collimated using the first parabolic mirror (PM1) and refocused after the test section using the second parabolic mirror (PM2). Prior to the focal point of the focusing mirror, the light passes through a second beam splitter cube which directs the light toward the two cameras. The arrangement of the imaging system allows for both cameras to have the same imaging plane while visualizing the full event.

The first camera (C1) was a Shimadzu HPV-X2 high-speed camera visualizing the shock propagation and early time fracture growth. C1 had a frame rate of 1Mfps. The sensor exposure was reduced to 10 ns using the SI-LUX laser and a band-pass filter at the same wavelength as the imaging laser was placed in front of the camera. The band-pass filter was used to filter out the white light from the SUGARcube and the illumination from the explosive detonation process. The late-time fracture growth was visualized using a second camera (C2) which was either a Photron SA-X2 (36kfps) or a Photron NOVA (30kfps). The SUGARcube

white light source was used as the illumination source for CM2. Pixel blur and external illumination were less of a concern for imaging the late-time fracture growth making the white light source the appropriate choice for visualization of the fracture growth.

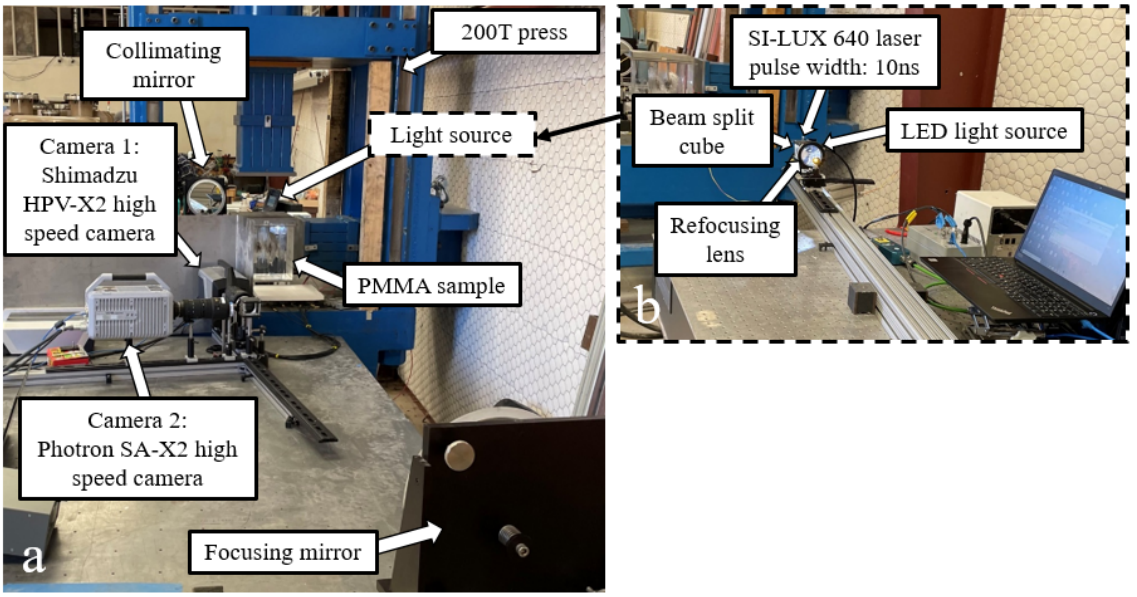

Figure 2.6: Images of the large scale experimental set up inside the Ballistic Science Lab (BSL). The (a) overall setup with the cameras, test section, and all optics is shown along with (b) a detailed view of the transmitting optics including the light sources.

2.3 Press operations

The refractive imaging system was built around a 200-Ton 40″ x 40″ Press with a 60 Ton side cylinder from Accudyne. The press was used to apply 2 MPa and 20 MPa of uni-axial external stress on the surface of the PMMA samples. The press has both a side cylinder and a top cylinder, however, for consistency the top cylinder was used for all tests. In order to use the top cylinder for the HS2-2 test the sample was turned 90 degrees. The direction of applied stress for the experiments is shown in Figure 2.3.

The sample surface was smaller than the pressing surface which was accounted for when calculating the applied stress. Once the applied stress was determined the value in Tons was converted to Pounds per square inch (PSI) using the conversion factors provided by the manufacture shown in Figure 2.7. The press operation instructions used for the testing are in Appendix B.

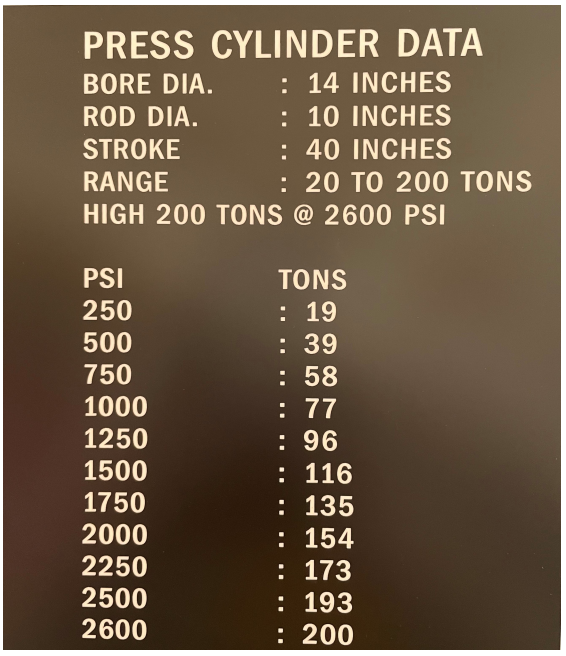

Figure 2.7: Conversion chart for the 200T press. Note that the units are in the imperial system of units from the manufacturer which was also reflected in the operation gages and controls.

2.4 Image Processing

Image processing was used to quantify the shock and fracture response of explosively loaded PMMA from the high-speed images. Quantitative information about the shock velocity and fracture rate was extracted from the high-speed images using MATLAB image processing techniques. Since the high-speed images were taken using the refractive imaging system with parallel light, geometric corrections or projection corrections based upon the event location were not necessary. The only requirement was a length-to-pixel calibration of the system.

2.4.1 Imaging Calibration

Calibration of the imaging system was quite simple and was preformed for every test series. A distance calibration was performed by relating the length scale of pixels in a image to a physical length scale. In order to preform the distance calibration an image of an object with a know length was used. The object selected for the present work was a circular lens holder shown in Figure 2.8. The lens holder had a diameter of 45.0 mm. Since the diameter of the lens holder was known the boundary of the lens holder was used to determine the number of pixels which spanned the lens holder.

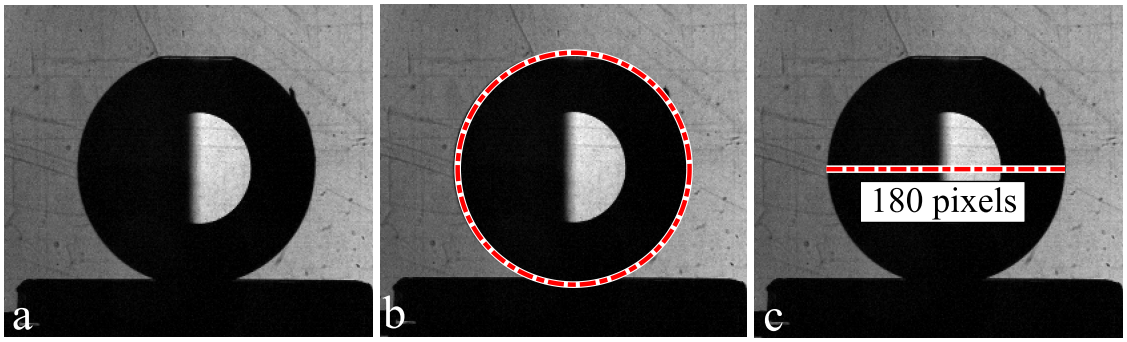

Figure 2.8: Images of (a) calibration object, (b) calibration object with the detected outer diameter and (c) pixels representing the object outer diameter.

Image processing was use to detect the boundaries of the lens holder. The method for detecting the boundary used the MATLAB function *imfindcirlces* which implements a circular Hough transform. A representative image of the detected lens boundary is shown in Figure 2.8b. The MATLAB function outputs the radius and center of the detected circle. The radius was doubled and used for the distance calibration. A representative image showing the lens diameter in pixels is presented in Figure 2.8c. The diameter in pixels and the diameter in millimeters were then used for the pixel-to-millimeter calibration using:

$$\text{Calibration Distance} = \frac{\text{\# of pixels}}{\text{object length in mm}} \tag{2.1}$$

The largest source of uncertainty was through imaging calibration therefore care was taken when extracting quantitative information from the images. Generally, the uncertainty in an image was quantified as 0.5 pixel. For the Shimadzu high-speed camera, which was the primary camera utilized in this work, an uncertainty of 0.5 of a pixel was quite large due to the small sensor size (400 pixels x 250 pixels). The uncertainty was increased when selecting the longer record length (256 images) because the pixels were interpolated. Another consideration was the imaging field-of-view. Based on the distance calibration the uncertainty would be larger for the LS tests as compared to the SS tests due to the imaging field-of-view. These considerations were accounted for when extracting quantitative information from the high-speed images.

2.4.2 Digital Streak Image

The distance calibration allows for the number of pixels the shock travels to be converted to a meaningful length scale. The time scale was determined using the frame rate of the camera. The time between frames is the inverse of the frame rate. Since the refractive imaging systems were used, the shock front

was easily detected. The refractive index change imparted by the shock allows for visualization of the shock propagation through the sample. Schlieren images are shown in Figure 2.9 a-d and shadowgrams are shown in Figure 2.11 a-d.

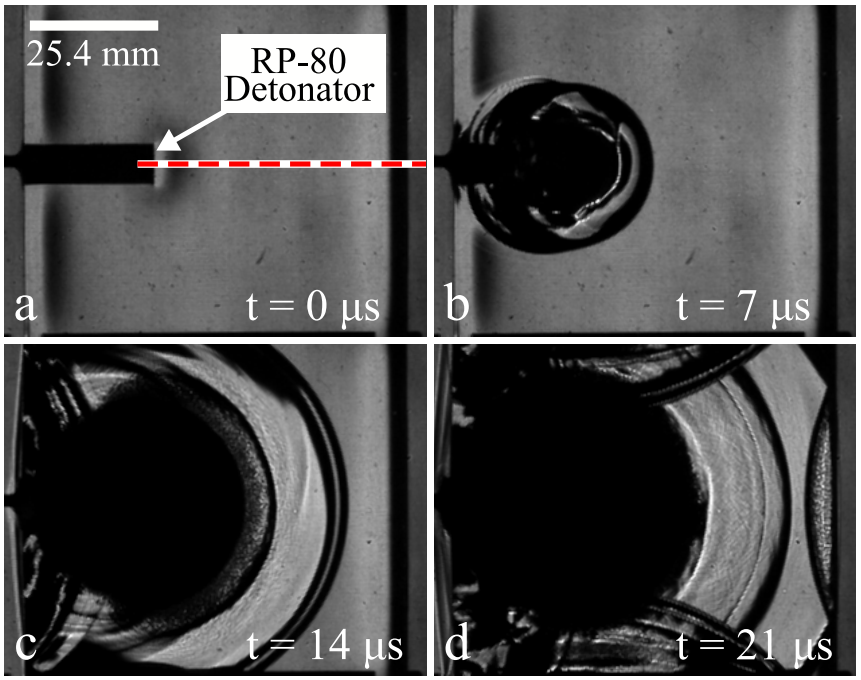

Figure 2.9: Schlieren images of shock propagation driven by an RP-80 EBW detonator in a Cubic PMMA sample at (a) t = 0 μs, (b) t = 7 μs, (c) t= 14 μs, and (d) t = 21 μs. The red dashed line indicates the location used to create the streak image. The distance the shock propagates internal to the material was 50.20 mm.

The schlieren images presented in Figure 2.9 were from a Cube test having an approximate propagation distance of 50.20 mm. The detonator location is indicated in (a). As time progressed, the shock from the explosive source was visualized as the expanding circular feature. After 14 μs the shock interacted with the top and bottom boundary of the sample and the front of the wave continued to propagate through the undisturbed PMMA. In the last image at 21 μs the shock had interacted with all boundaries of the sample revealing a reflected shock wave propagating back into the sample. From these images the shock position as a function of time can be determined. Rather than tracking the shock boundary from each individual image, an artificial digital streak image was created [45].

Traditionally, streak images are created using a streak camera which "sweeps" a slit of light across a camera sensor as the event progresses [2, 3]. Here, an artificial digital streak was created during post-processing. The red dashed line in Figure 2.9a represents the streak location. A single row of pixels centered on the detonator, starting 2 mm from the detonator face, was selected as the streak location. The selected row of pixels was extracted from every image in the data set

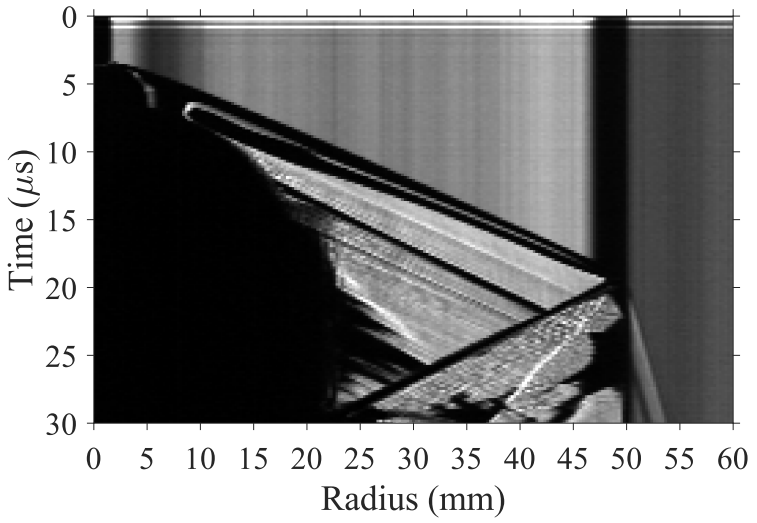

Figure 2.10: Digital streak image created using high-speed images taken of a shock driven by an RP-80 EBW detonator in a 73.9 mm x 25.4 mm x 76.2 mm PMMA sample. The high speed images were cropped revealing the first 2 mm of the detonator. The distance the shock propagates internal to the material is 48.5mm.

and stacked vertically downward such that time was on the y-axis and distance was on the x-axis. Figure 2.10 is the digital streak image created from the schlieren image set in Figure 2.9.

Digital streak images were also created for the LS shadowgrams. A digital streak image created from the NS2 test is presented in Figure 2.11e. To create the digital streak images for the LS tests, the images were first rotated 90° and the shock from one of the explosive sources was selected as indicated in Figure 2.11a. By rotating the images 90° the shock is extracted from the detonator face similar to the SS and cube tests. The benefit of a digital streak image is the shock propagation is shown as a function of time along the selected location. Such an arrangement allows for the shock velocity as a function of time and space to be measured. The streak image highlights features such as shock reflections, transmission into the free surface, and the fracture boundary in a graphical format. This allows for comparison to free surface motion measurements and visualization of the fracture velocity with respect to the shock velocity. From the digital streak image in Figure 2.11e the difference between the shock velocity and fracture rate is apparent.

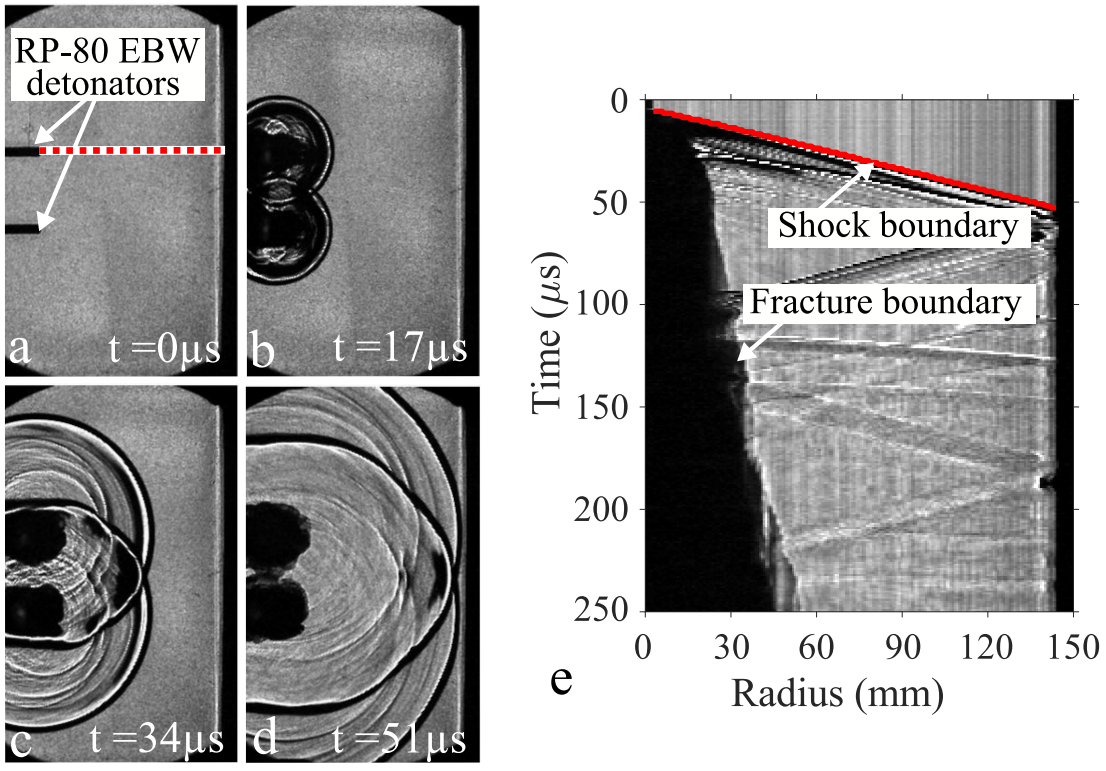

Figure 2.11: High-speed images of (a-d) shock wave propagation from two explosive sources epoxied into a PMMA cube with no applied stress. The red line indicates a row of aligned with the center of one of the detonators used to create a streak images. (e) is the streak imaged created. Note that images (a-d) were rotated 90°, as discussed.

2.4.3 Shock wave extraction

The shock boundary visualized in the digital streak images yields the shock position as a function of time. By extracting the boundary of the shock wave from the digital streak images the shock velocity could be determined. After applying the distance and time calibration to the digital streak image, the inverse of the slope from the extracted shock boundary is the velocity of the shock. The boundary of the shock visualized in the digital streak image was extracted using a MATLAB image processing routine. A flow chart of the steps taken to extract the shock wave front is shown in Figure 2.12.

The analysis starts with the raw streak image, Figure 2.12a, which was first normalized by the bit depth of the image. In the normalized raw streak image there are some artifacts from residual stresses on or near the boundaries of the sample from the manufacturing process. The residual stresses from drilling the detonator hole limits the ability to visualize the early time shock wave propagation. In order to remove the intensity difference from the residual stresses a background subtraction was preformed producing image (b). After the background subtraction, a threshold was applied. The threshold image (c) is a binary image where any pixel with an intensity value above the threshold value was set to one and all other pixels were set to zero. To enhance connectivity of the shock wave front across lines of the binary streak image a morphological erode followed by a morphological dilate was implemented resulting in a morphological open shown in (d). The boundaries of the image were detected to identify the shock front. Detecting boundaries (e) reduces the number of edges detected compared to several edge detection routines that were attempted. The boundary of interest, i.e. the shock front, was selected resulting in the final image with the detected shock position (f). A similar methodology was also applied to extract the fracture boundary from the digital streak images.

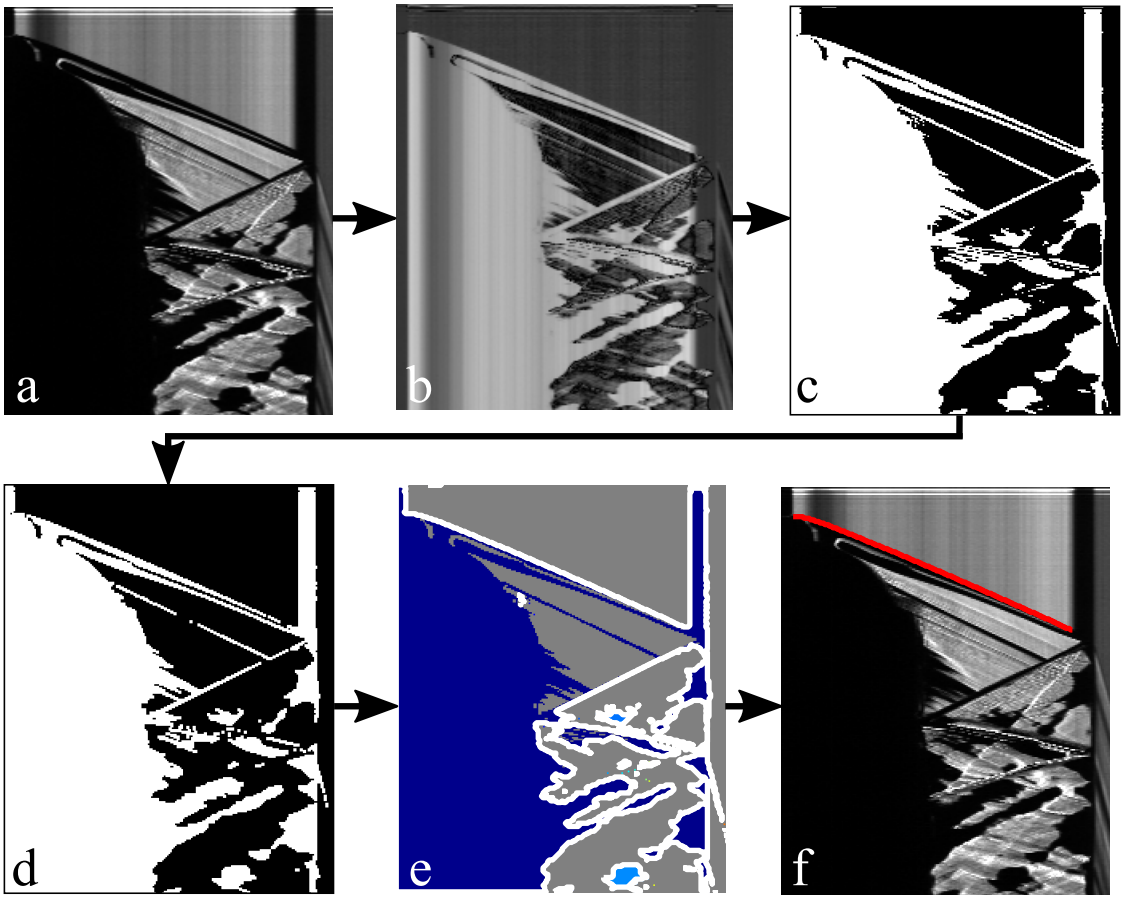

Figure 2.12: Image processing routine used to extract the shock boundaries from the digital streak images where (a) is the raw streak image, (b) is the background subtracted streak image, (c) is the streak image with a threshold applied (d) a morphological opening of (c), (e) are all boundaries in the image in (d), and (f) is the streak image with the shock front detected.

2.4.4 Image syncing

Time scale differences between the shock propagation and fracture growth and limited camera record time required two high-speed cameras for the LS testing. Both cameras were imagining the same event along the same imaging plane, as discussed. The Shimadzu HPV-X2 high-speed camera was implemented for visualization of shock propagation and early time fracture growth with a frame rate of greater than 1 Mfps, whereas the Photron was used to visualize the late time fracture growth at record rate of about 30 kfps. The two cameras started recording at the same time, but the Shimadzu high-speed camera finished recording within the first 10 frames captured by the Photron high-speed camera. The cameras differ in time scale, image resolution, and field-of-view, therefore, post-processing was used to sync the two data sets for fracture tracking.

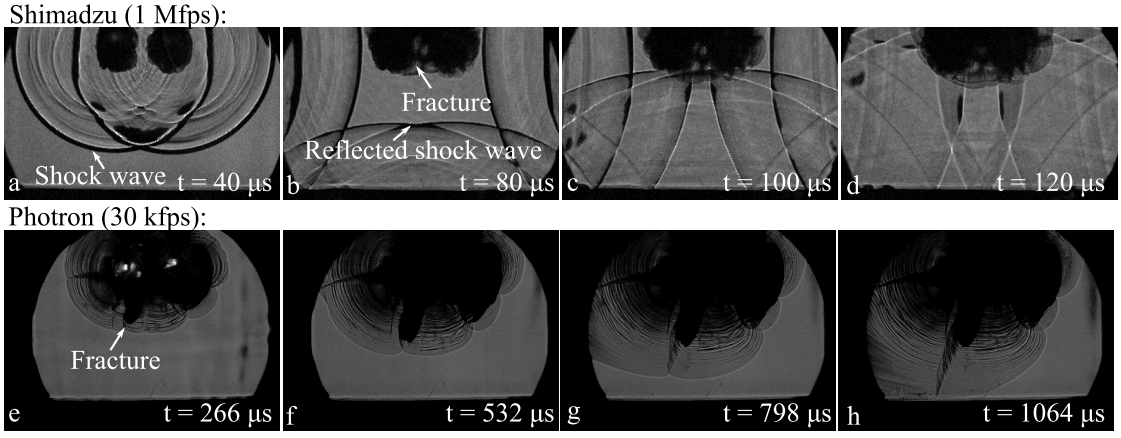

Figure 2.13: Representative images of (a-d) the shock wave propagation and early time fracture growth in a 0.3 m x 0.3 m x 0.3 m PMMA cube with no external stress captured using the Shimadzu HPV-X2 high-speed camera, and (e-h) The late time fracture growth for the same experiment using the Photron camera.

The two different camera sensors required magnification and pixel resolution corrections along with spatial corrections to align the features. Magnification differences were corrected by resizing the Photron data to match the pixel-to-millimeter calibration in the Shimadzu images. Next, images before the explosive detonation were used to spatially align the location of the drilled holes using image registration. Once the spatial location was determined, the Shimadzu HPV-X2 images were padded with a black border to match the image size of the Photron. The Shimadzu images were padded because the Photron high-speed camera had a larger field-of-view than the Shimadzu HPV-X2. Figure 2.14 shows images before the detonation for (a) the Shimadzu HPV-X2 camera, (b) the Photron, and (c) the spatially aligned images.

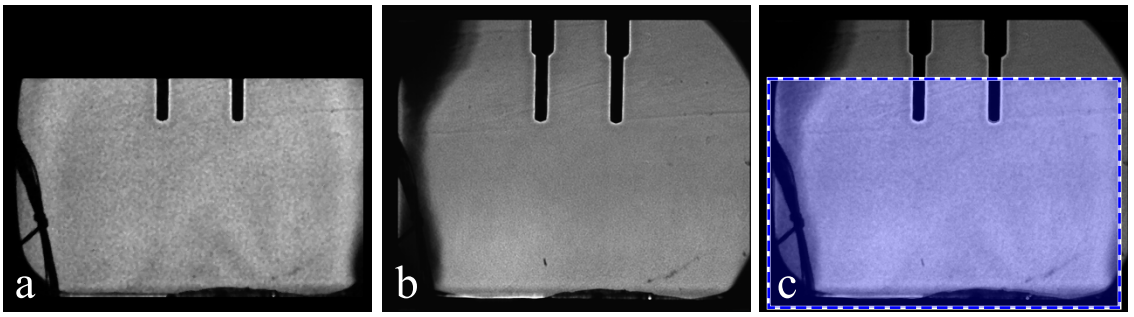

Figure 2.14: Image of 305 x 305 x 305 mm PMMA cube with 2MPa of vertical stress prior to detonation from (a) the Shimadzu HPV-X2 high-speed camera and (b) the Photron SA-X2. The imaged areas were aligned and registered as shown in (c) where (a) is shown overlaid on (b).

2.5 Photon Doppler Velocimetry

Photon Doppler velocimetry (PDV) is an interferometry technique used to detect surface motion or particle motion through light interference. The heterodyne method, as described by Strand [35], was implemented here to experimentally measure surface motion. A schematic of how the heterodyne system collects the data is shown in Figure 2.15. The recorded frequency information was converted to surface velocity history using Sandia InfraRed HEtrodyne aNalysis (SIRHEN) which is a data reduction program used for PDV measurements [105]. Free surface velocity was used to calculate particle velocity history at various distances from the explosive source.

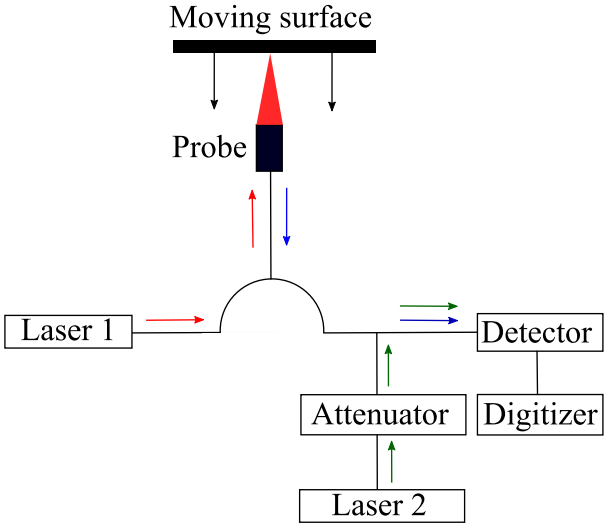

Figure 2.15: Schematics of the heterodyne PDV system.

The heterodyne PDV system uses two laser light sources. One of the lasers, (laser 1) is directed at the moving surface. As the surface moves the light is Doppler-shifted and reflected or scattered and recollected by the probe. The Doppler-shifted light is then combined with the second laser of a different frequency (laser 2), creating an interference pattern. Laser 2 does not directly observe the surface motion and is often referred to as a reference laser. The interference pattern, which is an optical signal, is then converted to an electrical signal, $s(t)$, using a photo detector which records the amplitude and determines the optical phase difference, Φ [105]:

$$s(t) = A\cos(\Phi - \bar{\omega}[t - \bar{t}]) \tag{2.2}$$

The optical phase difference describes the interference of the two optical paths which is found through [105]:

$$\Phi(t) \approx \Phi(t_1) - \bar{\omega}(\bar{t})[t - \bar{t}] \tag{2.3}$$

Where,

$$\bar{\omega} = 4\pi\bar{v}/\lambda_0 \tag{2.4}$$

Φ is a function of $\Phi(t_1)$ and $\bar{\omega}$ which represent the initial phase difference, and the radial beat frequency within the signal, respectively. An electrical power spectra can then be calculated using a short-time Fourier transform (STFT) using the electrical signal, $s(t)$, and specifying a window size, $w(t)$ [105].

$$S(\omega, \bar{t}) = \int_{-\infty}^{\infty} s(t)w(t)^{-i\omega t}dt \tag{2.5}$$

Since the PDV signal is digitized at a finite sampling rate, the SIRHEN processing applies a descrete Fourier transform converting the electrical signal, $s(t)$, to the frequency domain, $S(f)$. Equation 2.5 becomes [105]:

$$S(f) = \sum_{N-1}^{n=0} s_n w(t) e^{-12\pi f n} \tag{2.6}$$

Where $w(t)$ is a window function. The window function multiplied by the signal sets the surrounding frequency responses to zero reducing spectral leakage. The window functions available in SIRHEN are Boxcar, Hann, Hamming, and Blackman, which are respectively defined as:

$$w_n = 1 \tag{2.7}$$

$$w_n = 0.5\left[1 - cos\left(\frac{2\pi n}{N-1}\right)\right] \tag{2.8}$$

$$w_n = 0.54 - 0.46 \cos\left(\frac{2\pi n}{N-1}\right) \tag{2.9}$$

$$w_n = 0.42 - 0.5 \cos\left(\frac{2\pi n}{N-1}\right) + 0.08 \cos\left(\frac{4\pi n}{N-1}\right) \tag{2.10}$$

Where N is the total number of samples of the window function and n is an integer value from zero to $(N-1)$ [105]. The location of maximum frequency in the spectrograph are detected through a peak finding algorithm. SIRHEN has five peak finding methods, maximum, Gaussian, parabola, centroid, and robust where the program will implement the methods based upon the frequency ranges. For further details see [105] and [35].

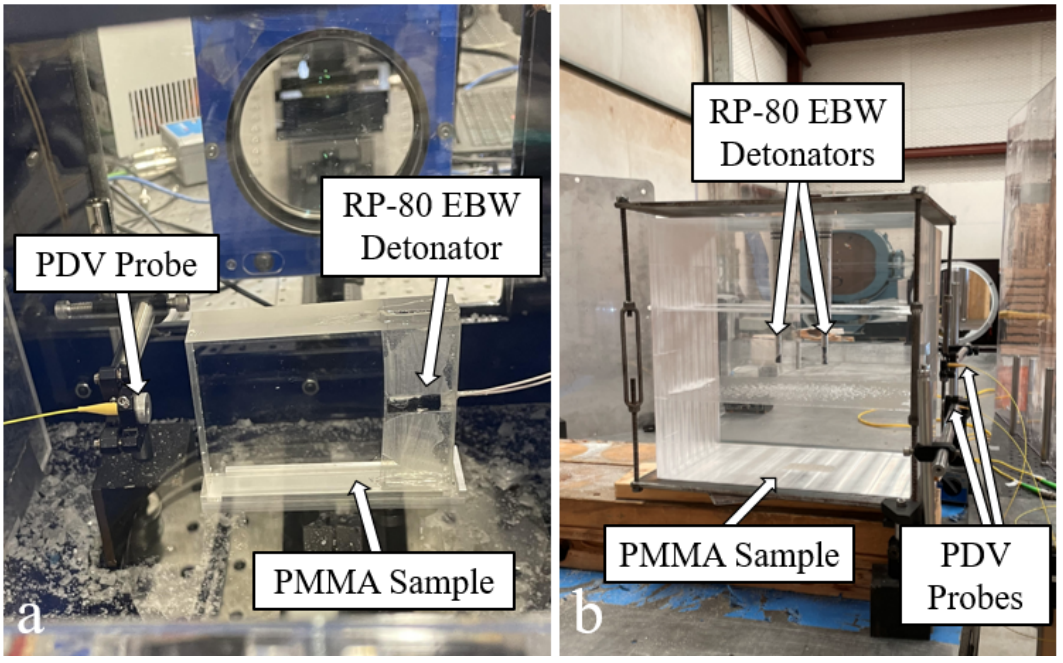

Figure 2.16: PDV measurement location for (a) small scale and (b) the large scale tests.

Surface motion detection requires a surface that diffusely reflects the laser light. To provide the desired reflective surface, a piece of retro-reflective tape was affixed to the surface at the desired measurement location. Here the free surface motion was measured and converted to particle velocity. The thickness of the diffuse reflector has minimal impact on the final velocity.

The propagation distance of the sample dictates the PDV measurement distance. The location of the PDV measurements relative to the detonator location for the NS2, SS, and cube tests are shown in Figure 2.16. On the small-scale, a single PDV probe was used to measure the free surface velocity history, and for

the large-scale tests two PDV probes were used. The location of the PDV measurement for the LS tests was the same for the NS2, VS2-2, and VS2-20 tests, Figure 2.17b. However, the PDV location was moved for the HS2-2 test, Figure 2.17c, in order to apply the horizontal stress. Figure 2.17 shows the location of the PDV measurement where (a) is a top down schematic of the PMMA cube showing the location of the PDV probes for (b) the NS2, VS2-2, and VS2-20 tests and (c) the HS2-2 test.

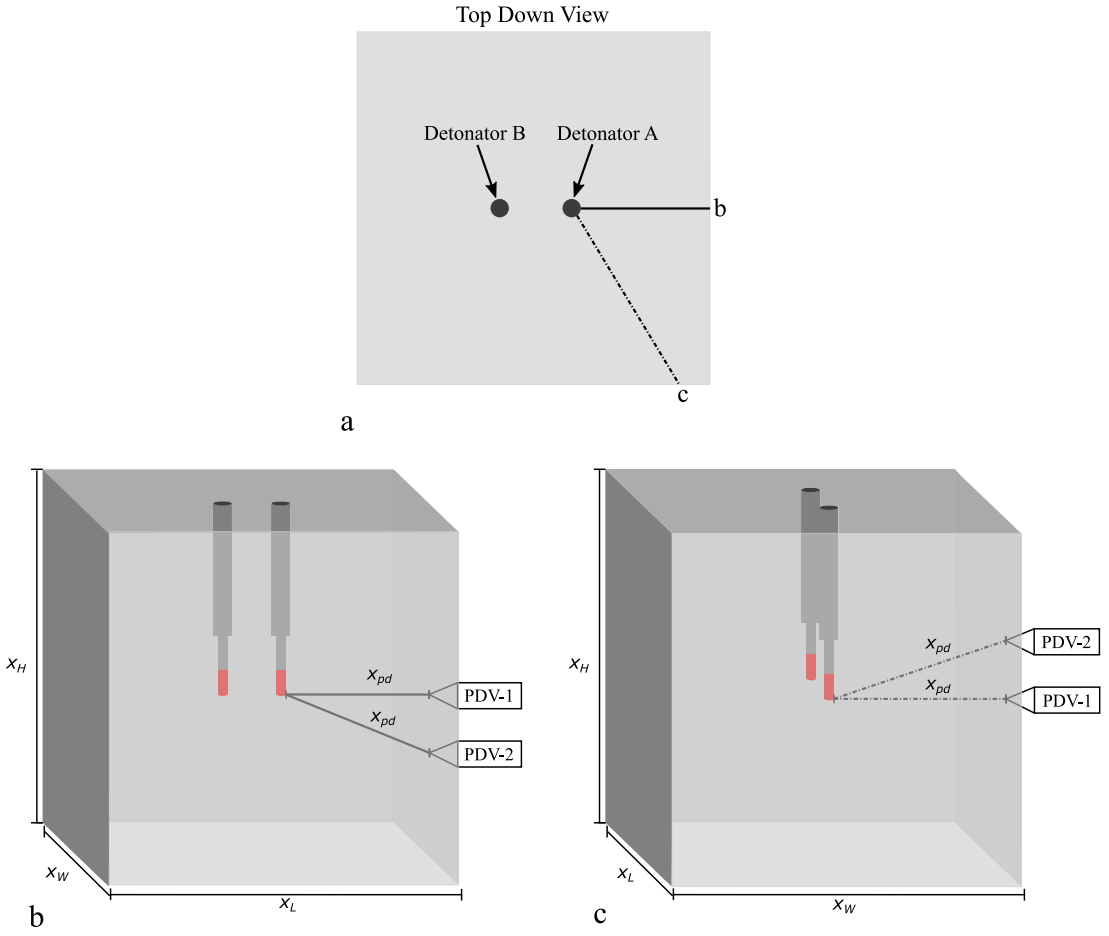

Figure 2.17: (a) A top down schematic of the PMMA cube showing the location of the PDV probes for (b) the NS2, VS2-2, and VS2-20 tests and (c) the HS2-2 test.

The probes used for all tests had a focal length of 20 mm which sets the distance from the measuring surface to the probe. The probes were purchased from OZ Optics. The PDV laser system was a Coherent Solutions LaserPXIe 1000 series. The beat frequency was recorded using a DSA70804C oscilloscope sampling at a rate of 25 Gs/s for a duration of 180 μs. The full record duration was 180 μs with a 10% pre-trigger indicating that the oscilloscope was continually recording and saving 18 μs before it received a trigger. The oscilloscope recorded

the beat frequency representing the interference pattern created by the free surface movement. Post-processing converts the frequency information to velocity history using Sandia InfraRed HEtrodyne aNalysis (SIRHEN) which is a data reduction program developed by Sandia National Labs. A description of the program can be found in [106].

2.5.1 SIRHEN Data Processing

SIRHEN was used to post-process the PDV data. The oscilloscope recordings of the beat frequencies were directly loaded into the program for post-processing. One of the beat frequency signals as captured by the oscilloscope for one of the small-scale tests is shown in Figure 2.18a. Figure 2.18b shows the full STFT of (a) created using SIRHEN. The program allows for the user to select the window function, the number of time points, the number of frequency points, and the overlap ratio. The number of time points was selected based on the user-defined experiment duration.

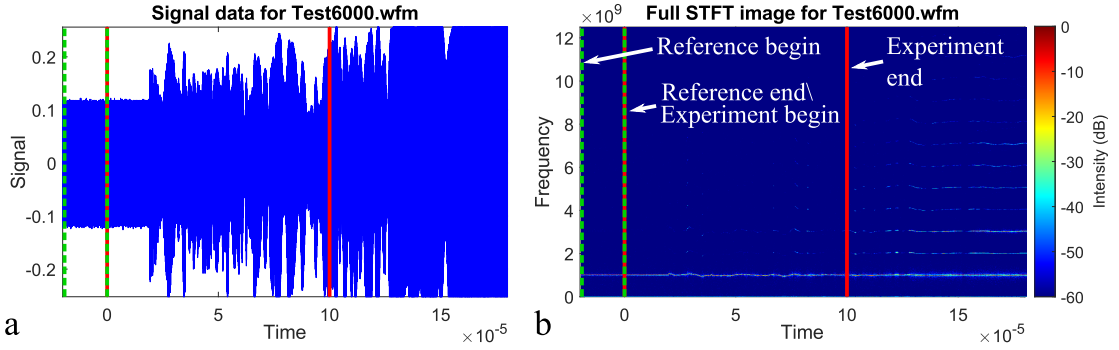

Figure 2.18: Plot of (a) the beat frequency and (b) SIRHEN output of the full short-time Fourier transform of the beat frequency. These data are from the small-scale explosively driven shock response of PMMA at the free surface for a propagation distance of 47.77 mm.

A region of time in the oscilloscope record was selected as the reference region. The reference region was generally selected as the first 10% of the recorded signal which was the pre-trigger. The reference region is the area between the green dashed lines in Figure 2.18. The start of the experimental region was selected as the end of the reference region (time zero) and had a duration of 100 μs. The experimental region is represented as the region between the red lines in Figure 2.18. The length of the experimental region was used to determine the number of time points based on the sampling frequency of the oscilloscope.

The number of time points selected was 1000 such that there was one a data point every 0.1 μs. The number of frequency points was also set to 1000 matching the number of time points. Various overlap ratios of 0, 5, 10, 15, and 20 were tested.

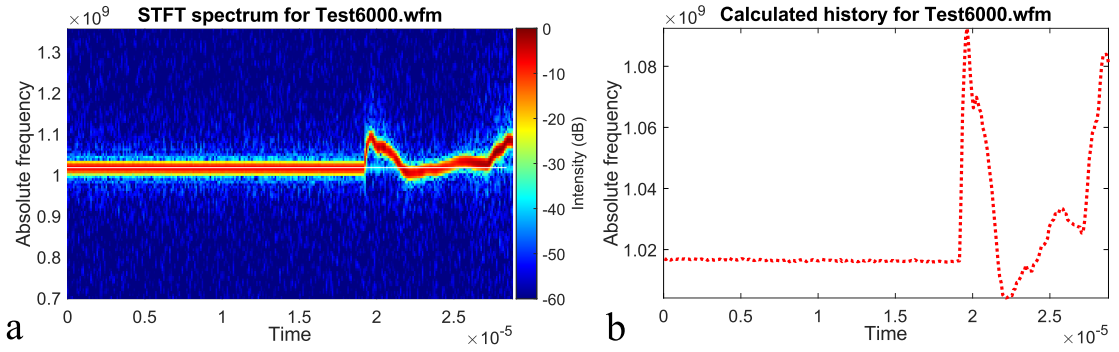

Figure 2.19: Output spectrogram of the data from Figure 2.18, which has been cropped and re-scaled, showing the STFT spectrum and (b) the resulting peak yielding the absolute frequency history.

The overlap ratio acts as a multiplier to expand the number of points in the STFT window. An overlap ratio of 0 was selected as it provided the best results. All window types were tested for this data set and there was a minimal difference. The window type selected for all experiments was Hamming (Eq. 2.9). The resulting SIRHEN STFT spectrum and absolute frequency history calculated using these parameters for the beat frequency in Figure 2.18 is shown in Figure 2.19.

Frequency limits were applied to Figure 2.19 in the analysis removing large amplitude peaks which appear after the region of interest. The frequency limits applied were static and the window size was dependent upon the signal. Signal strength varied from test to test but the same frequency limit window was applied to tests taken on the same day. The peak finding algorithm was applied to find the areas in the STFT spectrum with the highest intensity return which yields the absolute frequency as a function of time. The resulting frequency was exported and the heterodyning was corrected for using:

$$f_{abs} = f_b - f_o \tag{2.11}$$

Where f_{abs} is the corrected absolute frequency, f_b is the recorded absolute frequency, and f_o is the off set frequency. The corrected absolute frequency was then converted to surface velocity using the following relation:

$$1000 \text{ m/s} = 1.29 \text{ GHz} \tag{2.12}$$

The resulting surface velocity history graph is shown in Figure 2.20. Then surface velocity, u_{sf}, was converted to particle velocity, u_p, through:

$$u_p = \frac{u_{sf}}{2} \tag{2.13}$$

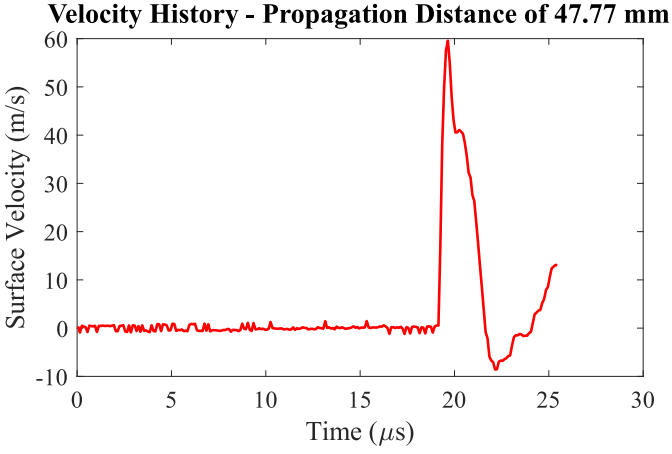

Figure 2.20: Surface velocity history for explosively loaded PMMA calculated from Figure 2.19.

CHAPTER 3

EXPERIMENTAL MEASUREMENTS OF EXPLOSIVELY DRIVEN SHOCK WAVE RESPONSE OF PMMA

The explosively driven shock response of PMMA was experimentally quantified using high-speed schlieren imaging and Photon Doppler Velocimetry (PDV). The high-speed images were used to visualize the shock response as a function of time. The imaging processing routine outlined in section 2.4 was used to determine the shock velocity. The corresponding particle velocity was experimentally determined using PDV. Free surface velocities were measured at nominal distances ranging from 0.97 mm to 133.3 mm from the explosive source. The particle velocity histories were analyzed to determine the attenuation of the explosively driven spherical shock wave.

3.1 Shock velocity

The explosively driven shock velocity was quantified using high-speed schlieren imaging. The high-speed imaging records were used to create digital streak images where the shock front was extracted using the methods outlined in Section 2.4.3. As shown in Figure 3.1 extracting the shock front yields a line representing the shock position as a function of time. The radius data was selected such that a radius of zero was at the interface between the detonator and the PMMA. The time data was shifted to correct for the detonator function time. This time correction, t_c, shifts the time axis such that $t_c = 0$ was the time when the shock began to propagate into the PMMA sample. Shifting the data allows for comparison across tests.

The shock front (blue line) extracted from the digital streak image presented in Figure 3.1a does not extend to the sample boundary. This was due to boundary effects at approximately 46 mm which caused the sample to not be optically transparent. Residual stresses from the manufacturing process caused the sample boundary to appear opaque. The boundary effects varied from sample to sample which limited the data collected at the sample boundary. It can also be seen from this data that the extracted shock boundary has a 'stair stepping' behavior. The behavior was due to the discrete nature of digital streak images from individual images, the camera resolution, camera frame rate, and the boundary extraction method. As such, there are multiple radius values for a single time value. The

extracted shock radii for the preformed tests, outlined in Table 2.1, are shown in Figure 3.2 with the addition of the shock extracted from the unstressed large scale test (NS2) having a propagation distance of 138.4 mm.

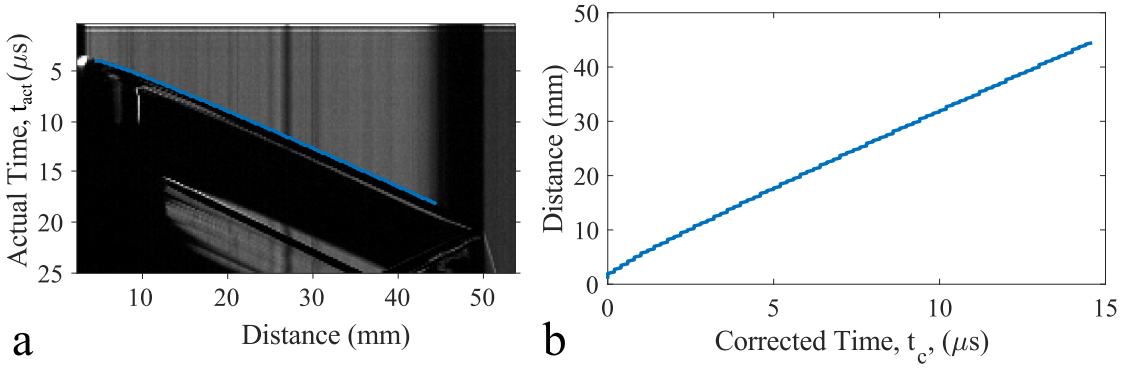

Figure 3.1: (a) The digital streak image for a cube sample having a propagation distance of 50.7 mm and (b) the corresponding shock radius position as a function of time.

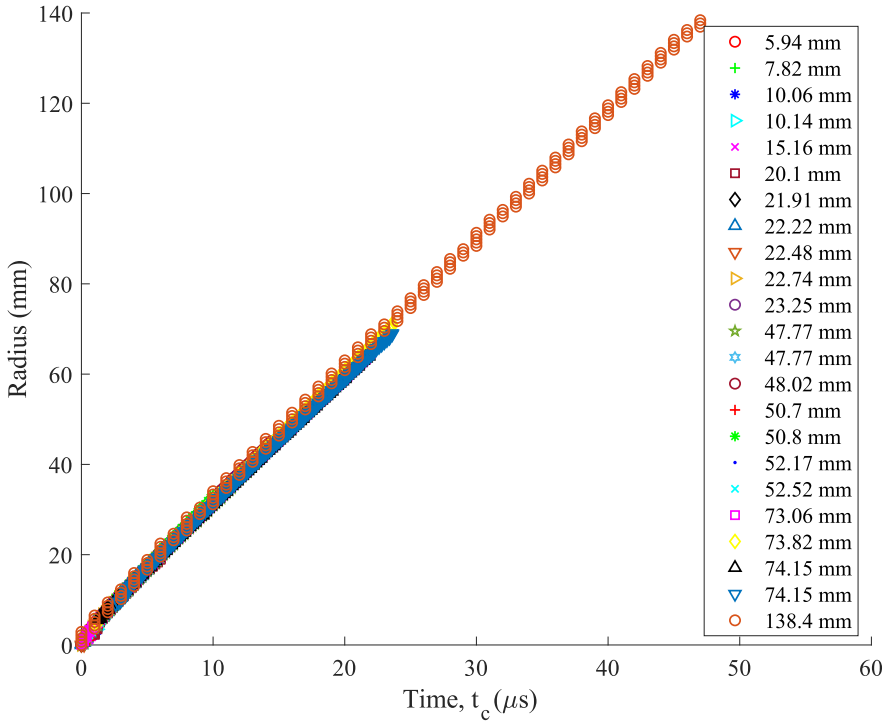

Figure 3.2: Extracted shock radius for every data set ranging in propagation distances from 22.5 mm to 137.4 mm.

Shock waves in PMMA attenuate to the sound velocity fairly rapidly which caused the linear relationship between shock position and time in Figure 3.2. However, there was non-linearity captured in the early time. Fitting a linear line to the data in Figure 3.2 and comparing it to the early time shock radii shows how rapidly the shock attenuates to the sound velocity in PMMA. A comparison between the early time data for propagation distances of 5.94 mm to 48.02 mm and the linear fit is presented in Figure 3.3. The later time data, $x_{pd} > 50$ mm, were excluded because there was an increase in uncertainty which is discussed later in this section. The comparison graph shows that the shock radius as a function of time becomes linear within the first microsecond of propagation.

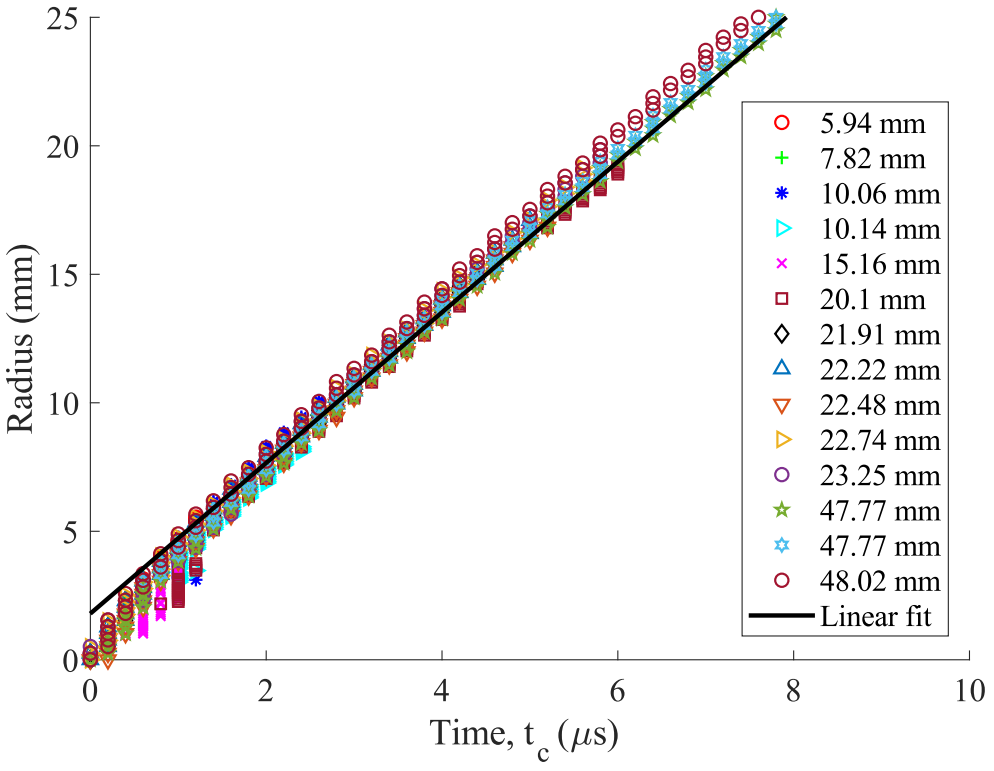

Figure 3.3: Shock radius versus time in PMMA showing the non-linear shock radius behavior in the early time.

Due to the non-linear shock behavior, the shock velocity for the specified propagation distances were determined by applying a linear least-squares regression (LSR) over an analysis window. The analysis window was centered over the propagation distance of interest. It also varied based on the distance from the detonator. Note that the propagation distances of 0.97 mm and 1.92 mm were not analyzed because the detonation process produced a significant amount of light causing over exposure in the images thus the shock was not visualized.

The window size varied based on the propagation distance, the reason for changing the analysis window size was to account for the non-linear behavior close to the explosive source and to reduce the uncertainty in the linear region. For propagation distances below 6 mm a window size of 0.5 μs was used, for propagation distances above 6 mm and below 21 mm the window size was 1 μs, for propagation distances above 21 mm and below 70 mm the window size was 2 μs and for propagation distances above 70 mm a window size of 4 μs was used. Graphs showing the linear fit over the analysis windows for the four different conditions are presented in Figure 3.4. The time axis was shifted such that $t = 0$ was aligned with the propagation distance of interest. This time correction was not necessary, and did not impact the calculated slope, however it was done for a direct comparison across data sets.

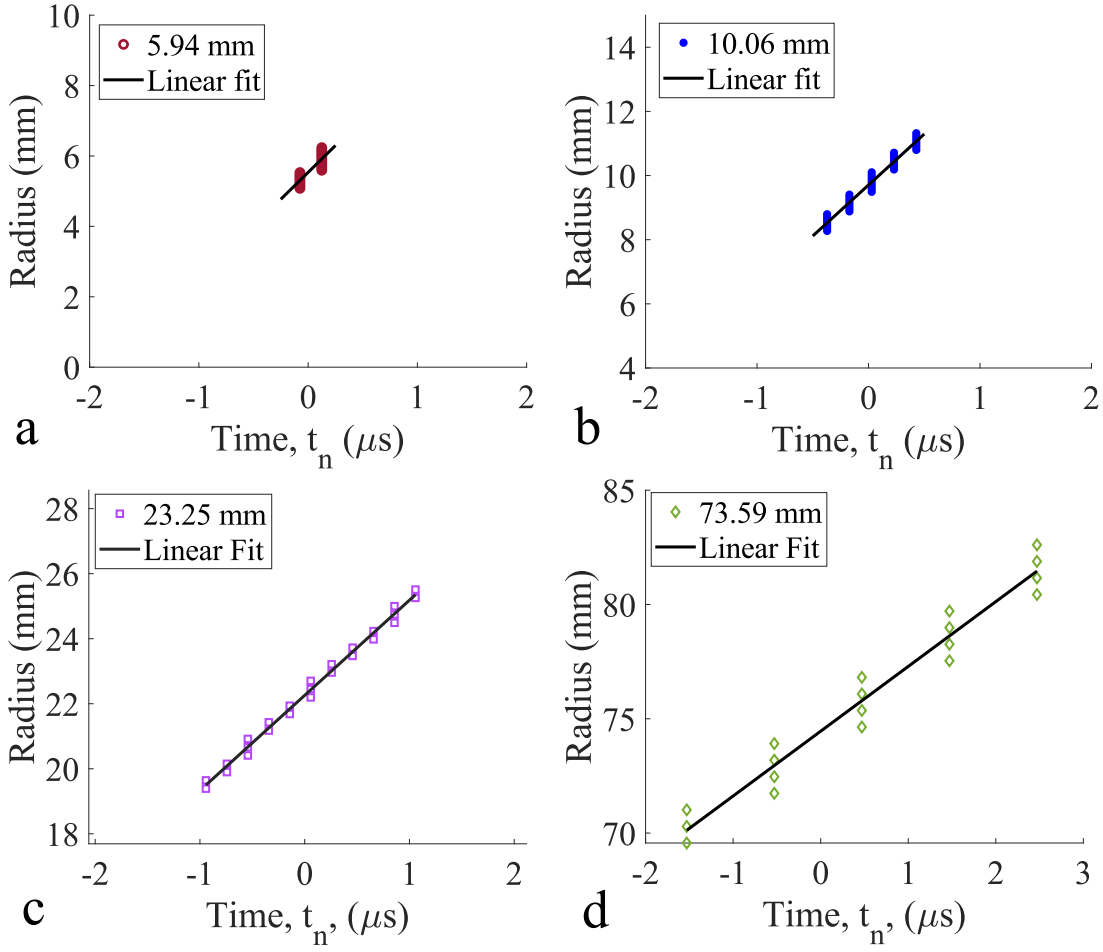

Figure 3.4: Graphs of the linear least-squares regression to the shock radius data at propagation distances of (a) 5.94 mm, (b) 10.06 mm, (c) 23.25 mm and (d) 74.59 mm with the respective window sizes of 0.5 μs, 1 μs, 2 μs, and 4 μs

The graphs of the selected analysis window sizes presented in Figure 3.4 reveals information about the available data and the uncertainty in the analysis. For the propagation distances below 6 mm (a) the analysis window contains two time values, with multiple radius values, which leads to the velocity calculation to be a differentiation over two time points centered over the time of interest. Extending the window size introduced larger error because the non-linearity was not accurately accounted for, and the residual stresses from drilling the hole for the detonator impacted the shock radii visualized close to the explosive source. For the propagation distances above 6 mm and below 21 mm (b) the linear fit goes directly through the center of the radius points for each time point. As for the propagation distances above 21 mm and below 70 mm there are less radius values per one time value, however, there are time points every 0.2 μs. For the propagation distances above 70 mm (d) the time points were every 1 μs.

For determination of the shock velocity at the desired propagation distances the linear least-squares regression was applied to each data set that spanned the propagation distance. The resulting slopes from LSR was then averaged to obtain the shock velocity corresponding to the desired propagation distance. The tests used for determination of the shock velocities varied similarly to the analysis window size. For propagation distances below 30 mm tests below a propagation distance of 70 mm were used, for propagation distances above 30 mm and below 70 mm all SS and Cube tests were used. For propagation distances above 70 mm the SS tests that spanned the desired propagation distance were used along with the LS test. The justification for selecting which tests were used for determining the shock velocity was based on the uncertainty associated with the imaging system. Due to imaging limitations, tests above a propagation distance of 70 mm had a larger uncertainty associated with them which would have a significant impact on the results below a propagation distance of 30 mm. The resulting shock velocities and analysis window size for the propagation distances of interest are presented in Table 3.1. The propagation distances presented in Table 3.1 were selected to compare to the collected PDV data.

The uncertainty in the shock velocity for propagation distances below 70 mm was based on the uncertainty in the average of the shock velocities. The reason for using the uncertainty in the average was because multiple tests were used to determine the shock velocity. As for propagation distances above 70 mm the data was limited, thus, the uncertainty was based on the uncertainty in the linear least-squares regression as outlined in [107]. The uncertainty in the data for propagation distances above 70 mm was significantly larger than values below 70 mm because there were less tests replicated and the uncertainty associated with the LS tests and SS tests above 70 mm was larger than the uncertainty in the Cube tests and SS tests below 70 mm. The LS tests had a larger uncertainty due to the scale relative to the camera resolution. As for the SS tests above a propagation distance of 70 mm, the interpolated resolution on the Shimadzu high-speed cameras was used to capture the full test duration which was not done for the SS tests below 70 mm. The uncertainty in the data close to the explosive source was increased due to external illumination from the detonation of the explosive source not being fully

filtered out with the band-pass filter.

Table 3.1: Measured shock velocities at varied propagation distances.

Sample Geometry used for analysis	Propagation Distance,x_{pd}, (mm)	Analysis window size (μs)	Shock velocity, U_s, (mm/μs)
SS/Cube	3.01 ± 0.01	0.5	4.04 ± 0.22
SS/Cube	3.03 ± 0.01	0.5	3.95 ± 0.14
SS/Cube	3.97 ± 0.01	0.5	3.72 ± 0.17
SS/Cube	5.94 ± 0.01	0.5	3.27 ± 0.11
SS/Cube	7.82 ± 0.01	1.00	3.22 ± 0.11
SS/Cube	10.06 ± 0.01	1.00	3.12 ± 0.07
SS/Cube	10.14 ± 0.01	1.00	3.12 ± 0.07
SS/Cube	15.16 ± 0.01	1.00	3.00 ± 0.13
SS/Cube	20.01 ± 0.01	1.00	2.99 ± 0.11
SS/Cube	21.91 ± 0.13	2.00	2.96 ± 0.02
SS/Cube	22.07 ± 0.13	2.00	2.96 ± 0.02
SS/Cube	22.22 ± 0.13	2.00	2.96 ± 0.02
SS/Cube	22.48 ± 0.13	2.00	2.96 ± 0.02
SS/Cube	22.74 ± 0.13	2.00	2.96 ± 0.02
SS/Cube	23.25 ± 0.13	2.00	2.95 ± 0.02
SS/Cube	47.77 ± 0.13	2.00	2.78 ± 0.06
SS/Cube	47.77 ± 0.13	2.00	2.78 ± 0.06
SS/Cube	48.02 ± 0.13	2.00	2.78 ± 0.06
SS/Cube	50.20 ± 0.12	2.00	2.79 ± 0.06
SS/Cube	50.45 ± 0.12	2.00	2.80 ± 0.06
SS/Cube	50.70 ± 0.12	2.00	2.80 ± 0.06
SS/Cube	50.80 ± 0.17	2.00	2.79 ± 0.06
SS/Cube	52.17 ± 0.17	2.00	2.82 ± 0.06
SS/Cube	52.52 ± 0.17	2.00	2.82 ± 0.06
SS/LS(NS2)	73.06 ± 0.13	4.00	2.72 ± 0.46
SS/LS(NS2)	73.59 ± 0.13	4.00	2.72 ± 0.52
SS/LS(NS2)	73.82 ± 0.13	4.00	2.72 ± 0.54
SS/LS(NS2)	74.15 ± 0.13	4.00	2.84 ± 0.35
LS(NS2)	123.2 ± 1.6	4.00	2.90 ± 0.36
LS(NS2)	133.3 ± 1.6	4.00	2.66 ± 0.46

The large scale tests were also used to understand the explosively driven shock response of PMMA under various uniaxial stress conditions. The same shock extraction methods were applied to the LS stress tests, VS2-2, VS2-20, and HS2-2, for comparison to the unstressed test, NS2. The extracted shock radii as a function of time for the four tests are presented in Figure 3.5. From this graph, the application of external stress does not not appear to impact the shock radius as a function of time.

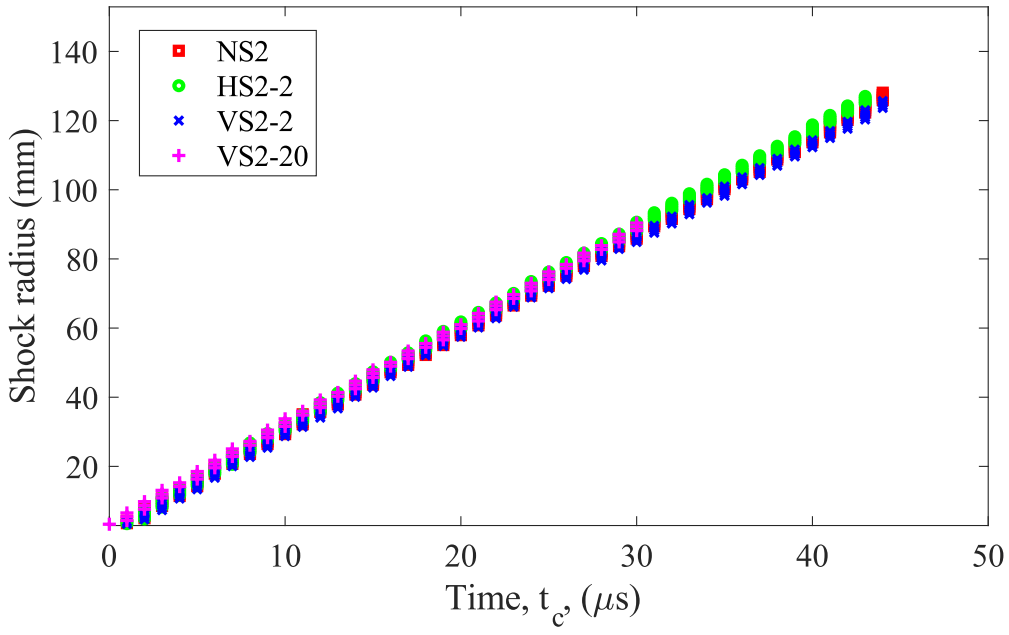

Figure 3.5: Extracted shock radius as a function of time for the Large-scale PMMA cubes having (NS2) no stress, (HS2-2) 2 MPa of uniaxial horizontal stress, (VS2-2) 2 MPa of uniaxial vertical stress, and (VS2-20) 20 MPa of vertical stress.

3.2 Free surface velocity histories

The PDV system and the schlieren images were triggered at the same time. The high-speed image record shows that there was a finite amount of time from the triggering of the camera to when the shock wave appears in the PMMA. This time is referred to as the "detonator function time" and is the time it took for the detonation process to occur after triggering the fireset. The detonator function time was determined using the schlieren images where it was based upon the time the camera was triggered to the time the shock entered the PMMA. The surface velocity histories presented in Figure 3.6 were corrected for the detonator function time such that zero time on the PDV traces matches the time when the shock wave was observed to enter the PMMA in the high-speed images, t_c.

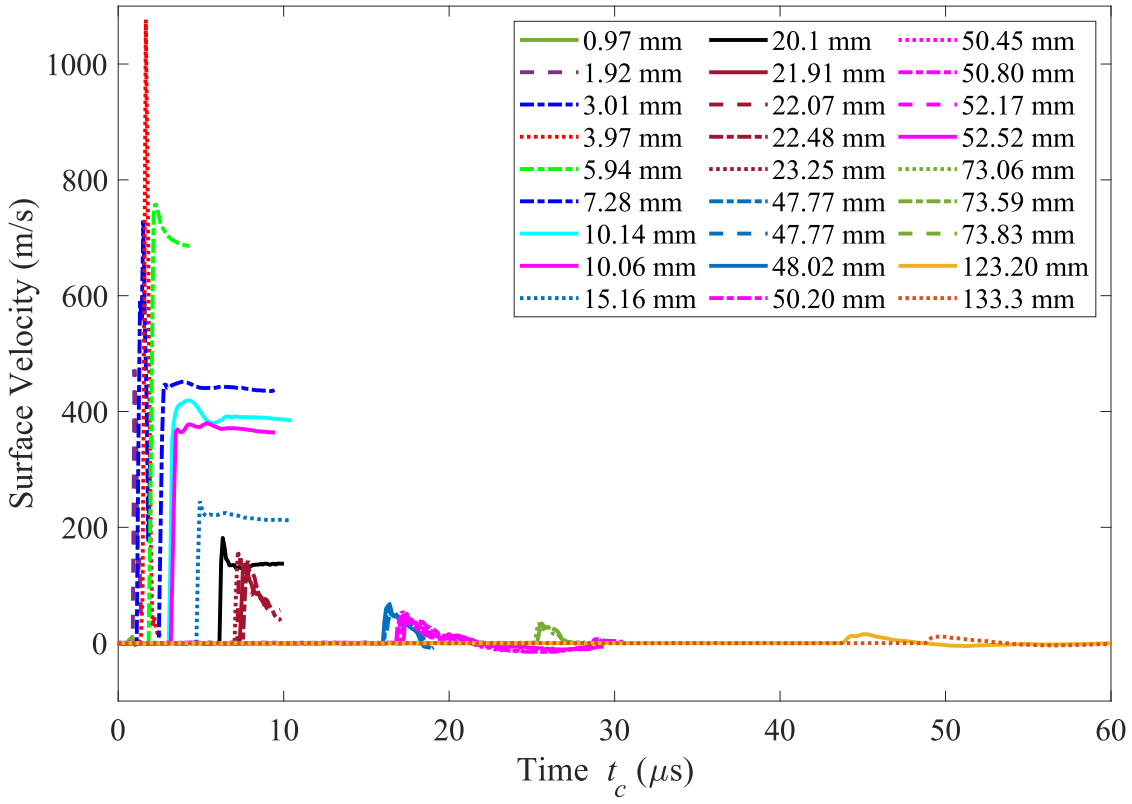

Figure 3.6: Free surface velocity histories for propagation distances of 3.97 mm to 133.3 mm.

The measured time corrected free surface velocity histories are presented in Figure 3.6. The maximum surface velocity is expected to decrease as time, or radius, is increased. The experiments having propagation distances of 0.97 mm to 3.01 mm should have velocities larger than that of the 3.97 mm, tests with the 0.97 mm test having the largest velocity. The expected decay in particle velocity from 0.97 mm to 3.97 mm was not reflected in the graph plotted in Figure 3.6. The non-physical behavior was attributed to the PMMA undergoing significant damage after the initial shock pulse. The sample boundary fully fragmented as shown in Figure 3.7a-e. The fragmenting boundary occurred for propagation distances of 0.97 mm to 7.28 mm but had a more significant impact on the propagation distances of 0.97 mm, 1.92 mm and 3.01 mm. Due to the significant observed fragmentation of the surface, the PDV measurements of surface velocity for the propagation distances of 0.97 mm through 3.01 mm were neglected.

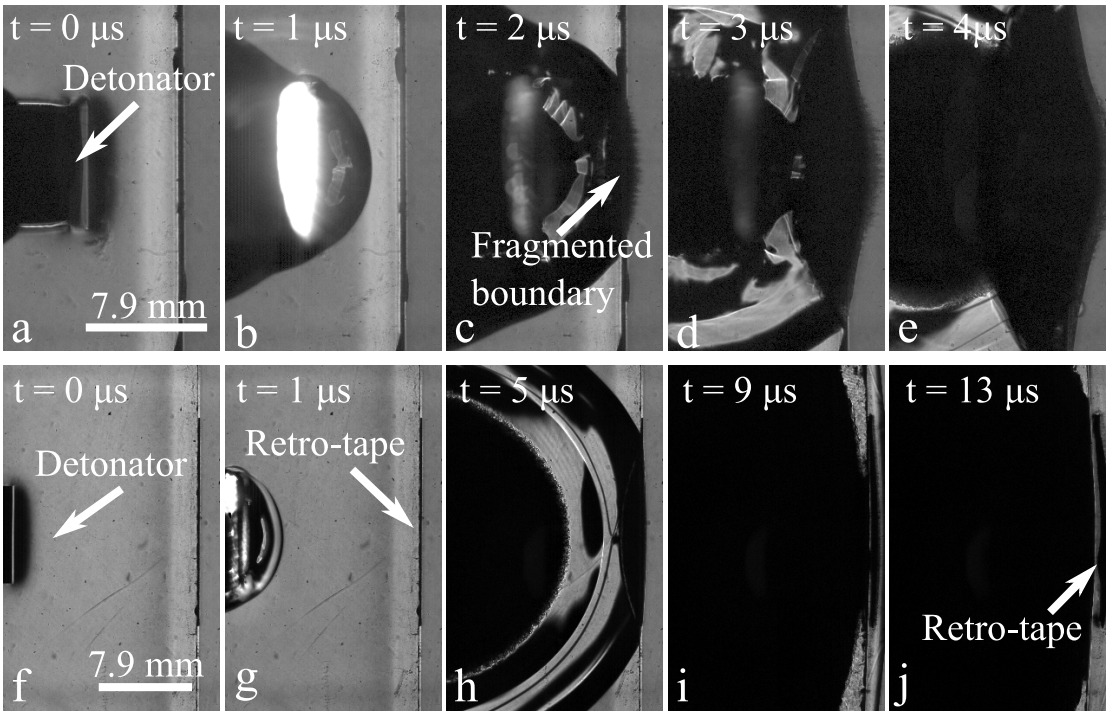

Figure 3.7: High-speed images of the shock propagating through PMMA samples having propagation distances of (a-e) 5.94 mm and (f-j) 15.16 mm. The time on the images were corrected for detonator function time, t_c.

Neglecting the first three PDV measurements in Figure 3.6, the maximum surface velocity decreased as the shock radius increased. The shock pulse and shape recorded using the PDV system was different for each test for a few different reasons. Starting with the shorter propagation distances, the significant damage the PMMA underwent caused a fragmenting boundary. The fragmented boundary was visible in the high-speed images for propagation distances of 3.97 mm to 7.28 mm. The fragmented boundary occurs right after the shock impacts the boundary shown in Figure 3.7c which can be compared to the intact boundary in (h). For some experiments the retro-reflective tape would detach from the sample which was clearly seen for a propagation distance of 15.16 mm, presented in Figure 3.7f-j. The beginning of the retro-reflective tape detaching from the sample is seen in (i) where the fully detached retro-reflective tape is visible in (j). The tape releasing from the sample boundary was visualized for the tests having propagation distance of 15.16 mm, 20.10 mm, and 23.25 mm. For the test having propagation distance of 22.48 and 21.91 mm, imaging limitations did not allow for the sample boundary to be visible and for the sample with a propagation distance of 22.07 mm the high-speed imaging system did not trigger. For the propagation distances of 5.94 mm to 23.23 mm the complications associated with the sample boundary fragmenting and the retro-reflective tape detaching only impacted the release wave captured in the PDV data which can be seen in Figure 3.6.

The full shock pulse duration was captured for experiments having propagation distances greater than 25 mm. To compare the shock pulse shape at the different shock radii (21.91 mm - 133.3 mm) the surface velocity histories were shifted in time such that $t = 0$ μs corresponded to the time the shock impacted the free surface, which is graphed in Figure 3.8. The shorter propagation distances (less than 21 mm) were left out of Figure 3.8 since the shapes of the PDV traces were significantly impacted by the fragmenting and tape dislodging. Figure 3.8 shows that along with the amplitude change, the shock pulse duration also varies. Since PMMA is a viscoelastic material, it is expected that the pulse shape varies as a function of radius. The viscoelasticity of PMMA is often attributed to "rounding up" to the peak particle velocity in the weak shock regime. The rounding up to the max surface velocity is apparent for the tests having nominal propagation distances of 73.76 mm (green), 123.2 mm (yellow), and 133.3 mm (orange). Furthermore, the decay behind the shock appears to behave differently across the nominal propagation distances presented in Figure 3.8.

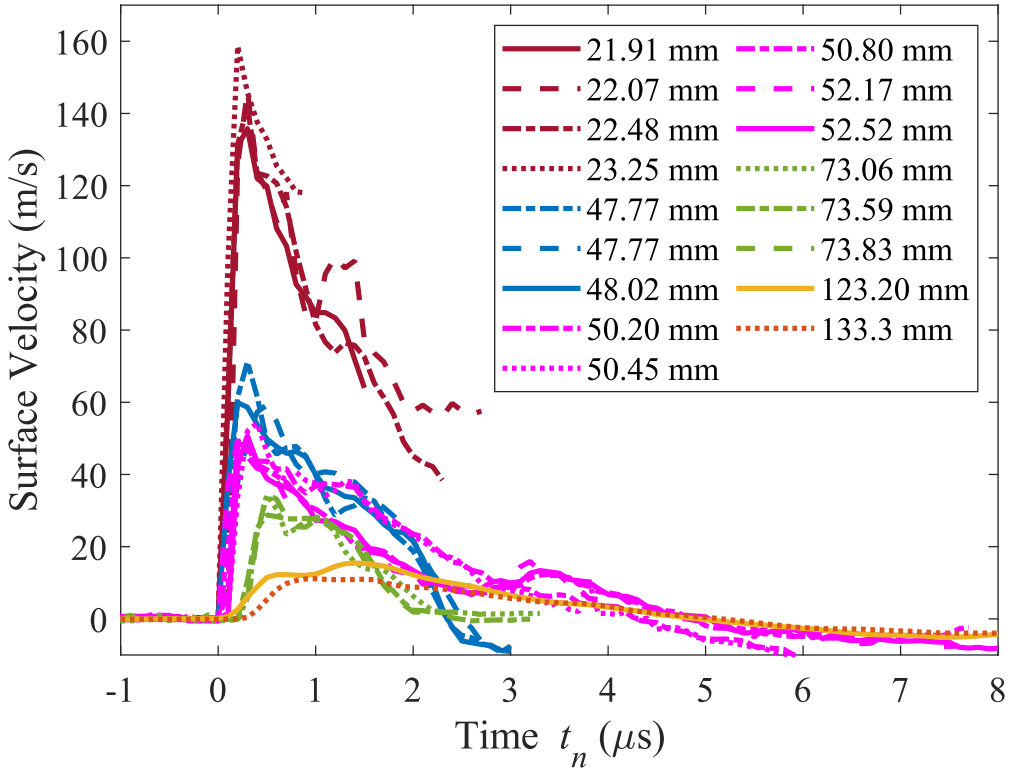

Figure 3.8: Free surface velocity histories for propagation distances from 21.91 mm to 133.3 mm aligned such that $t = 0$ μs was when surface motion was detected.

The surface velocity histories for the nominal propagation distances of 22.48 mm (red) were clipped due to the retro-reflective tape release visualized in the

high-speed images. The tests with nominal propagation distances of 47.85 mm (blue) and 51.14 mm (pink) initially follow a similar trend until approximately 1 to 2 μs where the 47.85 mm tests decay to zero velocity more rapidly than the 51.14 mm tests. The 47.85 mm tests were taken using the SS samples where the propagation distance was longer than the width of the sample, whereas the 51.14 mm tests were collected using cube samples. A rapid decay between 1 and 2 μs also occurred for the tests having a nominal propagation distance of 73.76 mm which were also SS samples. The propagation distance was greater than the sample thickness for the SS tests having nominal propagation distances of 47.85 mm and 73.76 mm, thus, the rapid decay was suspected to be due to surface interactions parallel to the imaging field-of-view. To better understand if the phenomena was due to boundary conditions, the shock radii and surface velocity histories for the SS tests having a nominal propagation distances of 47.85 mm were compared to measurements taken in cubic samples with the nominal propagation distances of 51.14 mm. The shock radii presented in Figure 3.9a are in good agreement, indicating that the shock velocity was not impacted by geometric effects. The surface velocity histories are presented in Figure 3.9b where the divergence between the data sets is more apparent. The two data sets follow the same trend until approximately 1.8 μs indicating that the velocity history was not impacted by geometric effects up to approximately 1.8 μs after the shock impacted the free surface. Based on the conclusions drawn from Figure 3.9, the free surface velocities at $t_n = 0$ μs in Figure 3.7 are not impacted by boundary effects. The shock pulse shape is further discussed in Section 3.3.1.

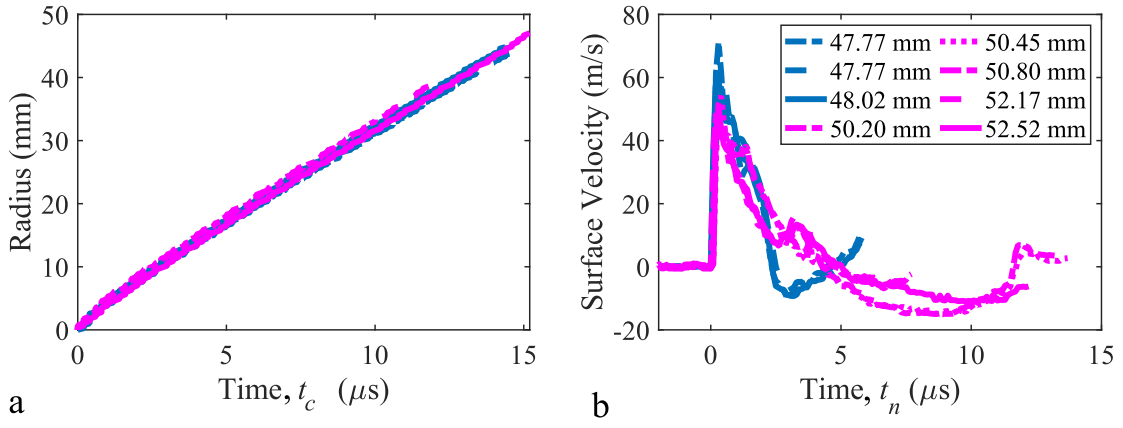

Figure 3.9: Graph of (a) the extracted shock radius versus time and (b) the PDV surface velocity histories for the small-scale samples and the cube samples. The PDV arrival times were shifted to align all the PDV traces to the same point to compare the decay behavior and peak velocities.

The surface velocities corresponding to the desired propagation distances are presented in Table 3.2. The uncertainty in the surface velocity was based on that explored by [36] in conjunction with an uncertainly analysis based on the shock angle impacting the free surface when the PDV probe was $\pm$ 1.8 mm off center line. The maximum surface velocity (u_{sf}) was used to calculate particle velocity (u_p). The presented surface velocities were used to calculate the particle velocities corresponding to the shock velocities presented in Table 3.1. Particle velocity was calculated using the relation:

$$u_p = \frac{u_{sf}}{2} \tag{3.1}$$

The resulting shock and particle velocities are presented in Table 3.4 with further discussion of the shock results in Section 3.3.

Table 3.2: Table summarizing the surface velocities for the varied propagation distances.

Sample Geometry used for analysis	Propagation Distance, x_{pd}, (mm)	Uncorrected Free Surface Arrival Time, t_{act} (μs)	Surface Velocity, u_{sf}, (m/s)
SS	0.97 ± 0.01	3.45	–
SS	1.92 ± 0.01	3.65	–
SS	3.01 ± 0.01	3.85	–
SS	3.03 ± 0.01	–	–
SS	3.97 ± 0.01	3.90	1076.32 ± 1.61
SS	5.94 ± 0.01	4.50	758.96 ± 1.14
SS	7.82 ± 0.01	5.10	447.80 ± 0.67
SS	10.06 ± 0.01	5.70	369.16 ± 0.63
SS	10.14 ± 0.01	5.80	419.26 ± 0.55
SS	15.16 ± 0.01	7.55	244.60 ± 0.37
SS	20.01 ± 0.01	8.95	181.67 ± 0.27
SS	21.91 ± 0.13	10.45	135.61 ± 0.20
SS	22.07 ± 0.13	10.25	146.66 ± 0.22
SS	22.22 ± 0.13	–	–
SS	22.48 ± 0.13	10.65	142.20 ± 0.21
SS	22.74 ± 0.13	–	–
SS	23.25 ± 0.13	10.55	159.55 ± 0.24
SS	47.77 ± 0.13	19.15	71.01 ± 0.11
SS	47.77 ± 0.13	19.45	58.80 ± 0.09
SS	48.02 ± 0.13	19.25	59.96 ± 0.09
Cube	50.20 ± 0.12	20.25	48.48 ± 0.07
Cube	50.45 ± 0.12	14.65 [1]	54.15 ± 0.08
Cube	50.70 ± 0.12	22.10	57.43 ± 0.09
Cube	50.80 ± 0.17	21.25	48.94 ± 0.07
Cube	52.17 ± 0.17	21.35	49.65 ± 0.07
Cube	52.52 ± 0.17	21.85	51.15 ± 0.08
SS	73.06 ± 0.13	28.35	32.88 ± 0.05
SS	73.59 ± 0.13	28.45	29.03 ± 0.04
SS	73.82 ± 0.13	28.45	34.70 ± 0.05
SS	74.15 ± 0.13	–	–
LS(NS2)	123.3 ± 0.13	47.05	15.47 ± 0.02
LS(NS2)	133.3 ± 0.13	52.15	11.13 ± 0.02

[1] Delayed trigger.

Surface velocity and uniaxial stress: Two PDV measurements were taken for the large-scale tests, one aligned with the detonator and the second 50.8 mm from the first PDV probe (See Figure 2.17). As discussed in Section 2.5 due to experimental limitations the PDV measurements for the HS2-2 tests were taken at a different location than the other three tests. Moving the PDV probe location for the HS2-2 test resulted in a slightly longer propagation distance, as presented in Table 3.3.

Table 3.3: A table summarizing the large-scale PDV results.

Sample	Probe #	Approximate Propagation Distance,x_{pd},	Max. Surface Vel. from Det. A (m/s)	Max. Surface Vel. from Det. B (m/s)
NS2	1	123	15.47	6.318
NS2	2	133	11.13	4.608
HS2-2	1	196	7.13	–
HS2-2	2	203	5.838	–
VS2-2	1	123	18.60	7.473
VS2-2	2	133	14.07	6.196
VS2-20	1	123	16.39	7.754
VS2-20	2	133	12.80	5.005

The surface velocity histories are presented in Figure 3.10. There was a weak double peak captured in the data from Detonator A, for example for the HS2 tests at the probe 1 location has an initial peak at a velocity of approximately 12.31 m/s but reaches a maximum velocity of approximately 15.47 m/s. The opposite occurs for the VS2-2 test at the probe 1 location. The velocity reaches the maximum velocity of approximately 18.6 m/s initially then there was a secondary peak on the decay having a velocity of approximately 12.29 m/s. For consistency the maximum surface velocities were used for comparison across the tests which are presented in Table 3.3. The standard deviation in the maximum velocity for the NS2, VS2-2 and VS2-20 tests recorded by probe 1 from detonator A was 1.61 m/s, by probe 2 from detonator A was 1.47 m/s, by probe 1 from detonator B was 0.76 m/s, and probe 2 from detonator B was 0.82 m/s. The standard deviation in the maximum velocity from the respective detonators was similar at the two probe locations. Generally the surface velocity histories for the NS2, VS2-2, and the VS2-20 are in good agreement indicating that the application of external stress does not impact the surface velocity measurements.

The extracted shock radii as a function of time and the surface velocity histories both independently indicate that in the present experiments the application of external stress does not impact the shock response of PMMA. To validate the alignment of the two measurements the surface velocity history and the digital streak images for the NS2 test were compared. The NS2 test was selected as the representative data set since it was found that the external stress did not impact the shock response. The comparison plot is presented in Figure 3.11. The two data sets were aligned based on time zero, which was the time both systems received a

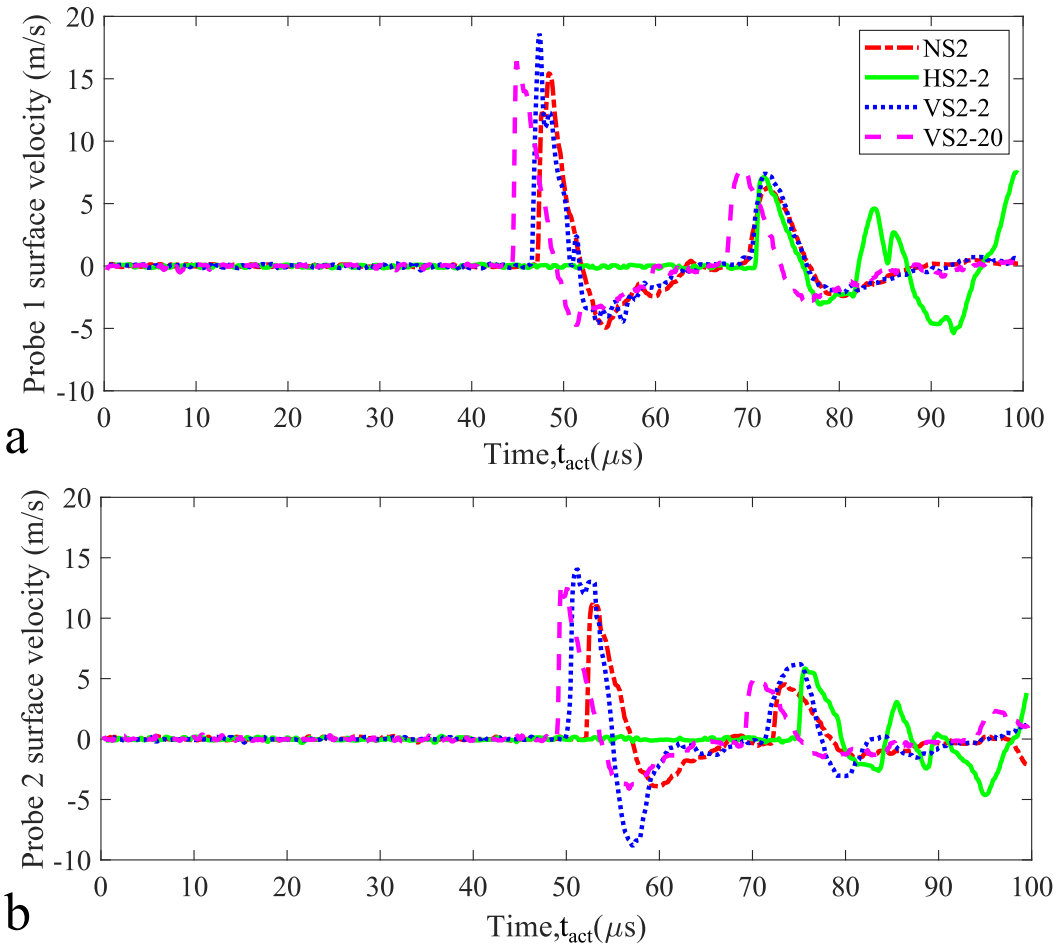

Figure 3.10: Graphs of free surface velocity history for all PMMA blocks with two explosive sources. (a) Surface velocities recorded at detonator level (Probe 1) and (b) free surface velocity history 50.8 mm off detonator level (Probe 2).

trigger signal, t_{act}. Although the boundary of the PMMA sample was not visible in the high-speed images due to imaging limitations, there is agreement between the PDV data and the digital streak images.

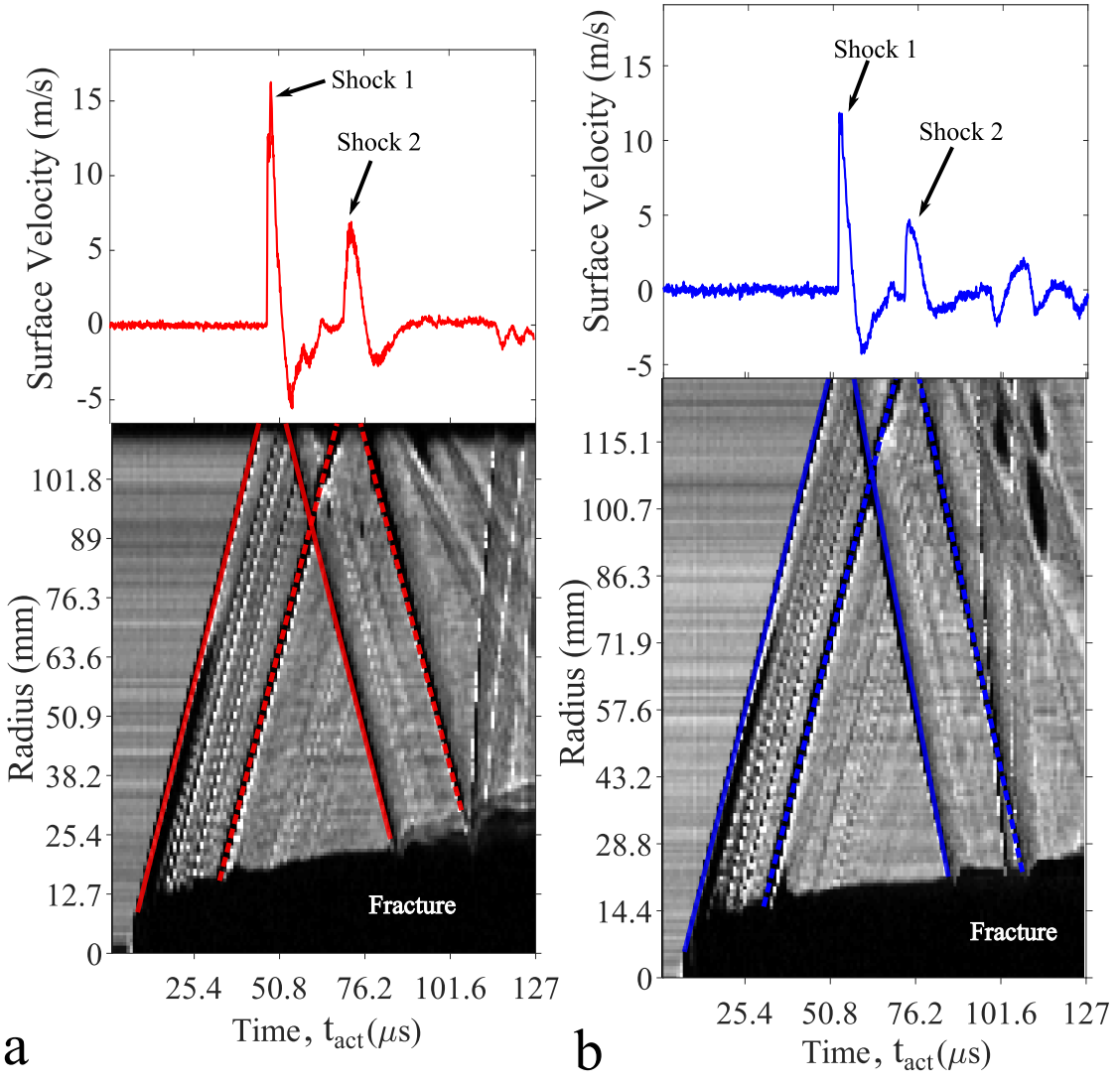

Figure 3.11: Digital streak images and the corresponding free surface velocity PDV trace for the large-scale NS2 tests (a) aligned with the detonator and (b) 50.8 mm below the detonator

3.3 PMMA shock response

Shock velocities and particle velocities for explosively induced shock waves in PMMA at distances from 3.97 mm to 133.3 mm from the explosive source were measured. The resulting shock and particle velocity measurements were plotted with the previously published shock Hugoniot data for PMMA which is shown in Figure 3.12. A summary of the experimentally measured shock parameters are presented in Table 3.4. Note that any test that did not have both shock and particle velocity data was not included in Table 3.4. The particle velocity was determined by converting the maximum free surface velocity history measured in the PDV trace to particle velocity.

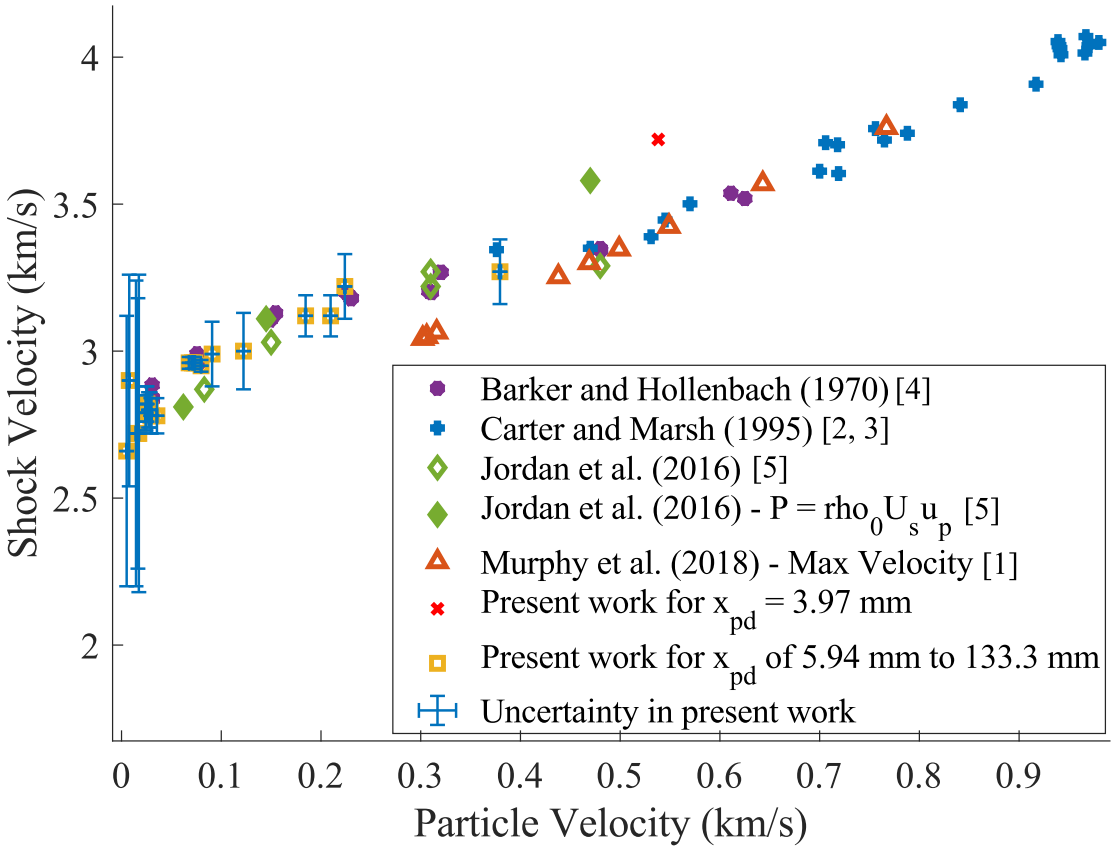

Figure 3.12: Shock Hugoniot for PMMA from explosive loading experiments conducted here and by Murphy et. al [1] and Marsh [2, 3], and impact experiments conducted by Barker and Hollenbach [4] and Jordan et. al [5].

Figure 3.12 shows that the present work is in agreement with the previously published work up to an approximate particle velocity of 0.4 km/s. In plotting the Hugoniot it was discovered that the data for the propagation distance of 3.97 mm did not agree with the previously published data when all the other data in

the present work did, thus the point was omitted from further analysis. The point was plotted on the Hugoniot as a red "x" for completeness, but above a particle velocity of 0.4 km/s the PDV data was significantly impacted by the damage imparted by the explosive event.

Table 3.4: Summary of the shock parameters for propagation distances from 5.94 mm to 133.3 mm.

Propagation Distance, x_{pd}, (mm)	Particle Velocity, u_p, (m/s)	Shock velocity, U_s, (mm/μs)	stress, σ_{PDV}, (MPa)
5.94 ± 0.01	379.48 ± 1.14	3.27 ± 0.11	1464 ± 49
7.82 ± 0.01	223.9 ± 0.67	3.22 ± 0.11	850 ± 29
10.06 ± 0.01	184.58 ± 0.63	3.12 ± 0.07	524 ± 17
10.14 ± 0.01	209.63 ± 0.55	3.12 ± 0.07	679 ± 15
15.16 ± 0.01	122.30 ± 0.37	3.00 ± 0.13	432 ± 19
20.01 ± 0.01	90.83 ± 0.27	2.99 ± 0.11	320 ± 12
21.91 ± 0.13	67.80 ± 0.14	2.96 ± 0.02	236 ± 2
22.07 ± 0.13	73.33 ± 0.15	2.96 ± 0.02	255 ± 2
22.48 ± 0.13	71.10 ± 0.14	2.96 ± 0.02	247 ± 2
23.25 ± 0.13	79.77 ± 0.16	2.95 ± 0.02	277 ± 2
47.77 ± 0.13	35.50 ± 0.07	2.78 ± 0.06	116 ± 3
47.77 ± 0.13	29.40 ± 0.06	2.78 ± 0.06	96 ± 2
48.02 ± 0.13	29.98 ± 0.06	2.78 ± 0.06	98 ± 2
50.20 ± 0.12	24.24 ± 0.05	2.79 ± 0.06	80 ± 2
50.45 ± 0.12	27.08 ± 0.05	2.80 ± 0.06	90 ± 2
50.70 ± 0.12	28.71 ± 0.06	2.80 ± 0.06	95 ± 2
50.80 ± 0.17	24.47 ± 0.05	2.79 ± 0.06	81 ± 2
52.17 ± 0.17	24.83 ± 0.05	2.82 ± 0.06	83 ± 2
52.52 ± 0.17	25.58 ± 0.05	2.82 ± 0.06	84 ± 2
73.06 ± 0.13	16.44 ± 0.03	2.72 ± 0.46	53 ± 9
73.59 ± 0.13	14.52 ± 0.03	2.72 ± 0.52	47 ± 9
73.82 ± 0.13	17.35 ± 0.03	2.72 ± 0.54	56 ± 3
123.3 ± 0.13	7.73 ± 0.02	2.90 ± 0.36	26 ± 3
133.3 ± 0.13	$5.15^{1} \pm 0.01$	2.66 ± 0.46	16 ± 3

[1] Geometric correction applied.

The previous experiments in the literature studied the material shock response using planar impact imparting a shock pulse proportional to the impactor thickness. Utilization of planar impact allows for control over the impact pressure, thus, the samples are a fixed length. Furthermore, planar impacts reduce the shock wave propagation to a one-dimensional problem. The data presented here and that published in [40] utilize explosives to impart the shock wave into the material of varying lengths. Explosively driven shock waves impart a spherical

shock producing a three-dimensional problem and by varying the sample length the pressure decay as a function of shock radius can thus be described. The shock Hugoniot presented in Figure 3.12 for propagation distances from 5.94 mm to 133.3 mm shows that there is agreement between the datasets despite the difference in the method in which the shock was initiated. The non-linear shock Hugoniot for PMMA is well documented in the literature [5] which is also consistent for the explosively driven shock response of PMMA.

The non-linear shock Hugoniot of PMMA is broken up into three regimes: weak shock, transition/non-linear, and the principal Hugoniot/strong shock regime. The regions are bounded by particle velocities and stress since there exists regions of the Hugoniot where multiple particle velocities exist for a singular shock velocity. The shock parameters in Table 3.4 and the measured density (ρ_0) of the PMMA can be used to calculate stress (σ_{PDV}) using conservation of momentum [8, 10]:

$$\sigma_{PDV} = \rho u_p U_s \tag{3.2}$$

The resulting stress for the present experiments are shown in Table 3.4. A graph of the shock pressure as a function of propagation distance is presented in Figure 3.13. In the literature the first segment of the linear region of the shock Hugoniot exists up to a particle velocity of approximately 0.13 km/s and a stress of approximately 0.75 GPa [12]. The majority of the data collected was in the weak shock regime, which corresponds to propagation distances greater than 15.16 mm. The next zone is the transitional zone which has been defined in the literature as having approximate stress of 0.75 GPa to 1.5 GPa. The lower end of the transitional zone however is typically defined as the Hugoniot elastic limit (HEL) of PMMA. In the literature the HEL of PMMA has been defined in the range of 0.7 GPa to 0.8 GPa [4, 22]. Based on the location of the points on the Hugoniot for the propagation distance of 5.94 mm to 10.06 mm it appears that they lie in the non-linear/transitional region, with the propagation distance of 10.06 and 10.14 mm having a stress on the lower end of the HEL of PMMA. The data for a propagation distance of 5.94 mm was right on the border of the non-linear Hugoniot, where the principal Hugoniot begins. Since the propagation distance of 5.94 mm is on the border of the non-linear and principal Hugoniot with a stress of approximately 1.5 GPa this indicates that the propagation distances from 0.97 mm to 3.97 mm were in the strong shock regime. Thus, the PMMA damage in the strong shock regime was too significant to measure surface velocities, therefore, interface window materials should be implemented.

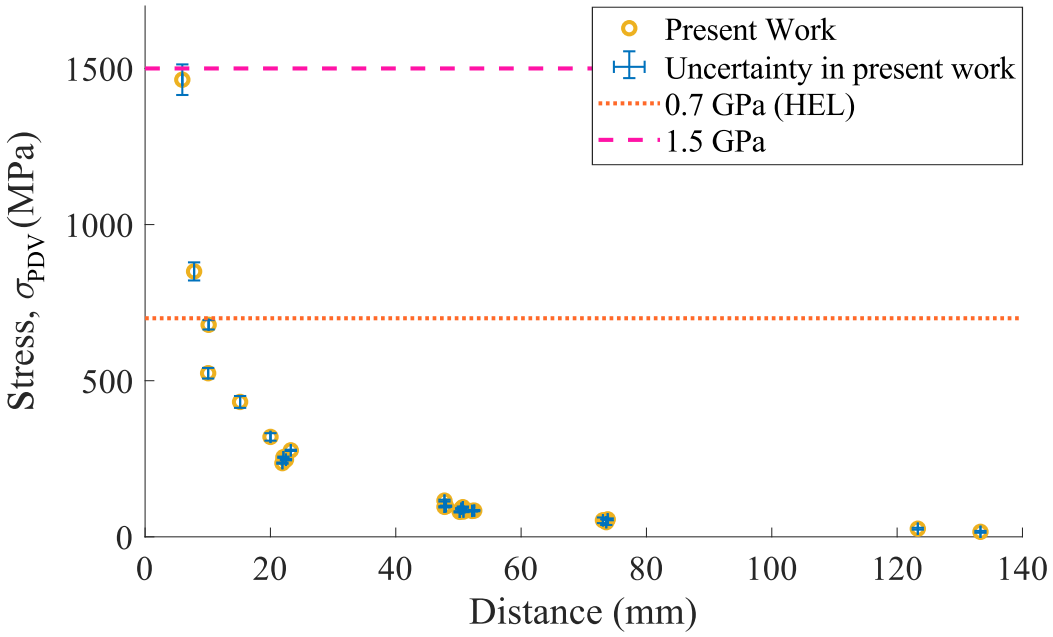

Figure 3.13: A plot of stress as a function of radius from an explosively drive shock wave for propagation distances from 5.94 mm to 133.3 mm.

3.3.1 Shock decay

Understanding where in the shock Hugoniot the experiments were conducted was also of importance for understanding the attenuation behavior of the material. Here, three classifications of the material response were considered: plastic, elastic, and elastic-plastic [10]. Plastic response of a material occurs at high pressures where the elastic portion of the response can be neglected. Below that regime there is the elastic-plastic behavior where a material will behave both plastically and elastically. There is a maximum amount of stress which a material will behave purely elastic which is the Hugoniot elastic limit of the material. In solids, the amplitude of spherical elastic waves decay proportional to a r^{-1} behavior [8].

The majority of the experiments in the present work were conducted below the Hugoniot elastic limit of PMMA, 0.7 - 0.8 GPa. However, the data points above 0.8 GPa are still in the non-linear region of the Hugoniot. In the non-linear region of the Hugoniot the material response is dictated by the viscoelasticity of the material. It is not until the strong shock regimen where the material response is fully plastic. In the present experiments the material response was elastic/viscoelastic. To better understand the material behavior a trend line was fit to the particle velocity versus distance data in Figure 3.14 and compared to the explosively loaded material response reported by Murphy et al. [1].

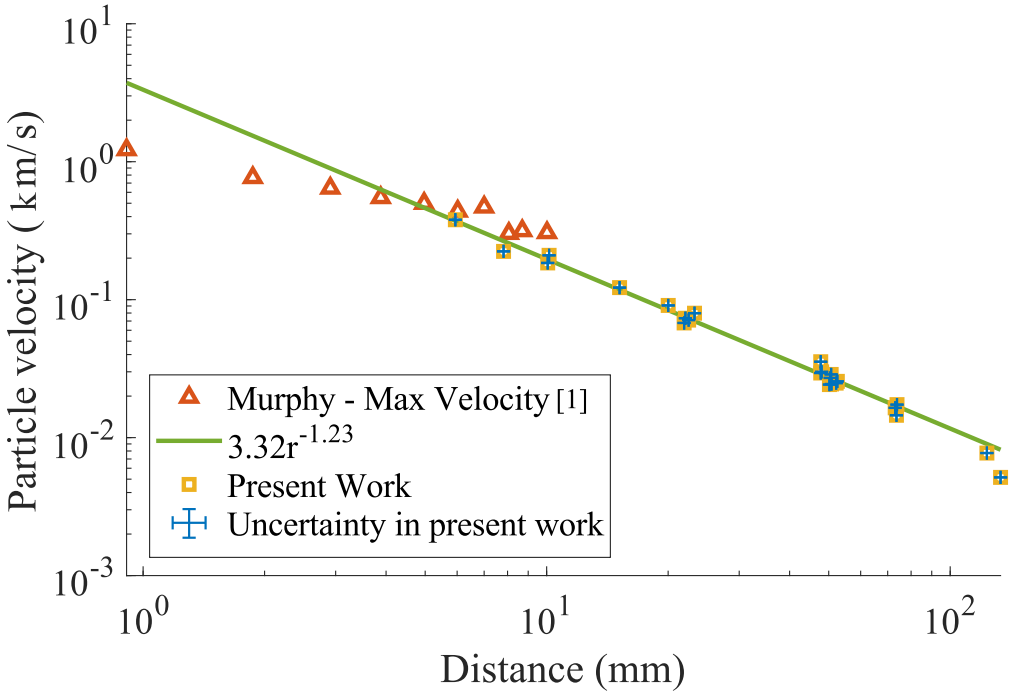

Figure 3.14: Logarithmic plot of particle velocity versus radius for explosively loaded PMMA from the present work and work collected by Murphy et. al [1].

The data from the weak shock regime through the transitional region behaved linear on the log-log axis. The linearity on the log-log axis is an exponential decay which is the expected decay behavior from an explosively driven shock. Fitting a trend line to the present experiments yields an equation of:

$$u_p = 3.32r^{-1.23} \tag{3.3}$$

The equation has an exponent that is slightly more negative than expected for an elastic wave (r^{-1}). The deviation from the elastic wave propagation is hypothesized to be caused by the viscoelastic behavior of PMMA. The particle velocity histories measured here were observed to have a more gradual particle velocity increase after the shock, rather than the immediate jump increase, which has been identified as a characteristic of a viscoelastic material response [4]. The explosively driven spherical shock waves cause the particle velocity decay behind the shock, which further causes the expected elastic peak particle velocity to not be achieved. These combined effects result in the slope of the fit equation being more negative.

PMMA has been observed to act viscoelastically in the non-linear region of the shock Hugoniot [4, 22], which is the area where these experiments are performed. There was a divergence between the trend line fit and the data collected by Murphy et al. [1] as the distance from the explosive source was reduced below about 2 mm, which aligns with the change in the shock behavior noted by Murphy et

al. [1] corresponding to the strong shock regime. Murphy et al. also reported a jump velocity and a maximum velocity. The two wave form is not discussed here, furthermore, in the present comparison only the maximum velocity recorded by [1] was reported. This analysis informs the material response, and the decay behavior of the shock as a function of radius. The particle velocity is proportional to the stress, thus, the shock pressure decay was further explored by plotting the stress as a function of shock radius shown in Figure 3.13.

The plot of stress as a function of radius (Figure 3.13) yields the expected exponential decay which approaches zero stress. The plot of stress as a function of radius gives information about the peak pressure decay of the shock as it propagates though the material. The cause of the shock wave attenuation is based on the release wave overtaking the shock wave. Explosively driven shock waves are significantly impacted by the decay caused by the release wave due to the pulse shape imparted by the explosive. For air blast, the shock pulse shape is well documented and represented by the Friedlander equation [108]:

$$p_I = p_0(1 - t/t_d)e^{-\alpha t/t_d} \tag{3.4}$$

Where p_I is the instantaneous over pressure, p_0 is the peak over pressure at $t_n = 0$, t_d is the pulse duration, and α is a waveform parameter. In air this wave profile decays and broadens with distance from the explosive source. This same behavior, broadening of the shock wave with increased radius as peak particle velocity decreases, was captured in the PDV data. The PDV data is proportional to pressure, or stress in solids. Analysis of the shock pulse shape gives insight into the shocked material behavior. In air it is well documented that the pulse duration informs the amount of damage to a structure imparted by the shock [108]. Quantification of air blast damage is generally further characterized through calculation of the shock impulse:

$$I/A = \int_0^{t_d} p dt = p_0 t_d \left[\frac{1}{\alpha} - \frac{1}{\alpha^2}(1 - e^{-\alpha})\right] \tag{3.5}$$

No equivalent shock profile evolution or quantification has been published for explosives embedded in a solid material and was of interest here. Since particle velocity is proportional to stress, the shock pulse shape analysis was explored using the PDV data converted to stress using Equation 3.2. As discussed in Section 3.2, the measured shape of the release wave was impacted by the detachment of the retro-reflective tape for propagation distances below 30 mm and by geometric effects for nominal propagation distances of 47.85 mm and 73.76 mm. Since the detachment of the retro-reflective tape was significant the shock pulse shape analysis was considered for the nominal propagation distances of 47.85 mm and 51.14 mm to see how the geometric effects impact the shock pulse shape.

Geometric effects relating to the propagation distance, x_{pd}, relative to the sample width, x_W, impacted the decay behavior for the experiments with nominal propagation distances of 47.85 mm and 73.76 mm approximately 1 to 2 μs into the release wave. The pulse shape for the experiments having a nominal propagation

distance of 51.14 mm were not impacted by the sample geometry because the propagation distance was shorter than the sample thickness. The difference in the shock pulse shape between the experiments with a nominal propagation distance of 47.85 mm and a nominal propagation distance of 51.14 mm compared to digital streak images are presented in Figure 3.15.

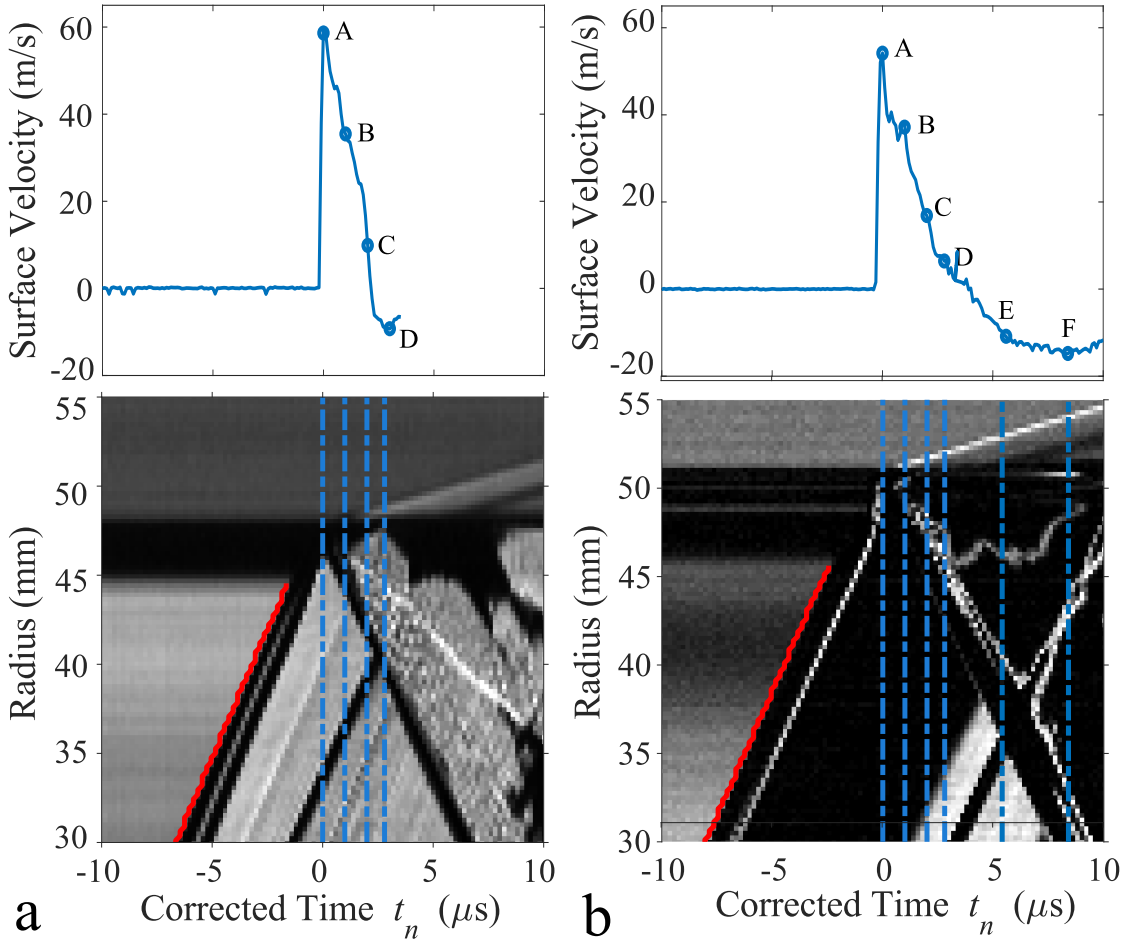

Figure 3.15: Digital streak images and the corresponding free surface velocity PDV trace for (a) a SS PMMA sample having a propagation distance of 48.02 mm and (b) a Cube PMMA sample having a propagation distance of 50.45 mm. Points A - F correspond to a normalized time of A) 0 μs , B) 1 μs, C) 2 μs, and D) 3 μs. Points E and F are 5.6 μs and 8.4 μs, respectively.

Figure 3.15 shows the comparison between the PDV trace and digital streak image for (a) the small scale sample with a propagation distance of 48.02 mm and (b) the cube sample with a propagation distance of 50.45 mm. The time was normalized such that time zero, point A, was when the shock wave reached the free surface. Through comparison of the digital streak images to the PDV data

there are artifacts which indicate differences in the shock response for the two geometries. After the first shock enters the field of view there is a second shock wave that enters the field of view at approximately -1 μs in the small scale sample which appears at approximately 3 μs for the cube sample. The time difference between the first shock and the second shock for the small scale sample and the cube sample is 5 μs and 10.8 μs, respectively. From the digital streak images it does not appear that the second shock arrival would impact the decay behind the shock.

In analyzing the PDV data, points A - D are fixed at the same time, 1 μs apart. Point B and C correspond to the approximate range of time when the two PDV decay traces deviate. Point D corresponds to the approximate time that the SS sample reaches a minimum. Point E and F are only shown on the cube sample to compare the PDV trace to the digital streak image as the decay curve reaches a minimum in the cube sample. The approximate pulse duration, t_d, based on the time when the shock impacts the free surface to the decay reaching a zero velocity, is 2.15 μs for the SS sample and 4.05 μs for the cube sample. These were the pulse durations used when fitting Equation 3.4 to the experimental data.

Since particle velocity and pressure are proportional, pressure was substituted for particle velocity in Equation 3.4 in order to determine the wave form parameter α for the PDV data:

$$u_{pI} = u_{pmax}(1 - t/t_d)e^{-\alpha t/t_d} \tag{3.6}$$

Substituting pressure for particle velocity the equation was rewritten such that u_{pI} was the calculated particle velocity history and u_{pmax} was the maximum particle velocity. The fit to the PDV data using Equation 3.6 for (a) the SS experiment having a propagation distance of 48.02 mm and (b) the cube experiment having a propagation distance of 50.45 mm are presented in Figure 3.16.

The wave form parameter was iterated to find the best fit for the two experiments, which were values of -0.1 for the SS experiment and 1.3 for the cube experiment. A negative value of alpha is not typical which could be caused by geometric effects. The fit using both values of α were plotted for both experiments shown in Figure 3.16. For the SS experiment a value of α = 1.3 under predicts the velocity history. Likewise, a value of α = -0.1 over predicts the velocity history for the cube experiment. As such, the vales of α = -0.1 for the SS experiment and α = 1.3 for the cube experiment were used to calculate the instantaneous over pressure using Equation 3.4. The pressure history are plotted in Figure 3.17

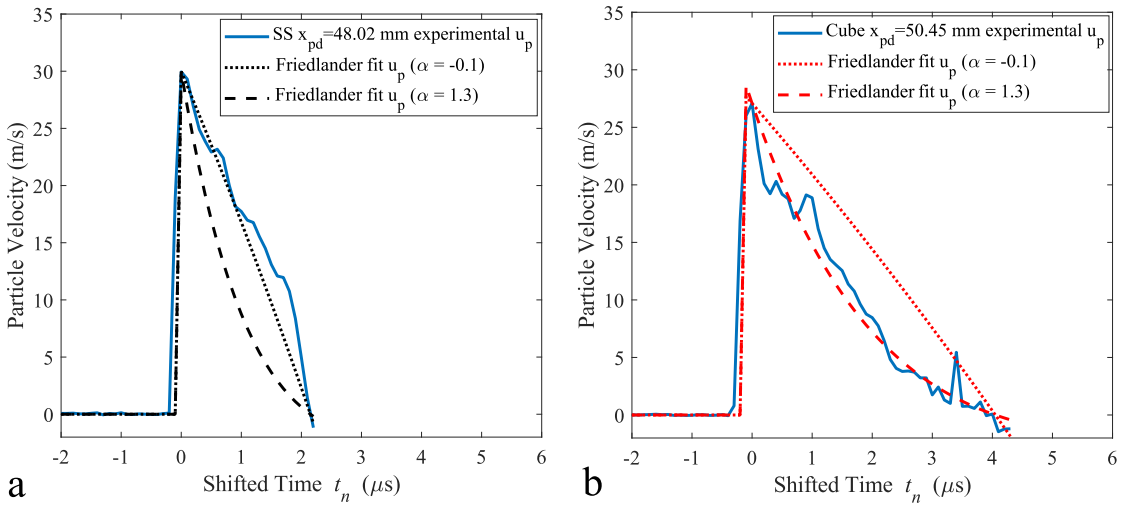

Figure 3.16: Particle velocity histories and the fit to the particle velocity histories using Equation 3.6 for two different values of α for (a) the SS experiment having a propagation distance of 48.02 mm and (b) the cube experiment having a propagation distance of 50.45 mm.

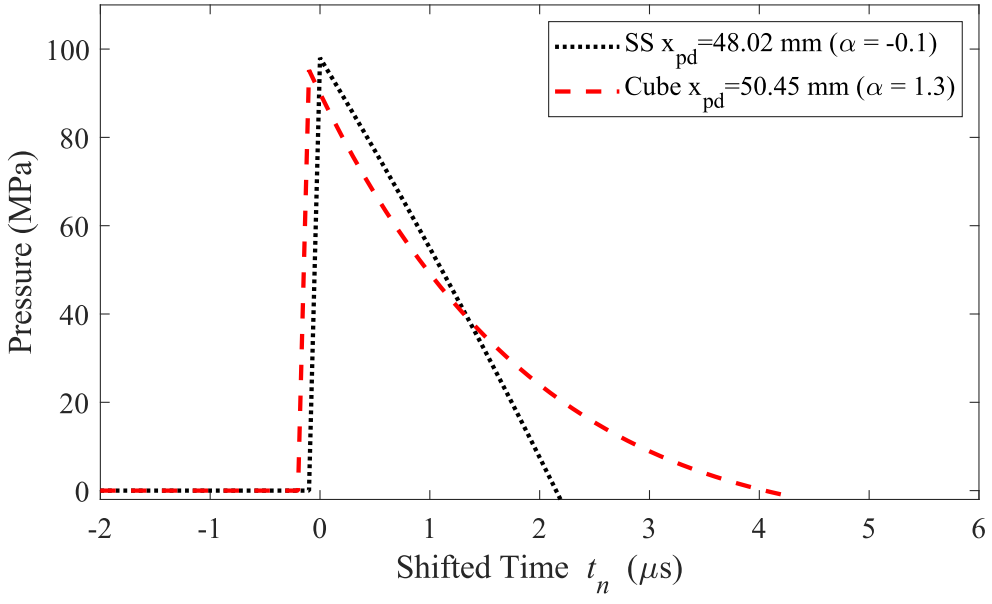

Figure 3.17: Plot of the calculated instantaneous over pressure using Equation 3.6 for (black dotted line) the SS experiment having a propagation distances of 48.02 mm and (Red dashed line) the cube experiment having a propagation distances of 50.45 mm.

The shape of the calculated shock wave pulse was significantly different for the SS test and the cube test. The cube test did have a slightly longer propagation distance, however, if the difference in the shock pulse shaped was due to radial attenuation there would also be a decrease in particle velocity. It does appear that the cube test had a slightly larger area under the curve which mathematically is described by the shock impulse per unit area, or the blast impulse. Knowing the wave parameter, the blast impulse was calculated using Equation 3.5. The blast impulse for the SS test was approximately 109 MPa-μs whereas the shock impulse for the cube test was approximately 124 MPa-μs. This indicates that the boundary interaction impacted the release wave behavior such that the blast impulse was reduced.

3.4 Discussion

The shock Hugoniot for PMMA has previously been defined using planar shock experiments reducing the shock wave propagation to a one-dimensional problem [4, 5]. In the present experiments, the shock response of explosively loaded PMMA was experimentally defined. Explosively driven shocks impart three-dimensional spherical shock waves which had not be extensively researched in the literature [40]. The explosively driven U_s-u_p Hugoniot through the weak shock regime to the upper boundary of the transitional region was in agreement with the previously published work for the planar shock experiments. The data collected in the strong shock regime was significantly impacted by the damage caused by the explosive event, thus, the strong shock region was not reached.

For planar shock experiments, fixed sample lengths are used and the impact pressure is varied to build the shock Hugoniot. In the present work the same explosive load was used for every experiment requiring samples of varying lengths to experimentally measure the shock and particle velocity. As such, the shock state of PMMA was defined at various distances, or shock radii, from the explosive source. This informed the shock attenuation as a function of shock radius in PMMA. In the log-log space there was a linear relationship between particle velocity as a function of radius indicating an exponential decay similar to that of an elastic material response. The decay exponent was slightly more negative than that of an elastic wave, which was attributed to the viscoelasticity of PMMA. The viscolasticity of PMMA has been indicated as the cause of the non-linear region of the shock Hugoniot which was the region studied here. Furthermore, the viscoelasticity also been attributed to rounding up to the peak particle velocity for PMMA shock experiments below the strong shock regime.

Particle velocity is proportional to stress in solids, thus, the particle velocity, shock velocity, and density were used to calculate the stress as a function of radius. However, the shock decay is dictated by the release wave. Since particle velocity is proportional to stress, the PDV data informed the release wave decay behavior. Air shock pulse analysis [108] was applied to shock pulse in PMMA. The analysis was used to describe geometric attenuation caused by reflected shock

waves interacting with the release wave behind the shock wave in samples where the propagation distance was longer than the width.

The shock velocity and particle velocity in PMMA was also used to determine if external stress impacted the shock response. In the present work it was found that external stress did not impact the shock response of PMMA.

CHAPTER 4

EXPERIMENTAL EXPLOSIVELY DRIVEN FRACTURE RESPONSE OF PMMA

The explosive induced fracture of PMMA was imaged using high-speed shadowgraphy. The high-speed video records were then analyzed to extract the fracture front, which was related to a fracture radius and volume in the samples. Post-test images of the PMMA sample cubes aided in the determination of three-dimensional effects not directly imaged by the cameras. The results show that the fractures are primarily driven by the high pressure gases produced by the explosive detonation.

4.1 Post-test fracture characteristics

The explosive induced fracture response of PMMA was recorded using two high-speed cameras which visualized the event along the same imaging axis. The imaging arrangement recorded the three-dimensional event as a projection onto a two-dimensional plane. Fracture directions were not visualized in the shadowgrams therefore post-test images of the samples were used to measure the fracture lengths and corresponding angles. Figure 4.1 shows images of PMMA samples from a top-down view along the bore hole (a-d) and a side view perpendicular to the imaging plane (e-h). The images are from the test configurations NS2 (a and e), HS2-2 (b and f), VS2-2 (c and g), and VS2-20 (d and h). The fracture angles were measured from a horizontal reference plane parallel to the imaging plane. The reference plane is shown schematically as the solid black line in Figure 4.1 a-d. Individual fractures were identified in the top-down image then their angle relative to the reference plane and their length was recorded. The approximate lengths and angles are listed in Table 4.1. The fracture angles measured here were used to make the geometric corrections in the fracture radius calculations.

The fractures were numbered for identification purposes and the numbers in Figure 4.1 correspond to the numbers in in Table 4.1. Letters, in conjunction with the fracture number, were used to identify fractures which appeared to change direction. For fractures that changed directions, the lengths reported in Table 4.1 are for each segment, i.e., HS2-2 (Figure 4.1b) fracture 1a starts at an angle of 51.1 degrees for a length of 11 mm then changes direction and classification to fracture 1b for the next 50 mm. The total length of that fracture surface is the sum of the

two length segments. Analysis of the post-test images revealed differences in the fracture behavior for the four different stress cases.

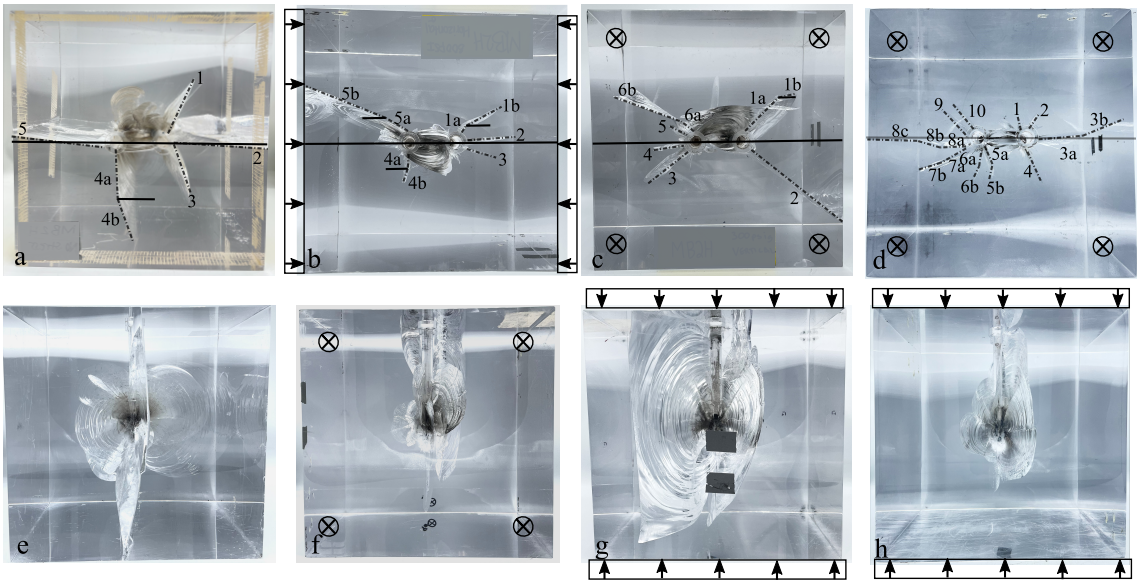

Figure 4.1: (a-d) Top and (e-h) side view of the fractured PMMA cubes for the (a and e) NS2, (b and f) HS2-2, (c and g) VS2-2, and (d and h) VS2-20 test configurations.

As expected, the fracture lengths for the unstressed test configuration, NS2, were longer than the fractures observed in the stressed test cases, HS2-2, VS2-2, and VS2-20. Although there was at least one fracture that reached the sample boundary in each experiment, the fractures in the NS2 test broke the sample in two pieces which can be seen in Figure 4.1a. For the unstressed test case the longest fractures, 2 and 5, were aligned with the imaging plane with small fracture angles of approximately 5° and 8°, respectively. The longest fractures for the tests with 2 MPa of uniaxial stress had the longest fractures off axis from the imaging plane. The horizontal stress case, Figure 4.1b, had the longest fracture initially at an angle of approximately 30° which then changed direction to an angle of approximately 20°. For the vertical stress test with 2 MPa of uni-axial stress, Figure 4.1c, the longest fractures grow symmetrically at approximate 45° from the imaging plane. In the experiment with the largest amount of uni-axial stress, Figure 4.1d, the longest fractures are in the same direction as the NS2 tests but did not fracture the cube in two pieces and experienced minor direction change.

Looking at the general fracture trends across the four different tests it is apparent that the application of external stress impacted the overall explosive induced fracture behavior. The differences in the fracture behavior was visible when comparing the top down images in Figure 4.1a-d of the fractured cubes post test. As the amount of external stress was increased the length of the fractures decreased but the number of fractures increased. For the tests with the externally applied stress, regardless of stress direction and the amount of applied stress, the

fractures experienced a fracture direction change. The fracture direction change is distinct in the HS2-2 test (Figure 4.1b) where fractures 1, 4, and 5 change fracture direction 10 - 35 mm from the explosive source. The fracture direction change for the VS2-2 (Figure 4.1c) test was more gradual but still occurred. For the VS2-20 test (Figure 4.1d), the fracture direction change occurs at a location similar to the HS2-2 tests but most of the fracture growth was terminated before the fracture changes direction. The fractures either terminate, or change direction in the 10 - 35 mm range. The fracture direction change, or termination, in the 10 - 35 mm for the HS2-2 test and the VS2-20 test could be due to the transition from the shock driven fracture to gas driven fracture.

Table 4.1: Summary of fracture length and angles measured using the post-test images presented in Figure 4.1

		NS2		HS2-2		VS2-2		VS2-20	
Frac. #		Angle	Length (mm)	Angle	Length (mm)	Angle	Length (mm)	Angle	Length (mm)
1	(a)	63.8°	74	51.1°	11	45.2°	59	61.7°	14
	(b)			29.9°	50	18.0°	22		
2	(a)	5°	112	6.5°	57	38.5°	141	54.9°	23
3	(a)	69.4°	63	19.5°	38	38.8°	63	7.3°	52
	(b)							24.5°	53
4	(a)	85.3°	60	78.8°	18	12.0°	37	63.1°	39
	(b)	68.1°	54	66.5°	19				
5	(a)	8°	112	32.7°	33	29.6°	25	63.1°	21
	(b)			22.7°	104			74.2°	16
6	(a)					39.3°	22	75.2°	19
	(b)					20.9°	86	58.4°	17
7	(a)							31.9°	36
	(b)							20.1°	31
8	(a)							7.0°	30
	(b)							20.0°	28
	(c)							3.9°	58
9	(a)							46.7°	42
10	(a)							50.0°	40

The evenly distributed radial fractures were imparted by the high-pressure shock pulse greatly exceeding the yield strength of the material. Then the high pressure confined explosive gases begin to drive the fractures but, the in-situ stresses began to have an effect on the fracture direction. The fractures changed direction to align with the direction of maximum principal stress. The impact of the radial distribution of the fractures due to the fracture direction change can be seen in the side view of the post-test images.

The side view of the fractures, Figure 4.1e-h shows the vertical and horizontal extent of the fractures not captured in the high-speed images. Comparing the NS2 test (Figure 4.1e) and the VS2-20 test (Figure 4.1h) it is apparent that the radial distribution of the fractures is smaller for the VS2-20 test. From the images of the HS2-2 test (Figure 4.1b and f) and the VS2-2 (Figure 4.1c and g) there are some differences between the fracture patterns but they are fairly similar. It is expected that the horizontal stress would arrest the cracks sooner than the vertical stress, however, qualitative analysis is not sufficient for making that assessment.

4.2 Fracture boundary identification

Two methods for determination of fracture position as a function of time were explored. The first method extracted the fracture area visualized in the high-speed images using image processing techniques and the second method tracked the fracture radius along nine angles aligned with the centers of the two detonators.

4.2.1 Method 1: Fracture area extraction

The fracture area was extracted using an image processing routine written in MATLAB. Inspection of the images shows that the fracture surface has a gray-scale intensity value which differed from the intact PMMA surface. The MATLAB routine uses an intensity threshold to segment the image into fractured and un-fractured PMMA, from which the boundary can be extracted. A representative image of the extracted fracture boundary for the NS2 test is shown in Figure 4.2a. The blue shaded area indicates the extracted fracture area from the high-speed image. The pixels in the blue section were then summed to approximate a fracture surface area. The fracture area was in pixels squared, thus, the distance calibration was used to convert pixels squared to millimeters squared. The extracted surface area as a function of the actual time, t_{act}, across the two high-speed camera images is presented in Figure 4.2b. The two cameras were represented as different symbols on the plot, camera 1 was the fracture area extracted from the Shimadzu high-speed camera which were represented as solid squared and camera 2 was the fracture area extracted from the Photron high-speed camera represented by open circles. The total imaged area was also presented in the plot as a black dashed line. The image area excluded areas of the image which were not PMMA.

The fracture area plot reveals fluctuations in the average fracture area as a function of time which were due to shock wave interactions with the fracture surface. A representative digital streak image is presented in Figure 4.3 where the fluctuations in the boundary are visible. The shock wave propagation caused an optical refraction which resulted in an apparent distortion of the fracture boundary. Although the visualized boundary was distorted, the wave interactions did not appear to impact the fracture response of the material.

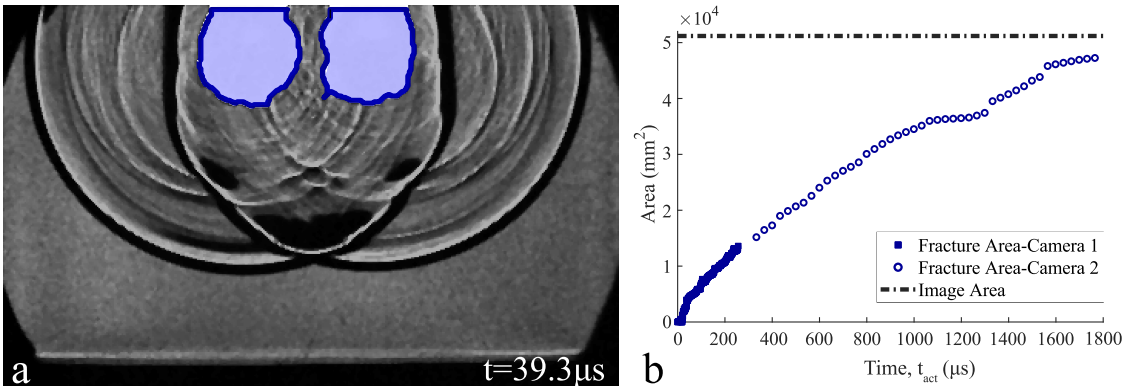

Figure 4.2: (a) Representative image of shock propagation and fracture growth with the extracted fracture boundary used to determine fracture area. (b) Graph of fracture area as a function of time for NS2 PMMA block consisting of two EBW detonators and no external applied stress.

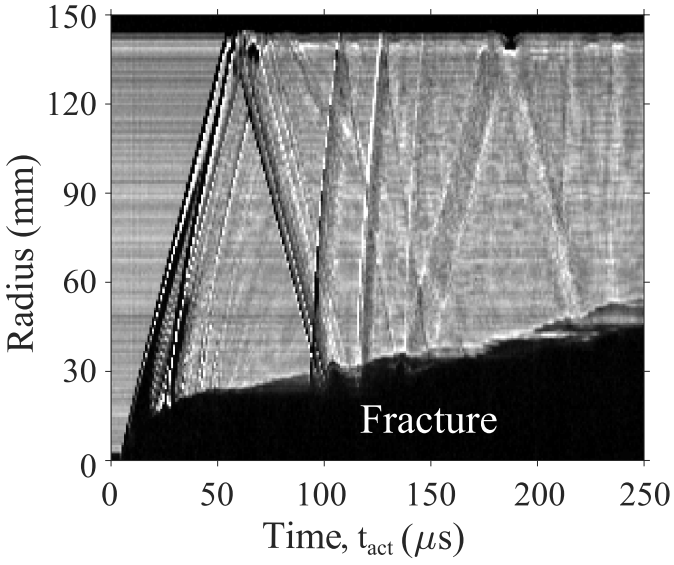

Figure 4.3: Digital streak image image visualizing the fracture boundary distorted by wave interactions.

For comparison to the numerical simulations, fracture radius was of interest. In order to get an approximation of the fracture radius from the fracture area, A, the fractures were approximated as a circle. This allowed for fracture radius, r, to simply be approximated using:

$$r = \sqrt{\frac{A}{\pi}} \tag{4.1}$$

Fracture radius as a function of time calculated using the fracture area in Figure 4.2 and equation 4.1 is presented in Figure 4.4. The calculated fracture radius generally followed the same trend as the fracture area plot. There was uncertainty in the early time fracture radius associated with the approximation of the fracture networks as one circular fracture. The fractures do not connect, making the circular approximation more appropriate, until approximately 50 ns. To better account for the two separate detonators and the two fracture networks, a second method for estimating the fracture radius was explored.

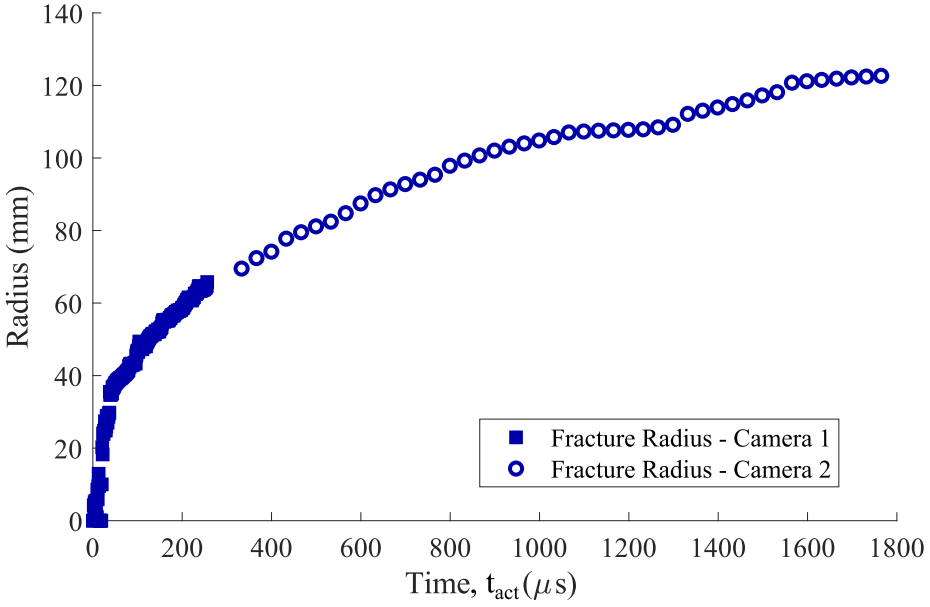

Figure 4.4: Fracture radius as a function of time calculated from the fracture area in Figure 4.2 using Equation 4.1.

4.2.2 Method 2: Fracture radius tracking

In order to better account for the two fracture networks, a second approach was developed to track the fracture boundary at various angles from both detonators as a function of time. The two detonators were identified in the high-speed images and four radial lines from each detonator were then considered: 0°, 30°, 60°, and 90°. The fracture position as a function of time along each of the radial angles was tracked. This approach is shown graphically in Figure 4.5 with high-speed images indicating the fracture locations tracked. Open circles were used to indicate the fracture radii tracked relative to detonator A, closed circles were used to indicate the fracture radii tracked relative to detonator B, and the cyan diamond was used to indicate the center line fracture. The points along the radial angles were color coded to indicate the angle at which the fracture was tracked.

Red was used to indicate a radius at 0°, blue was used to indicate a radius at 30°, green was used to indicate a radius at 60°, and pink was used to indicate a radius at 90° from the respective detonators.

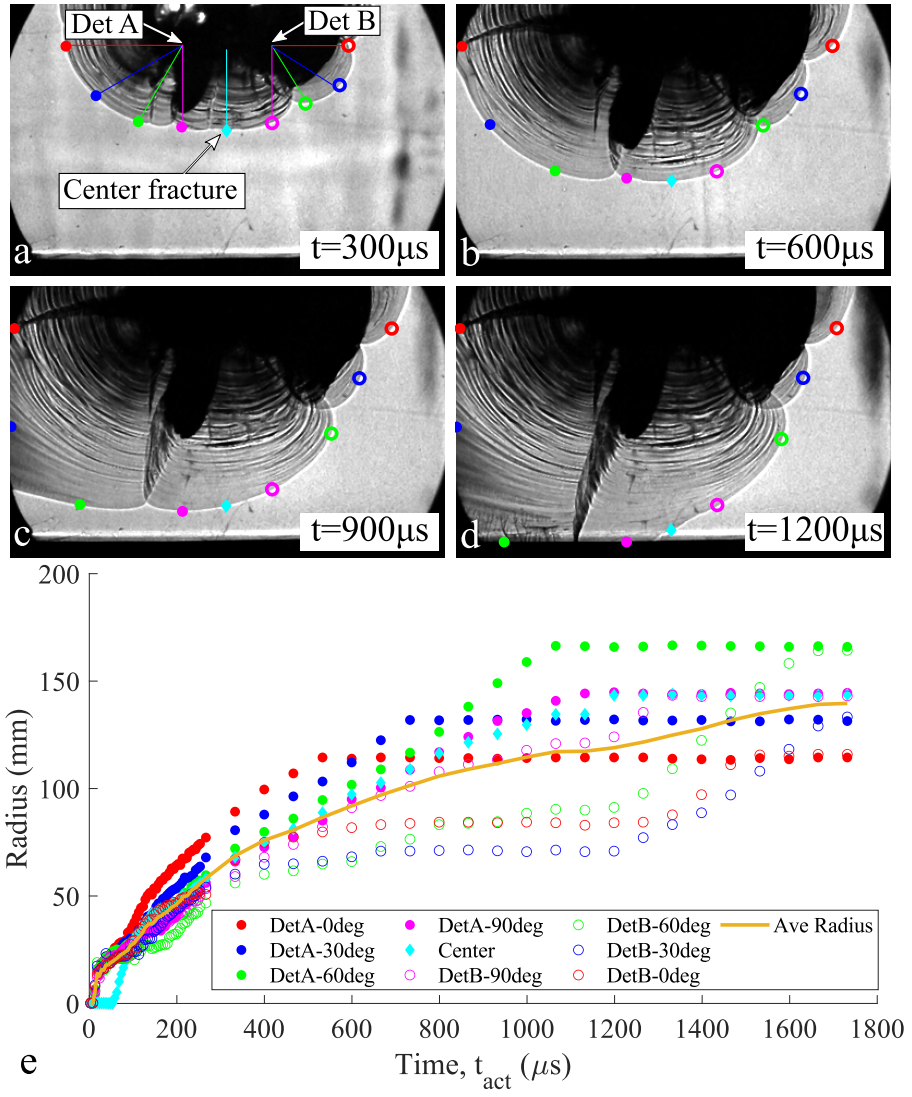

Figure 4.5: Fracture radius as a function of time for the NS2 test. The fractures were tracked 0° (red), 30° (blue), 60° (green), and 90° (magenta) from detonator A (solid circle) and detonator B (open circle). Fracture growth along the symmetry line between the two detonators was tracked as the cyan point. Note that the angle designations are symmetry-line mirrored for detonators A and B.

From the graph of fracture radius as a function of time presented in Figure 4.5e there appears to be an asymmetry in the fracture growth. Comparison to the high-speed images validates the fracture asymmetry. Representative images

showing the fracture asymmetry and the fracture radii tracked are presented in Figure 4.5 a-d. Since the fractures were tracked radially around the two detonators for this method, the fracture asymmetry was actual captured unlike method 1. Once the fracture radii as a function of time were tracked at all radial locations, the average fracture radius as a function of time was calculated.

The average fracture radius as a function of time for both methods were compared to determine which method would be used to analyze the fracture data. The comparison plot is presented in Figure 4.6. The early time fracture growth calculated using method 1 rapidly increases up to about 50 μs which was approximately the time when the two fracture networks connect. Method 2 does not capture the same anomaly, rather, it had a steady increase in fracture radius which better agrees with the late time fracture growth behavior. The two methods follow the same tend with method 2 estimating a shorter average fracture radius than that calculated using method 1. Method 1 and 2 yield similar results, but method 2 better describes the fracture asymmetry therefore, the average fracture lengths were calculated using method 2.

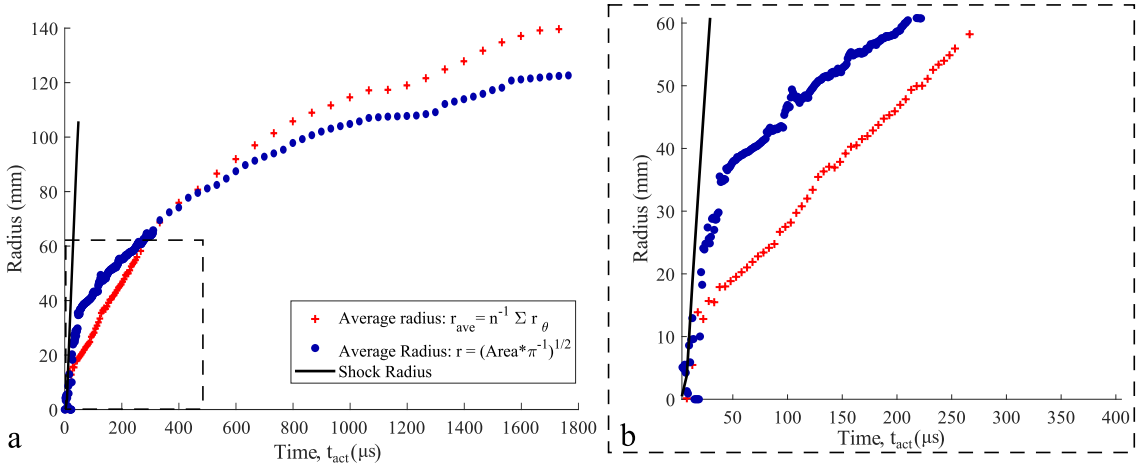

Figure 4.6: (a) Comparison of average fracture radius for the NS2 test using the fracture area plotted in Figure 4.4 and the average of radii at various angles plotted in Figure 4.5. With (b) showing a zoomed in axis range.

4.2.3 Fracture Radius

The second method where the fracture radii were tracked along symmetric angles from the two detonators was the selected method for processing the fracture data. This method was applied to all large-scale tests. The resulting fracture radii as a function of time for the experiments with two detonators are presented in Figure 4.7. The presented fracture radii were corrected for the fracture angles measured using the post-test images.

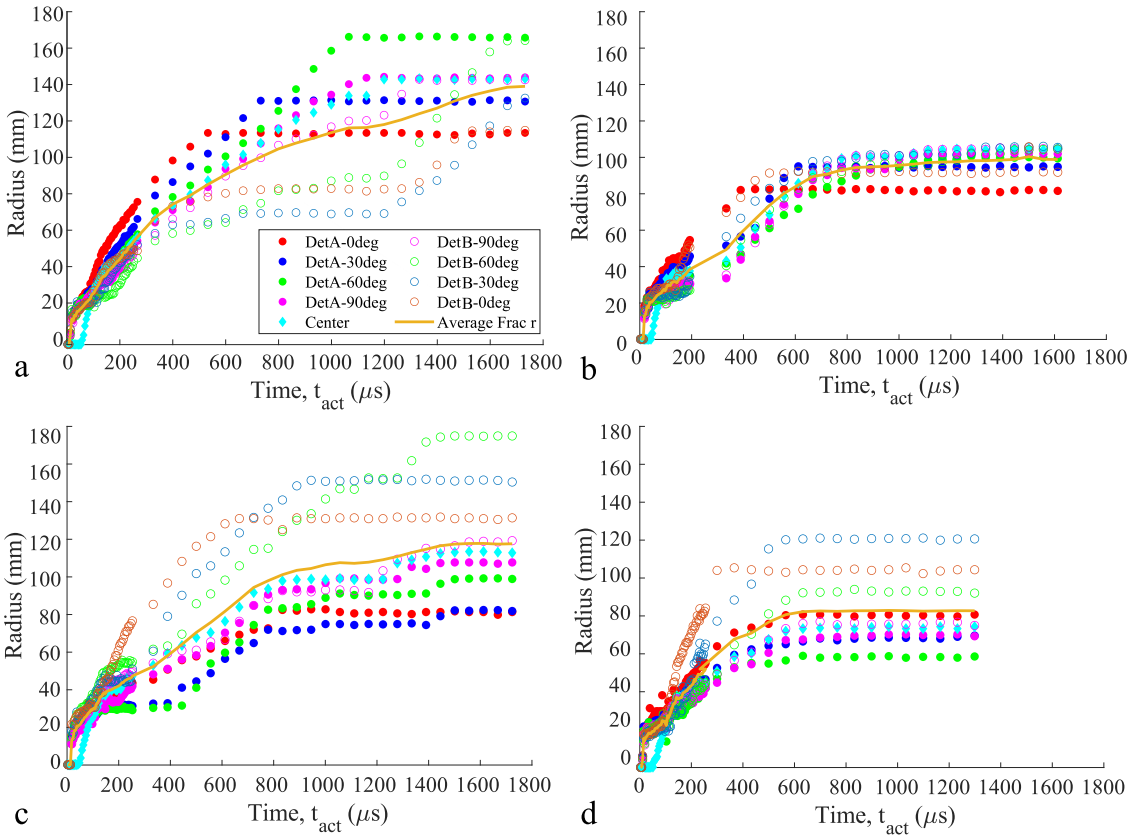

Figure 4.7: Fracture radius as a function of time from the schlieren images for the (a) NS2 test, (b) HS2-2 test, (c) VS2-2 test, and (d) VS2-20 test at angles of 0° (red), 30° (blue), 60° (green), and 90° (magenta) from detonator A (solid circle) and detonator B (open circle). Fracture growth along the symmetry line between the two detonators was tracked as the cyan point. The radii for (b-d) were corrected for out of plane fracture growth. The plots without the correction applied are in Appendix C.

The post-test images revealed out of plane fracture growth for all of the experiments. The schlieren images are 2D projections of the 3D fracture event to which the fractures along the imaging plane were dynamically measured. Any fractures growing perpendicular to the imaging plane were not visualized. For the fractures that were visualized in the high-speed images, the post test images were used to correct for the angle at which the fractures were growing. From the post-test images the fracture radii presented in Figure 4.7 for (b) the HS2-2 test, (c) the VS2-2 test, and (d) VS2-20 test were corrected.

The geometric corrections were applied as follows using VS2-2 experiment as an example: The right-running fracture, from Detonator B, in VS2-2 was assumed to be fracture 2 in Figure 4.1. The fracture position visualized in the high-speed images was a projection of the fracture leading edge, r_{proj}, the actual position of

the fracture, r_{act}, was positioned at an angle θ. The actual fracture length was calculated using:

$$r_{act} = \frac{r_{proj}}{\cos\theta} \tag{4.2}$$

The geometric corrections were applied with the assumption that the fracture surface being imaged was the most horizontal fracture or the fracture which was projected in the camera direction. The data in Table 4.1 was used for each respective fracture to perform the geometry corrections. In instances where the fracture angle was small, no geometric corrections were applied. For the VS2-2 experiments the geometric correction from Detonator B was applied based on fracture 2 rather than fracture 1 because fracture 2 was the longer of the two fractures. Fracture 1 and 2 also grow at similar angles from the detonator reducing uncertainty in the fracture selection. The fractures extending from Detonator A were corrected such that the first 49.1 mm was fracture 3 and the last 48.3 mm was fracture 6b. Similarly to the fractures extending from Detonator B, fractures 3 and 6 are growing at similar angles, in opposite directions. The uncorrected fracture radii for the three experiments are presented in Appendix C. There were no corrections applied to the NS2 test, Figure 4.7a, or the NS1 test presented in Figure 4.8.

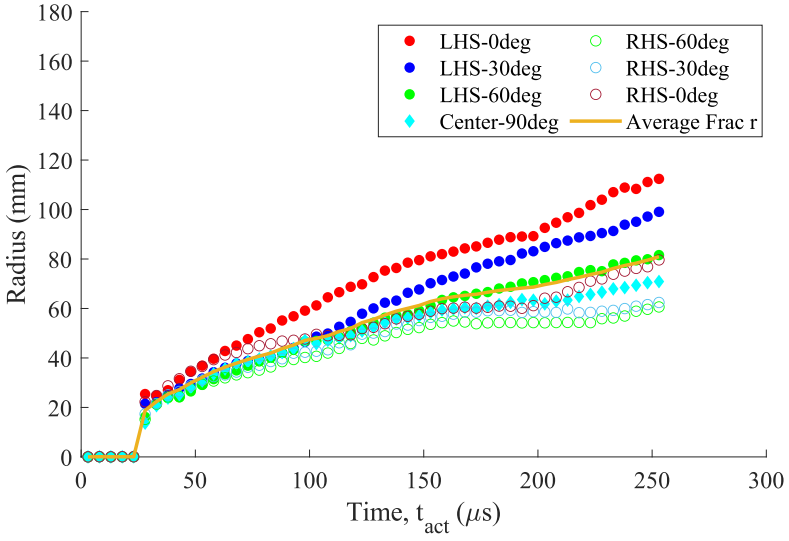

Figure 4.8: Fracture radii as a function of time at angles of 0° (red), 30° (blue), 60° (green), and 90° (cyan) symmetrically around the explosive source for the NS1 test.

The NS1 test was only recorded with a single camera, therefore the radii as a function of time from the experiments did not span the same record time as the two detonator experiments. The NS1 experiment also contained a different

explosive load than the 2 detonator tests. The explosives used for the NS1 test was 750 mg of PETN detonated with the spark from an RP-80 exploding bridge-wire and the camera was recorded at a frame rate of 1 Mfps. Since a single camera was used, the fracture radius tracking is limited to the first 253 μs of fracture growth. Despite the fracture tracking being limited for the NS1 test there was early time divergence in the fracture growth. The fractures on the left-hand-side grew faster than the fractures on the right-hand-side of the detonator which also occurred for the two hole tests.

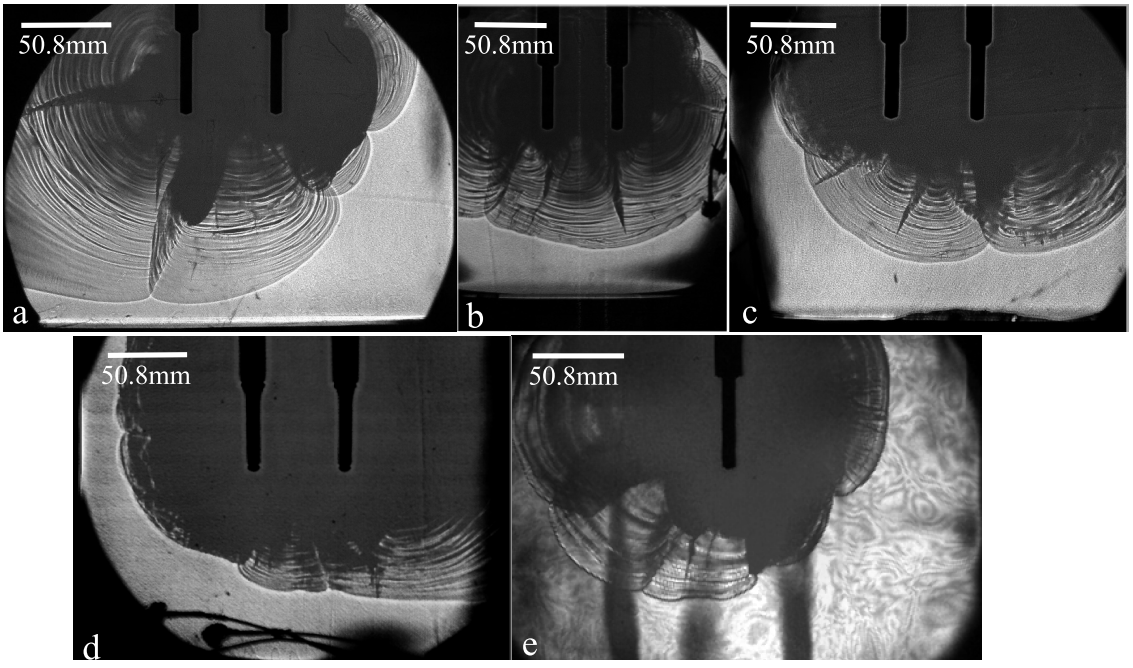

Figure 4.9: Fractured large-scale PMMA cubes overlaid with images prior to detonation for the (a) NS2 test, (b) HS2-2 test, (c) VS2-2 test, and the (d) VS2-20 test at a time of t_{act} = 900 μs and (e) the NS1 test at a time of t_{act} = 253 μs.

There was a distinct fracture asymmetry visualized in the NS2 test (Figure 4.7a) where the fractures around detonator A grew at a faster velocity than the fractures around detonator B. The fracture asymmetry was less distinct in the VS2-2 or VS2-20 tests and was not captured in the HS2-2 test. The application of external stress restricts the fracture growth leading to the less distinct fracture asymmetry in the stressed tests. The direction of stress in the HS2-2 test impacts the horizontal extent of the fractures compared to the other experiments with the 2 detonators which could be a cause for the lack of fracture asymmetry visualized.

The fracture radii plotted in Figure 4.7 were limited by the imaging field-of-view. Images from the experiments presented in Figure 4.9 show the imaging field of view for all of the tests. From the images of the experiments, the fracture asymmetry relative to the location of the explosives is shown. The images in Figure 4.9 also revealed the imaging limitations. The field of view was limited by

the size of the schlieren optics used which had a diameter of 304.8 mm. Since the full sample could not be visualized, the imaging system was arranged to image the bottom half of the cube. The full horizontal extent of the cube was not visible, therefore, when presenting the average fracture radii in Figure 4.10 the center fracture length was also included.

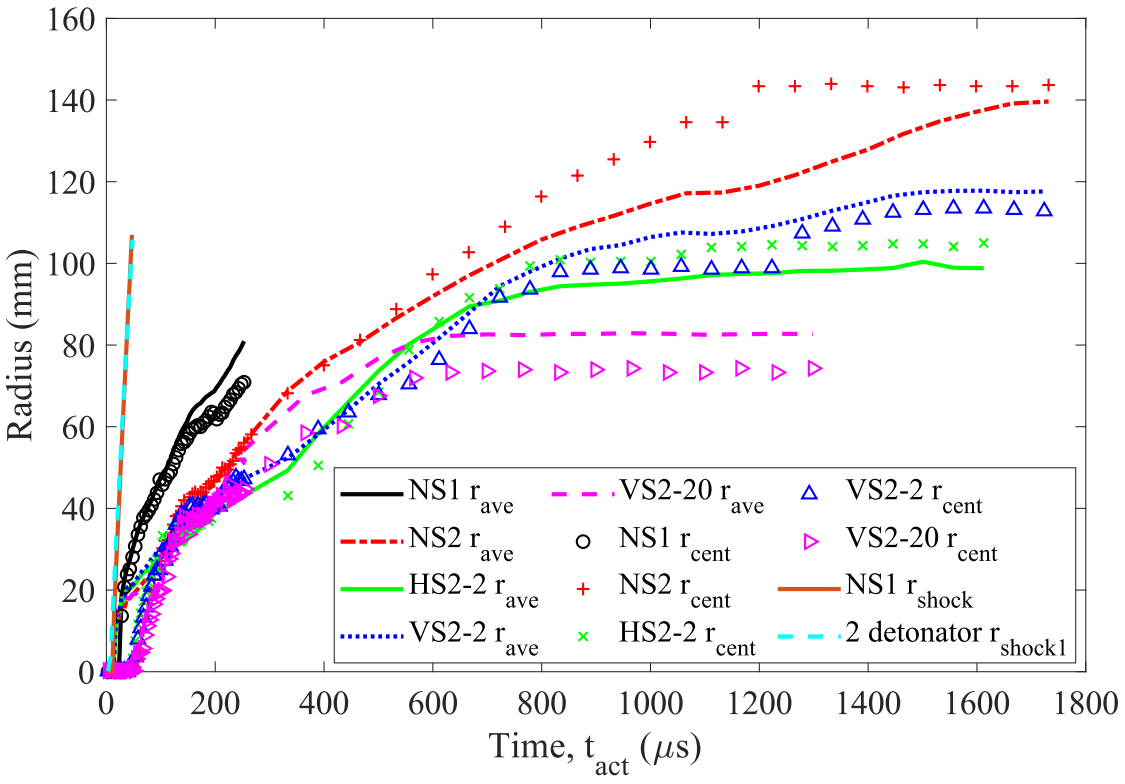

Figure 4.10: Plot of the average fracture radius (lines) and center fracture radius (points) for the NS1 test represented as the black solid line and 'o', NS2 test represented as the red double-dashed line and '+', HS2-2 test represented as the green solid line and 'x', VS2-2 test represented as the blue dashed line and '△', and the VS2-20 test represented as the pink dashed line and '▷'. The average shock radius for the experiments were also plotted.

Through comparison of the average fracture radii and center fracture radii for the two detonator tests, NS2, HS2-2, VS2-2, and VS2-20, the experiment with the longest fracture lengths was the NS2 test. The NS2 test was the test with no external stress applied. The experiment with the shortest fracture length was the test with the most external stress applied, the VS2-20 test, which was the expected result. Comparing the two tests with the same amount of stress in different directions, the HS2-2 and VS2-2 tests, the sample with the horizontal stress resulted in the shorter fracture lengths as compared to the sample with the same amount of external stress in the vertical direction. The average fracture

radii and center fracture radii for the two detonator tests are summarized in Table 4.2. The data from the NS1 test was excluded from Table 4.2 since the high-speed images did not capture the total fracture response. Figure 4.10 does however reveal that the fractures in the NS1 test were growing more rapidly than the fractures in the tests with the two explosive sources. This behavior implies that the amount of explosives impact the fracture rate.

Table 4.2: The final fracture radii and the center fracture radii determined using method 2 for the two detonator experiments.

Sample Configuration	Average fracture radius (mm)	Center fracture radius (mm)
NS2	140	144
HS2-2	99	105
VS2-2	118	113
VS2-20	83	74

The NS1 test was preformed with 750 mg of PETN, whereas the other four experiments were preformed with two RP-80 EBW detonators. The two detonators had a combined explosive weight of about 400 mg of explosives. The NS1 test had almost double the amount of explosives as the other experiments. Since the NS1 test was preformed with no external stress the fracture results were compared to the NS2 test. From the graph of fracture radius as a function of time, the NS1 test produced a longer average fracture length as compared to the NS2 test at the same instance in time. The NS1 and NS2 test follow a similar trend and have a similar slope from about 200 μs to the end of the NS1 test. In order to compare the fracture rate for the NS1 and NS2 tests the fracture velocity was calculated by taking the derivative of the average fracture radius presented in Figure 4.11.

The fracture velocity was plotted against corrected time, t_c, which was corrected for the detonator function time, such that t_c=0 μs for both experiments was when the shock wave first entered the PMMA in the high speed video records. The velocity graph shows that initially both experiments have a fairly large fracture velocity, with the NS1 being almost double that of the NS2 test. The initial rapid fracture rate was attributed to the shock driven fracture. The black line at 20 μs indicates the time that the shock driven fracture ended according to the numerical simulations discussed in Chapter 5. At about 20 μs there was a rapid reduction in the fracture velocity for both experiments. After about 20 μs the two experiments experience a more gradual decay. From 20 μs to about 50 μs the fracture velocity for the NS1 test was much larger than the NS2 test. After about 50 μs the NS1 velocity was reduced aligning more closely with the NS2 test. the two data sets follow a the same trend up until the end of the NS1 imaging record time of 250 μs. The average velocity for the last 100 μs for the two experiments was about 160 m/s for the NS2 test and 180 m/s for the NS1 test. This implies that the explosive amount has a more significant impact on the fracture length in the early time, however, no conclusion can be made about the final fracture length because the

experiments did not extend the full event duration for the NS1 test. It can be noted that the cube for the NS2 test fractured in two for the experiment, and the NS1 test fractured in to four pieces.

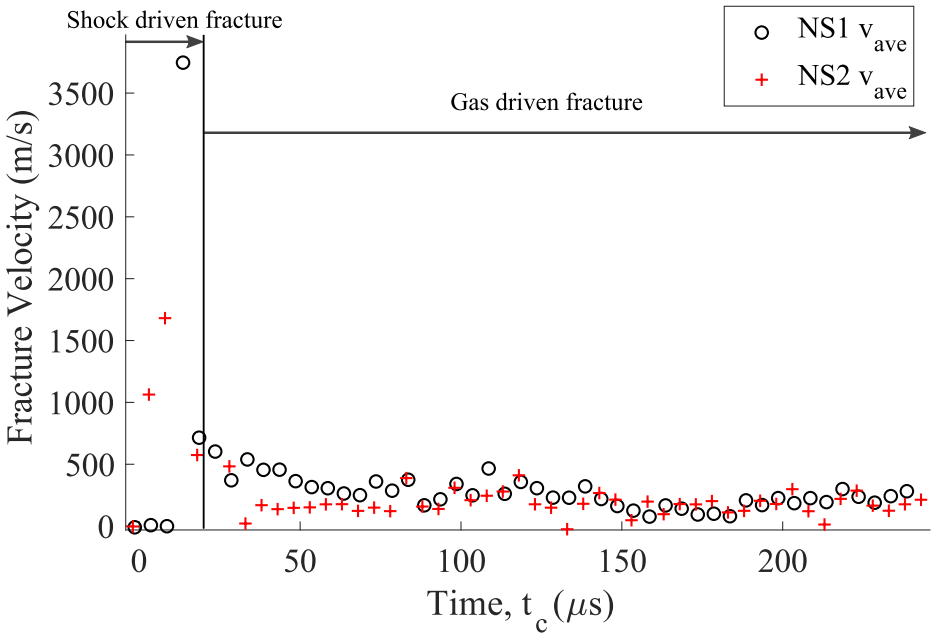

Figure 4.11: A comparison of fracture velocity calculated using the average fracture radii plotted against corrected time, t_c, for the NS1 and NS2 tests.

The same analysis used to compare the fracture velocities from the NS1 and NS2 test was extended to the other large scale experiments. The average fracture radii presented in Figure 4.10 were used to calculate the fracture velocity as a function of time for the NS2, HS2-2, VS2-2, and VS2-20 experiments. The experimental fracture velocities presented in Figure 4.12 were calculated for the full fracture event up until crack arrest. In Figure 4.12 time on the x-axis was corrected for the detonator function time. The noise caused by reflective waves distorting the images captured during the fracture tracking was amplified once the derivative was taken. Similarly to the unstressed test presented in Figure 4.11, there was a significant reduction in the fracture velocity at approximately 20-30 μs for all tests. The fracture velocities for the tests were similar up until crack arrest when the fractures would stop growing. The average fracture velocity for all of the experiments from 30 μs up until crack arrest was about 150 m/s.

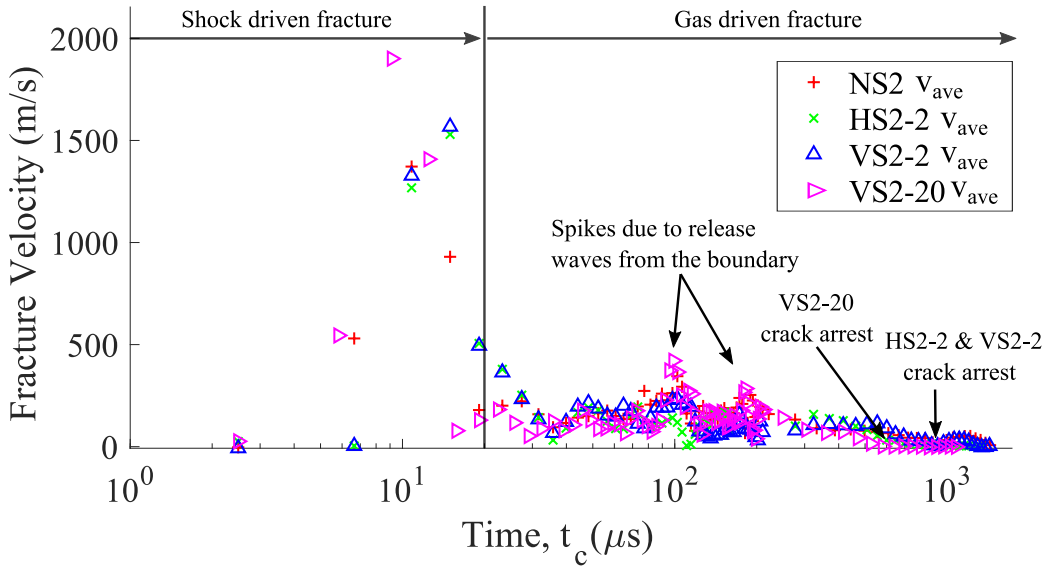

Figure 4.12: The calculated fracture velocity for the NS2, HS2-2, VS2-2, and VS2-20 explosively driven fracture experiments from the average fracture radii plotted in Figure 4.12.

4.3 Fracture driving force

There are two mechanisms driving the explosive induced fractures: the shock wave and the confined explosive gases. In order to determine which mechanism is the main driving factor, the fracture radius data and shock wave motion measurements are examined together.

There are three fracture zones created from shock induced fracture [7], the first zone is the crushing region where the shock strength greatly exceeds the compressive strength of the material. Significant amount of energy is consumed in the first zone causing the material to be crushed. In the transitional zone, the strength of the shock is still higher than the compressive strength of the material. In this zone there is crushing due to plastic deformation which transitions to partial fracture bringing the fracture process to the third zone, the elastic fracture. In the elastic region the wave strength is less than the elastic limit of the material [7]. This means that the wave looses the majority of it's strength early in the fracture process. The results from from the small scale, unstressed shock propagation tests in Chapter 3 showed that shock wave from the RP-80 EBW detonators attenuates to the longitudinal wave speed within the first 25 mm to 45 mm. Furthermore, the shock response for the large scale experiments NS2, HS2-2, VS2-2, and VS2-20, showed that the shock response was consistent regardless of the amount of applied stress. Therefore, the application of external stress did not impact the material shock response, but there was a clear variation in the average fracture lengths and the fracture directions captured post-test with the application of external stress.

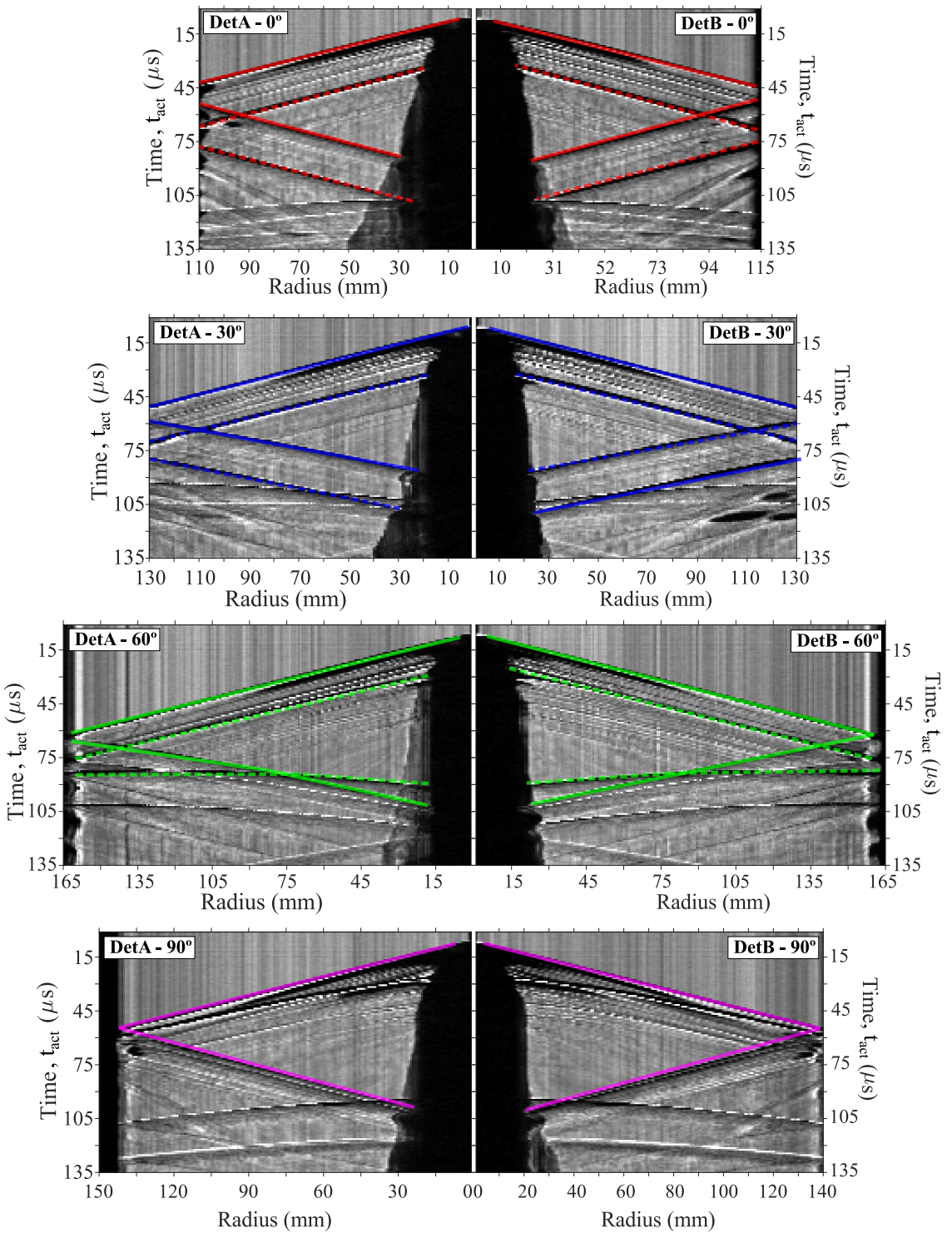

Figure 4.13: Digital streak images for the NS2 test 0°, 30°, 60° and 90° from both detonators.

From the post-test images there was a clear difference caused by the application of external stress. For all four experiments a zone of material crushing was visible. The zone was larger for the NS2, HS2-2, and VS2-2 tests, but was still present in the VS2-20 test. It is also noted that fracture inter-connectivity was achieved for all experiments. The post-test images also revealed fracture direction change, or fracture termination around 10 - 35 mm from the explosive source when external stress was applied. This range corresponds to the approximate length when the shock wave attenuates to the longitudinal wave speed, approximately 25 - 45 mm. From the fracture analysis it was also found that there was a significant reduction in the fracture velocity with in the first 20 - 30 μs which corresponds to a fracture length of approximately 15 mm. This was further explored using digital streak images, Figure 4.13.

Digital streak images were used to approximate when the shock wave separates from the fracture surface. Figure 4.13 shows streak images aligned with both detonator A and B at 0°, 30°, 60°, and 90°. From the digital streak images, the shock wave appears to separate from the fracture surface at approximately 18 μs which yields a fracture length of approximately 15 mm. The digital streak images also show interactions between the reflected shock waves and the fracture surface. There are distortions in the fracture front but since the shock strength is reduced below the elastic limit of the material the reflected shock waves do not impact the fracture growth rate.

From this analysis the shock driven fracture was estimated to occur within the first 10 - 35 mm of explosive driven fracture. Approximating the percent of fracture growth attributed to the shock for the given range were 7- 25% for the NS2 test, 10 - 35% for the HS2-2 test, 8 - 30% for the VS2-2 test, and 12 - 42 % for the VS2-20 test. It appears that the main mechanism driving the fracture growth was the confined explosive gases, however, as the in-situ stresses are increases, there is a decrease in the over all fracture lengths. In the present work, the in-situ stresses did not appear to impact the shock driven fracture, but did impact the gas driven fracture.

CHAPTER 5

NUMERICAL MODELING OF PMMA SHOCK RESPONSE

Numerical simulations of the shock response of PMMA were carried out for comparison to the experimental results. The simulations were preformed using GEODYN, a massively parallel Eulerian hydrocode developed at Lawrence Livermore National Laboratory (LLNL) [109]. The GEODYN simulations show shock propagation through the PMMA material as well as fracture propagation near the explosive source. The shock velocity and free surface velocity measurements were compared between the simulations and the experiments.

Simulating high strain-rate shock and fracture material response is a multi-physics process. The hydrocode utilizes adaptive-mesh refinement (AMR) to compute material response for multiple materials at multiple different states. Modeling the explosively induced shock generation in solids requires the use of thermodynamics consistent constitutive models. Due to the nature of shock propagation the model extends to velocities up to rates of 10^6 Hz, pressures of 100 GPa and temperatures up to 100's of degrees.

5.1 Constitutive model

The numerical modelling software, GEODYN, implements thermodynamically consistent isotropic continuum models for solid materials under high rate loading. The model used here was developed for porous rocks [110] and has been used to model the dynamic behavior of granite at various temperatures and confinement pressures [111]. The continuum model incorporates a baseline equation of state for the material with strain rate dependent material property behavior models. These aspects of the material response allow calculation of pressure, density and stress variation under high rate loading. The model is tuned for a particular material through incorporation of a material specific equation of state and parameters. The EOS used to describe the shock loading conditions was in the Mie-Gruneisen form using experimental Hugoniot data [53]. A table of parameters used for modeling PMMA are shown in Table 5.1.

Table 5.1: Basic model parameters for PMMA

Parameter	Description	Value
ρ_0 (g/cc)	Reference density	1.182
Y_{c0} (GPa)	Unconfined compressive strength	0.11
C_0 (km/s)	Reference bulk sound speed	2.18
m	Pressure hardening rate	1
$\dot{\epsilon}_0$ (1/ s)	Reference strain rate	0.01
n_s0	rate power, n_0	0.085
n_s1	rate power, n_1	0.001
n_s2	rate power, n_2	0.01
Γ_0	Mie Gruneisen parameter	0.85
S_1	Shock Hugoniot parameter S1	2.088
S_2	Shock Hugoniot parameter S2	-1.124
S_3	Shock Hugoniot parameter S3	0

The RP-80 EBW detonator was simulated using the total energy output of the explosive and JWL parameters. The net energy output of an RP-80 detonator is 1.14 kJ [112, 113]. The energy for the cylinder of explosive is calculated as:

$$E = \pi r^2 h e \rho \tag{5.1}$$

Where r is the cylinder radius, h is cylinder height, e is energy per unit mass, and ρ is the density of the explosive.

Granite has a 1% nominal porosity whereas PMMA is not a porous material. PMMA response under high rate loading, however, is mathematically similar to porous compaction rocks as PMMA exhibits effects of densification [114]. Due to the mathematical similarities, the granite model was applied here for PMMA because it can describe the brittle-ductile transition, dilatancy in brittle regime, porous compaction in ductile regime, rate-dependence, pressure dependence and thermal softening behaviors.

The model utilizes the Cauchy stress tensor, $\mathbf{T}$ to describe the stress state:

$$\mathbf{T} = -p\mathbf{I} + \mathbf{T}' \tag{5.2}$$

p and $\mathbf{T}'$ are the volumetric and deviatoric components respectively, and $\mathbf{I}$ is the second order unity tensor. Based on the isotropic assumption, the stress tensor

is decomposed into volumetric and deviatoric parts:

$$p = \frac{1}{3} tr(\mathbf{T}) \tag{5.3}$$

Then,

$$\mathbf{T}' = \mathbf{T} - \frac{1}{3}(tr(\mathbf{T}))\mathbf{I} \tag{5.4}$$

The volumetric part of stress, which describes the pressure, is calculated using the PMMA equation of state (EOS) while the deviatoric stress, is calculated using a distortional deformation tensor [115]. Isotropic plasticity theory is applied to return the stress to the yield surface and to calculate the level of damage within the material. The von Mises effective stress σ_e is bounded by the yield strength Y in uniaxial stress.

$$\sigma_e = \sqrt{\frac{3}{2}\mathbf{T}' \cdot \mathbf{T}'} \leq Y(p) \tag{5.5}$$

5.2 Three-Dimensional PMMA model

A Three-dimensional (3D) model of the simultaneous initiation of two RP-80 EBW detonators in two separate holes was compared to the experimental results captured with high-speed shadowgraphy and PDV. The simulation only simulates the shock response of the material. Since the experiments showed that there was no variation in the shock response as the external stress was increased, the NS2 test was used to compare to the simulation results. The 3D simulation setup is show in Figure 5.1 where the geometry was selected such that the simulation would match the NS2 test

The simulation results were compared to the high-speed imaging results at at various times, which are shown in Figure 5.2. Figure 5.2 a-d shows the experimental image and Figure 5.2 e-h shows the measured images and calculated density gradients at approximately the same time. Experimental limitations constrained the field of view but the simulations were performed throughout the entire PMMA block. The black dashed square overlaid on the simulation results indicates the approximate experimental imaging field of view. The experimental images and calculated images show generation of two spherical shock waves propagating through the PMMA. Initially the two shock waves propagate independently from the two sources. As time progresses the shock waves from the two sources interact with the holes for the two sources designated with index 1 in Figure 5.2 c and g. The fracture surface is also visible in both the experiments and the simulations indicated with the index 2. In the final image presented, the shock front flattens after passing through the damage zone, the shock flattening is indicated with the index 3 in Figure 5.2 d and h.

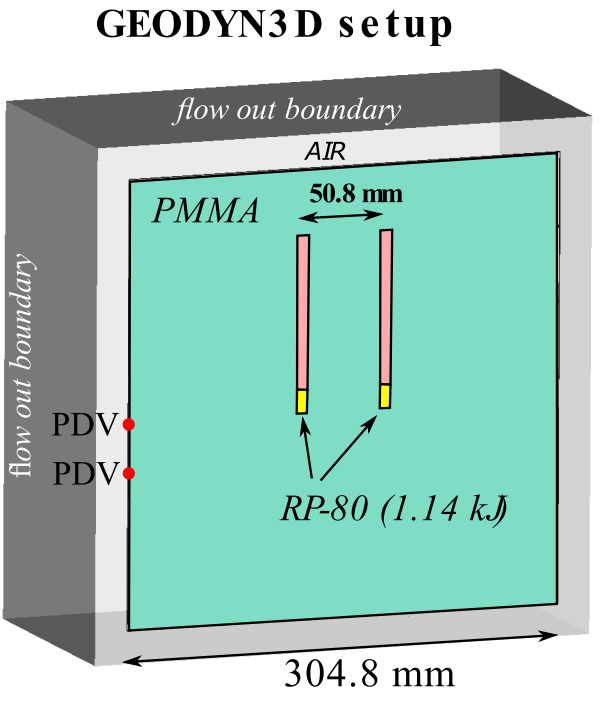

Figure 5.1: Image of the simulated NS2 experiment in GEODYN 3D. The colors designate different materials. Green indicates PMMA, yellow indicates the RP-80 detonators, pink indicates the tamping material, and gray corresponds to air.

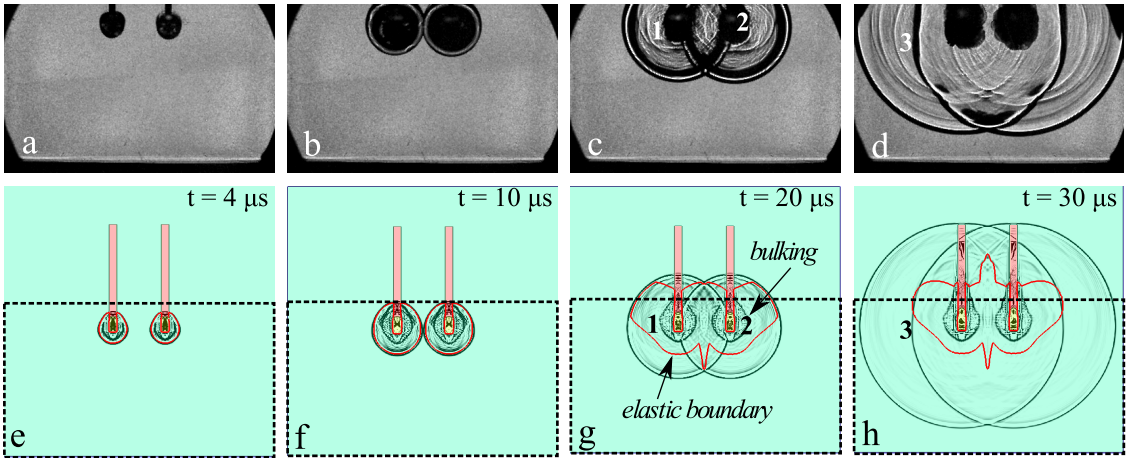

Figure 5.2: Comparison between (a-d) the experimental results and (e-f) the simulated results. At nominally the same time. The experiments were corrected for the detonator function time such that (a,e) t = 4 μs, (b,f) t = 10 μs, (c,g) t = 20 μs and (d,h) t = 30 μs.

The calculated images (e-f) show the elastic boundary contours calculated on the plane indicated with red solid lines. Initially, the simulated damage zone size, dark area around each source, grows similarly to the experiments. At approximately 20 μs the damage zone growth stops in the simulations but continues to grow in the experiment. This behavior indicates that the shock drives the fracture up to approximately 20 μs. Since the fractures continue to grow in the experiment a secondary mechanism is assumed to be driving the fractures further. The secondary mechanism driving the fracture is believed to be the confined explosive gases. The damage model used in GEODYN is not capable of capturing the explosive products flow, which is why this later time behavior is not captured in the model.

The simulated shock wave and shock driven fracture response of the material presented in Figure 5.2 agreed well with the experimental results. Further comparison of the shock response was achieved through surface velocity measurements. Similar to the experiments, the simulated PMMA surface velocity measured aligned with the detonator and 50.8 mm below the detonator as indicated in Figure 5.1. The resulting simulated surface velocities compared to the experiments are presented in Figure 5.3. The numerical results agree with the experimental results on both the time of shock wave arrival and the velocity amplitude. The shock wave arrival time is defined by the shock wave velocity, so the agreement shows that the shock propagation through the PMMA is well represented. The velocity amplitude is proportional to the stress amplitude.

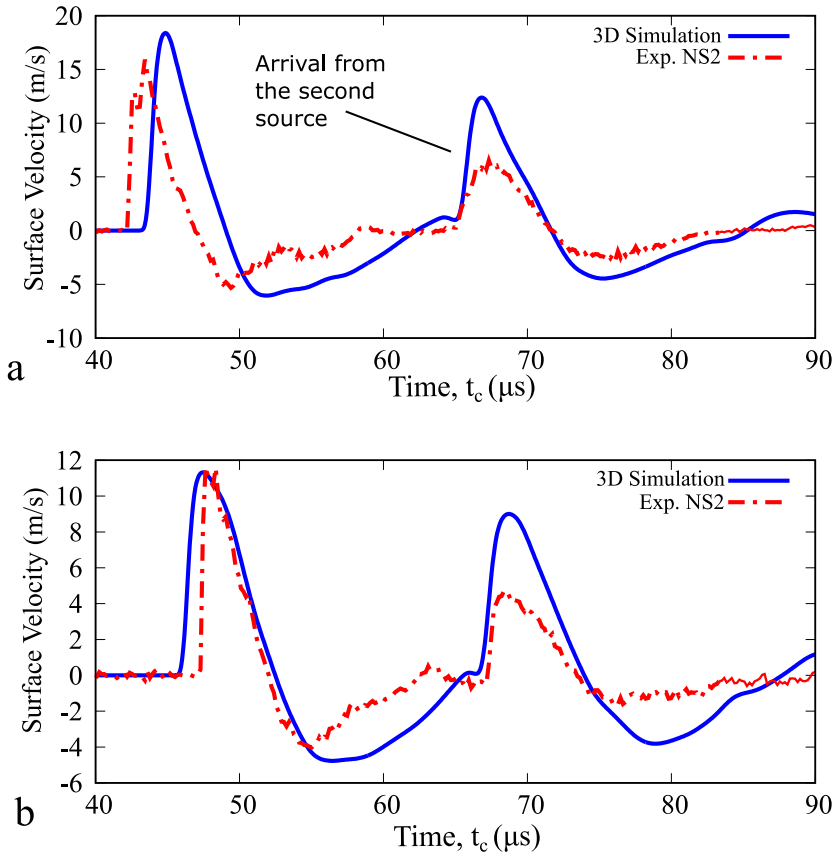

Figure 5.3: Comparison of the experimentally measured surface velocities (double dashed lines) with calculated ones (solid lines) at (a) detonator level and (b) 50.8 mm below detonator level.

5.3 Two-Dimensional PMMA model

Three-dimensional simulations are computationally expensive and run for a long duration of time. To reduce computation time and expense, additional GEODYN simulations were run in two-dimensions (2D). The 2D geometry was set up such that the simulation was run as cylindrical axisymmetric, around the center-line of the detonator as depicted in Figure 5.4a. Figure 5.4b shows the sample geometry as depicted in the simulation. The sample had a propagation distance of 25.4 mm and the same simulated RP-80 EBW detonator as the explosive source.

The calculated images corresponding to the geometry presented in Figure 5.4 are shown in Figure 5.5 compared to experimental measurements. The simulated shock wave was visualized by taking the divergence of the density gradient in the PMMA, yielding the Laplacian. Visualization of the Laplacian of the density field

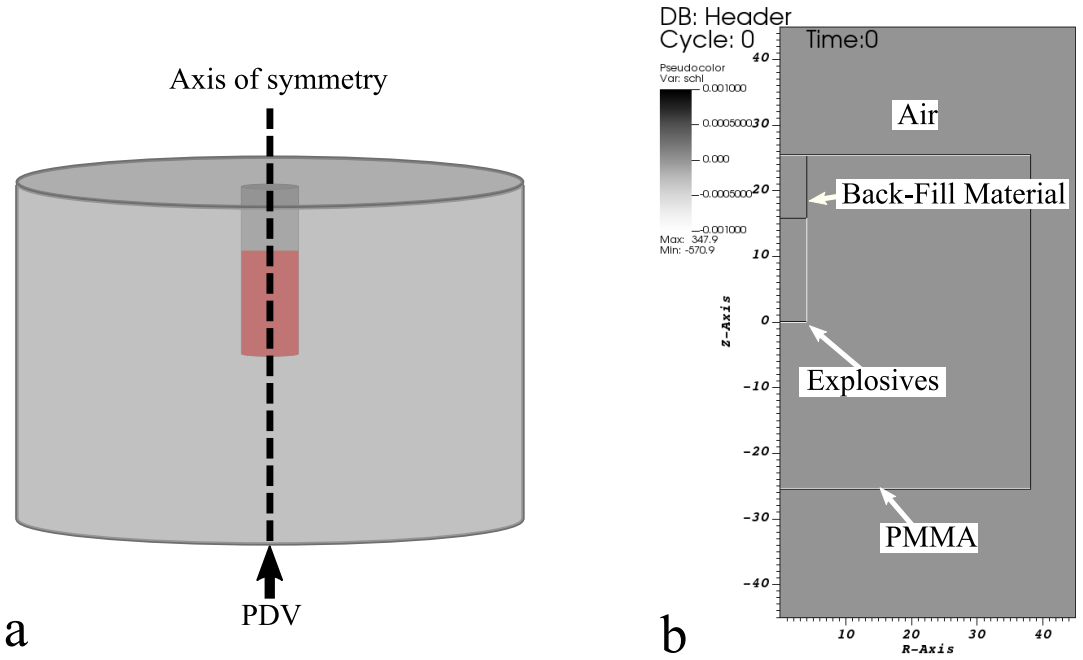

Figure 5.4: (a) Cylindrical approximation of the small scale test samples. (b) Simulated PMMA sample with a propagation distance of 25.4 mm, RP-80 detonator, and rubber as the back-fill

is equivalent to in-plane shadowgraphy. The experimental images presented were taken using schlieren imaging which is the gradient of density, and shows more texture on the shock wave front. The experiments and simulations are compared at approximately the same time yielding similar results. Initially the simulated shock appears to propagate slightly faster than experimentally observed. After the shock reflects from the end wall the wave visualized in the experiments propagates slightly faster. Note that the cylindrical symmetry for the computations well represents the initial spherical shock propagation, but is likely a poor representation of the reflected shock wave propagation from the side walls which explains the difference in results. Reflection from the end wall is likely well represented in this simulated geometry until the side wall reflected shock wave arrivals.

Simulations were run to calculate the shock induced material response of PMMA in 2D for nominal propagation distances of 25.4 mm, 50.8 mm, 76.2 mm, 123.2 mm, and 133.3 mm from the explosive source. Surface velocity measurements were recorded in the simulations, as shown in Figure 5.4, where a "marker" was placed on the sample surface. The marker tracked the surface velocity in the Z-direction. The simulated surface velocities were compared to the experimental results shown in Figure 5.6. The simulations underpredict the maximum surface velocity for the nominal propagation distance of 25.4 mm, for all other propagation distances the maximum particle velocity predicted using GEODYN-2D is in good

agreement with the experiments.

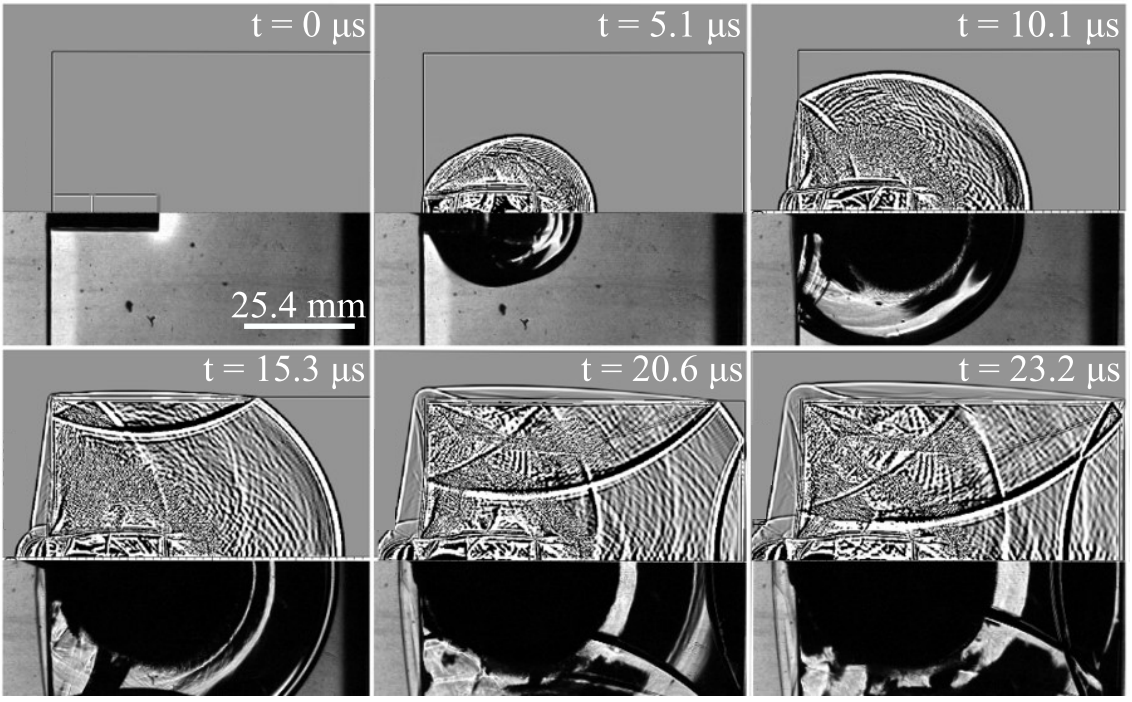

Figure 5.5: Comparison of experimental shock propagation and the simulated shock propagation.

Although the maximum velocity is underpredicted in the simulations for the nominal propagation distance of 25.4 mm the wave shape of the velocity history is the same for the simulation and the experiment. The simulations for the nominal propagation distances of 123.3 mm and 133.3 mm were cut short due to simulation run time, but the peak particle velocity was similar. Furthermore, the PDV measurements for these propagation distances were already compared for the three-dimensional simulation in Figure 5.3.

The wave shape for the nominal propagation distances of 50.8 mm and 76.2 mm was different for the simulation and the experiments. The simulation decay and the experimental decay deviate in behavior approximately 2 μs after the shock reaches the free surface for the 50.8 mm nominal propagation distance which was the approximate time the the small scale sample decay deviated from the cube decay behavior as discussed in section 3.3.1. The axisymmetric simulation geometry does not allow for direct calculation of similar shock wave side wall reflections which occur in the experiments. However, the simulations validate the geometric effects discussed in section 3.3.1.

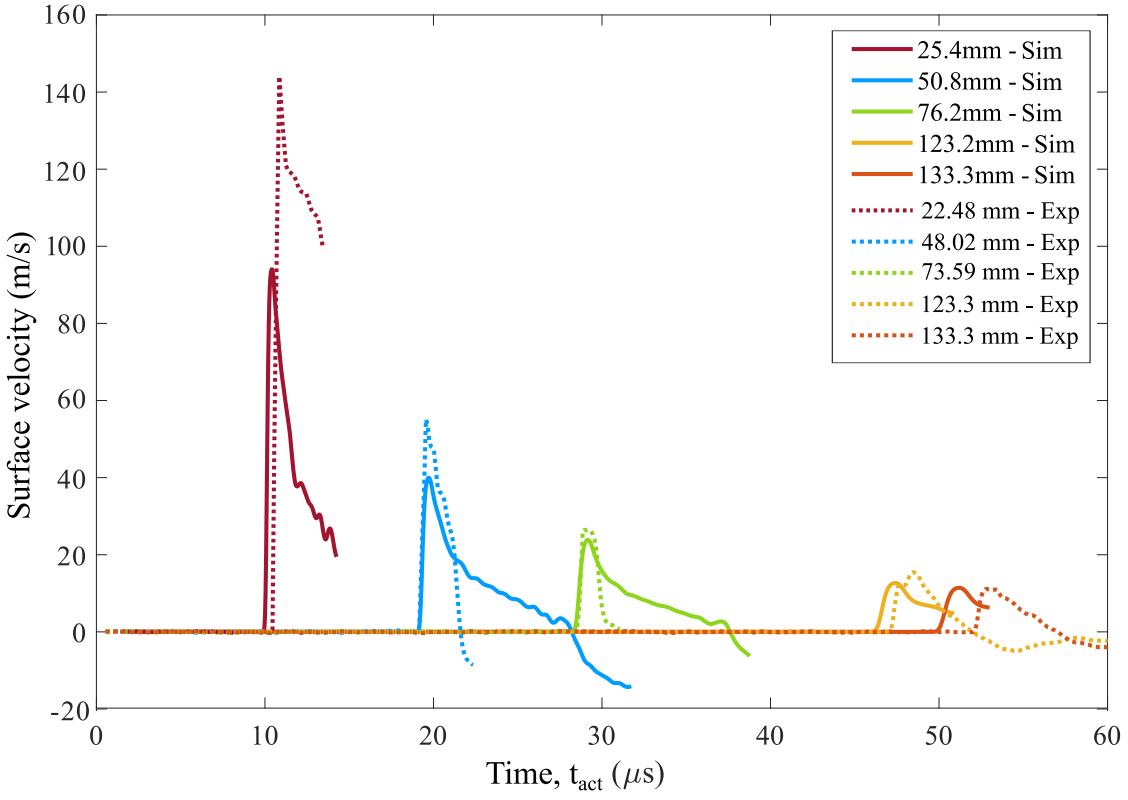

Figure 5.6: Comparison of experimental and simulated free surface velocity histories for nominal propagation distances of 25.4mm, 50.8 mm 76.2 mm, 123.2 mm, and 133.3 mm.

CHAPTER 6

QUANTITATIVE SCHLIEREN IMAGING MEASUREMENT METHODS

Quantitative schlieren measurements in air have been implemented and validated [47, 48]. For schlieren images, the gray-scale intensity in the image is proportional to the refraction angle which is proportional to the gradient of the refractive index. The refractive index of an optical disturbance is determined using the refraction angle and an intensity calibration. The refractive index can then be used to determine pressure, temperature, or density with the appropriate equation of state. Applying quantitative schlieren methods to transparent solids introduces additional complexities associated, with and not limited to, boundary effects, refraction through the sample, and material stress response.

6.1 Governing equations

Compression of a material increases the thickness of the body due to the Poisson effect, and the inverse is true for a body in tension. The volume change causes a change in optical density, thus, changing the refractive index. The stresses imparted by an external load also cause a change in optical properties of the material. The change in optical properties are associated with an optical path length change (Δs). The optical path length change caused by deformation is represented, in a general form, as [9]:

$$\Delta s = (n_0 - 1)\Delta d_{eff} + d_{eff}\Delta n \tag{6.1}$$

Where n_0 is the refractive index of the undisturbed material, d_{eff} is the effective thickness of the material, Δd_{eff} is the change in effective thickness of the material, and Δn is the change in refractive index. Refractive index can vary with direction in solids and for birefingent, optically transparent materials the indices of refraction are related to the normal stresses through the the Maxwell-Newmann law:

$$\Delta n_x = A_c\sigma_{xx} + B_c(\sigma_{yy} + \sigma_{zz}) \tag{6.2}$$

$$\Delta n_y = A_c\sigma_{yy} + B_c(\sigma_{xx} + \sigma_{zz}) \tag{6.3}$$

$$\Delta n_z = A_c\sigma_{zz} + B_c(\sigma_{xx} + \sigma_{yy}) \tag{6.4}$$

Where Δn_x, Δn_y and Δn_z are the change in refractive indices in the x-, y-, and z- directions, respectively, A_c and B_c are the stress-optic constants, and σ_{xx}, σ_{yy}, and σ_{zz} are the normal stress in their respective directions. Maxwell's equations were derived for birefringent materials but have been extended to optically isotropic materials such that $A_c \approx B_c$. Generalized Hooke's law describes Δd_{eff} for a direction of light propagation in the z-direction as [9]:

$$\Delta d_{eff} = \frac{1}{E_y}\left[\sigma_{zz} - \nu(\sigma_{xx} + \sigma_{yy})\right] d_{eff} \tag{6.5}$$

Where ν and E_y are the Poisson's ratio and Young's modulus for the material, respectively. Equations 6.1 through 6.5 can then be used to define the optical path length change caused by external stress in the respective directions. For a two-dimensional case only the deflections in the x- and y- directions are considered:

$$\Delta s_x = d_{eff}\frac{(n_0 - 1)}{E_y}\left[\sigma_{zz} - \nu(\sigma_{xx} + \sigma_{yy})\right] + d_{eff}\left[A_c\sigma_{xx} + B_c(\sigma_{yy} + \sigma_{zz})\right] \tag{6.6}$$

$$\Delta s_y = d_{eff}\frac{(n_0 - 1)}{E_y}\left[\sigma_{zz} - \nu(\sigma_{xx} + \sigma_{yy})\right] + d_{eff}\left[A_c\sigma_{yy} + B_c(\sigma_{xx} + \sigma_{zz})\right] \tag{6.7}$$

Applying a plane stress assumption, $\sigma_{zz} = 0$, and simplifying:

$$\Delta s_x = d_{eff}\left[\left(A_c - \frac{\nu(n_0 - 1)}{E_y}\right)\sigma_{xx} + \left(B_c - \frac{\nu(n_0 - 1)}{E_y}\right)\sigma_{yy}\right] \tag{6.8}$$

$$\Delta s_y = d_{eff}\left[\left(A_c - \frac{\nu(n_0 - 1)}{E_y}\right)\sigma_{yy} + \left(B_c - \frac{\nu(n_0 - 1)}{E_y}\right)\sigma_{xx}\right] \tag{6.9}$$

For PMMA the stress optic coefficients are approximately equal, $A_c \approx B_c$ implying optical isotropy. The two values were averaged in the present work to get a general isotropic stress optic coefficient D_c [9]. As such, The equations can be further simplified as:

$$\Delta s_x = \Delta s_y = d_{eff}C_\sigma\left[\sigma_{xx} + \sigma_{yy}\right] \tag{6.10}$$

Where,

$$C_\sigma = D_c - \frac{\nu(n_0 - 1)}{E_y} \tag{6.11}$$

The values σ_{xx} and σ_{yy} are the normal stress components averaged over the thickness of the sample [93, 94]. The elasto-optic coefficient, C_σ, accounts for the change in optical properties, refractive index and volume due to the Poisson effect [93]. The presented equations are the governing equations for experimental techniques including Coherent Gradient Sensing (CGS) [93, 100], optical method of caustics [9], and Digital Gradient Sensing (DGS) [94, 95].

Table 6.1: PMMA constants used for quantitative schlieren analysis.

PMMA Constant	Value
A_c (m^2/N)	-0.530×10^{-10}
B_c (m^2/N)	-0.570×10^{-10}
n_o	1.49
ν	0.35
E_y (Pa)	2.8×10^9

The experiment methodologies then relate optical path length change, $\Delta s_x \approx \Delta s_y \approx \Delta s(x, y)$, to the propagation unit vector, $\hat{d}$, which is then related to measurable values. Using schlieren imaging the angle the light ray has been deflected in the xz- and yz-plane, ϵ_x and ϵ_y respectively, can be experimentally determined, as depicted in Figure 6.1.

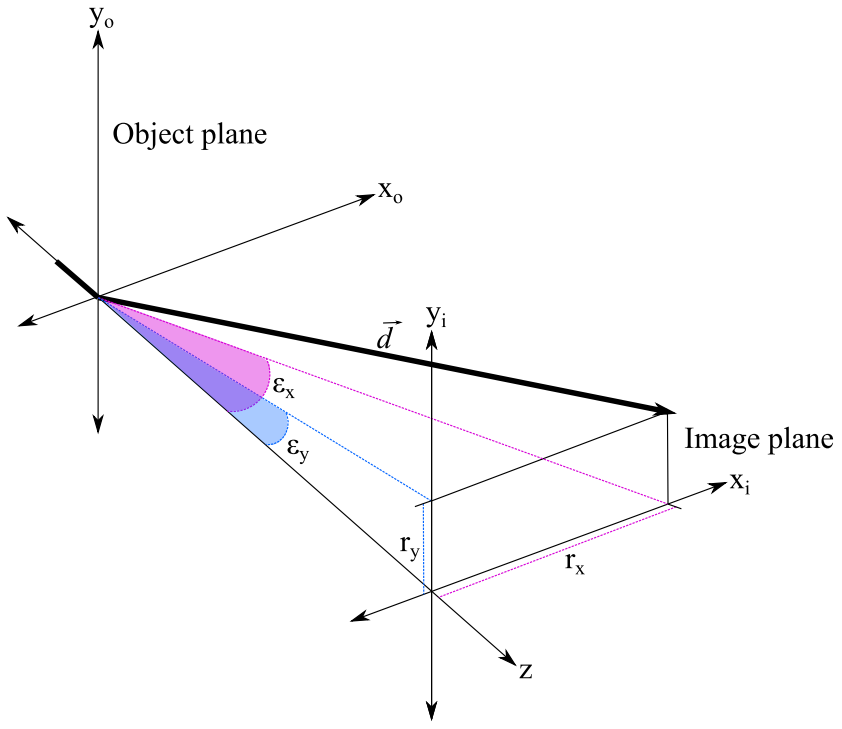

Figure 6.1: Schematic of a perturbed light ray propagating from the object plane to the image plane. The refractive disturbance is images in the image plane as location (r_x, r_y)

A generic light ray can be expressed as a unit propagation vector, $\hat{d}$, in terms of direction cosines. The direction cosines, a, b, and c, for a light ray are the cosines of the angles, α, β and γ, between the propagation vector, $\vec{d}$, and the three positive coordinate axes as shown in Figure 6.2.

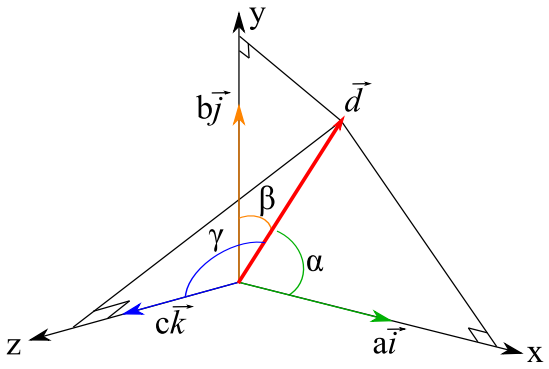

Figure 6.2: Schematic of a generic propagation vector, $\vec{d}$, with the direction angles and direction cosines.

The direction cosines are related to the angles relative to the coordinate axes through:

$$a = \cos(\alpha) \tag{6.12}$$

$$b = \cos(\beta) \tag{6.13}$$

$$c = \cos(\gamma) \tag{6.14}$$

Expressing the unit propagation vector, $\hat{d}$, in terms of direction cosines [94, 100]:

$$\hat{d} = a\hat{i} + b\hat{j} + c\hat{k} \tag{6.15}$$

For a light ray propagating through an undisturbed specimen the unit propagation vector becomes $\hat{d} = c\hat{k}$. However in the case where the specimen has been deformed, the unit vector in the $\hat{i}$ and $\hat{j}$ directions are required. The unit vector $\hat{d}$ for the perturbed light vector, $\vec{d}$, in Figure 6.1 can be related to optical path length change using the following relation [100]:

$$\begin{aligned} \hat{d} &= \frac{\boldsymbol{\nabla}(\Delta s)}{|\boldsymbol{\nabla}(\Delta s)|} \\ &= \frac{\frac{\partial(\Delta s(x,y))}{\partial x}\hat{i} + \frac{\partial(\Delta s(x,y))}{\partial y}\hat{j} + C\hat{k}}{\sqrt{\left(\frac{\partial(\Delta s(x,y))}{\partial x}\right)^2 + \left(\frac{\partial(\Delta s(x,y))}{\partial y}\right)^2 + C^2}} \end{aligned} \tag{6.16}$$

Where C is a constant. In the case of small deflections ($C \approx 1$), small stress gradients exist such that $\left(\frac{\partial(\Delta s(x,y))}{\partial x}\right)^2 << 1$ and $\left(\frac{\partial(\Delta s(x,y))}{\partial y}\right)^2 << 1$. Therefore, the unit propagation vector becomes:

$$\hat{d} \approx \frac{\partial(\Delta s(x,y))}{\partial x}\hat{i} + \frac{\partial(\Delta s(x,y))}{\partial y}\hat{j} + \hat{k} \tag{6.17}$$

Thus, for small deflections, this implies that the direction cosines, a and b, are related to the normal stress gradients, $(\sigma_{xx} + \sigma_{yy})$, using Equations 6.10 and 6.17:

$$a = \cos\alpha = d_{eff} C_\sigma \frac{\partial\left(\sigma_{xx} + \sigma_{yy}\right)}{\partial x} \tag{6.18}$$

$$b = \cos\beta = d_{eff} C_\sigma \frac{\partial\left(\sigma_{xx} + \sigma_{yy}\right)}{\partial y} \tag{6.19}$$

The direction cosines, a and b, can then be related to the refraction angles, ϵ_x and ϵ_y, using trigonometry. Figure 6.3 is a schematic showing the angles relative to an arbitrary perturbed light ray which has traveled a distance d from the object plane to the image plane separated by a distance, Δ.

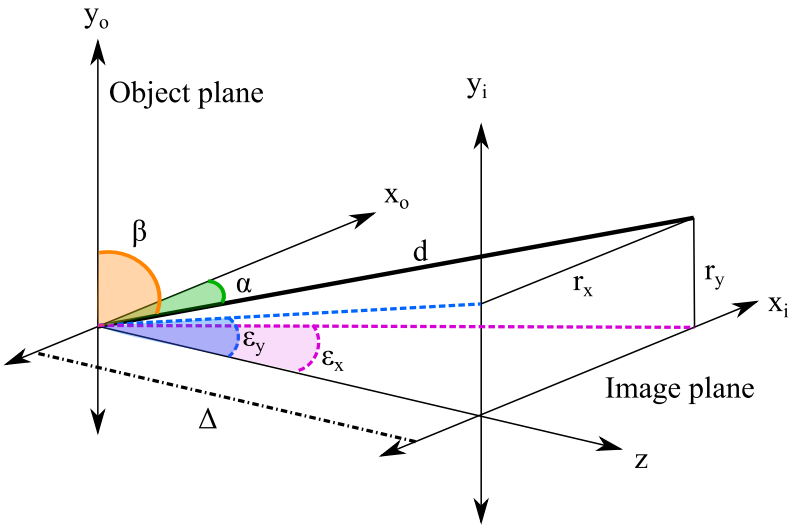

Figure 6.3: Schematic showing the direction angles, α and β, for the propagation vector relative to the refraction angles, ϵ_x and ϵ_y.

The refraction angles, ϵ_x and ϵ_y, can be used to calculate the displacements of the light ray in the imaging plane, r_x and r_y:

$$\tan\epsilon_x = \frac{r_x}{\Delta} \quad \text{and} \quad \tan\epsilon_y = \frac{r_y}{\Delta} \tag{6.20}$$

For small deflections, the small angle approximation can be applied:

$$\epsilon_x \approx \frac{r_x}{\Delta} \quad \text{and} \quad \epsilon_y \approx \frac{r_y}{\Delta} \tag{6.21}$$

Similarly, the direction cosines, a and b, are related to the displacements, r_x and r_y, through:

$$a = \cos\alpha = \frac{r_x}{d} \quad \text{and} \quad b = \cos\beta = \frac{r_y}{d} \tag{6.22}$$

Rearranging Equations 6.22 in terms of r_x and r_y and substituting them into Equations 6.21 yields:

$$\epsilon_x \approx \frac{d}{\Delta}a \quad \text{and} \quad \epsilon_y \approx \frac{d}{\Delta}b \tag{6.23}$$

Using trigonometry, the length of the ray can then be expressed as, $d = \sqrt{r_x^2 + r_y^2 + \Delta}$.

$$\epsilon_x \approx a\sqrt{\frac{r_x^2 + r_y^2}{\Delta} + 1} \tag{6.24}$$

$$\epsilon_y \approx b\sqrt{\frac{r_x^2 + r_y^2}{\Delta} + 1} \tag{6.25}$$

For small deflections relative to to distance between the object plane and imaging plane the relation of $\sqrt{\frac{r_x^2+r_y^2}{\Delta} + 1} \approx 1$, thus:

$$\epsilon_x \approx a = d_{eff}C_\sigma \frac{\partial\left(\sigma_{xx} + \sigma_{yy}\right)}{\partial x} \tag{6.26}$$

$$\epsilon_y \approx b = d_{eff}C_\sigma \frac{\partial\left(\sigma_{xx} + \sigma_{yy}\right)}{\partial y} \tag{6.27}$$

These equations are the governing equations for obtaining the stress gradients from schlieren images. The refraction angles, ϵ_x and ϵ_y, are measured through calibration of the schlieren imaging system the same as typically done in gases [47, 48]. The stress state can then be calculated.

6.2 Experimental methods for quasi-static experiments

Quantitative schlieren analysis was applied to PMMA samples which were quasi-statically compressed using a Mark-10 Motorized Force Tester. The PMMA sample had a thickness of 9.4 mm, a length of 177.8 mm, and a height of 88.9 mm. The sample geometry was selected such that a plane stress assumption could be made and it was similar to previous works [94]. The sample also had to be thin enough to minimize light ray perturbations caused by the unstressed PMMA. The sample length and width allowed for a semi-infinite body assumption. The base of the sample was stabilize using a piece of aluminum on the bottom compression head which supported the length of the PMMA sample.

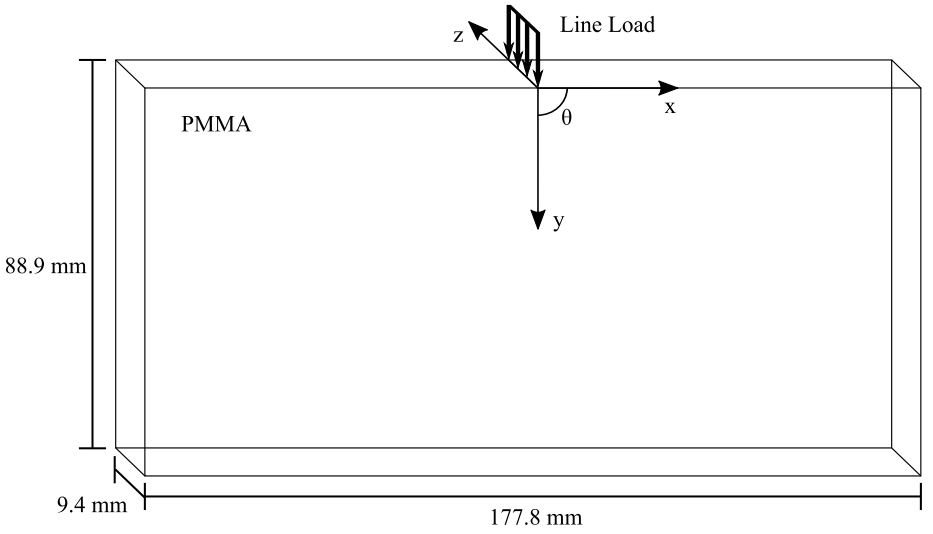

Figure 6.4: A schematic of the PMMA sample with dimensions and the location of the applied force.

In the interest of creating a point load in the imaging plane, a 4 mm steel pin was attached to the top compression head, creating a line load. The PMMA was placed in the Mark-10 such that the loading pin was centered along the length of the PMMA sample as shown in Figure 6.4. The Mark-10 compression head speed was set to the minimum, 0.167 mm/sec. The load cell used to measure the applied force was a tension and compression force sensor series R01. Different loading conditions were tested: a ”stair stepping” up to the maximum force and a displacement controlled ramp loading up to the highest force. The force as a function of time was recorded with a sample rate of 50 Hz.

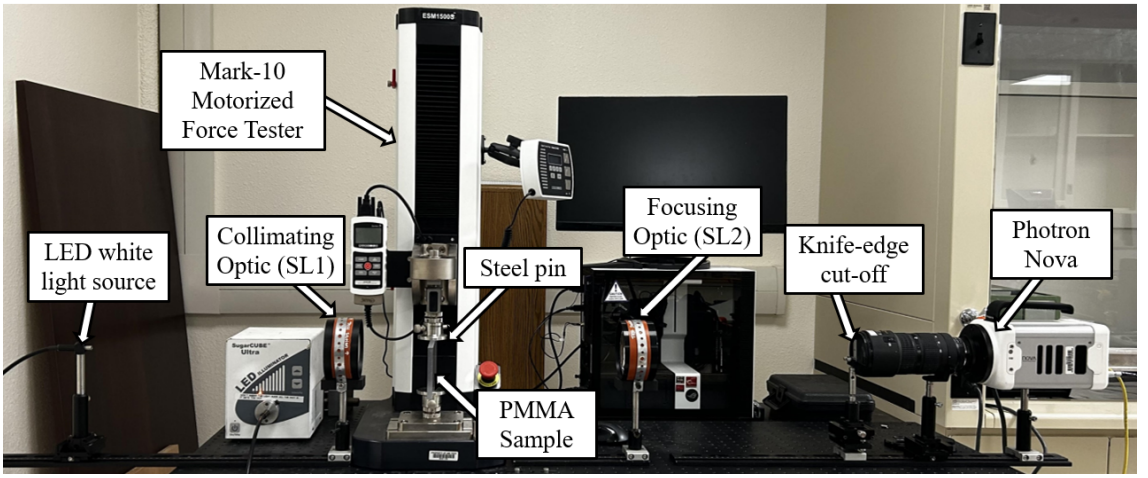

Figure 6.5: Image of the quasi-static experimental set up.

The Mark-10 was centered in a schlieren imaging system test section. The schlieren system was a simple lens-type schlieren system. The schlieren lenses had focal lengths of 400 mm (f/# $\approx$ 4) and a SUGARcube white LED light was used as the light source. The camera used to record the event was a Photon Nova operating at a frame rate of 50 fps which matched the sample rate of the force measurements. Two knife-edge cut-off orientations, vertical and horizontal, were studied separately allowing for calculation of refraction angles in two directions.

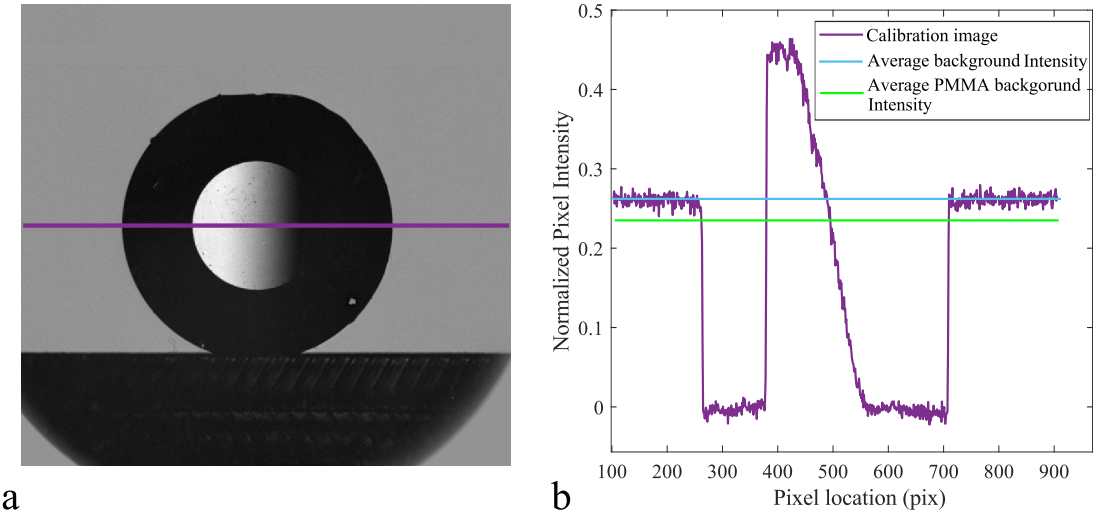

Figure 6.6: (a) An image of a plano-convex calibration lens with a vertical knife-edge cut off and (b) a plot of the pixel intensity values as a function of position for the purple line in (a) and the average background intensity with (green line) and without (blue line) PMMA.

The schlieren imaging system sensitivity is dependant on the amount of light that is being cut-off. The amount of cut-off was determined using a plano-convex calibration lens, with a 2 m focal length, such that pixel values brighter and darker than the background pixel value were visible as shown in Figure 6.6. The focal length of the calibration lens is of particular importance and should be selected such that the focal length of the calibration lens is longer than the distance from the object to the cut-off. If the calibration lens focal length is too long then the full range of gray scale values will not be visible thus the system can not be fully calibrated. Refraction angles also play an important role when selecting a sample and sample thickness.

6.3 Experimental methods for explosive experiments

To quantify the explosively driven material response of PMMA, two synchronized high-speed cameras were used to image the event. The two high-speed cameras were Shimadzu HPV-X2s which recorded at 2Mfps. The light source was a SI-LUX laser pulsed at a pulse width of 15 ns. The laser had a wavelength of 640 nm allowing for a bandpass filter of the same wavelength to be placed in front of the cameras, reducing external illumination from the detonation event. The explosive was an RP-80 EBW detonator placed in contact with the PMMA as shown in Figure 6.7. Silicon grease was placed on the interface between the PMMA and the detonator face to improve the contact between the two materials.

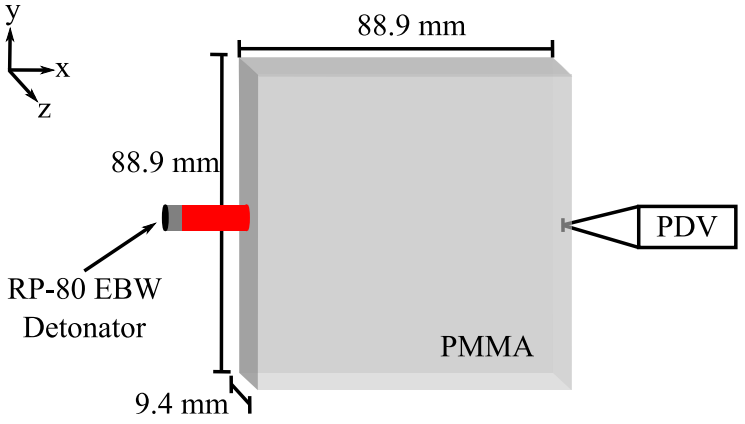

Figure 6.7: Schematic of the PMMA sample used for the explosively loaded PMMA experiments.

The PMMA sample was the same thickness as the quasi-static experiments, 9.2 mm, which was also approximately the diameter of the detonator. The length and width of the sample were both 88.9 mm. Surface velocity measurements using Photon Doppler Velocimetry (PDV) were taken on the surface opposite of the

detonator. A piece of retro-reflective tape was placed on the surface where the PDV measurement was taken. The explosive event was contained in a boom box, as shown in Figure 6.8. The boom box was centered in the parallel light schlieren system test section. Optical glass was used as the window material in order to reduce distortions in the parallel light test section. The same schlieren lenses used for the quasi-static experiments were used for the dynamic tests, having a focal length of 400 mm ($f/\# \approx 4$). After the focusing optic, prior to the focal point, the light path was split toward the two different cameras. The two cameras had different knife-edge cut offs, one vertical and one horizontal. An image of the experimental setup is shown in Figure 6.8.

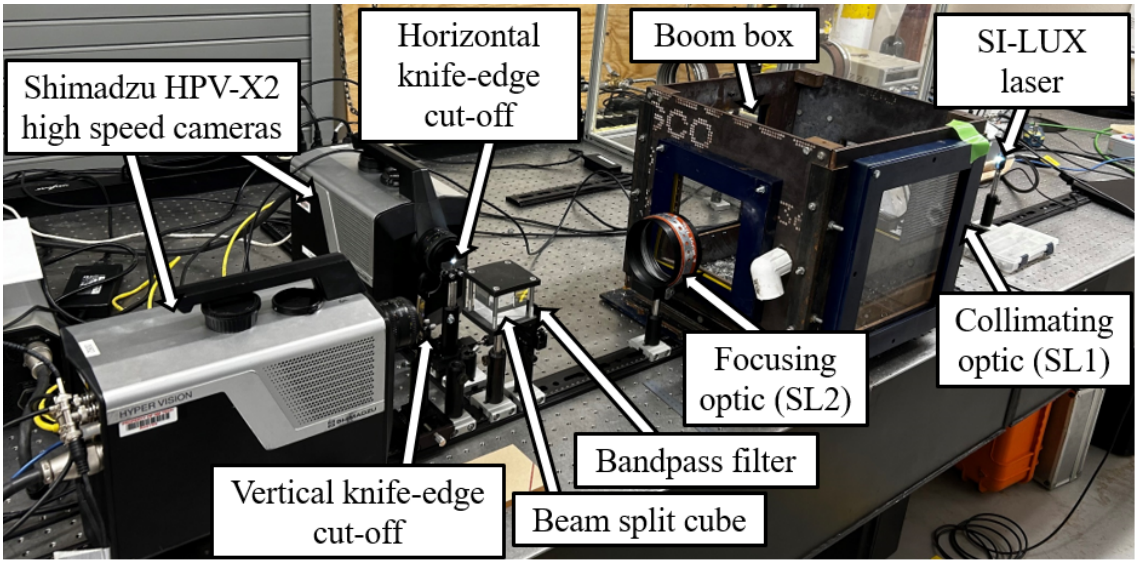

Figure 6.8: Image of the experimental setup used for conducting the explosively loaded PMMA experiments.

6.4 Imaging analysis methods

The application of external force introduced grayscale intensity variations in the PMMA. In order to quantify the stress gradient from the external force, vertical and horizontal refraction were separately measured. The knife-edge direction dictates the direction of the refraction angle being measured. Schlieren images of the grayscale intensity variations experimentally observed from quasi-static loading are shown in Figure 6.9.

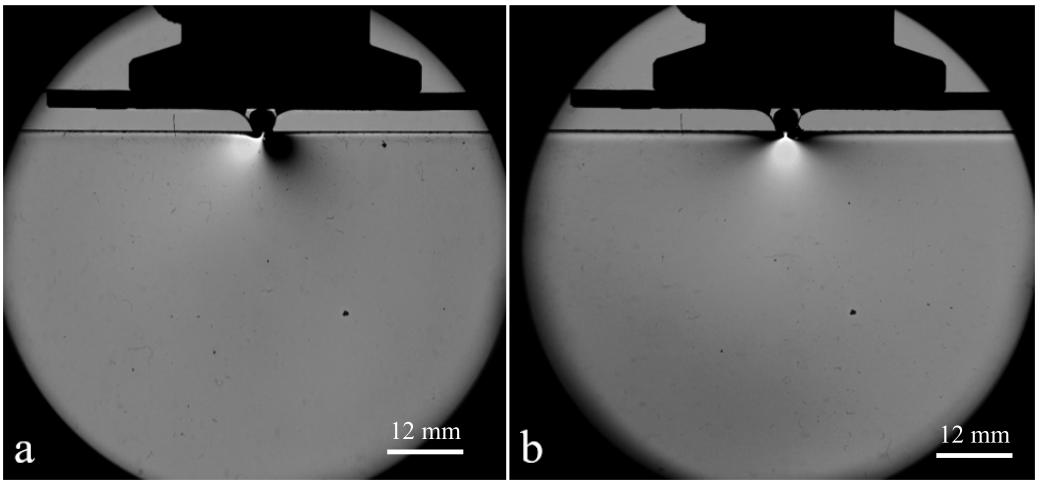

Figure 6.9: (a) vertical knife edge and (b) horizontal knife-edge schlieren images of the PMMA sample subject to a line load of 2365 N.

6.4.1 Quasi-static experiment data syncing

The camera trigger and the Mark-10 trigger were not synchronized, therefore, image processing was used to synchronize the two data sets. Syncing the data was based on the highest amount of stress having the largest stress grayscale intensity variations. The image processing is described in Figure 6.10. The images were normalized by the bit depth of the image so the pixel intensity values were between 0 and 1. A background subtraction was applied in order to remove the residual stresses on the boundary of the PMMA sample due to the manufacturing process (Figure 6.10b). The translation of the compression head was amplified after the background subtraction, therefore, the image was cropped to remove the compression head from the image as shown in Figure 6.10c. The image with the largest grayscale intensity variations was determined by converting the cropped and background subtracted images (c) to binary images using the MATLAB function *imbinarize* with the same threshold value for all of the images in a singular data set (Figure 6.10d). The threshold value did vary from data set to data set based on the image intensity. Once the images were binarized the number of white pixels in each image were summed. The image with the most white pixels was taken as the image with the maximum force applied. Once the image, and image number, with the maximum force applied was known, the corresponding sample number from the Mark-10 data was determined. The two data sets were then aligned based on the frame rate and sample rate from the two data sets.

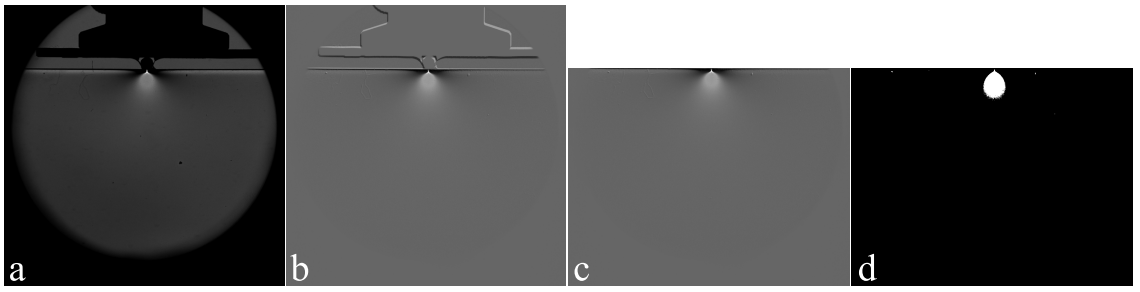

Figure 6.10: (a) A schlieren image a PMMA sample with a horizontal cut-off under quasi-static compression. (b) A background subtraction was applied to (a). (c) The background subtracted image was cropped and (d) binarized.

6.4.2 Explosive experiment data syncing

Two high-speed cameras were used to image the explosive event because the deflections in the x- and y- direction are required to calculate the stress gradients. Since both displacements were required, the data needed to be aligned in both time and space. The two cameras were synchronized in time, however, the spatial alignment was slightly off. The alignment of the two data sets was achieved using image registration in MATLAB. A marker was placed on the PMMA samples prior to testing with the intent of aligning the two image sets shown in Figure 6.11 a and b. The marker also indicates the y-location of the PDV measurement.

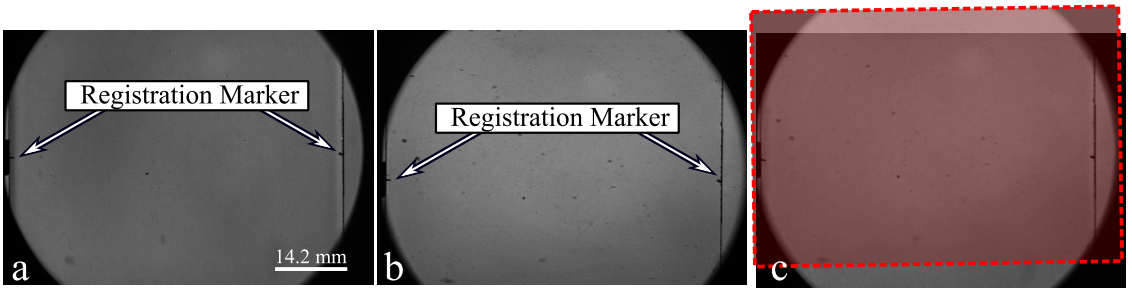

Figure 6.11: Images of data collected from the camera with (a) a vertical cutoff, (b) a horizontal cut-off, and (c) the two images aligned using the marker.

6.4.3 Experimental refraction angle calculation

Two cut-off directions were used to calculate vertical (y-direction) and horizontal (x-direction) displacements. A horizontal cut-off allows for the refraction angles in the y-direction, ϵ_y, to be calculated, whereas a vertical cut-off allows for the refraction angles in the x-direction, ϵ_x, to be calculated. The refraction angles are calculated through calibration of the imaging system grayscale intensities to a known refraction angle. This was done using a weak positive focal length lens allowing for relatively small angular deflection of light rays, as the calibration object. The calibration lens used for both the quasi-static and dynamic tests was a plano-convex lens with a focal length of 2 m purchased from CVI Laser Optics (part number: PLCX-25.4-1030.2-C). Images of the calibration lens with the vertical and horizontal cut-off are presented in Figure 6.12a and c, respectively.

A gradient of "light" pixels to "dark" pixels was captured in the calibration lens. The gradient is a grayscale gradient where the images have been normalized by the camera bit depth. The grayscale value of the pixels will be referred to as the pixel intensity. The calibration lens was used to relate pixel intensity to refraction angle, ϵ, using the light to dark gradient of pixel intensities in the center of the calibration lens. The row of pixels in the center of the calibration lens was determined using the method outlined in section 2.4.1, plotted in Figure 6.12 as the solid purple line. Once the center of the lens was determined, a section of pixels in the center of the lens, depicted as the dashed orange line in Figure 6.12 a and c, were averaged at each pixel location yielding an average pixel intensity at each pixel location. A polynomial was fit to the averaged data which is plotted as the dashed orange line in Figure 6.12 b and d. The polynomial was fit such that the pixel location in the calibration lens, R_x and R_y, was a function of the pixel intensity, I. Fitting the data in this manner allows for determination of the location in the calibration lens from a pixel intensity value.

The location in the calibration lens, R_x and R_y, are used to calculate the refraction angle for a specific intensity value. First, the average background intensity for the uncompressed PMMA sample was calculated, green dot-dash line in Figure 6.12 b and d, then the corresponding lens location, r_{PMMA}, was determine using the polynomial fit to the calibration lens data. This average PMMA background intensity was taken as a value of zero refraction ($\epsilon = 0$). Once the location of zero refraction was known then the lens geometry was used to calculate the refraction angles.

Calculating a vertical refraction angle, ϵ_y, for an arbitrary perturbed light ray, begins with the pixel intensity of the light ray from the image. The intensity of the perturbed light ray, I_p, was then used to determine where in the calibration lens the same pixel intensity value exists using the polynomial fit, $R_y(I_p)$. The location of the pixel value inside the calibration lens, R_y, then allows for the calibration lens geometry to be used to calculate the refraction angle, ϵ_y. The ray displacement, r_y, depicted in Figure 6.13 was calculated using the location in the calibration lens R_y

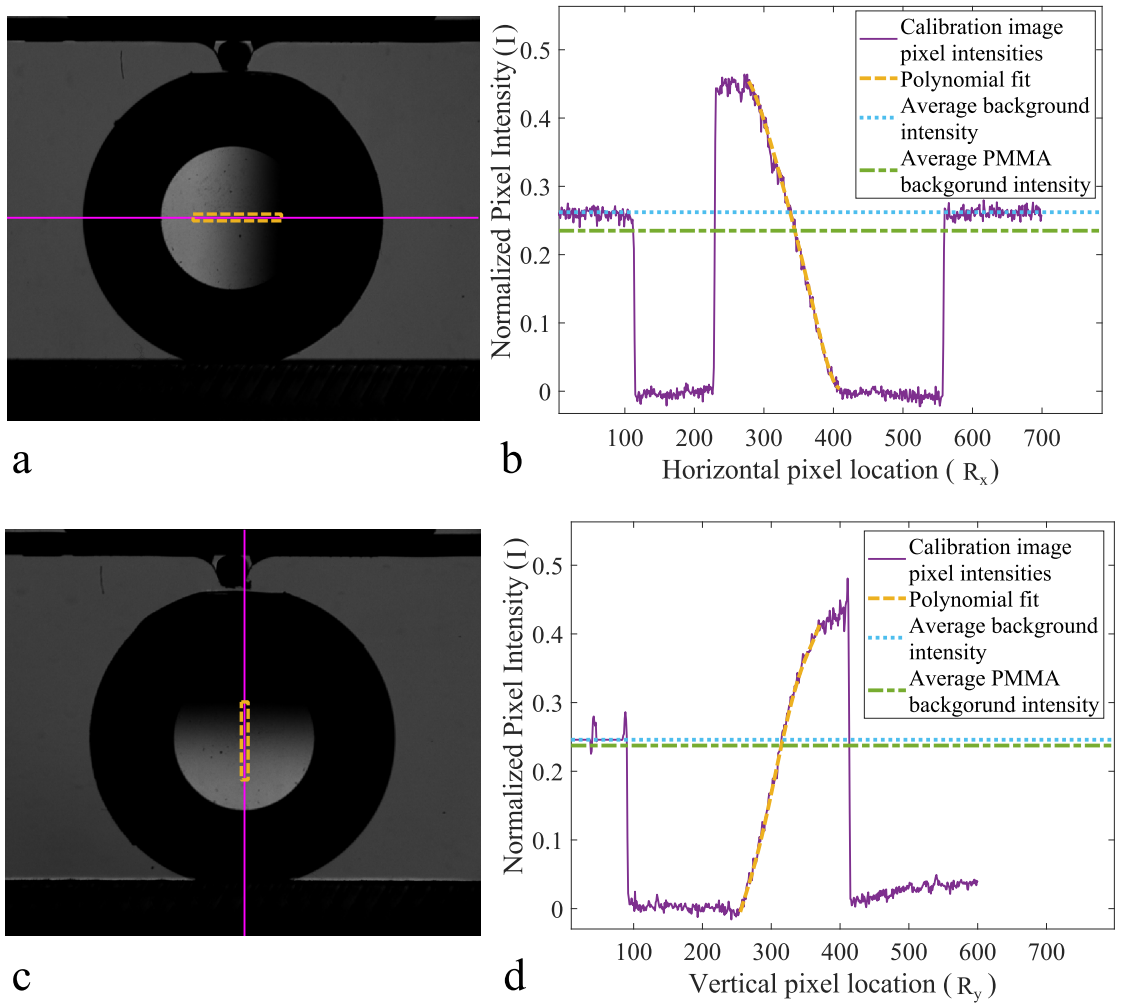

Figure 6.12: Images of the calibration lens with (a) a vertical knife-edge cut off and (c) a horizontal knife-edge cut-off with (b and d) corresponding plots of (solid purple lines) pixel intensities as a function of location, (dashed orange lines) the polynomial fit to the calibration data, (double dashed blue lines) the average background pixel intensity without PMMA and (dash-dot green lines) the average background pixel intensity of the PMMA.

relative to the location of zero refraction, r_{PMMA}:

$$r_y = R_y - r_{PMMA} \tag{6.28}$$

Then, r_y and the focal length of the calibration lens f were used to calculate ϵ_y using trigonometry:

$$\epsilon_y = \arctan \frac{r_y}{f} \tag{6.29}$$

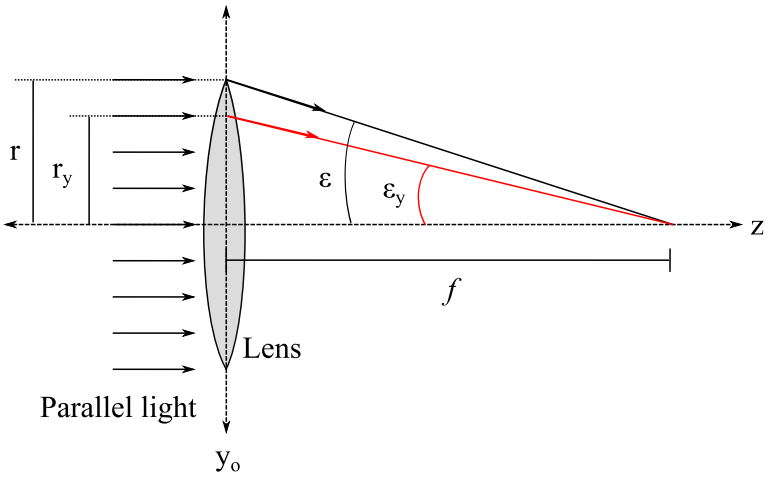

Figure 6.13: Schematic of a calibration lens.

The same analysis was applied to the vertical cut-off images in order to calculate ϵ_x.

CHAPTER 7

QUANTITATIVE SCHLIEREN IMAGING RESULTS

The quantitative schlieren imaging methodology for transparent solids outlined in Chapter 6 was applied to quasi-static and dynamic loading experiments in PMMA. The quasi-static experiments were baseline experiments used to implement the analysis method. The experiments studied vertical and horizontal deflections independently. The independent images were then analyzed at the same load to calculate the refraction angles in the x- and y- directions. The resulting refraction angles from the quasi-static experiments were compared to the analytical Flamant solution. The resultant angle was then used to calculate stress contours.

The method was extended to dynamic experiments where the refraction angles from an explosively driven shock wave in PMMA were determined. The refraction angles were integrated to get the stress state of the material which was compared to stress calculated using Photon Doppler Velocimetry.

7.1 Quasi-static results

The quasi-static experiments in PMMA were conducted such that the two knife-edge cut-off directions were studied independently. Using the synchronization outlined in Section 6.4.1 the images corresponding to the desired force for both data sets were determined. The experimental results were compared to the Flamant solution.

7.1.1 The analytical Flamant solution

The French mechanist Alfred-Aimé Flamant modified the three-dimensional Boussinesq solution to provide a solution for a linear elastic, homogeneous, isotropic body subjected to a line load in an elastic half-space [116] depicted in Figure 7.1. For a normal force acting in the y-direction in a half space there exists a simple radial load distribution [117].

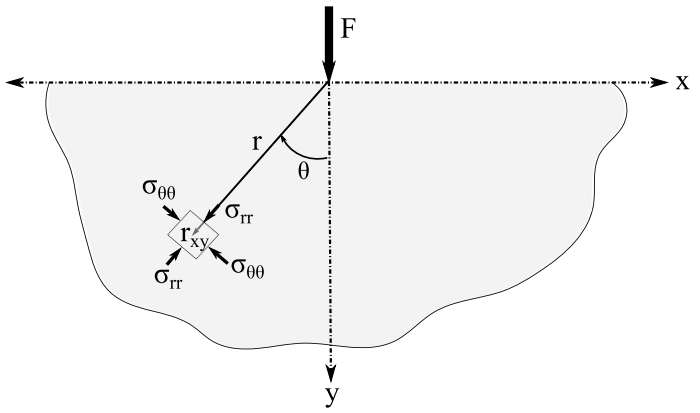

Figure 7.1: Schematic of an elastic half-space loaded with a point load.

Any element, r_{xy}, which is a distance r from the load undergoes a compression in the radial direction. The stress components for the compression of a body having a thickness of d_{eff} are given in polar coordinates [94, 117]:

$$\sigma_{rr} = -\frac{2F}{\pi d_{eff}} \frac{\cos\theta}{r} \tag{7.1}$$

$$\sigma_{\theta\theta} = 0 \tag{7.2}$$

$$\sigma_{r\theta} = 0 \tag{7.3}$$

The Hoop stress, $\sigma_{\theta\theta}$, and shearing stress, $\sigma_{r\theta}$ are zero satisfying the equilibrium equation. Rewriting equation 7.1:

$$\sigma_{rr} = -\frac{2F}{\pi d_{eff}} \frac{y/r}{r} \tag{7.4}$$

Or, in all Cartesian coordinates:

$$\sigma_{rr} = -\frac{2F}{\pi d_{eff}} \frac{y}{(x^2 + y^2)} \tag{7.5}$$

The relationship between σ_{rr} and $(\sigma_{xx} + \sigma_{yy})$ for the Flamant solution is as follows:

$$(\sigma_{xx} + \sigma_{yy}) = \sigma_{rr}(\cos^2\theta + \sin^2\theta) = \sigma_{rr} \tag{7.6}$$

A light ray passing through the stress field will be distorted according to Equations 6.26 and 6.27. For the Flamant solution the light ray deflection in the x- and y-directions becomes:

$$\epsilon_x = d_{eff} C_\sigma \frac{\partial(\sigma_{rr})}{\partial x} \tag{7.7}$$

$$\epsilon_y = d_{eff} C_\sigma \frac{\partial(\sigma_{rr})}{\partial y} \tag{7.8}$$

Substituting Equation 7.5 into Equations 7.7 and 7.8 and solving, the analytical solution for ϵ_x and ϵ_y are:

$$\epsilon_x = C_\sigma \frac{2F}{\pi} \frac{\sin 2\theta}{r^2} \tag{7.9}$$

$$\epsilon_y = C_\sigma \frac{2F}{\pi} \frac{\cos 2\theta}{r^2} \tag{7.10}$$

7.1.2 Experimental results

The experiments required a vertical and horizontal cut-off in order to calculate the refraction angles in the x- and y- directions, respectively. A force of 2365 N was selected for the analysis, and the corresponding schlieren images are presented in Figure 7.2. The refraction angles were calculated as outlined in section 6.4.3. The pixel intensities from the images of the experiments were found inside of the calibration lens which was then used to calculate the refraction angles. The resulting matrix of refraction angles were plotted using the MATLAB function *contour* with contour levels of $-5:1:5$ milliradians creating isolines. The resulting isolines for the experimental refraction angles are presented in Figure 7.2 b and d. The contour plots were created such that the load was applied at the origin. The analytical refraction angles were calculated using Equations 7.9 and 7.10. A matrix that was the same size as the experimental matrix was created for the analytically calculated refraction angles. The analytical solution was plotted in the same manner as the experimental refraction angles, creating isolines. The isolines from the analytical solution were plotted over the experimental isolines resulting in the plots in Figure 7.3.

The isoline patterns created from the refraction angles follow the same shape that was created from the grayscale pixel intensity variation in the raw schlieren images, which was expected. The analysis method and the orientation of the knife-edge resulted in the high intensities (white) pixels for ϵ_x to be negative, where as high intensity pixels for ϵ_y are positive. The isolines for ϵ_x does reveal a slight asymmetry (Figure 7.2b). The isolines in the positive x-direction are slightly larger than the isolines in the negative x-direction. The zero refraction line between the two isolines is also biased slightly in the negative x-direction. The bias direction was more apparent when comparing the experimental solution to the analytical solution presented in Figure 7.3a. Relative to the analytical solution, the zero refraction angle is approximately 12° in the negative x-direction. Post-processing revealed that during the loading process the compression head was translating at a slight angle. The angle the compression head translated was approximately equal to the angle of the zero refraction from the experiments. Therefore, the asymmetry in the isolines was attributed to slight translation of the top compression head. The translation of the compression head did not appear to impact the experimental isolines for the refraction in the y-direction, ϵ_y. Comparing the experimentally determined isolines for ϵ_y to the analytical solution reveals agreement between the two solutions.

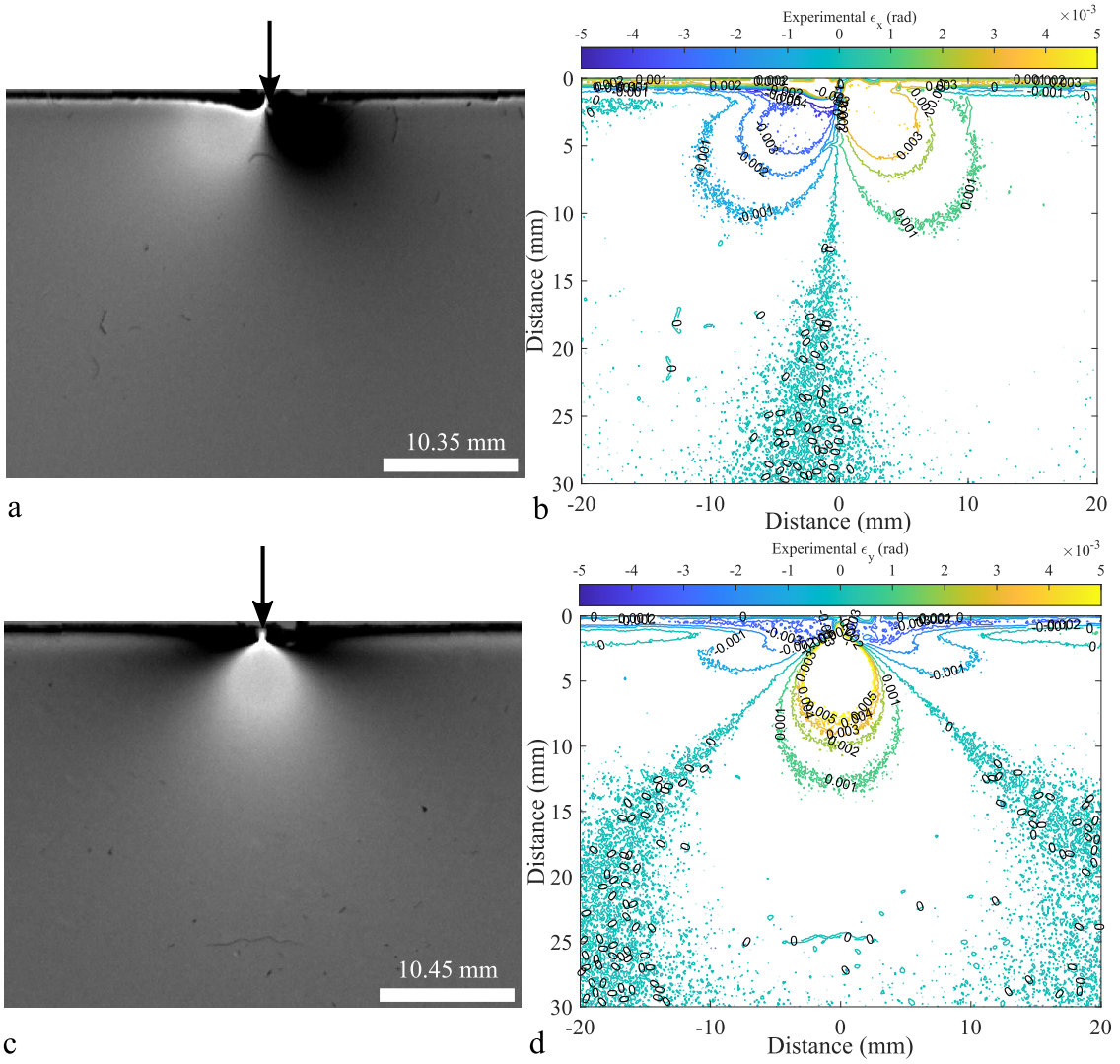

Figure 7.2: (a and c) Schlieren images and (b and d) the resulting refraction angles, with contour levels of $-5 : 1 : 5$ milliradians, for the PMMA sample with a compressive line load of 2365 N for (a and b) a vertical knife-edge cut off (ϵ_x) and (c and d) a horizontal knife-edge cut off (ϵ_y).

It is expected that the analytical solution and experimental solution up to $r/d_{eff} = 1/2$ will differ because the plane stress assumptions are violated close to the loading point where a zone of dominant triaxiality exisits [94]. There are also isolines that appear close to the sample boundary which are caused by boundary effects. Images of the experimental solution compared to the analytical solution with the zone of dominant triaxiality highlighted in red and the boundary effects highlighted in gray for three different load cases of (a and b) 2365 N $\pm$5 N, (c and d) 1860 N $\pm$5 N, (e and f) 1360 N $\pm$5 N are presented in Figure 7.4.

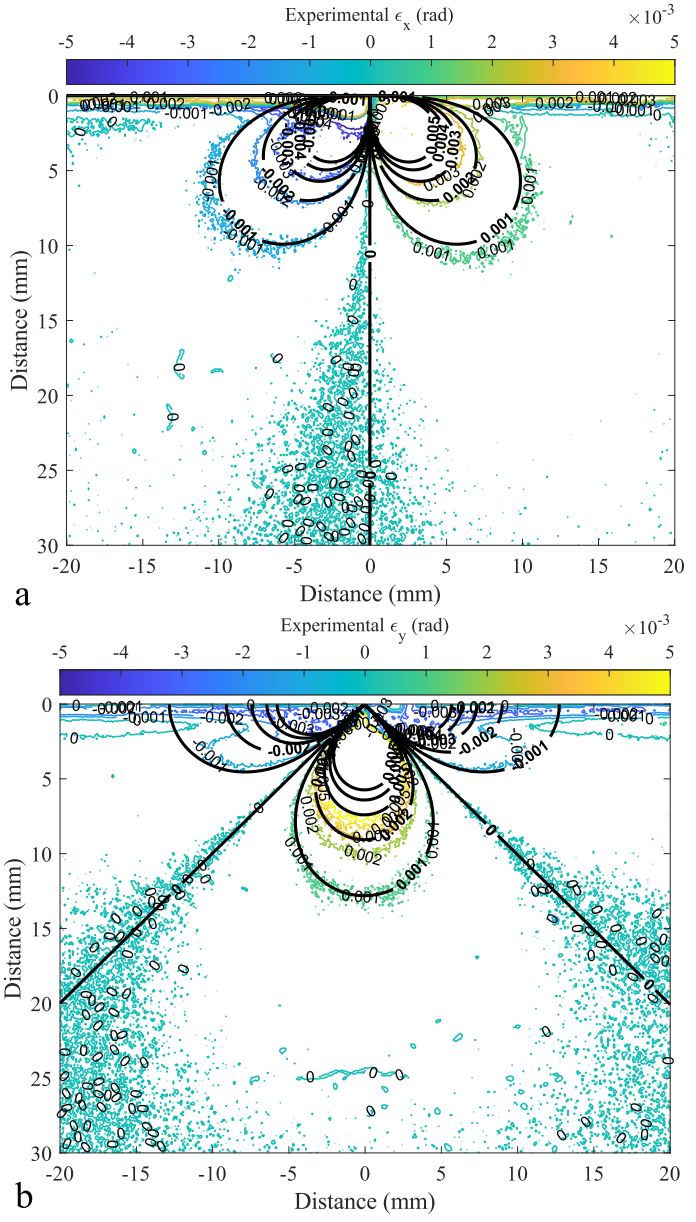

Figure 7.3: The experimental refraction angles (colored contours) for (a) refraction angles in the x direction (ϵ_x) and (b) refraction angles in the y direction (ϵ_y) compared to the analytical solution (black lines).

The zone of dominant triaxiality for the present experiments was at a radius of approximately 4.6 mm. Comparing the experimental results to the analytical solution for the three different load cases it can be seen that outside of the zone of dominant triaxiality the two solutions are in good agreement. As expected, the isoline sizes increase with an increase in compressive force. For the vertical cut-off

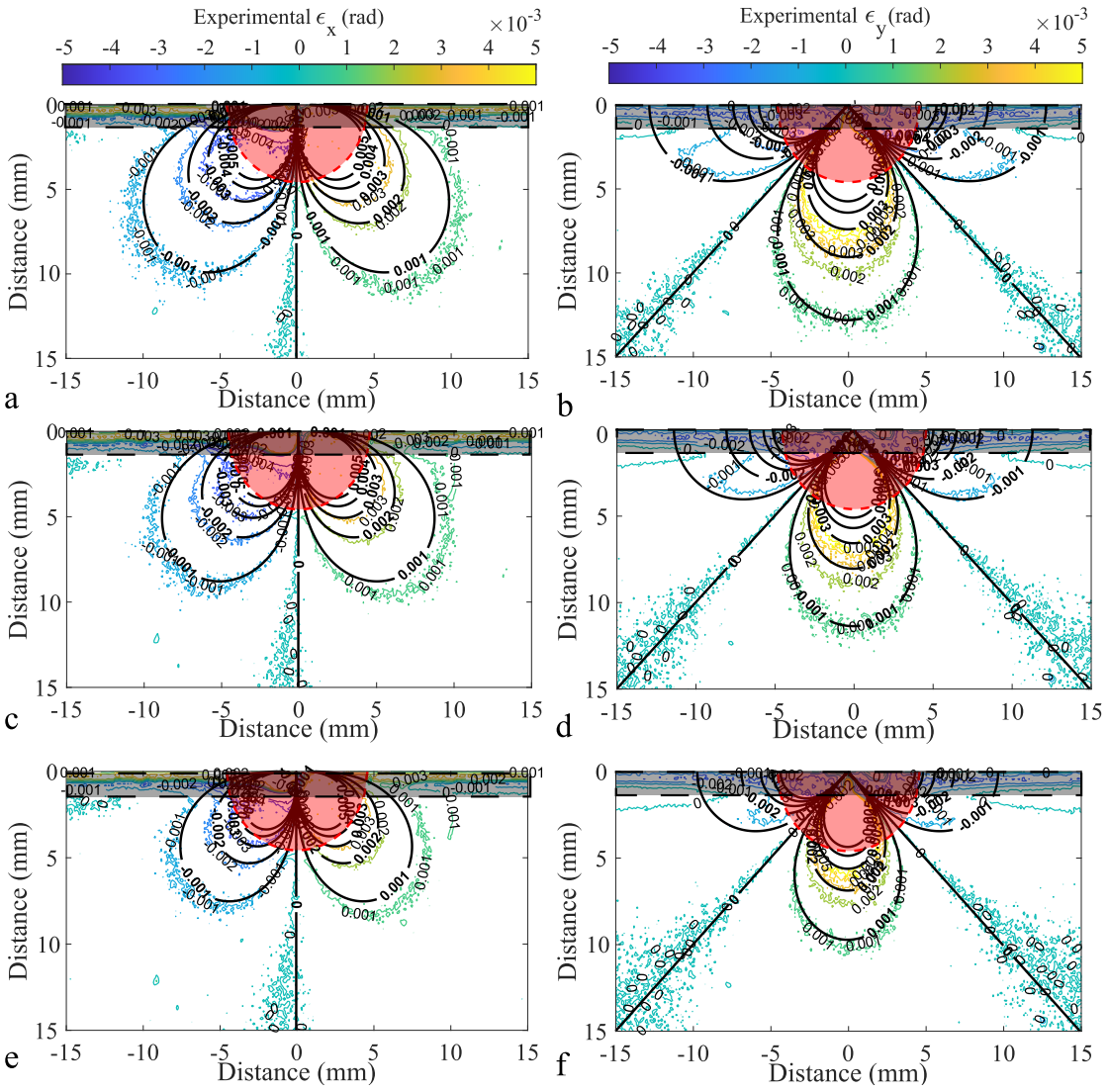

Figure 7.4: The experimental refraction angles (colored contours) for (a, c, and e) ϵ_x and (b, d, and f) ϵ_y compared to the analytical solution (black) at compressive loads of (a, b) 2365 N $\pm$5 N, (c, d) 1860 N $\pm$5 N, and (e, f) 1360 N $\pm$5 N. The zone of dominant triaxiality is plotted as the red shaded area and boundary effects are highlighted in the gray shaded area. The contour levels are in radians.

experiments (Figure 7.4a, c and e) the experiments align well with the analytical solution despite the asymmetry. The isolines in the negative x-direction are slightly smaller than the isolines in the positive x-direction. The asymmetry appears to have a more significant impact on the outer isolines, $\epsilon_x = \pm$ 0.001 radians, with the asymmetry being more apparent for the lower load (e). The inner isolines, $\pm$ 0.002 radians and $\pm$ 0.003 radians, do not appear to be asymmetric and align with the analytical solution. Although the line of zero refraction for the experiments

was slightly angled, it still aligned with the analytical solution, and at the highest load seems to be the most vertical.

The horizontal cut-off images had two lines of zero refraction. The two lines of zero refraction for the experiment and analytical solution aligned. Since the lines of zero refraction aligned with the analytical solution it appeared that the translation of the compression head did not impact the experimental measurement significantly. For these experiments, the measurement was in agreement with the analytical solution for the outer isoline at an angle of 0.001 radians. However, for the isolines at an angle of 0.002 radians there was some slight misalignment. The misalignment was attributed to the calibration data. The calibration pixel intensities did not span the full dynamic range of the camera and the intensities observed in the images. The center isolines were calculated from the light side of the calibration image, to which the calibration data ranged from approximately 0 to 0.45, the pixel intensity values right outside the zone of dominant triaxiality were close to the boundary of the pixel intensities measured in the calibration lens. At the calibration lens boundaries there is increased uncertainty in the calculated refraction angles. From Figure 7.4b, along center line, x = 0 mm, the analytical solution for ϵ_y = 0.002 radians was approximately at y = 9.01 mm and the experimental solution for the same refraction angle was at y = 9.96 mm therefore the difference in position was approximately 0.95 mm. There are also boundary effects impacting the outer isolines for the contours in Figure 7.4b, d, and f which are caused by residual stresses in the PMMA from the manufacturing process which are highlighted in gray.

The refraction angles in the x- and y-direction were then used to estimate the stresses, $\sigma_{rr} = (\sigma_{xx} + \sigma_{yy})$. Two different approaches could be used to estimate the stresses. The first method would be direct numerical integration of Equations 6.26 and 6.27 which requires knowledge of far field boundary conditions. If the far field boundary conditions are not known then a second approach can be used which is leveraging the analytical solution. The analytical expression of the Flamant solution was used for the quasi-static tests because clear boundary conditions were not known. From the Flamant solution the stress state, σ_{rr}, was estimated using [94]:

$$\sigma_{rr} = (\sigma_{xx} + \sigma_{yy}) = \frac{\epsilon_R}{C_\sigma d_{eff}}(r\cos\theta) \tag{7.11}$$

Where, ϵ_R is the resultant refraction angle calculated using [94]:

$$\epsilon_R = \sqrt{\epsilon_x^2 + \epsilon_y^2} = C_\sigma d_{eff}\frac{2F}{\pi d_{eff} r^2} \tag{7.12}$$

The resultant refraction angles and the corresponding stress contours for a compressive force of 2365 N $\pm$5 N are presented in Figure 7.5. The resultant refraction angle compared to the analytical solution, Figure 7.5a, revealed some slight asymmetry from approximately -3 mm to 3 mm in the x-direction for refraction angles below 2 milliradians. This was caused by the slight misalignment

in the horizontal cut-off data presented in Figure 7.4 as discussed previously. The outer isoline at ϵ = 0.001 radians aligns well with the analytical solution and the inner isolines are in agreement with the analytical solution above x = 3 mm and below x = -3 mm. As for the stress contours, Figure 7.5b, the experimental results do reveal noise in the data, however, the experiments are still in agreement with the analytical solution.

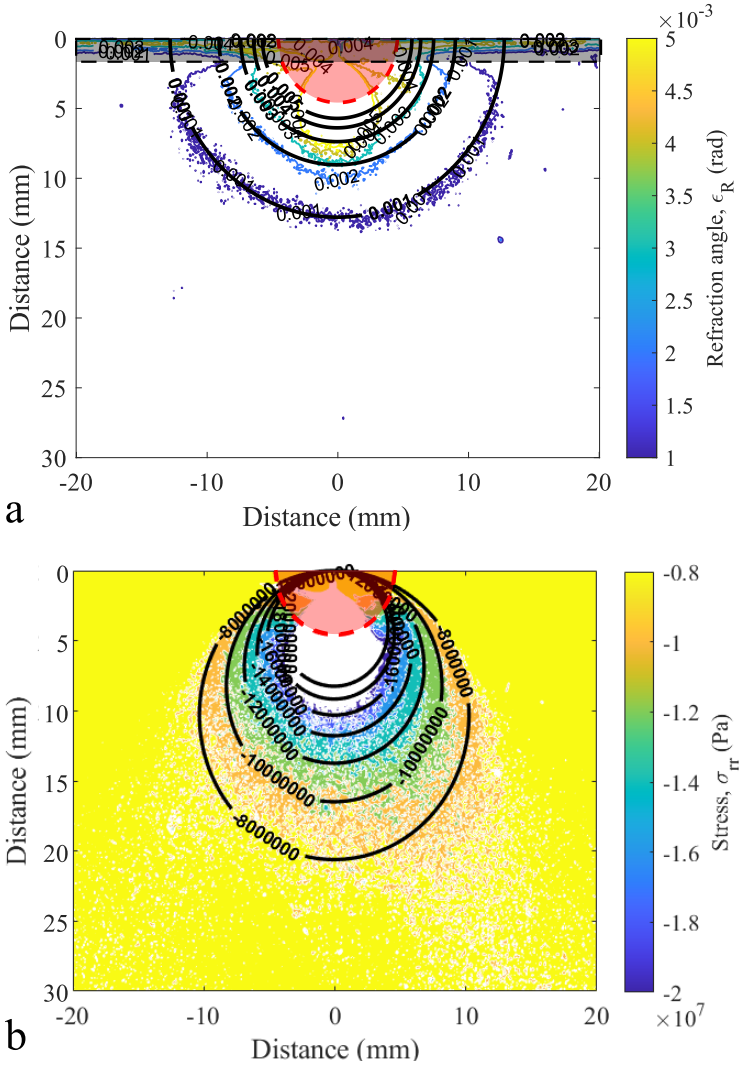

Figure 7.5: (a) the resultant refraction angles and (b) the stress contours for the experiments (colored contours) and the analytical solution (black contours) for a compressive force of 2365 N. The zone of dominant triaxiality is plotted as the red shaded area and the boundary effects in (a) are highlighted as the gray shaded area. The contour levels are in radians.

7.1.3 Increased dynamic range

The quasi-static experiments were re-run to correct for the translation of the compression head and to increase the dynamic measurement range for the pixel intensities. The pixel intensity range for the updated experiments were 0 to 0.85 for the vertical cut-off images and 0 to 0.8 for the horizontal cut-off images.

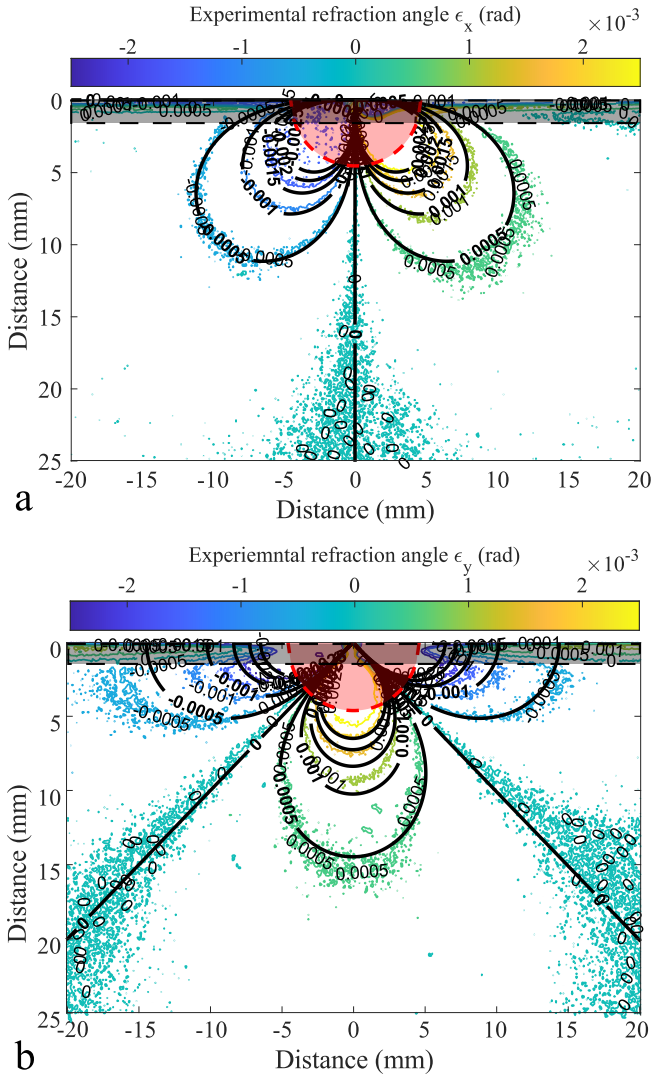

Figure 7.6: The experimental refraction angles for a larger dynamic measurement range (colored contours) for (a) refraction angles in the x direction (ϵ_x) and (b) refraction angles in the y direction (ϵ_y) compared to the analytical solution (black lines). The contours are at levels of $-2.5 : 0.5 : 2.5$ milliradians. The zone of dominant triaxiality is plotted as the red shaded area and boundary effects are highlighted in the gray shaded area.

The experimental refraction angles compared to the analytical solution for the updated experiments are presented in Figure 7.6. The applied force was 1505 N for the two experiments. By reducing the translation of the compression head, the asymmetry in the vertical cut-off data, ϵ_x, was reduced. The center line of zero refraction was also no longer at an angle. Increasing the dynamic range did reduce some of the noise in the data as the distance from the point load increased. This was due to the fact that the grayscale pixel intensities are further away from the upper and lower boundaries of the calibration data pixel values. There was also better alignment between the analytical solution and the experimental solution for the horizontal cut-off data, ϵ_y. However, refraction angles measured in the original experiments above 2.5 millirad and below -2 millirad were not detected in the updated experiments. This implies that increasing the dynamic range resulted in a reduction in the amount of measurable data close to the load.

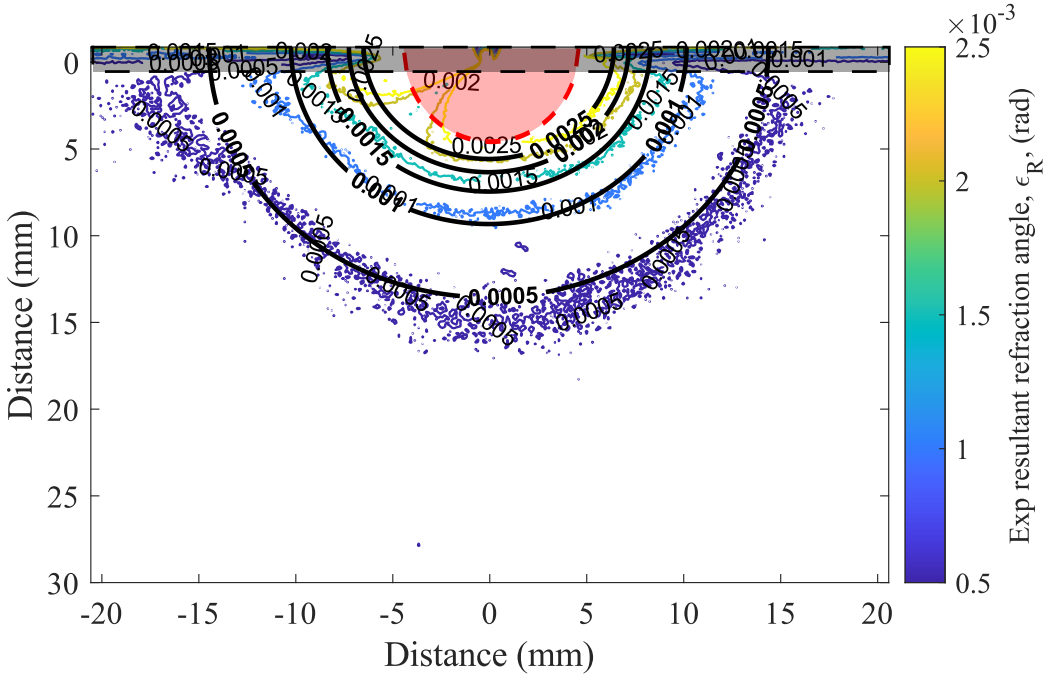

Figure 7.7: The experimental refraction angles for a larger dynamic measurement range (colored contours) compared to the analytical solution (black lines) for a Force of 1505 N. The contours are at levels of $-2.5 : 0.5 : 2.5$ milliradians. The zone of dominant triaxiality is plotted as the red shaded area and boundary effects are highlighted in the gray shaded area.

The resultant refraction angles, ϵ_R, for the experiments in Figure 7.6 were calculated and are presented in Figure 7.7. There was good agreement between the experiment and analytical solution for the updated experiments. Re-running the experiments also resulted in more symmetric resultant refraction angles from -5 mm to 5 mm as compared to the results in Figure 7.5a. The residual stresses from the manufacturing process did impact the angles below -15 mm.

7.1.4 Experimental uncertainty

The primary experimental uncertainty was attributed to the calibration of the imaging system. There are two forms of calibration that were applied, the first was the distance calibration. The distance calibration was estimated at $\pm$ 0.05 millimeters which is based on a pixel uncertainty of $\pm$ 0.5 of a pixel. The second calibration process was the polynomial fit to the calibration lens pixel intensities. With respect to the pixel to meter calibration, the value for the location of a pixel intensity inside of the calibration lens was performed in pixels and converted to meters during the last step to reduce a compounding error. The resulting uncertainty in ϵ based on the uncertainty in the distance calibration was $\pm$ 0.02 milliradians. The largest source of uncertainty was associated with the polynomial fit to the calibration lens.

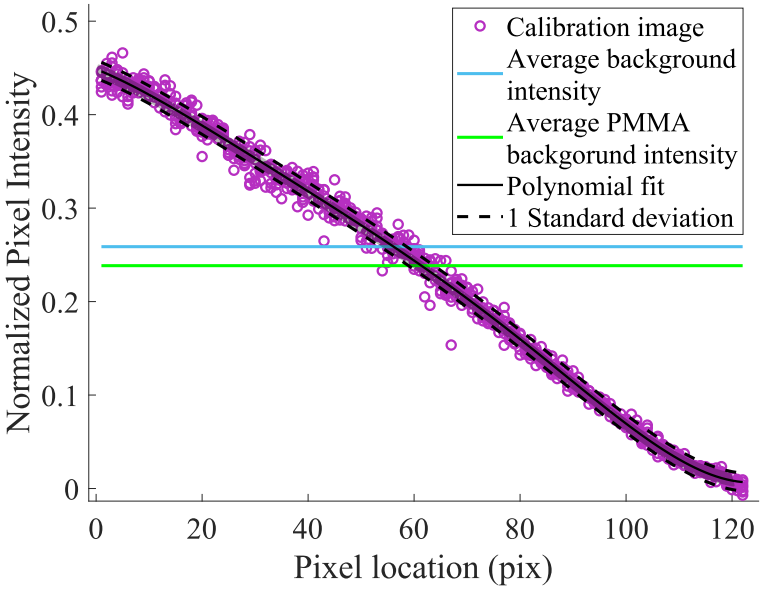

Figure 7.8: Plot of the pixel intensity values (purple points) from the calibration lens with the polynomial fit (black line) along with the polynomial fit for $\pm\sigma_{SD}$ (dashed black line).

The polynomial fit was used to determine a location in the calibration lens based on the pixel intensity in the experimental image. The average standard deviation for the fit to the calibration lens intensities was 0.0095, for pixel intensity values scaled from 0 to 1. The standard deviation in both pixel location at intensity directions relative to the polynomial fit are plotted in Figure 7.8 as the dashed black lines. In order to quantify the uncertainty based on one standard deviation, the polynomial fit was shifted by one standard deviation in both axes directions and the refraction angles in the x- and y- directions, ϵ_x and ϵ_y, were calculated.

Figure 7.9 shows the resulting refraction angles by shifting the pixel intensities by (a) $+\sigma_{SD}$ and (b) $-\sigma_{SD}$.

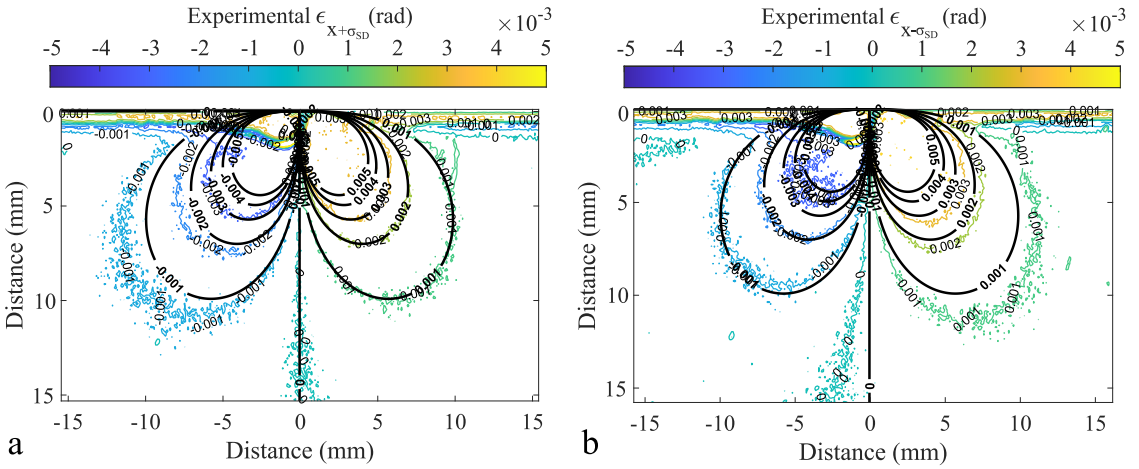

Figure 7.9: Images of the refraction angles in the x-direction,ϵ_x, for (a) $+\sigma_{SD}$, and (b) $-\sigma_{SD}$ compared to the analytical solution for a compressive force of 2365 N $\pm$5 N.

The refraction angles calculated based on one standard deviation results in the experimental uncertainty bounding the analytical solution. Subtracting the refraction angles for $+\sigma_{SD}$ and $-\sigma_{SD}$ from the actual values of epsilon yields the contours that are plotted in Figure 7.10. Subtraction of the two images results in a fairly consistent change in refraction angles, $\Delta\epsilon_{+\sigma x}$ and $\Delta\epsilon_{-\sigma x}$. The average angles for $\Delta\epsilon_{+\sigma x}$ and $\Delta\epsilon_{-\sigma x}$ were approximately -0.12 milliradians and 0.12 milliradians, respectively.

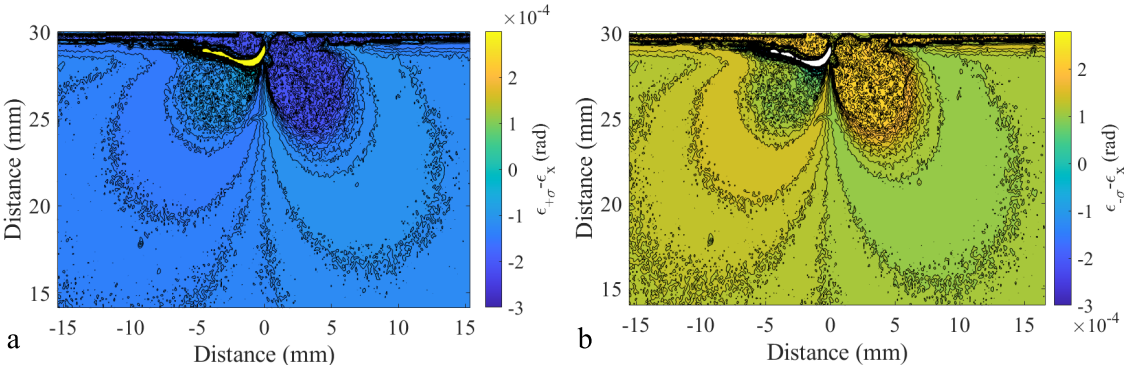

Figure 7.10: Contours of (a) $\Delta\epsilon_{+\sigma x}$ and (b) $\Delta\epsilon_{+\sigma x}$ at contour levels of -0.3:0.1:0.3 radians.

7.2 Quantitative schlieren explosive experiments

The quantitative schlieren analysis based on the stress-optic law was extended to explosive induced shock experiments. For the shock studies two synchronous high-speed cameras were used to visualise the event. The exposure for the two high-speed cameras differed by 100 ns, however, the pulse width for the laser used as the illumination source for the schlieren system was approximately 15 ns, reducing the uncertainty in the temporal alignment of the two image sets. The two cameras had different knife-edge cut-off directions such that the refraction angles in the x- and y-directions were captured. A vertical knife-edge cut-off was used to visualize the x- direction refraction angles, ϵ_x, and a horizontal knife-edge cut-off was used to visualize the y-direction refraction angles, ϵ_y. Images of the shock propagation through the PMMA are presented in Figure 7.11 for (a-d) a vertical cut-off and (e-h) a horizontal cut-off.

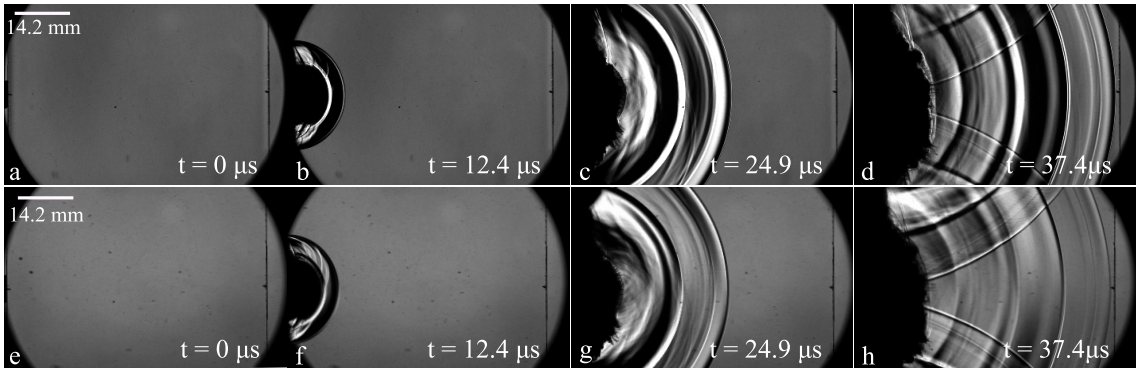

Figure 7.11: Images of the shock propagation through a PMMA sample with (a-d) a vertical knife-edge cut-off and (c-h) a horizontal knife-edge cut-off. The time of each image relative to the detonator initiation is shown.

A visual comparison of the two image sets shows that in the early time, t $\approx$ 12 μs, the shock in both image sets appear to be similar. As time progressed the differences in the schlieren images for the two knife-edge orientations became more apparent. In the last image before the shock impacts the free surface, t $\approx$ 37 μs, it was apparent that the refraction in the x-direction are stronger than the refraction in the y-direction, which was expected.

7.2.1 System calibration

The dynamic range of pixel intensity values captured during the calibration process sets upper and lower limits for the refraction angles that can be calculated. Thus, it is important that the pixel intensities visualized in the calibration lens span the dynamic range of the camera sensor, which is 0 to 1 on a normalized pixel

intensity scale. It was of particular importance for the calibration image values to span the dynamic range of the camera sensor for the explosively induced shock experiments because shock waves are high pressure pulses which induce large light refraction angles. Care must be taken when analysing the refraction angles because values which are equal to the extremes of the dynamic range could indicate refraction angles which are larger than the systems measurement capabilities. The calibration image dynamic range for the present work are presented in Figure 7.12.

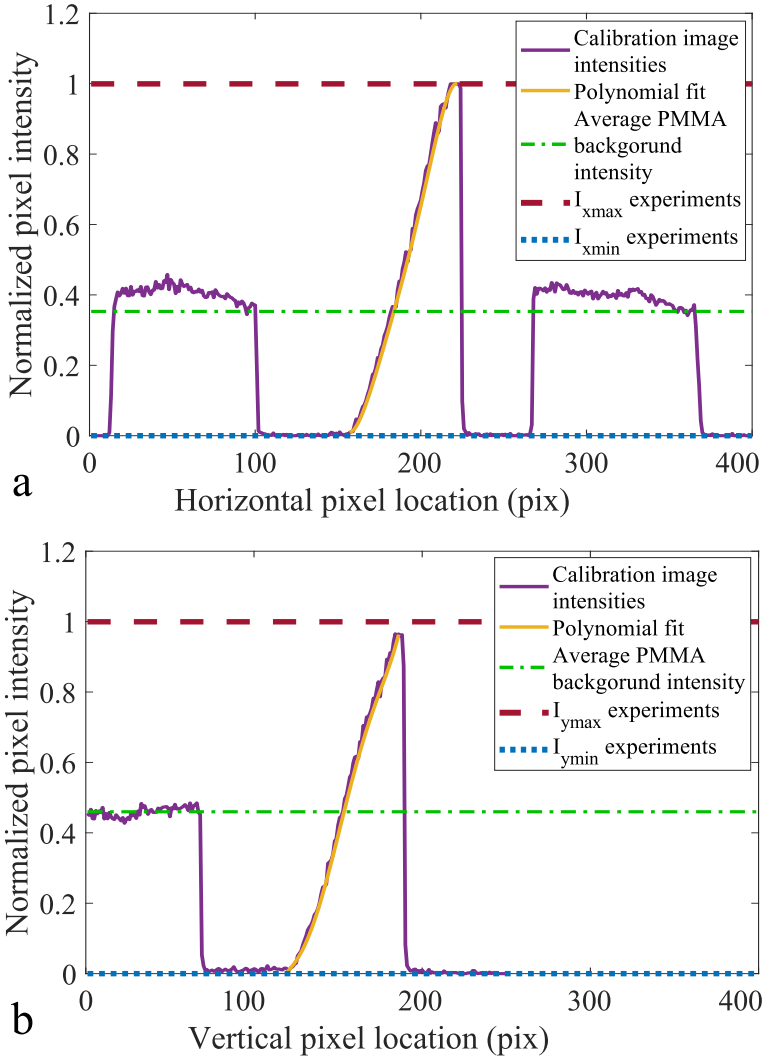

Figure 7.12: Graphs of the calibration lens pixel intensities, average background intensity of the PMMA, and the maximum and minimum pixel intensity values from the experiments for (a) the vertical knife-edge cut-off and (b) the horizontal knife-edge cut-off.

The calibration data for the vertical knife-edge cut-off, Figure 7.12a, did capture the full dynamic range of the camera sensor. However, the maximum intensity value from the calibration data for the horizontal knife-edge cut-off, Figure 7.12b, was slightly lower than 1, it was approximately 0.96. Since the refraction angles that can be calculated are restricted by the intensity values inside of the calibration lens any value outside of the pixel intensity values in the calibration lens were discarded in MATLAB.

7.2.2 Experimental results

The resulting refraction angles from the shock experiments are calculated using the calibration lens pixel intensities. The pixel intensity from the image of the experiment is correlated to a radius in the calibration lens. The refraction angles were then calculated by taking the arctangent of the location in the calibration lens divided by the focal length of the calibration lens. Representative image intensities and the resulting refraction angles for the shock experiment are plotted in Figure 7.13c.

The intensity values plotted in Figure 7.13c, I_x and I_y, correspond to the lines plotted in the schlieren images of the shock propagating through the PMMA sample with (a) a vertical and (b) horizontal knife-edge cut-off respectively. The plot of pixel intensities as a function of position compared to the refraction angles as a function of position shows that the pixel intensity and refraction angle follow the same trend. Thus, large changes in pixel intensity relative to the background correspond to large refraction angles. The background intensity of the undisturbed PMMA corresponds to the area of PMMA prior to the shock wave. In general, the displacements in the x-direction were much larger than the displacements in the y-direction, especially along center line, $y = 0$ mm, which was expected due to the wave propagation direction relative to the knife-edge direction. For the vertical cut-off, I_x, there was a single high intensity pixel at the shock front. The same anomaly appears as an equal and opposite shift in pixel intensity in the horizontal cut-off test, I_y. After the initial intensity change, indicated as "shock front" the vertical cut-off images undergo a large intensity change in the opposite direction, whereas the horizontal data returns to the average background intensity.

In areas where the shock wave was not traveling parallel to the knife-edge direction for the horizontal tests, $y \approx \pm 20$ mm, the area behind the shock front begins to show a change in intensity similar to the vertical cut-off images. However, the area of interest was along the center line which corresponded to the location of the PDV measurement.

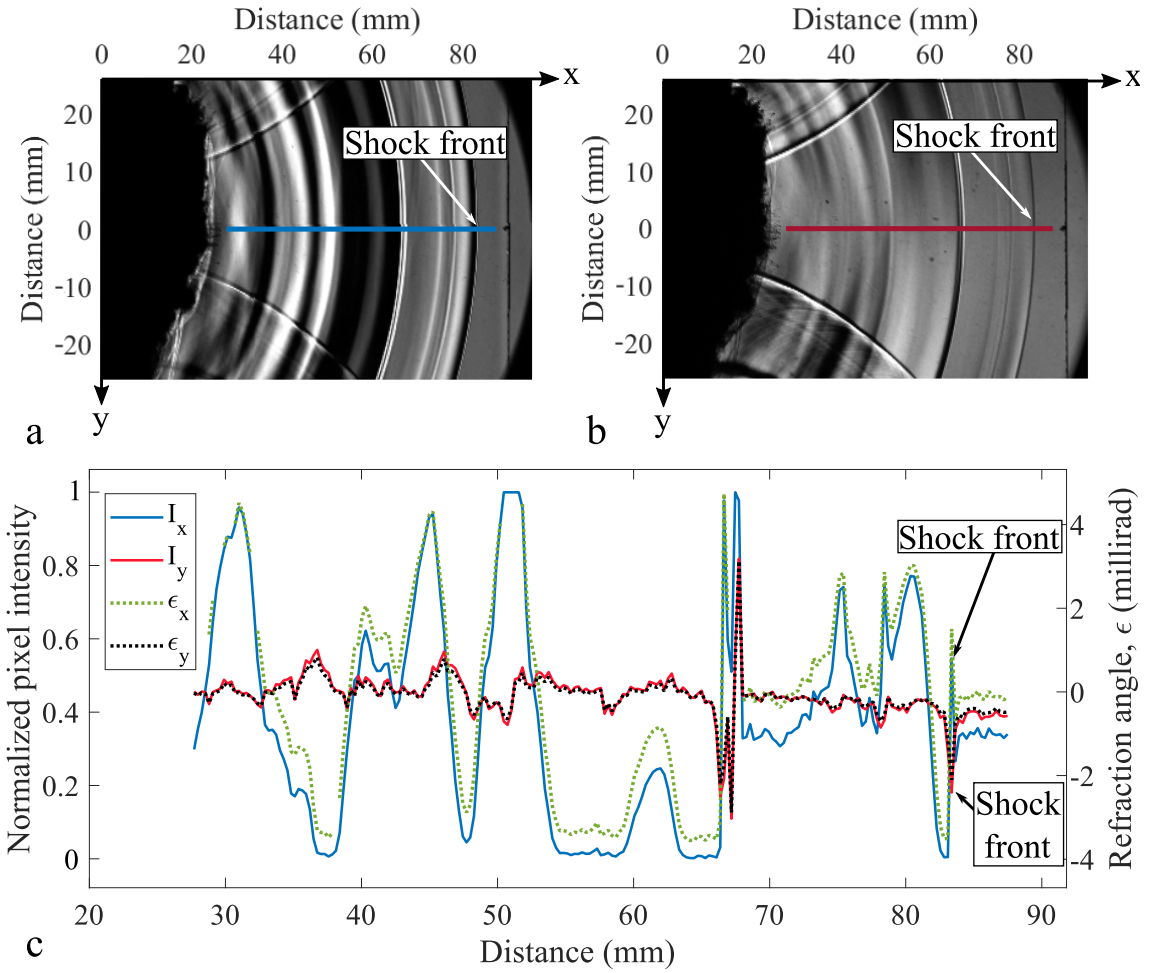

Figure 7.13: Schlieren images of the explosively driven shock propagating through the PMMA sample at approximately 35 μs after detonation with (a) a vertical knife-edge cut off and (b) a horizontal knife edge cut-off with (c) a plot of the pixel intensities, I_x and I_y, and the calculated refraction angles, ϵ_x and ϵ_y, corresponding to the lines on (a) and (b).

Since the area of interest was along the center line of the images, y=0 mm in Figure 7.13(a) and (b), digital streak images of the shock wave along the center line were created and are presented in Figure 7.14. Digital streak images were created from of the schlieren images for (a) a vertical cut off and (c) a horizontal cut off along with the respective calculated refraction angles (b) and (d). As expected, the horizontal cut-off images detect little to no refractions in the y-direction resulting in a digital streak image of mostly zero radians, whereas the refraction angles in the x-direction are much larger.

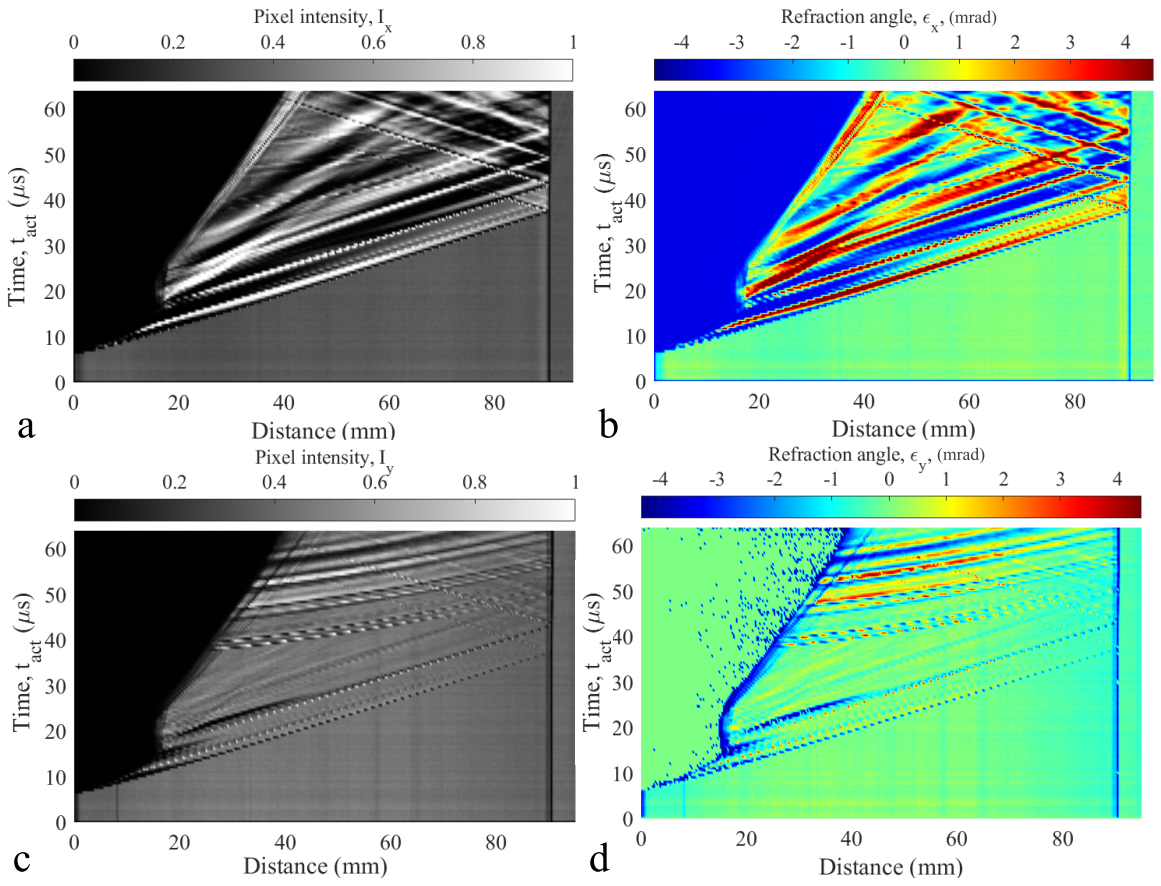

Figure 7.14: Digital streak images of the shock propagation through the PMMA for (a) the vertical knife-edge cut off and (c) the horizontal knife-edge cut-off along with (b and d) the calculated refraction angles.

The digital streak images reveal that for the deflections in the x-direction (vertical cut-off images), the singular white pixel proceeds the shock for the full event duration. This was validated through comparison of the pixel intensities at different times from the digital streak image presented in Figure 7.15. The segments of the pixel intensity values at three different times from the digital streak image were extracted and plotted in Figure 7.15b. The position of pixel intensity values extracted were aligned such that the position of the shock front was at $x_s = 0$ mm. The plot of the pixel intensities where the shock front was aligned at $x_s = 0$ mm shows that the white pixel was present in every image. The orientation of the knife-edge cut-off caused the shock wave to be detected as white pixel intensity values rather than black. However, the decay behind the shock wave was detected as black. From Figure 7.14 c and d, the shock wave was also visualized in the horizontal cut-off images. The shock was detected as the same pixel, but was detected as a dark pixel intensity.

The area of interest for the shock analysis was the centerline of the image which corresponds to the surface velocity measurements recorded using Photon Doppler Velocimetry (PDV). The PDV measurements only measure the apparent

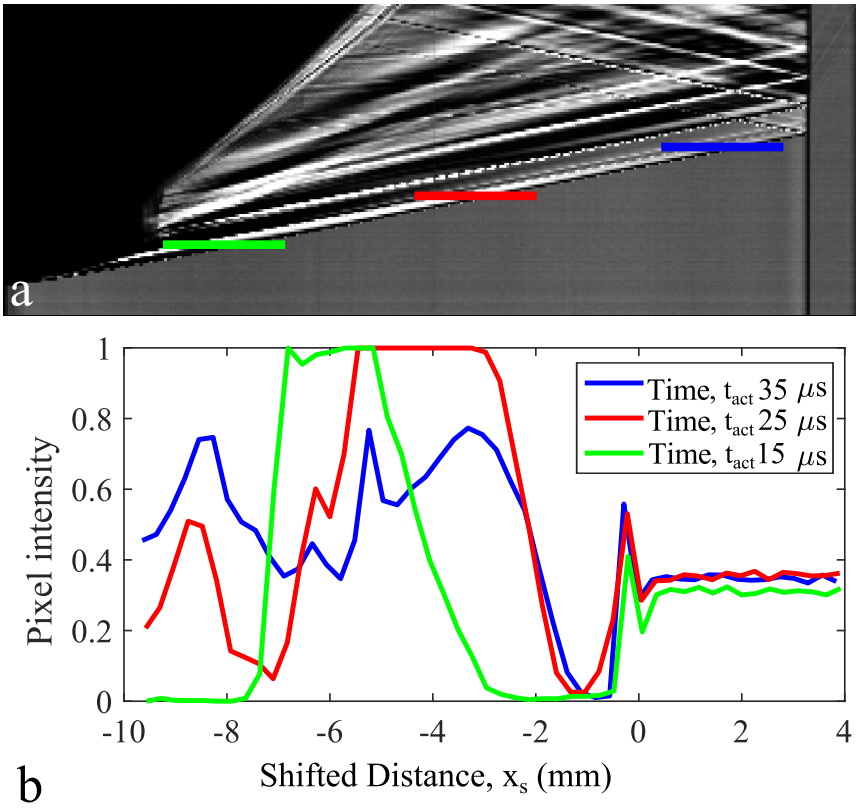

Figure 7.15: (a) The digital streak image presented in Figure 7.14a with segments indicating the rows of pixels extracted. (b) The pixel intensity values detected for the shock wave along the green (t_{act} = 15 μs), red (t_{act} = 25 μs), and blue (t_{act} = 35 μs) lines.

velocity normal to the surface therefore any velocity components parallel to the surface would not be detected. The surface velocity measurements were compared to the schlieren images with the vertical knife-edge cut-off. The surface velocity history was recorded by the PDV system and processed with SIRHEN, using the methods outlined in section 2.5. The data for the present experiments are plotted in Figure 7.16. The time has been corrected for detonator function time, t_c, such that t_c = 0 μs was the time right before the shock wave was first visualized in the PMMA.

The PDV measurements yield a surface velocity history, i.e. surface velocity as a function of time. For comparison to the schlieren images time was converted to distance using the average shock velocity. The shock velocity was calculated using the digital streak image. The boundary of the shock wave visualized in the digital streak image was extracted using the method outlined in section 2.4.3. A linear fit was applied to the extracted shock front to which the slope of the linear fit, 2.83 mm/μs, was used as the average shock velocity. Finally, the surface velocity as a function of distance was mirrored over an x-distance of approximately 88 mm

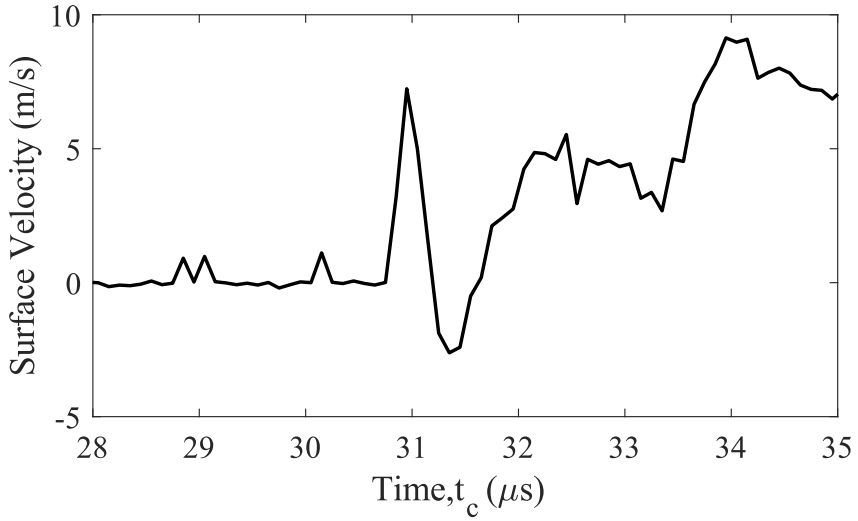

Figure 7.16: Surface velocity history for an explosively driven shock propagating through PMMA at a free surface approximately 88 mm from the explosive source for a 9.16 mm thick PMMA sample.

which was the distance the shock wave traveled in the PMMA. The resulting PDV measurement was compared to the refraction angle, ϵ_x, calculated using the pixel intensity values extracted from the digital streak image in Figure 7.16a at an approximate time of t_{act} = 35.5 μs. The two data sets were aligned by shifting the distance axis based on the location of the shock front such that x_s = 0 mm was the location of the shock front.

Comparison of the PDV data and the refraction angles calculated from the schlieren images presented in Figure 7.17 shows that the two data sets follow the same trend. However, the amplitude of the shock wave detected in the schlieren images was lower than the amplitude of the shock detected in the PDV data. The difference in the shock amplitude for the two data sets was attributed to the PDV system having a higher resolution than the schlieren images. From the PDV measurement the shock rise time, from u_{sf} = 0 m/s to u_{sf} = 7.2 m/s, occurred over a time of approximately 0.20 μs which corresponds to a distance of approximately 0.55 mm. The inter-frame time for the high-speed images was 0.5 μs and the distance between the center of two pixels from the schlieren images was approximately 0.3 mm with added uncertainty associated with the time that the camera exposure was open. There is also uncertainty in the distance it takes for the shock to rise to peak velocity determined from the PDV measurements associated with converting time to distance. Based on this analysis, the distance between pixels did not allow for the shock to be resolved in the high-speed images, but the shock was resolved in the PDV data.

The row of pixels extracted from the digital streak image corresponded to a time of t_{act} = 35.5 μs which was not the time that the shock wave impacted the free

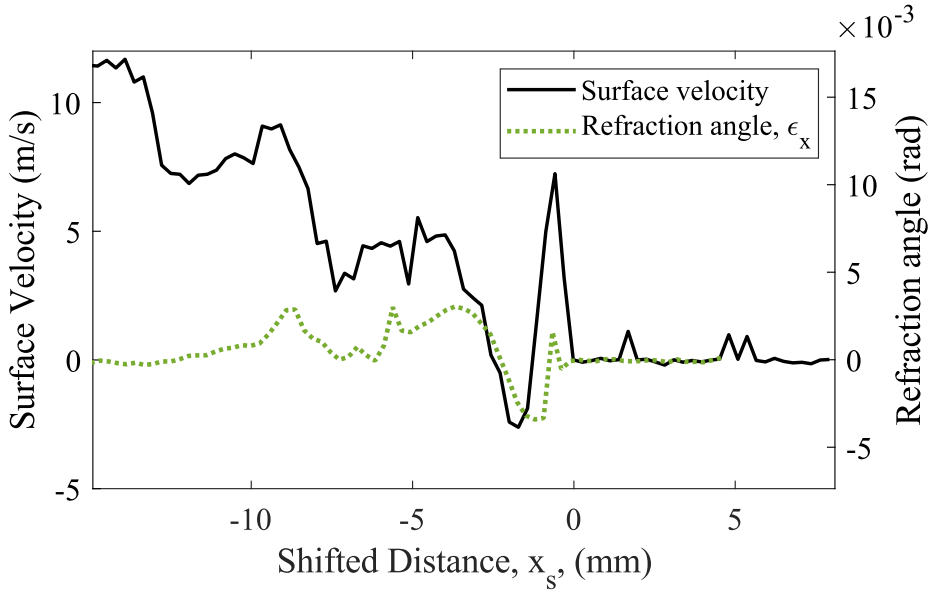

Figure 7.17: A plot comparing the surface velocity measurements recorded using the PDV system to the refraction angles in the x-direction, ϵ_x, calculated from the schlieren images.

surface. The shock wave was visualized impacting the PMMA boundary at t_{act} = 38 μs. Selecting an earlier time was done such that numerical integration could be applied from the far field with known boundary conditions, i.e. undisturbed PMMA. The reason for selecting a time of 35.5 μs was due to the fact that there was a slight stress gradient on the PMMA boundary from residual stresses from the manufacturing process. The gradient spans approximately 8 pixels from the boundary and is visualized in the digital streak images presented in Figure 7.15a and Figure 7.14. Numerical integration of the refraction angles, ϵ_x, was used to determine the stress state at the location of integration. Rearranging Equation 6.26 to solve for stress ($\sigma_{xx} + \sigma_{yy}$) yields:

$$\sigma_{xx} + \sigma_{yy} = \frac{1}{C_\sigma d_{eff}} \int \epsilon_x dx \tag{7.13}$$

Furthermore, σ_{yy} can be expressed in terms of σ_{xx} using Poisson's ratio, ν, as follows:

$$\sigma_{yy} = \frac{\nu}{1-\nu} \sigma_{xx} \tag{7.14}$$

Equation 7.13 then becomes:

$$\sigma_{xx} = \frac{1-\nu}{C_\sigma d_{eff}} \int \epsilon_x dx \tag{7.15}$$

The numerical integration of the refraction angle was done using the trapezoid method over the distance between pixels. Likewise, the stress calculated using

PDV signal, σ_{PDV}, was approximated using the surface velocity, u_{sf}, shock velocity, U_s, and bulk density, ρ_0:

$$\sigma_{PDV} = \frac{u_{sf}}{2} U_s \rho_0 \tag{7.16}$$

σ_{PDV} is the same stress calculated using the schlieren analysis. The results of the numerical integration and the calculation of σ_{PDV} using the PDV measured surface velocity are presented in Figure 7.18.

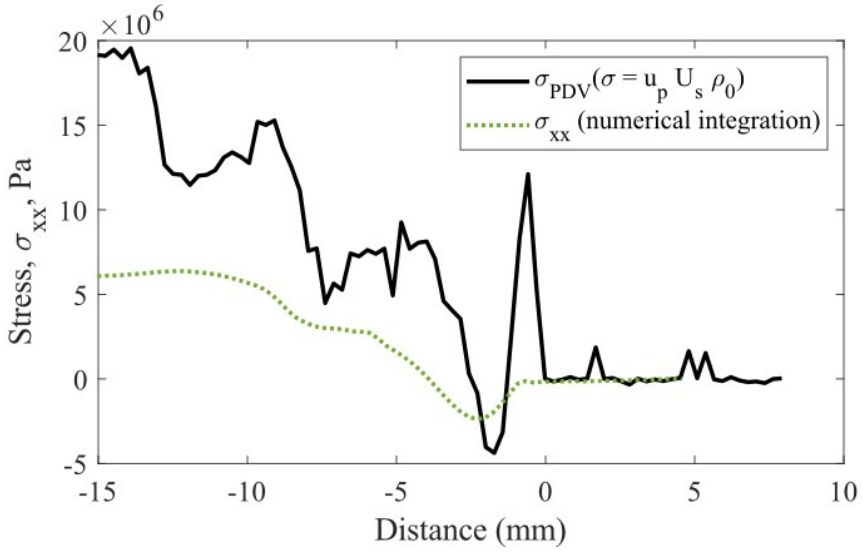

Figure 7.18: A plot of the mean stress calculated from the surface velocity measurements and the stress calculated by numerical integration of refraction angle. Note that the sign convention for the compressive stress is opposite than the normal convention.

Integration of the refraction angle caused the detected shock wave to be completely lost during the integration process because it was only observed in one pixel. However, the negative phase of the shock wave was still present after integration which was similar to the negative phase of the shock wave detected using the PDV measurement with a minimum stress of -2.4 MPa and -4.3 MPa, respectively. The stress for the shock front calculated using PDV was approximately 12 MPa. Despite the shock wave being fully lost during the integration process, the two data sets follow similar trends.

7.2.3 Experimental uncertainty

The experimental uncertainty for the quantitative schlieren shock wave experiments was dependant on the system calibration similar to the quasi-static

experiments as discussed in section 7.1.4. The largest source of error for both methods stems from the distance calibration and the polynomial fit to the calibration lens. Unlike the the quasi-static experiments, the explosive experimental results are highly dependant on the distance calibration. The distance calibration encompasses the camera resolution which was significantly lower for the high-speed cameras used to image the explosive event.

The distance calibration was used to calculate the refraction angle, ϵ_x, and was also used to convert pixels to millimeters when calculating the shock velocity. The shock velocity calculation had additional uncertain which was not of interest in this experiment but was discussed in Chapter 3. For the explosive induced shock wave quantitative schlieren analysis the distance calibration uncertainty resulted in a distance uncertainty of $\pm$ 0.14 mm. The uncertainty in the distance calibration resulted in a refraction angle uncertainty of approximately $\pm$ 0.07 milliradians. The uncertainty in the polynomial fit for the explosives experiment was determined using the same method that was used for the quasi-static experiments discussed in Section 7.1.4. The resulting refraction angle confidence interval calculated using the polynomial fit at +σ_{SD} and -σ_{SD} relative to the actual refraction angle calculated is presented in Figure 7.19b.

The average uncertainty for the refraction angles presented in 7.19b was $\pm$ 0.11 milliradians. The uncertainty was averaged over approximately 15 mm. The uncertainty increases as the magnitude of the refraction angle increased. At approximately x_n = -1 mm the refraction angle was approximately -3.4 $\pm$ 0.22 millirad which corresponds to a pixel intensity value of 0.01. Whereas in the positive refraction direction at approximately x_n=-3.5 mm the refraction angle was approximately 3.1 $\pm$ 0.09 millirad corresponding to a pixel intensity of 0.77. The calibration lens covered the full intensity range, 0 to 1, therefore, the uncertainty was larger for pixel intensities closer to the boundary of the calibration lens.

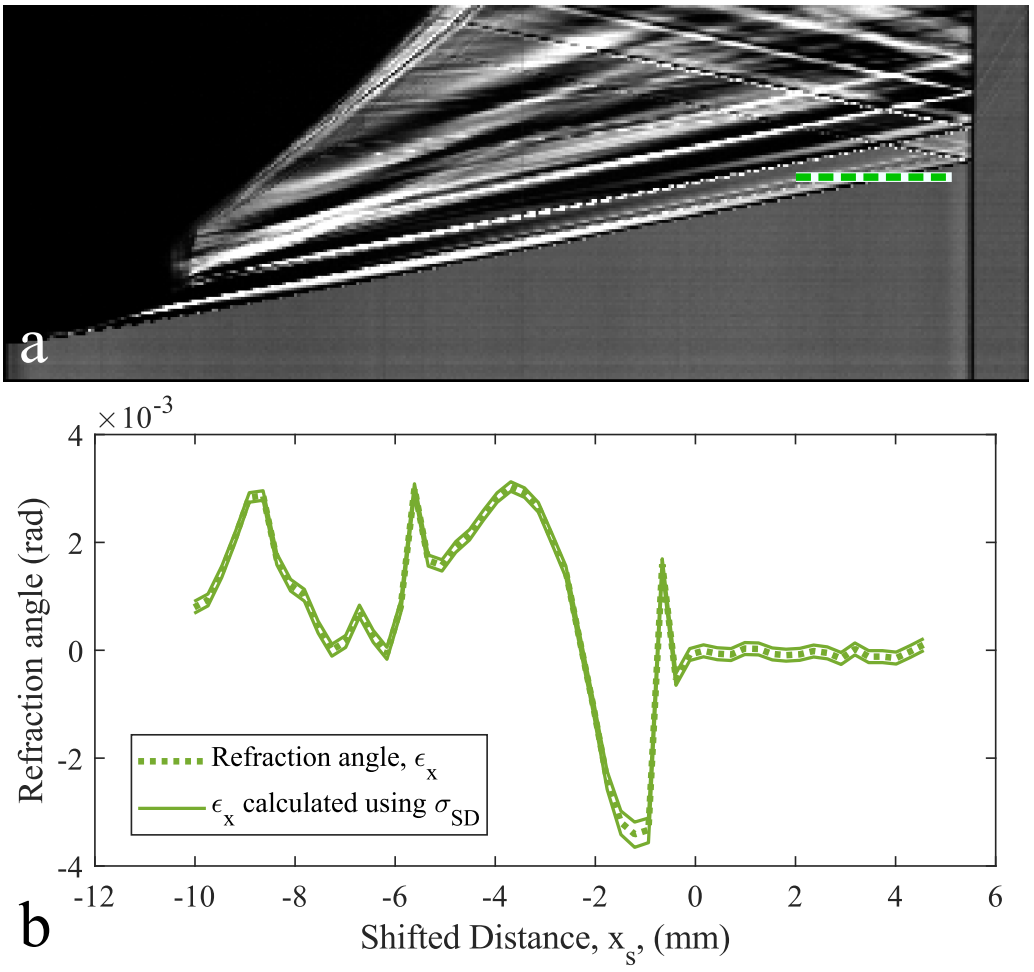

Figure 7.19: (a) A streak image indicating the segment of pixels used to calculate the refraction angles in (b). (b) A plot of the refraction angles calculated as a function of position with the refraction angles calculated using the polynomial fit at $+\sigma_{SD}$ and $-\sigma_{SD}$.

7.3 Discussion

Quantitative schlieren imaging has been extended here to optically transparent PMMA. Quasi-static and dynamic experiments were preformed. The largest source of uncertainty for this method was based on the uncertainty in the calibration data. There was the uncertainty in the polynomial fit, discussed for both experiments, and uncertainty relating to the calibration data pixel intensities covering the dynamic range of pixel intensities for the camera. The calibration lens focal length relative to the test set up, i.e schlieren lens focal length, object distance from the schlieren lens, type of cut-off and the camera lens were found to impact the calibration data.

The schlieren lens focal length relative to the calibration lens focal length impacts the gradient visualized in the calibration lens. If the calibration lens focal length is too short relative to the schlieren lens focal length then the knife-edge cut off will be visualized in the calibration lens as a binary image. If the focal length of the calibration lens is too long then there will be no gradient visualized in the calibration lens. The object distance relative to the schlieren lens is important because focusing issues can occur requiring interceding corrector optics [118]. The impact of interceding focusing optics on quantitative schlieren has not been studied but could have an impact on the final results. The camera lens zoom has an impact on the overall brightness of the image which can make it difficult to image the full dynamic range of the camera in the calibration lens.

In the quasi-static experiments the full dynamic range of pixel intensity values for the camera was not visualized in the calibration lens. The upper range of the pixel intensity values, 0.46 to 1 on a normalized scale, were not visualized. The range of pixel intensities in the calibration lens did have a slight impact on the horizontal cut-off images and did not appear to have an impact on the vertical cut-off images. The area with the brightest pixels would be in the zone of dominant triaxiality ($r/d_{eff} = 1/2$) where it is not expected for the results to agree with the analytical Flamant solution. There was slight asymmetry in the refraction angles in the x-direction, ϵ_x, which was attributed to translation of the compression head during testing. Despite the translation of the compression head the experimental results were in good agreement with the analytical solution.

The quasi-static experiments were re-run to correct for the translation of the compression head, and to increase the dynamic measurement range of pixel intensities. The updated experiments resulted in better symmetry for the vertical cut-off data, and better alignment between the experiments and analytical solution for the horizontal cut-off data. However, increasing the dynamic range did result in a reduction of measurable refraction angles close to the point load. The updated experiments resulted in symmetric resultant refraction angles which were in agreement with the analytical solution.

Due to the agreement between the experiments and the analytical solution this method was validated for small angular deflections. The Flamant solution was used further to calculate the stress gradients. Use of the analytical solution allowed for stress, $\sigma_{rr} = (\sigma_{xx} + \sigma_{yy})$, under plane stress conditions to be directly

calculated. The stress gradients calculated for the quasi-static experiments (Figure 7.5) revealed an increase in noise as the distance from the point load increased. As the distance from the point load increased, the deflection decreased thus the change in pixel intensity from the background was less significant. Since the deflections were small in the far field, the noise was attributed to sensor noise which is not easily removed. Despite the noise in the far field the experimental stress field was in good agreement with the analytical solution. If there is no analytical solution available then direct numerical integration can be used to estimate the stresses, which was the approach for the explosive experiments.

The explosive experiments were used to attempt to experimentally determine the stress state imparted by an explosively driven shock wave. For the shock experiments it was important that the measurement range of pixel intensity values in the calibration lens captured the full dynamic range of the camera. The calibration data did span the full range for the vertical cut-off images which was the data of most interest. The shock wave is thin, propagates rapidly through the sample, and imparts large deflections which can extend outside of the measurement range of the system making shock waves difficult to image in general. For the present work, the difficulties in imaging of the shock impacted the results. The shock wave was not fully imaged in the high-speed images which can be seen when comparing the amplitude of the shock from the pixel intensities compared to the PDV trace shown in Figure 7.17. The negative phase was captured in both data sets in which the amplitude for the two measurements was similar. As for the shock front, the amplitude of the shock was much greater in the PDV data compared to the schlieren images. The graph highlights the camera resolution limitations. Although the shock was not fully captured in the high-speed images, the resulting refraction angles were still integrated to see what the resulting stress gradients would be compared to the PDV results.

Integrating the refraction angle, ϵ_x, to estimate the stress gradients from the schlieren images leverages the stress optic law. The explosive induced shock is a large stress gradient which violates the assumption of small stress gradients and small refraction angles when relating the light propagation vector to the change in optical path length (Equation 6.17). However, the integration was performed and compared to the stress calculated using PDV shown in Figure 7.18. The resulting stresses, although not the same, follow a similar trend. As expected, the detected shock wave was lost during the integration process, however, the negative phase of the shock wave was detected and was similar to the PDV measurement. The numerical integration was also greatly impacted by the camera resolution. In general, the calculated stresses from the PDV measurement and the schlieren images follow the same trend.

The analysis and experiments presented here shows that the quantitative schlieren analysis can be used to estimate stresses in transparent materials.

CHAPTER 8

CONCLUSIONS AND RECOMMENDATIONS FOR FUTURE WORK

8.1 Conclusions

The explosive induced material shock response of polymethyl methacrylate (PMMA) was quantified experimentally. The high pressure shock pulse fractures the material and then the confined explosive gases drive the fractures to grow. Definition of the material response required experiments ranging over various sample sizes and time scales. The shock response of PMMA was validated against previously published works, the measured stress states were validated against analytical solutions, and the fracture response was compared to numerical simulations.

The explosive induced shock response of PMMA in the present work was studied at various distances from the explosive source. The shock response of PMMA has been extensively researched in the literature for one-dimensional planar impact experiments [4, 5, 22]. However, only limited works have studied a three-dimensional spherical wave propagation. PMMA exhibits a non-linear, rate-dependant behavior up to a pressure corresponding to plastic deformation. In the regions below the plastic deformation threshold the $U_s - u_p$ shock Hugoniot exhibits a non-linear behavior for both the one-dimensional planar impact experiments and the three-dimensional explosively driven shock waves. The non-linearity in the Hugoniot has been attributed to the magnitude of the forces along the polymer chain backbones being much larger than the forces between polymer chains [5]. In the present work, the $U_s - u_p$ Hugoniot was validated in the weak shock region through the transitional region of the Hugoniot. No data was collected in the strong shock region because the high-speed images were impacted by the illumination caused by the detonator close to the explosive source. The surface velocity measurements in the strong shock region were significantly impacted by the damage imparted by the shock wave.

The surface velocity measurements in the non-linear and weak shock regime for one-dimensional shock studies have indicated a viscoelastic material response [5, 22]. For the explosively driven shock waves here, the PDV measurements for propagation distances above 70 mm exhibited a rounding of the peak particle velocity which is representative of the viscoelastic response. However, the shape of shock pulse, i.e. the shape of the particle velocity history, for explosively driven

shocks are largely impacted by the release waves, unlike one-dimensional shocks from planar impact experiments. The explosively driven shock is an instantaneous jump followed by a subsequent decay. As such, the explosively driven shock attenuates rapidly as a function of radius.

The PDV measurements were used to define the shock attenuation as a function of the shock radius. For the regions studied the shock wave decayed exponentially through the non-linear and weak shock region. In the log-log space the relationship between particle velocity and radius was linear. In the literature it has been found that in the strong shock region the explosively driven shock decay behavior changes [1, 40], however, the strong shock region was not studied here.

In the present work the sample thickness was found to impact the shock wave decay behavior. In the case of propagation distances which were longer than the thickness of the sample, it was found that the shape of the shock pulse differed compared to sample with the thickness longer than the propagation distance. A Friedlander fit to the shock pulse shapes for the two geometries was used to describe the differences between the decay behavior. It was found that shock waves in samples with propagation distances longer than the thickness of the sample will decay more rapidly due to three-dimensional effects.

Thin PMMA samples were required for the quantitative schlieren analysis. Quantitative schlieren analysis had not been applied to solids in the literature, as such quasi-static experiments were conducted to validate the methodology prior to dynamic testing. Thin PMMA samples were required such that a plane stress assumption was valid, thin samples also were used to reduce the amount that the light rays refracted through the undisturbed PMMA. The angles at which the light rays were refracted due to a stress induced disturbance in the material were determined through calibration of the imaging system. The refraction angles were then used to estimate the stress state of the PMMA using the stress-optic law. The derived equations using the stress-optic law relates the refraction angles to the stress gradients.

The experimental arrangement for the quasi-static experiments allowed for the analytical Flamant solution to be used to estimate the stress state of the material. The analytical solution was used to validate the refraction angles measured in the experiments. The comparison between the experimental refraction angles and the analytical refraction angles for the quasi-static experiments validated the quantitative schlieren analysis. The schlieren lens calibration data was found to have a significant impact on the measurable data. For experiments with a larger dynamic pixel measurement range, the noise in the data was reduced, but, larger refraction angles were not measured. Regardless, there was good agreement between the isolines measured in the experiments compared to the analytical solution.

The quasi-static experiments and the dynamic experiments were explored with both a vertical and horizontal knife-edge cut-off. The quasi-static experiments validated the refraction angles measured for both cut-off directions, however, only the vertical knife-edge cut-off data was used to estimate the stresses for the dynamic experiments. The stresses were compared to stresses measured using

Photon Doppler Velocimetry (PDV), which was aligned with the centerline of the sample where the vertical displacements were dominant.

Due to imaging limitations in the dynamic experiments, the shock wave was not adequately resolved in the high-speed images but was captured in the PDV measurements. Only a singular pixel of the shock was visualized in the images therefore, when integrating the refraction angles to estimate stress, the shock wave was fully lost. However, the wave structures behind the shock wave were captured and followed the same trend as the stresses calculated from the PDV measurements.

Understanding the explosively driven shock state of the material informs the explosively driven fracture response. There are two mechanisms which contribute to the explosively driven fracture response of a material, the high pressure short duration shock pulse and the lower pressure long duration confined explosive gases. The present work explored how the two mechanisms work on a large scale to achieve the final fracture lengths. Furthermore, the impact that in-situ stresses have on the shock response, final fracture patterns, and final fracture lengths was defined.

The experiments in conjunction with numerical simulations validated that the shock pulse fractured the PMMA within the first 20 μs of propagation. This time corresponds to a fracture length of approximately 15 mm in the experiments. The application of external stress caused the fractures to change direction to align with the direction of the maximum principal stress which occurred over an approximated length of 10 mm to 35 mm bounding the approximate length that the simulation estimated the shock drives the fracture. The shock radii as a function of time and the PDV data was similar for all of the experiments, thus, the shock response of the material was not impacted by the application of external stress. As such, the variations in the fracture pattern occurred during the gas driven fracture process. The fracture direction change was attributed to the fracture response transitioning from shock driven to gas driven fracture. As such, increasing the applied external stress increased the percent of the fracture driven by the shock pulse. However, the main fracture driving mechanism was attributed to confined explosive gases for all of the experiments.

8.2 Recommendations for future work

Quantification of the explosively driven shock response of PMMA was defined from the weak shock region through the transitional region of the shock Hugoniot. These measurements correspond to propagation distances of 5.94 mm to 133.3 mm with an RP-80 EBW detonator as the explosive source. However, measurements in the strong shock regime were not made. It has been found that in the strong shock region close to the explosive load, PMMA yields an initial rapid decay in peak shock pressure [1, 40]. Thus, experiments defining the explosively driven shock Hugoniot in the strong shock regime should be explored. The particle velocities could be used to define the decay behavior as a function of radius in the strong shock regime to define an equation for the shock pressure decay in PMMA. The same experiments could also be run at propagation distances up to 25 mm where the interface velocity is measured rather than the surface velocity. This would correct for the issues associated with the retro reflective tape detaching from the surface of the PMMA and the shock driven fracture.

Further definition of the shock response of PMMA could be achieved by resolving the shock wave in the schlieren images. Quantitative schlieren analysis could be applied to high resolution images of the explosively driven shock wave, or images of a shock imparted by a flyer plate. Increasing the number of pixels that the shock is visualized over would reduce the probability of the shock wave being lost during the integration process. Starting with flyer plate experiments would allow for the duration of the shock pulse to be larger increasing the probability of resolving the shock wave. Through resolving the shock wave over a range of pixels, the calculate refraction angles could be integrated and compared to PDV measurements.

The quantitative schlieren analysis can also be extended to fracture studies. Stresses around crack tips have been visualized in the explosive PMMA testing presented in Figure 8.1a and in a spark gap test presented in Figure 8.1b-d. The PMMA in Figure 8.1b was pre-fractured where the stresses around the pre-fractures were visualized. Quantitative schlieren could be extended to the determination of static and dynamic stress intensity factors.

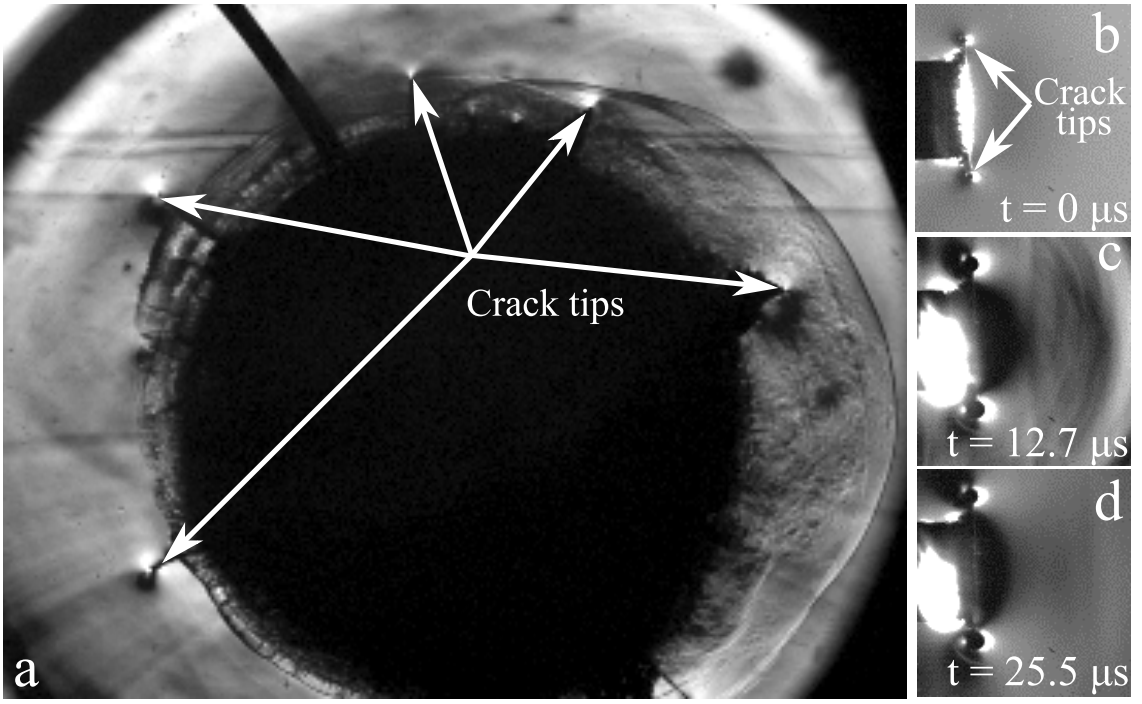

Figure 8.1: (a) A high speed schlieren image of explosively driven fractures in a PMMA disk where the stresses around the crack tip were visualized and schlieren images of (b) pre-fractured PMMA and (c and d) the crack tip growth imparted by a spark gap.

REFERENCES

[1] Michael J. Murphy, Mark A. Lieber, and Matthew M. Biss. Novel measurements of shock pressure decay in PMMA using detonator loading. In *AIP Conference Proceedings*, 2018.

[2] W.J. Carter and S.P. Marsh. Hugoniot equation of state of polymers. Technical report, 1995.

[3] Stanley P Marsh. Lasl shock hugoniot data, 1980.

[4] L. M. Barker and R. E. Hollenbach. Shock-wave studies of PMMA, fused silica, and sapphire. *Journal of Applied Physics*, 41(10):4208–4226, 1970.

[5] Jennifer L. Jordan, Daniel Casem, and Michael Zellner. Shock response of polymethylmethacrylate. *Journal of Dynamic Behavior of Materials*, 2(3):372–378, 2016.

[6] H. P. Rossmanith, R. E. Knasmillner, A. Daehnke, and L. Mishnaevsky. Wave propagation, damage evolution, and dynamic fracture extension. Part II. blasting. *Materials Science*, 32(4):403–410, 1996.

[7] H. K. Kutter. On the fracture process in blasting. *International Journal of Rock Mechanics*, 8(3), 1971.

[8] Marc A. Meyers. *Dynamic Behavior of Materials*. John Wiley and Sons, 1994.

[9] Albert S. Kobayashi. *Handbook on experimental mechanics*. VCH ; SEM, New York, N.Y., Bethel, CT, USA, 2nd rev. ed edition, 1993.

[10] Paul Cooper. *Explosives Engineering*. John Wiley and Sons, 1996.

[11] K. W. Schuler and J. W. Nunziato. The unloading and reloading behavior of shock-compressed polymethyl methacrylate. *Journal of Applied Physics*, 47(7):2995–2998, 1976.

[12] E. B. Zaretsky and G. I. Kanel. Response of poly(methyl methacrylate) to shock-wave loading at elevated temperatures. *Journal of Applied Physics*, 126(8):085902, 2019.

[13] Gerald I. Kerley. Calculation of release adiabats and shock impedance matching. 2013.

[14] George E. Duvall. Concepts of shock wave propagation. *Bulletin of the Seismological Society of America*, 52(4):869–893, 1962.

[15] Clive R. Siviour and Jennifer L. Jordan. High strain rate mechanics of polymers: A review. *Journal of Dynamic Behavior of Materials*, 2(1):15–32, 2016.

[16] L. M. Barker and R. E. Hollenbach. Interferometer technique for measuring the dynamic mechanical properties of materials. *Review of Scientific Instruments*, 36(11):1617–1620, 1965.

[17] K.W. Schuler. Propagation of steady shock waves in polymethyl methacrylate. *Journal of the Mechanics and Physics of Solids*, 18(4):277–293, 1970.

[18] Jace W. Nunziato and Karl W. Schuler. Evolution of steady shock waves in polymethyl methacrylate. *Journal of Applied Physics*, 44(10):4774–4775, 1973.

[19] J. R. Asay and L. M. Barker. Interferometric measurement of shock-induced internal particle velocity and spatial variations of particle velocity. *Journal of Applied Physics*, 45(6):2540–2546, 1974.

[20] G Kister, D C Wood, G J Appleby-Thomas, J A Leighs, M Goff, N R Barnes, and P J Hazell. An overview on the effect of manufacturing on the shock response of polymers. *Journal of Physics: Conference Series*, 500(19):192022, 2014.

[21] F.R. Svingala, M.J. Hargather, and G.S. Settles. Optical techniques for measuring the shock Hugoniot using ballistic projectile and high-explosive shock initiation. *International Journal of Impact Engineering*, 50:76–82, 2012.

[22] J. C. F. Millett and N. K. Bourne. The deviatoric response of polymethylmethacrylate to one-dimensional shock loading. *Journal of Applied Physics*, 88(12):7037–7040, 2000.

[23] E. K. Walsh and K. W. Schuler. Acceleration wave propagation in a nonlinear viscoelastic solid. *Journal of Applied Mechanics*, 40(3):705–710, 1973.

[24] David James Chapman, Daniel E. Eakins, David Martin Williamson, and William Proud. Index of refraction measurements and window corrections for PMMA under shock compression. In *AIP Conference Proceedings*. AIP, 2012.

[25] Mithun Bhowmick, Will P. Basset, Sergey Matveev, Lawrence Salvati, and Dana D. Dlott. Optical windows as materials for high-speed shock wave detectors. *AIP Advances*, 8(12):125123, 2018.

[26] Yasemin Şengül. Nonlinear viscoelasticity of strain rate type: an overview. *Proceedings of the Royal Society A: Mathematical, Physical and Engineering Sciences*, 477(2245), 2021.

[27] David Lacina, Christopher Neel, and Dana Dattelbaum. Shock response of poly[methyl methacrylate] (PMMA) measured with embedded electromagnetic gauges. *Journal of Applied Physics*, 123(18):185901, 2018.

[28] Y. M. Gupta, D. D. Keough, D. Henley, and D. F. Walter. Measurement of lateral compressive stresses under shock loading. *Applied Physics Letters*, 37(4):395–397, 1980.

[29] Satish C. Gupta and Y. M. Gupta. Piezoresistance response of longitudinally and laterally oriented ytterbium foils subjected to impact and quasi-static loading. *Journal of Applied Physics*, 57(7):2464–2473, 1985.

[30] James P Billingsley. The decay limit of the hugoniot elastic limit. *International Journal of Impact Engineering*, 21(4):267–281, 1998.

[31] J. R. Asay, G. R. Fowles, G. E. Durall, M. H. Miles, and R. F. Tinder. Effects of point defects on elastic precursor decay in lif. *Journal of Applied Physics*, 43(5):2132–2145, 1972.

[32] James R. Asay, Lalit C. Chhabildas, R. Jeffery Lawrence, and Mary Ann Sweeney. *Impactful Times*. Springer-Verlag GmbH, 2017.

[33] C. F. McMillan, D. R. Goosman, N. L. Parker, L. L. Steinmetz, H. H. Chau, T. Huen, R. K. Whipkey, and S. J. Perry. Velocimetry of fast surfaces using Fabry–Perot interferometry. *Review of Scientific Instruments*, 59(1):1–21, 1988.

[34] D. D. Bloomquist and S. A. Sheffield. Optically recording velocity interferometer system (orvis) for subnanosecond particle velocity measurements in shock waves. In Lincoln L. Endelman, editor, *15th Intl Congress on High Speed Photography and Photonics*, volume 348, pages 523 – 528. SPIE, 1983.

[35] O. T. Strand, D. R. Goosman, C. Martinez, T. L. Whitworth, and W. W. Kuhlow. Compact system for high-speed velocimetry using heterodyne techniques. *Review of Scientific Instruments*, 77(8):083108, 2006.

[36] B. J. Jensen, D. B. Holtkamp, P. A. Rigg, and D. H. Dolan. Accuracy limits and window corrections for photon Doppler velocimetry. *Journal of Applied Physics*, 101(1):013523, 2007.

[37] D. H. Dolan. Extreme measurements with photonic doppler velocimetry (PDV). *Review of Scientific Instruments*, 91(5):051501, 2020.

[38] E A Moro. New developments in photon doppler velocimetry. *Journal of Physics: Conference Series*, 500(14):142023, 2014.

[39] Matthew Ellsworth Briggs, Larry Hill, Larry Hull, and Michael Shimas. Applications and principles of photon-doppler velocimetry for explosive testing. In *Proceedings - 14th International Detonation Symposium*, pages 414–424, 2010.

[40] Michael Murphy and Steven A. Clarke. Simultaneous photonic doppler velocimetry and ultra-high speed imaging techniques to characterize the pressure output of detonators. In *AIP Conference Proceedings*. AIP, 2012.

[41] Matthew Biss, Michael Murphy, and Mark Lieber. Qualification of a multi-diagnostic detonator-output characterization procedure utilizing PMMA witness blocks. In *AIP Conference Proceedings*. AIP, 2018.

[42] Dennis Hayes. Unsteady compression waves in interferometer windows. *Journal of Applied Physics*, 89(11):6484–6486, 2001.

[43] S. Raha and P.B. Bowden. Birefringence of plastically deformed poly(methyl methacrylate). *Polymer*, 13(4):174–183, 1972.

[44] J.E. Field, S.M. Walley, W.G. Proud, H.T. Goldrein, and C.R. Siviour. Review of experimental techniques for high rate deformation and shock studies. *International Journal of Impact Engineering*, 30(7):725–775, 2004.

[45] G. S. Settles. *Schlieren and Shadowgraph Techniques*. Springer Berlin Heidelberg, 2006.

[46] Michael J. Murphy. Ultra-high-speed imaging for explosive-driven shocks in transparent media. Technical report, 2012.

[47] Jesse D. Tobin and Michael J. Hargather. Quantitative schlieren measurement of explosively-driven shock wave density, temperature, and pressure profiles. *Propellants, Explosives, Pyrotechnics*, 41(6):1050–1059, 2016.

[48] Michael J. Hargather and Gary S. Settles. A comparison of three quantitative schlieren techniques. *Optics and Lasers in Engineering*, 50(1):8–17, 2012.

[49] N. K. Bourne and Z. Rosenberg. Manganin gauge and VISAR histories in shock-stressed polymethylmethacrylate. *Proceedings of the Royal Society of London. Series A: Mathematical, Physical and Engineering Sciences*, 455(1984):1259–1266, 1999.

[50] R. Feng and Y. M. Gupta. Determination of lateral stresses in shocked solids: Simplified analysis of piezoresistance gauge data. *Journal of Applied Physics*, 83(2):747–753, 1998.

[51] P. F. Chartagnac. Determination of mean and deviatoric stresses in shock loaded solids. *Journal of Applied Physics*, 53(2):948–953, 1982.

[52] Joshua D. Coe, Meghan Lentz, Kirill A. Velizhanin, J. Tinka Gammel, John Kaushagen, Keith Jones, and Kyle R. Cochrane. The equation of state and shock-driven decomposition of polymethylmethacrylate (pmma). *Journal of Applied Physics*, 131(12), 2022.

[53] T.J. Holmquist, J. Bradley, A. Dwivedi, and D. Casem. The response of polymethyl methacrylate (PMMA) subjected to large strains, high strain rates, high pressures, a range in temperatures, and variations in the intermediate principal stress. *The European Physical Journal Special Topics*, 225(2):343–354, 2016.

[54] S. Matsumoto, Y. Nakamura, and S. Itoh. Visualization and numerical analysis of stress waves in blasting process. *Journal of Visualization*, 6(3):235–244, 2003.

[55] T V Popova, A E Mayer, and K V Khishchenko. Numerical investigations of shock wave propagation in polymethylmethacrylate. *Journal of Physics: Conference Series*, 653:012045, 2015.

[56] T V Popova, A E Mayer, and K V Khishchenko. Two-dimensional modeling of high-velocity impingement of polymethylmethacrylate plates. *Journal of Physics: Conference Series*, 774:012066, 2016.

[57] T. V. Popova, A. E. Mayer, and K. V. Khishchenko. Evolution of shock compression pulses in polymethylmethacrylate and aluminum. *Journal of Applied Physics*, 123(23):235902, 2018.

[58] L. V. Al'tshuler. Use of shock waves in high-pressure physics. volume 8. Soviet Physics Uspekhi, 1965.

[59] S. A. Bordzilovskii, S. M. Karakhanov, L. A. Merzhievskii, and M. S. Voronin. Temperature measurements for shocked polymethylmethacrylate, epoxy resin, and polytetrafluoroethylene and their equations of state. *Journal of Applied Physics*, 120(13), 2016.

[60] Z. Rosenberg and Y. Partom. Direct measurement of temperature in shock-loaded polymethylmethacrylate with very thin copper thermistors. *Journal of Applied Physics*, 56(7):1921–1926, 1984.

[61] Ralph Menikoff. Constitutive model for polymethyl methacrylate at high pressure. *Journal of Applied Physics*, 96(12):7696–7704, 2004.

[62] Ted L. Anderson. *Fracture Mechanics*. Taylor and Francis Inc, 2017.

[63] Alan Arnold Griffith. The phenomena of rupture and flow in solids. *Philosophical Transactions of the Royal Society of London. Series A, Containing Papers of a Mathematical or Physical Character*, 221(582-593):163–198, 1921.

[64] A. S. Paine and C. P. Please. An improved model of fracture propagation by gas during rock blasting - some analytical results. *International Journal of Rock Mechanics and Mining Sciences*, 32(4):A156, 1995.

[65] R. H. Nilson. Gas-driven fracture propagation. *Journal of Applied Mechanics*, 48(4):757–762, 1981.

[66] Peng Qiu, Zhongwen Yue, and Renshu Yang. Experimental study on mode-i and mixed-mode crack propagation under tangentially incident p waves, s waves and reflected waves in blasts. *Engineering Fracture Mechanics*, 247:107664, 2021.

[67] Balamurugan M. Sundaram and Hareesh V. Tippur. Dynamic mixed-mode fracture behaviors of PMMA and polycarbonate. *Engineering Fracture Mechanics*, 176:186–212, 2017.

[68] Y. I. Voitenko. Fracture of solids by weak blasts. *Combustion, Explosion, and Shock Waves*, 31(4):492–499, 1995.

[69] S. M. Torres, O. Y. Vorobiev, R. E. Robey, and M. J. Hargather. A study of explosive-induced fracture in polymethyl methacrylate (PMMA). *Journal of Applied Physics*, 134(7), 2023.

[70] Hoyoung Jeong, Byungkyu Jeon, Seungbum Choi, and Seokwon Jeon. Fracturing behavior around a blasthole in a brittle material under blasting loading. *International Journal of Impact Engineering*, 140:103562, 2020.

[71] Zhongwen Yue, Peng Qiu, Renshu Yang, Shichun Zhang, Kai Yuan, and Zhanfei Li. Stress analysis of the interaction of a running crack and blasting waves by caustics method. *Engineering Fracture Mechanics*, 184:339–351, 2017.

[72] N.A. Kazarinov, V.A. Bratov, N.F. Morozov, Y.V. Petrov, V.V. Balandin, M.A. Iqbal, and N.K. Gupta. Experimental and numerical analysis of PMMA impact fracture. *International Journal of Impact Engineering*, 143:103597, 2020.

[73] K. Arakawa and T. Mada. Unsteady dynamic crack propagation in a brittle polymer. *Experimental Mechanics*, 47(5):609–615, 2007.

[74] H. Z. Xing, Q. B. Zhang, C. H. Braithwaite, B. Pan, and J. Zhao. High-speed photography and digital optical measurement techniques for geomaterials: Fundamentals and applications. *Rock Mechanics and Rock Engineering*, 50(6):1611–1659, 2017.

[75] X. F YAO and W. XU. Recent application of caustics on experimental dynamic fracture studies. *Fatigue and Fracture of Engineering Materials and Structures*, 34(6):448–459, 2011.

[76] Peng Qiu, Zhongwen Yue, and Renshu Yang. Mode i stress intensity factors measurements in PMMA by caustics method: A comparison between low and high loading rate conditions. *Polymer Testing*, 76:273–285, 2019.

[77] Peng Xu, Renshu Yang, Yang Guo, Cheng Chen, Yang Yang, and Jinjing Zuo. Investigation of the interaction mechanism of two dynamic propagating cracks under blast loading. *Engineering Fracture Mechanics*, 259:108112, 2022.

[78] Chuanjin Pu, Xin Yang, Han Zhao, Zhenlin Chen, and Dingjun Xiao. Numerical investigation on crack propagation and coalescence induced by dual-borehole blasting. *International Journal of Impact Engineering*, 157:103983, 2021.

[79] Chuanjin Pu, Xin Yang, Han Zhao, Zhenlin Chen, Dingjun Xiao, Changlin Zhou, and Bing Xue. Numerical study on crack propagation under explosive loads. *Acta Mechanica Sinica*, 38(1), 2022.

[80] Chenglong He, Jun Yang, and Qi Yu. Laboratory study on the dynamic response of rock under blast loading with active confining pressure. *International Journal of Rock Mechanics and Mining Sciences*, 102:101–108, 2018.

[81] Linzhi Peng, Zhongwen Yue, Shengnan Xu, Heng You, and Zenghui Liu. Experimental study on the influence of biaxial confining pressure on dynamic cracks and its interaction with blasting stress wave. *Theoretical and Applied Fracture Mechanics*, 123:103719, 2023.

[82] Michał Kucewicz, Paweł Baranowski, Łukasz Mazurkiewicz, and Jerzy Małachowski. Comparison of selected blasting constitutive models for reproducing the dynamic fragmentation of rock. *International Journal of Impact Engineering*, 173:104484, 2023.

[83] E.V. Dontsov and A.P. Peirce. Modeling planar hydraulic fractures driven by laminar-to-turbulent fluid flow. *International Journal of Solids and Structures*, 128:73–84, 2017.

[84] A.S. Paine and C.P. Please. An improved model of fracture propagation by gas during rock blasting—some analytical results. *International Journal of Rock Mechanics and Mining Sciences andamp; Geomechanics Abstracts*, 31(6):699–706, 1994.

[85] A.R. Hajibagherpour, H. Mansouri, and M. Bahaaddini. Numerical modeling of the fractured zones around a blasthole. *Computers and Geotechnics*, 123:103535, 2020.

[86] Xiao Liu, Peng Yan, Wenbo Lu, Jin Zhu, Xiangyu Zhang, Ang Lu, Ming Chen, and Gaohui Wang. Investigation of dynamic crack formation mechanism based on a new crack dynamic driving model. *Computers and Geotechnics*, 159:105471, 2023.

[87] Xiaoli Liu, Sijing Wang, Shanyong Wang, and Enzhi Wang. Fluid-driven fractures in granular materials. *Bulletin of Engineering Geology and the Environment*, 74(2):621–636, 2015.

[88] N. N. Smirnov and V. P. Tagirova. Problem of propagation of a gas fracture in a porous medium. *Fluid Dynamics*, 43(3):402–417, 2008.

[89] Jiehao Wang, Derek Elsworth, Yunxing Cao, and Shimin Liu. Reach and geometry of dynamic gas-driven fractures. *International Journal of Rock Mechanics and Mining Sciences*, 129:104287, 2020.

[90] Shan Guo, Quan Zhang, Manchao He, Seokwon Jeon, Yubing Gao, and Chao Wang. Crack propagation behavior and damage extent of rock mass under instantaneous expansion in borehole. *Rock Mechanics and Rock Engineering*, 57(2):869–888, 2023.

[91] Emmanuel E. Gdoutos. The method of caustics. In *Solid Mechanics and Its Applications*, pages 129–159. Springer International Publishing, 2021.

[92] W. Xu, X.F. Yao, H.Y. Yeh, and G.C. Jin. Fracture investigation of PMMA specimen using coherent gradient sensing (CGS) technology. *Polymer Testing*, 24(7):900–908, 2005.

[93] H. V. Tippur. Coherent gradient sensing (CGS) method for fracture mechanics: a review. *Fatigue andamp Fracture of Engineering Materials andamp Structures*, 33(12):832–858, 2010.

[94] Chandru Periasamy and Hareesh V. Tippur. Full-field digital gradient sensing method for evaluating stress gradients in transparent solids. *Applied Optics*, 51(12):2088, 2012.

[95] C. Periasamy and H. V. Tippur. Measurement of orthogonal stress gradients due to impact load on a transparent sheet using digital gradient sensing method. *Experimental Mechanics*, 53(1):97–111, 2012.

[96] A Muñoz-Ibáñez, M Herbón-Penabad, and J Delgado-Martín. Photoelastic stress analysis of mode i fracture toughness tests using pmma samples. *IOP Conference Series: Earth and Environmental Science*, 833(1):012031, 2021.

[97] Yongyut Manjit, Apichart Limpichaipanit, and Athipong Ngamjarurojana. Mechanical analysis of square shaped pmma using reflection photoelasticity. *Optik*, 240:166943, 2021.

[98] Emmanuel E. Gdoutos. The optical method of caustics. *Optics and Lasers in Engineering*, 79:68–77, 2016.

[99] Hareesh V. Tippur, Sridhar Krishnaswamy, and Ares J. Rosakis. A coherent gradient sensor for crack tip deformation measurements: analysis and experimental results. *International Journal of Fracture*, 48(3):193–204, 1991.

[100] Hareesh V. Tippur, Sridhar Krishnaswamy, and Ares J. Rosakis. Optical mapping of crack tip deformations using the methods of transmission and reflection coherent gradient sensing: a study of crack tip k-dominance. *International Journal of Fracture*, 52(2):91–117, 1991.

[101] A.J. Rosakis. Application of coherent gradient sensing (cgs) to the investigation of dynamic fracture problems. *Optics and Lasers in Engineering*, 19(1–3):3–41, 1993.

[102] Gary S Settles and Michael J Hargather. A review of recent developments in schlieren and shadowgraph techniques. *Measurement Science and Technology*, 28(4):042001, 2017.

[103] Markus Raffel. Background-oriented schlieren (bos) techniques. *Experiments in Fluids*, 56(3), 2015.

[104] Gary S. Settles and Alex Liberzon. Schlieren and BOS velocimetry of a round turbulent helium jet in air. *Optics and Lasers in Engineering*, 156:107104, 2022.

[105] D. H. Dolan. Accuracy and precision in photonic doppler velocimetry. *Review of Scientific Instruments*, 81(5):053905, 2010.

[106] Daniel H Dolan and Tommy Ao. SIRHEN : a data reduction program for photonic doppler velocimetry measurements. Technical Report SAND2010-3628, 2010.

[107] John R Taylor. *An introduction to error analysis : the study of uncertainties in physical measurements*. University Science Books, Sausalito, California, second edition. edition, 1997.

[108] Gilbert Ford Kinney and Kenneth Judson Graham. *Explosive Shocks in Air*. Springer Berlin Heidelberg, 1985.

[109] I Lomov, R Pember, J Greenough, and B Liu. Patch-based adaptive mesh refinement for multimaterial hydrodynamics. *Joint Russian-American Five-Laboratory Conference on Computational Mathematics/Physics, Vienna, Austria, Jun 19 - Jun 23, 2005*, 2005.

[110] O Yu Vorobiev, BT Liu, IN Lomov, and TH Antoun. Simulation of penetration into porous geologic media. *International journal of impact engineering*, 34(4):721–731, 2007.

[111] Oleg Y Vorobiev and Joseph P Morris. Modeling dynamic fracture in granite under in situ conditions at high temperatures and pressures. *International Journal of Rock Mechanics and Mining Sciences*, 113:241–254, 2019.

[112] L. Smilowitz, D. Remelius, N. Suvorova, P. Bowlan, D. Oschwald, and B. F. Henson. Finding the "lost-time" in detonator function. *Applied Physics Letters*, 114(10):104102, 2019.

[113] Daniel Guildenbecher, Ann Dallman, Elise Hall, Benjamin Halls, Elizabeth Jones, Sean Kearney, Ryan Marinis, Christopher Murzyn, Daniel Richardson, Francisco Perez, Phillip Reu, Andrew Thompson, Marc Welliver, Ellen Mazumdar, Timothee Pourpoint, Catriona White, Alex Brown, S. Balachandar, and Ryan Houim. Advancing the science of explosive fragmentation and afterburn fireballs though experiments and simulations at the benchtop scale. Technical report, 2020.

[114] HW Bree, J Heijboer, LCE Struik, and AGM Tak. The effect of densification on the mechanical properties of amorphous glassy polymers. *Journal of Polymer Science: Polymer Physics Edition*, 12(9):1857–1864, 1974.

[115] M.B. Rubin, O.Yu. Vorobiev, and L.A. Glenn. Mechanical and numerical modeling of a porous elastic–viscoplastic material with tensile failure. *International Journal of Solids and Structures*, 37(13):1841–1871, 2000.

[116] P. Podio-Guidugli and A. Favata. *The Flamant Problem*, pages 55–77. Springer International Publishing, 2013.

[117] S.P. Timoshenko and J.N. Goodier. *Theory of elasticity*. McGraw-Hill Book Company, 3rd edition, 1970.

[118] Sivana M. Torres, Maria N. D'Orazio, and Michael J. Hargather. Focus enhancement in long schlieren imaging systems using corrector lenses. *Applied Optics*, 62(29):7744, 2023.

APPENDIX A

PMMA SAMPLE MACHINE DRAWINGS

A.1 Small-Scale PMMA samples

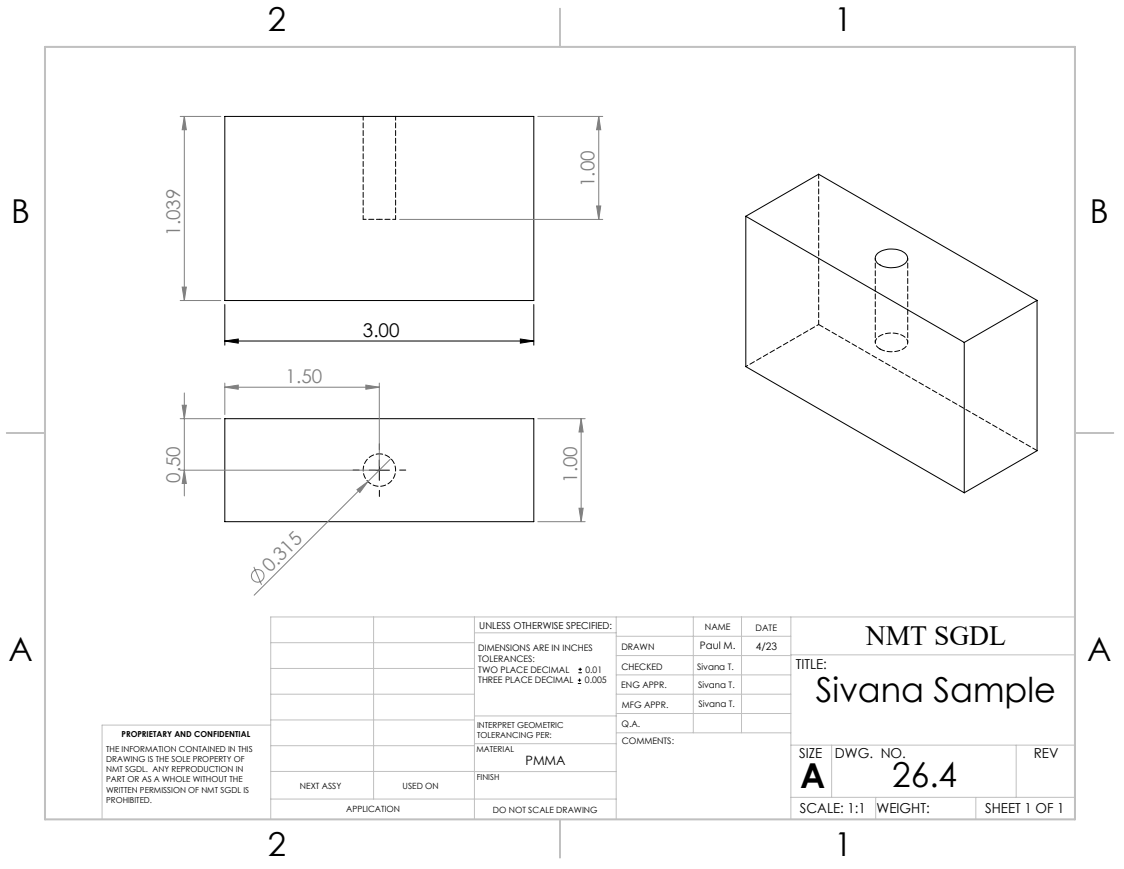

Figure A.1: Machine Drawing for the small-scale PMMA sample with a nominal propagation distance of 0.97 mm.

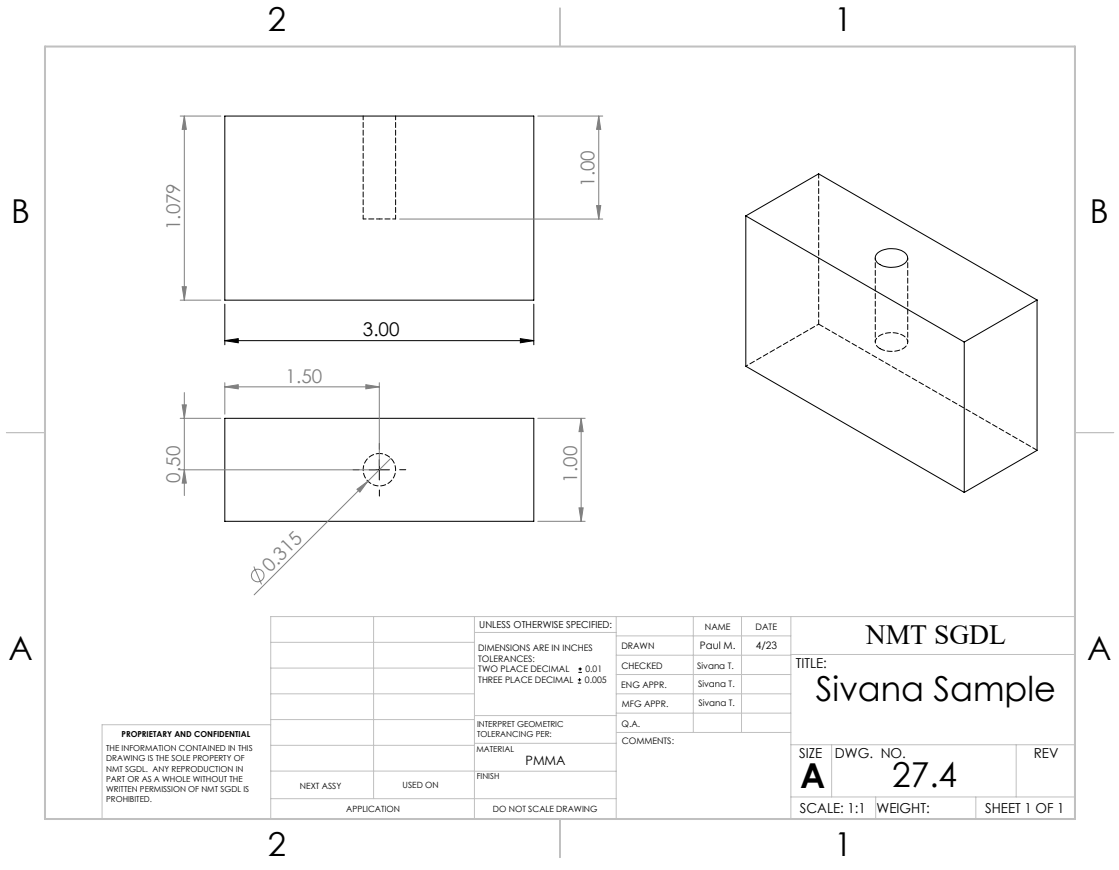

Figure A.2: Machine Drawing for the small-scale PMMA sample with a nominal propagation distance of 1.92 mm.

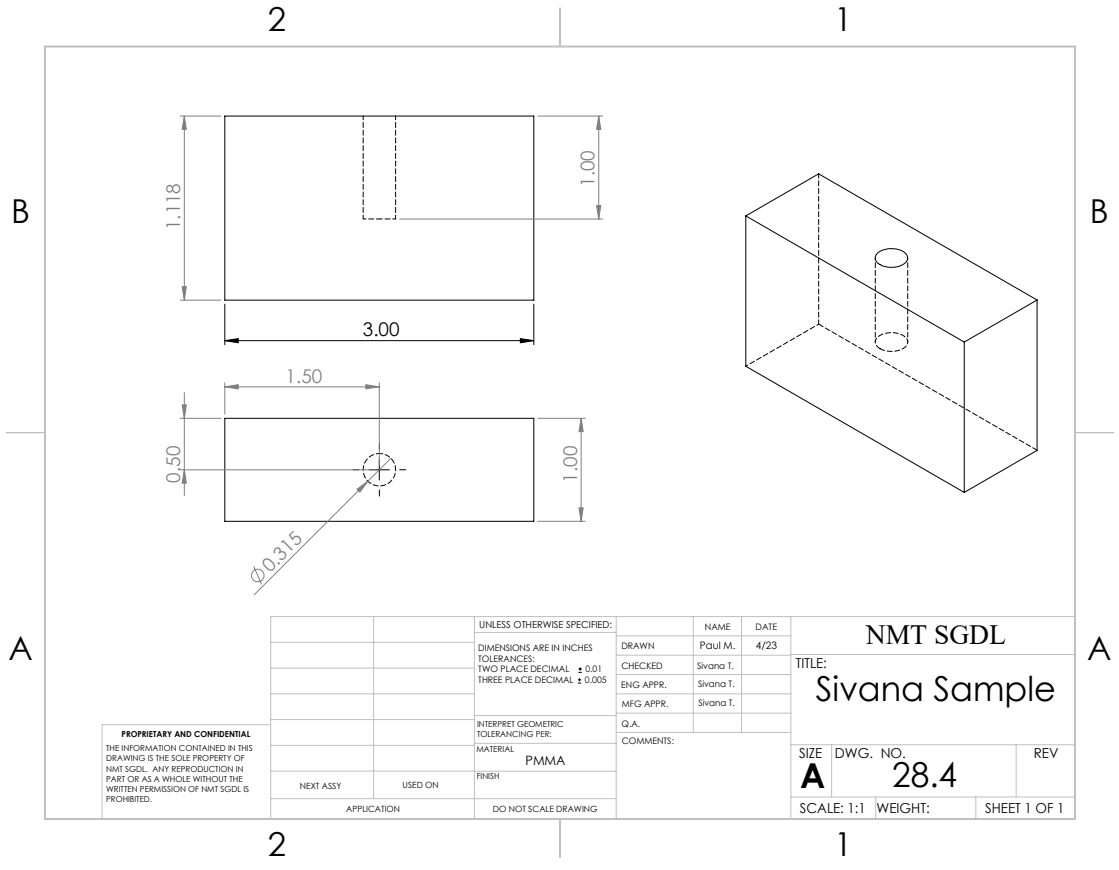

Figure A.3: Machine Drawing for the small-scale PMMA sample with a nominal propagation distance of 3.02 mm.

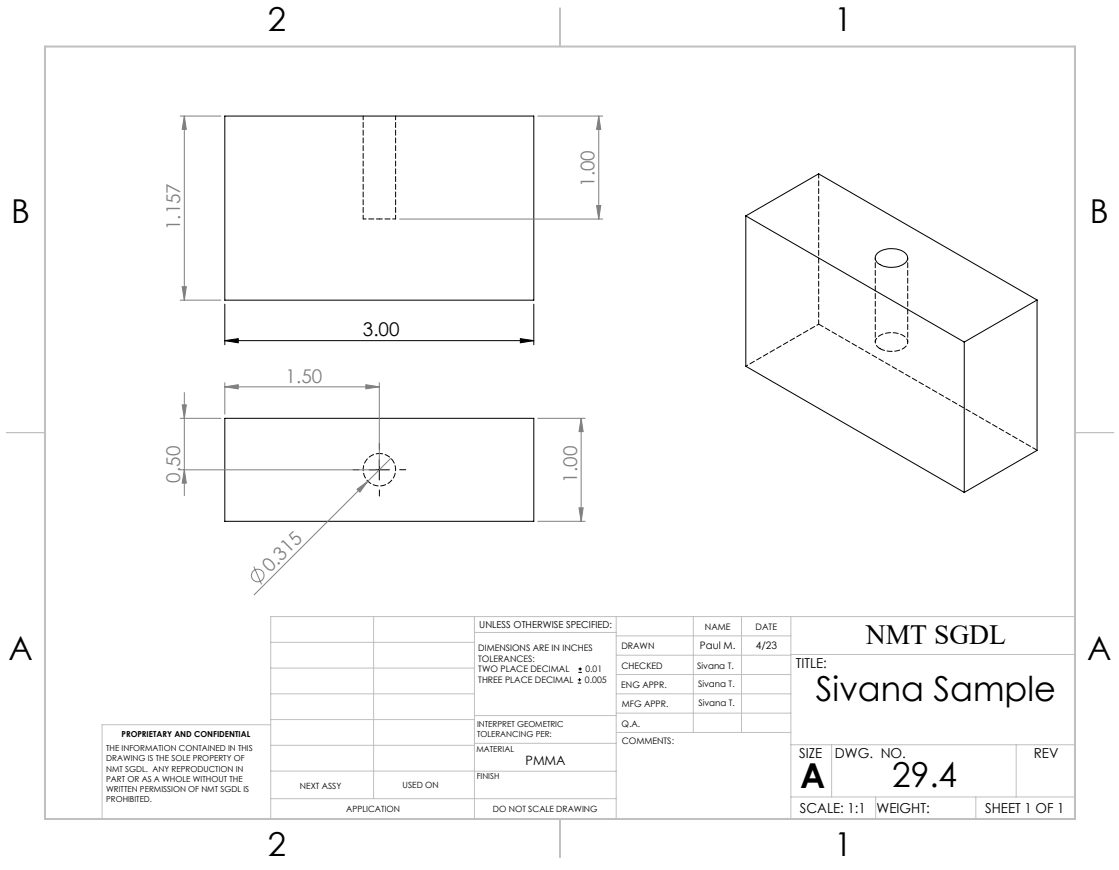

Figure A.4: Machine Drawing for the small-scale PMMA sample with a nominal propagation distance of 3.97 mm.

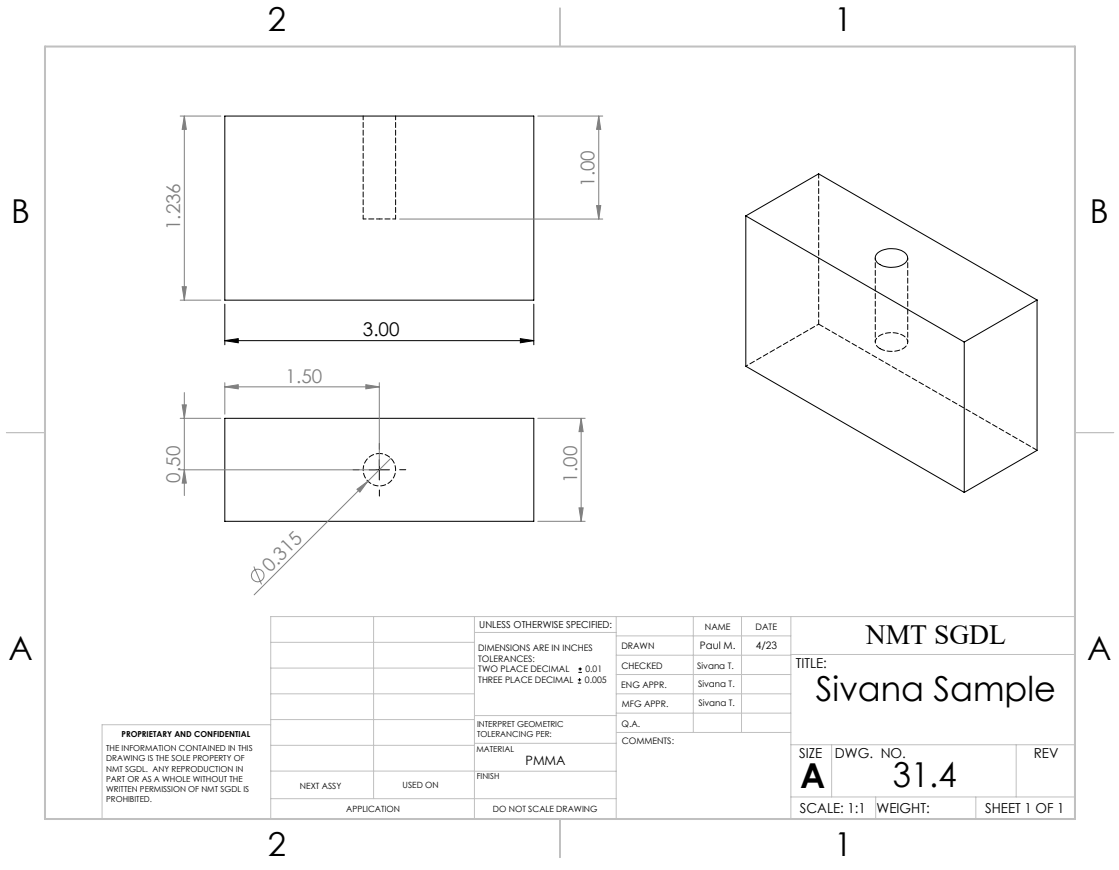

Figure A.5: Machine Drawing for the small-scale PMMA sample with a nominal propagation distance of 5.94 mm.

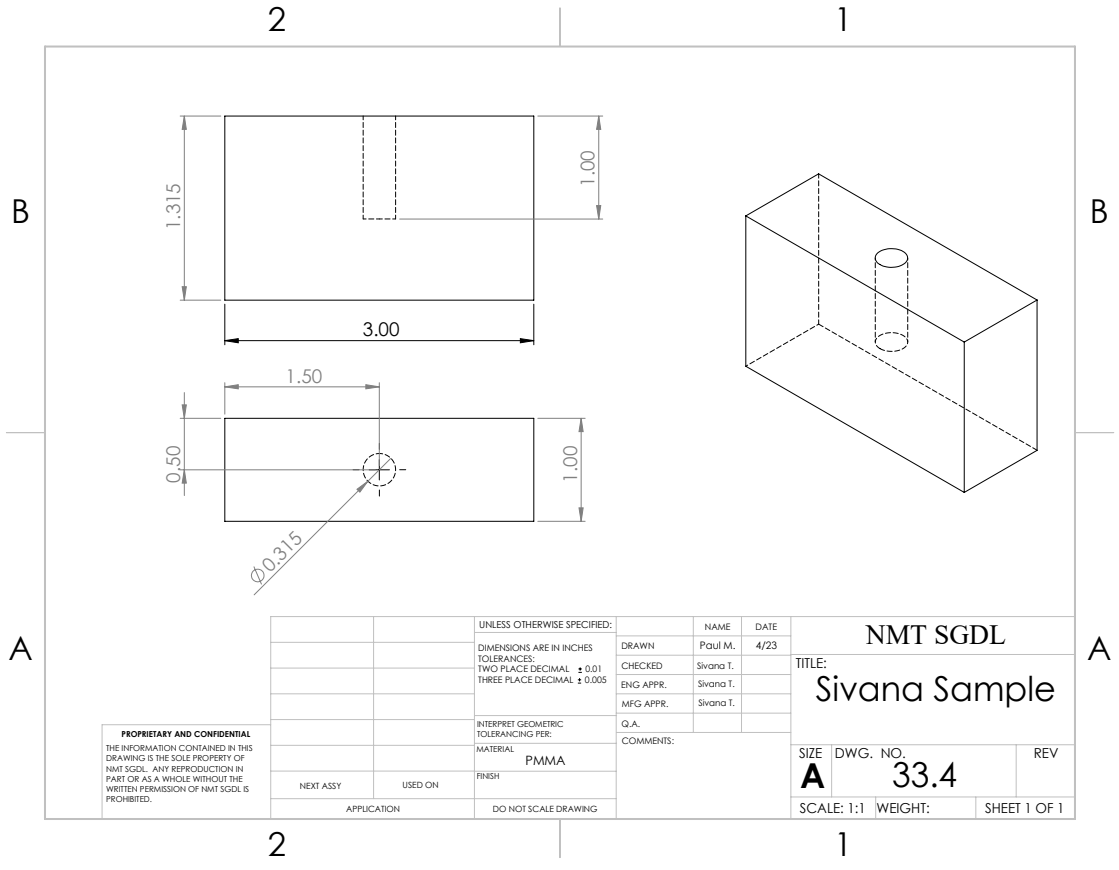

Figure A.6: Machine Drawing for the small-scale PMMA sample with a nominal propagation distance of 7.82 mm.

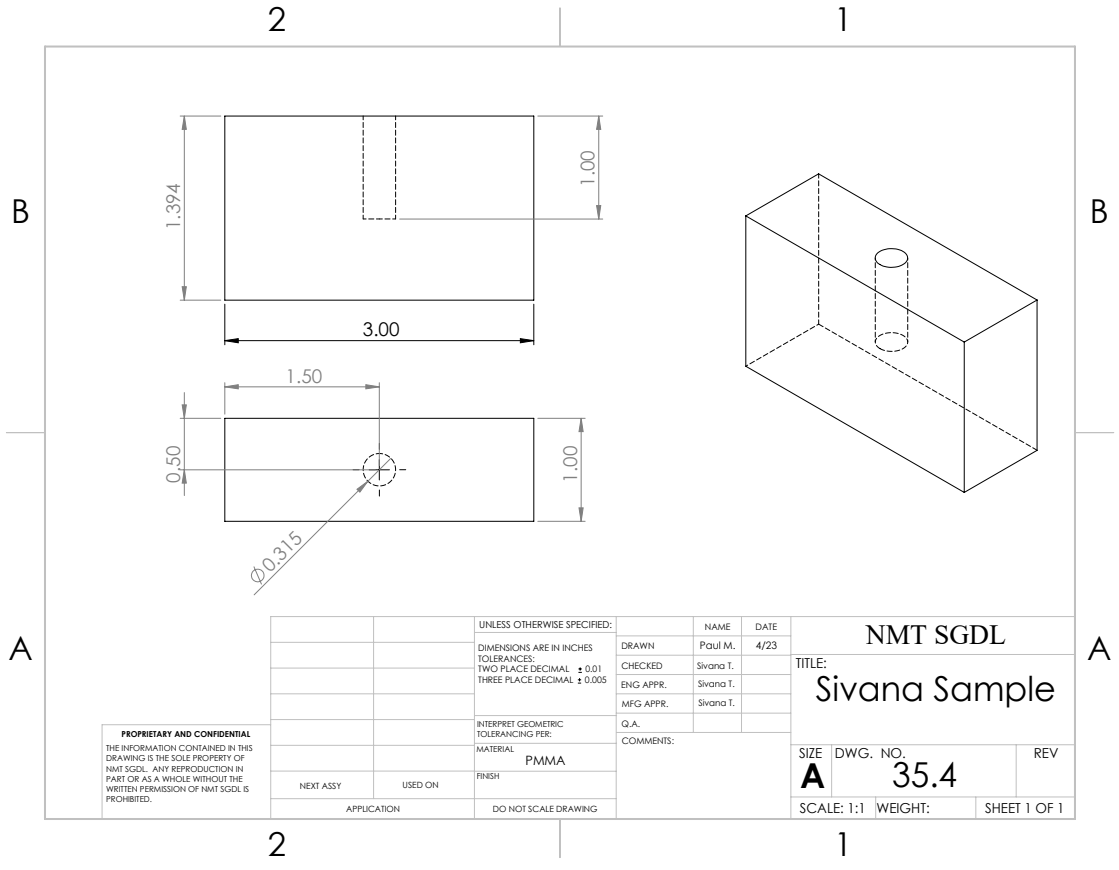

Figure A.7: Machine Drawing for the small-scale PMMA sample with a nominal propagation distance of 10.10 mm.

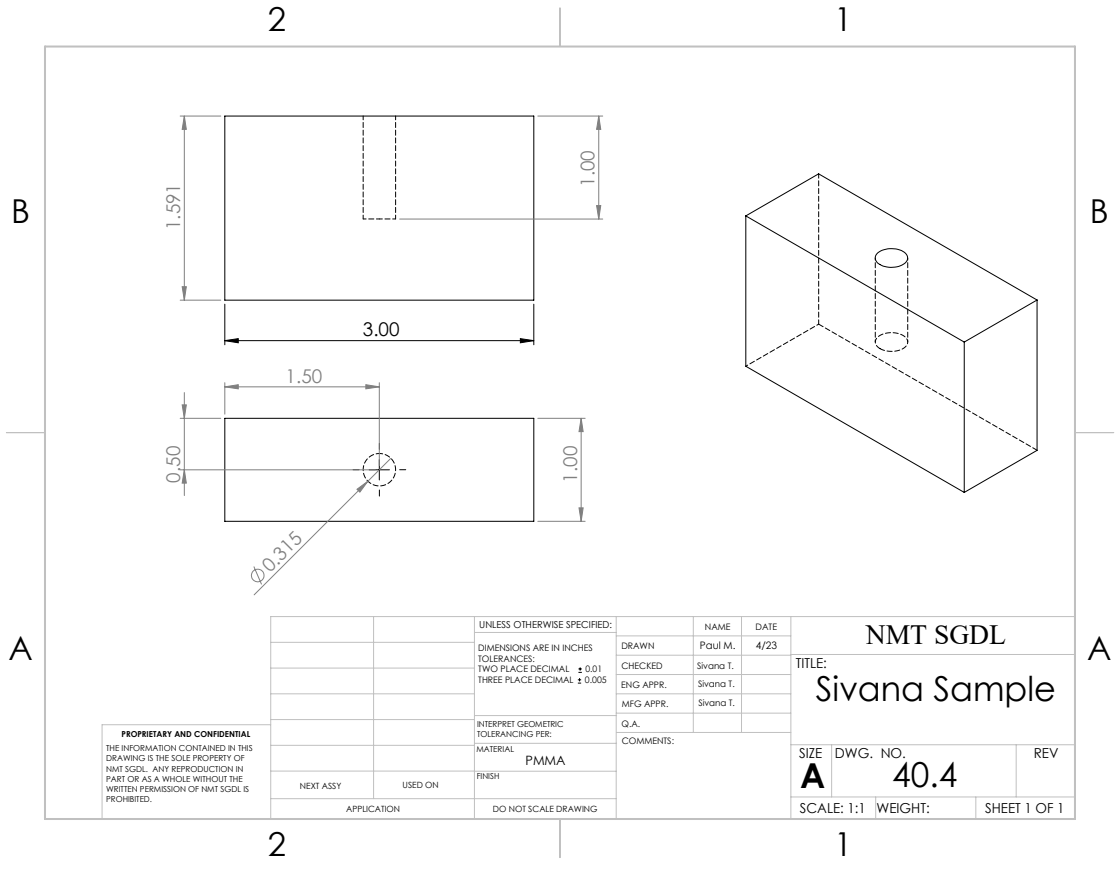

Figure A.8: Machine Drawing for the small-scale PMMA sample with a nominal propagation distance of 15.16 mm.

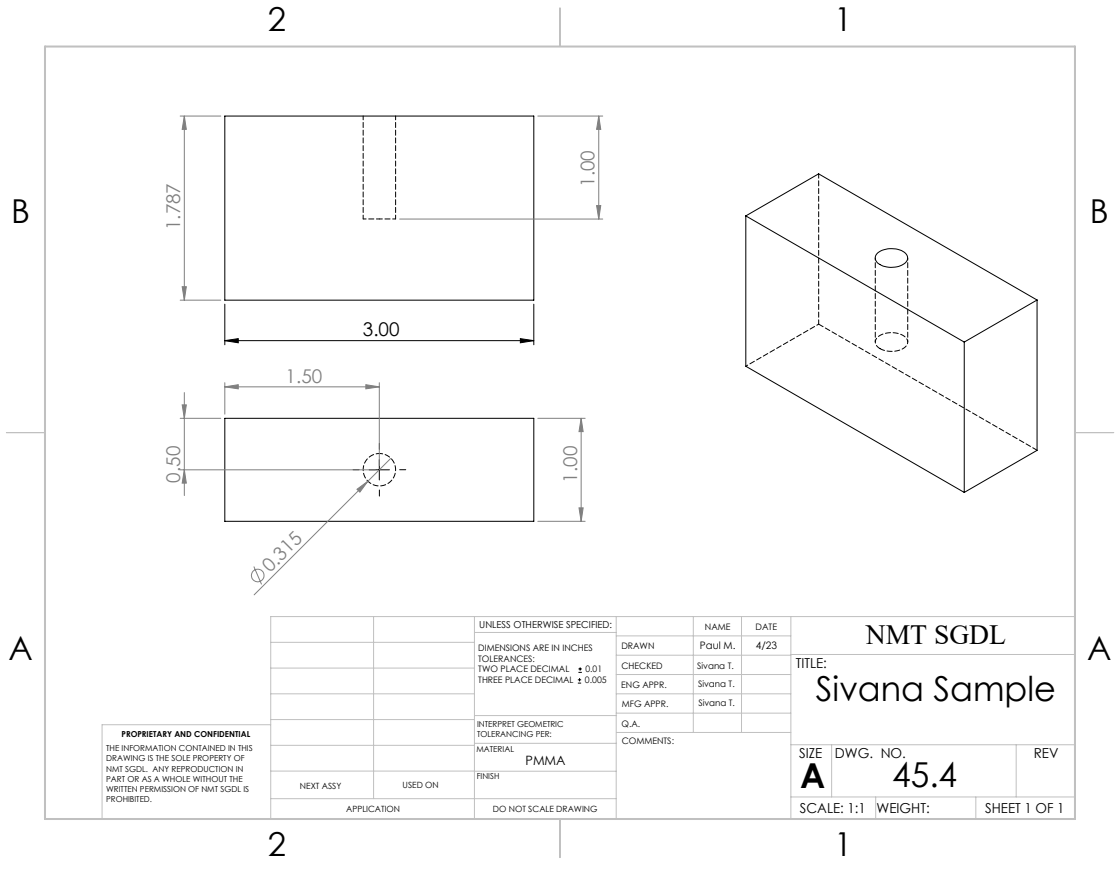

Figure A.9: Machine Drawing for the small-scale PMMA sample with a nominal propagation distance of 20.01 mm.

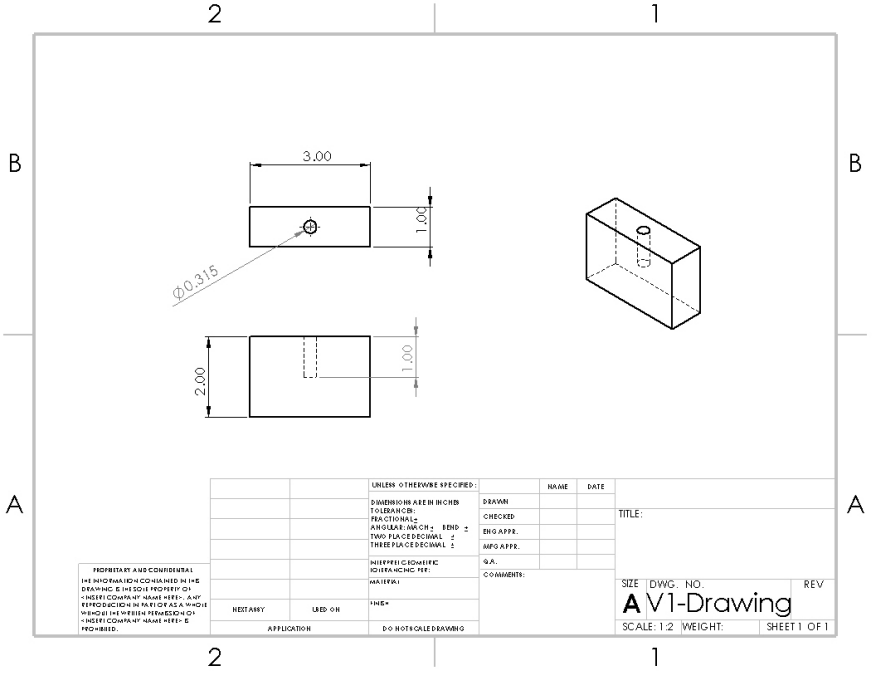

Figure A.10: Machine Drawing for the small-scale PMMA sample with a nominal propagation distance of 23.2 mm.

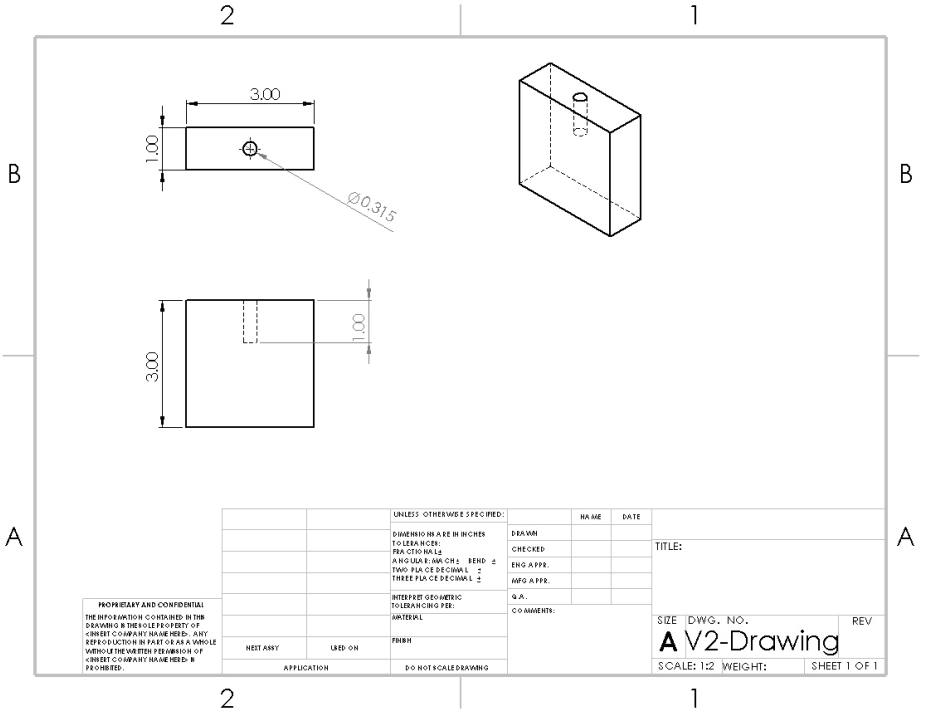

Figure A.11: Machine Drawing for the small-scale PMMA sample with a nominal propagation distance of 48.2 mm.

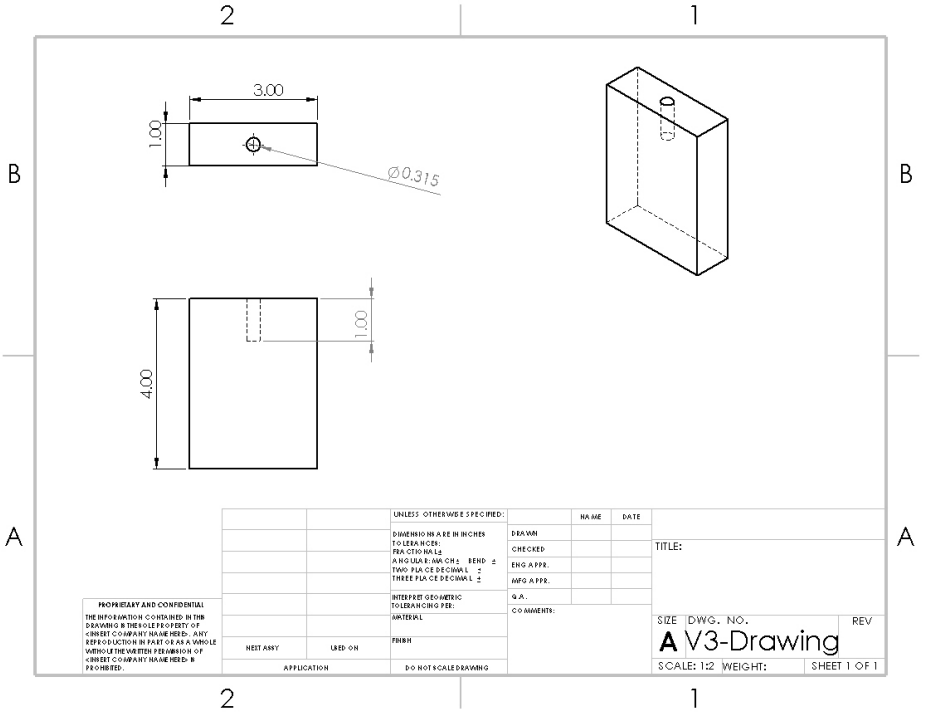

Figure A.12: Machine Drawing for the small-scale PMMA sample with a nominal propagation distance of 74.1 mm.

A.2 Large-Scale PMMA samples

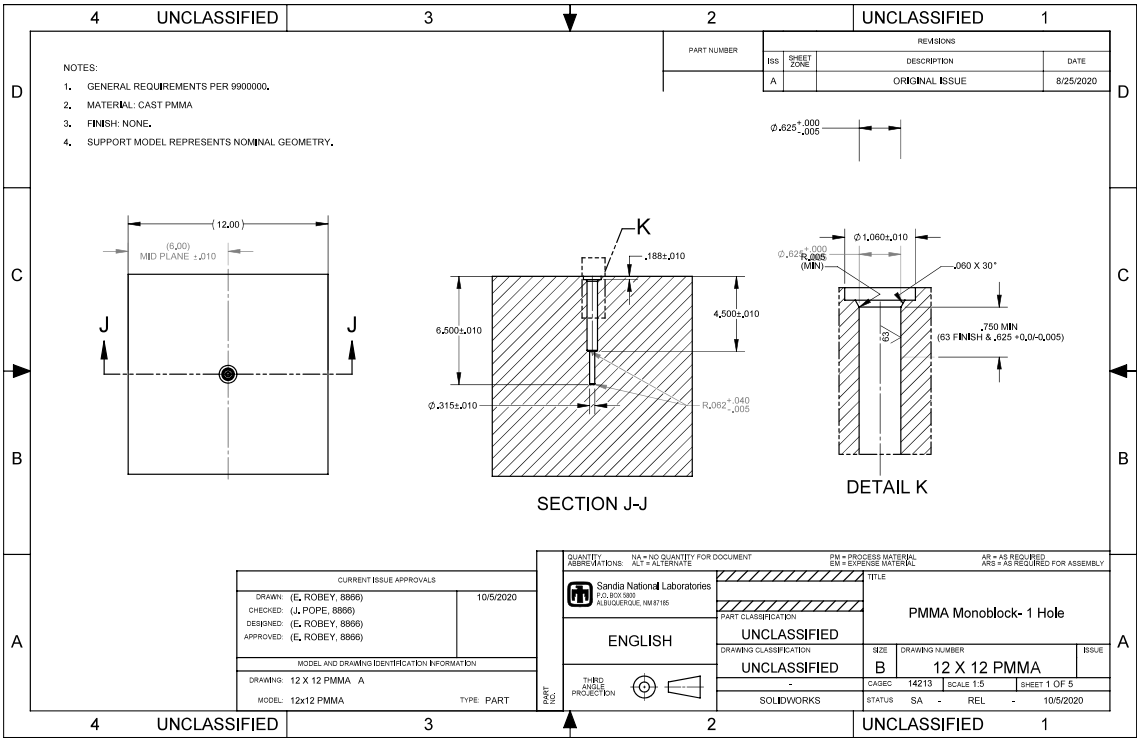

Figure A.13: Machine Drawings for the large-scale PMMA samples with 1 hole.

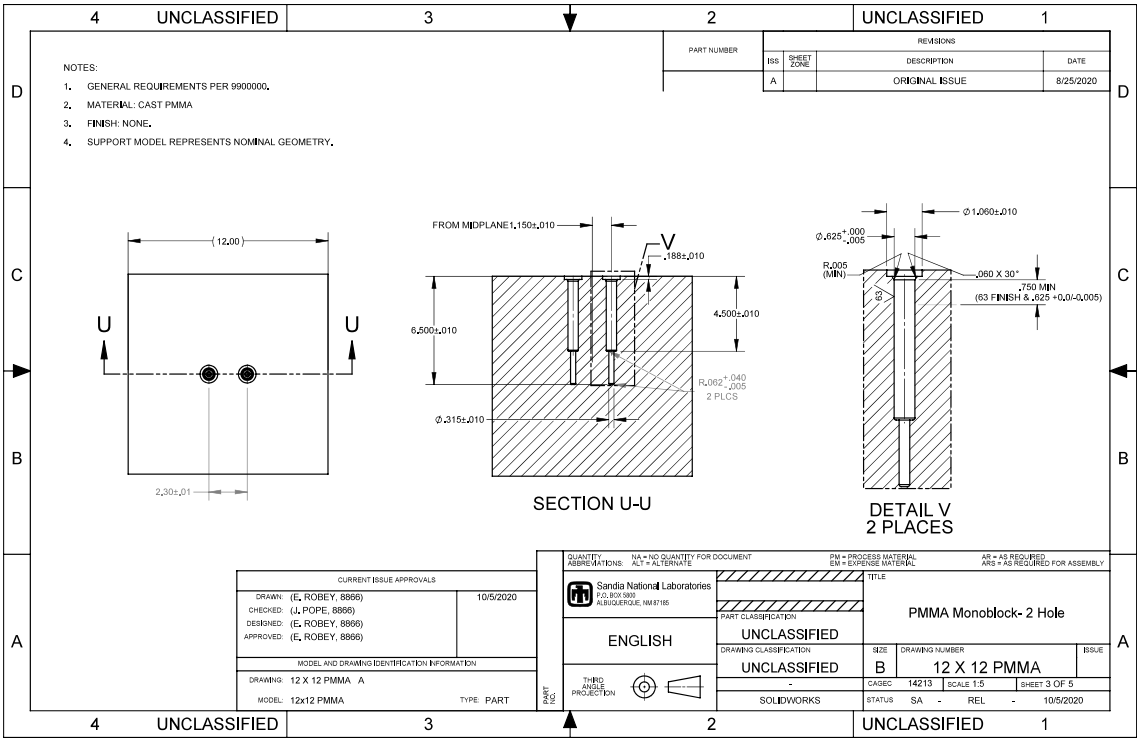

Figure A.14: Machine Drawings for the large-scale PMMA samples with 2 holes.

APPENDIX B

LARGE-SCALE TEST PLAN

1. **Purpose:**
   A series of tests will be conducted to evaluate the shock wave propagation, shock wave interaction, and fracture behavior of 1ft x 1ft poly methyl methacrylate (PMMA) and granite cubes. A subset of the PMMA samples will be composed of PMMA layers, and stress will be applied to mimic borehole environments. The expansion of shock waves and their interactions in the PMMA cubes will be visualized using schlieren imaging. Photon Doppler Velocimetry (PDV) will be used to track the particle velocity on the surface of both the PMMA and granite cubes. The shock wave propagation through both mediums will be created RP - 80 detonators. The detonator will be epoxied in place.

2. **Test Overview/Summary:**

   2.1. A detonator will be loaded into the PMMA samples in the BSL. The detonator will be secured using an ordnance approved epoxy.

   2.2. The explosively loaded PMMA and granite samples will be detonated in the BSL. The sample will be placed in a press supplied by Sandia National Laboratories used to simulate borehole environments.

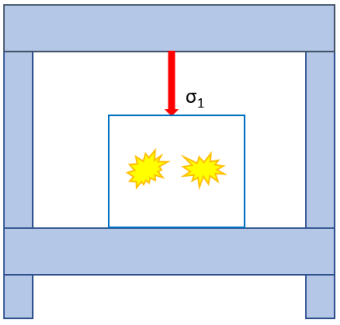

Figure 1: Schematic of the PMMA sample with applied stress location within the press.

   2.3. The shock waves generated by the explosive event in the PMMA sample will be visualized using a z-type schlieren imaging system assembled and operated by the Shock and Gas Dynamics Lab (SGDL), Dr. Hargather's laboratory group. The system will consist of two 12 inch parabolic mirrors (schlieren optics maybe changed to a lens system or 1 meter mirrors), a high speed camera and a light source. During setup the light source will be a LED light source for system alignment. During system checks and testing the light source will be the SI-LUX 640 laser system which is a Class 3b laser.

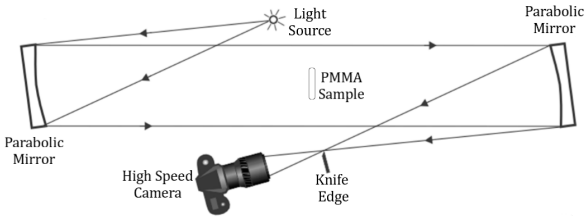

Figure 2: Top down view of imaging system.

3. Location of Test:

3.1. The PMMA and granite samples will be prepped and detonated in the Ballistics Sciences Laboratory (also known as BSL or Butler Building).

4. Sequence of Steps: (See Attachment 4 for checklist)

5. Test Matrix:

5.1. A series of test will be conducted using RP-80 detonators to visualize the shock wave propagation through PMMA under different stress loads. Table 1 outlines the general test matrix.

Table 1 – Test Matrix

Test #	Type of block	Stress	Amount/ Type of Explosives
1	Homogenous (MB 1H)	0 psi	RP - 80 detonator
2	Homogenous (MB 2H)	2900 psi	2 RP - 80 detonators

6. Construction: (non-standard items only)

6.1. Optical systems will be provided and set up by SGDL.

6.2. Press is supplied by Sandia National Lab

7. Firing Detail Schematic:

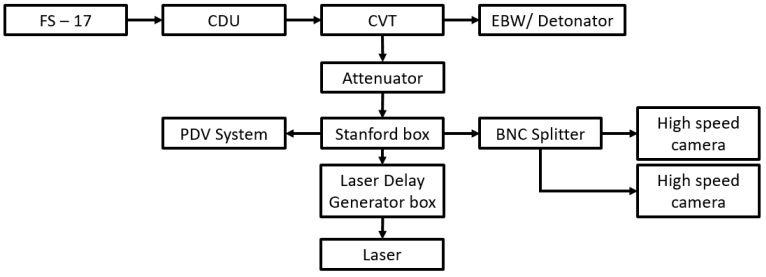

Figure 3: Firing Schematic.

8. Energetic Materials:

8.1. Detonator: Special order RP - 80 containing a delrin sleeve

8.2. RP-3 detonator per the misfire procedure

9. Instrumentation:

9.1. PDV and high-speed imaging provided by SGDL

10. Specific Tools and Equipment: (Includes specialty tools, heavy equipment, Fire Sets, etc.)

10.1. FS-17 fire set

10.2. SI-Lux Laser

10.3. PDV Laser

Documentation: (Includes videos, reports, etc.)

10.4. High speed video

10.5. Security cameras

10.6. Still pictures

10.7. Laboratory notebooks

11. Instructions for Spill Cleanup and Disposal of any Scrap and Residual A&E: (if different than those listed in Attachment 2)

12. Specific Hazards: (Include hazards in Safety Data Sheets (SDS))

12.1. Explosion

12.2. Fire

12.3. High voltage

12.4. Static EMR

12.5. Laser illumination

13. PPE Required: (As determined by JHA; include setup, test and post-test operations)

13.1. Laser safety glasses rated at OD5 or greater for 640nm

13.1.1. SI-LUX laser glasses are needed within working distance (20ft) whenever the laser key is inserted and in the on position. Others at outside of the working radius do not need PPE.

13.2. Laser safety glasses rated at OD2 or greater for 1550nm

13.2.1. PDV glasses are needed within 10ft radius of the PDV probe when the PDV laser system is activated. Others at outside of the working radius do not need PPE.

13.3. Hearing protection

13.4. Cotton clothing

13.5. Safety glasses/ laser goggles

14. Emergency Procedures: (if different than those listed in Attachment 2)

15. Proposed Test Schedule:

Each sample will be prepped then immediately detonated. No initial sample preparation will be needed.

16. References: (Include all references pertinent to the project/test)

- DoD 4145.26-M, DoD Contractors Safety Manual for AA&E
- SOP 101, Health and Safety
- SOP 102, Field Laboratory Safety
- SOP 103, Industrial Safety
- SOP 108, HAZCOM Program
- SOP 201, Grounding Procedures
- SOP 202, Initiation of Energetic Materials
- SOP 203, Arms, Ammunition and Explosives Procedures
- SOP 402, Emergency Action Plan
- SOP 403, Risk Management
- LLNL-TR-520411, PETN Sample Preparation Safety Limits

17. Attachments:

1. Job Hazard Analysis
2. Safety and General Requirements
3. Site Closure Map
4. Test Checklist
5. Tailgate Briefing Form
6. Safety Data Sheets
7. PETN Sample Preparation Safety Limits, LLNL-TR-520411
8. RP-80 Detonator SDS
9. SI-LUX and PDV Laser Safety Guide

Attachment 2 – Safety and General Requirements

Fire Sets:

- The fire set will have a positive interlock (e.g., key/shorting device) which will prevent the inadvertent firing of the system when removed.
- The Ordnance Technician/Gunner will keep the key/shorting device in their possession at all times.
- No duplicate keys or shorting devices will be allowed on site at any time.

Laser System:

- The laser safety unit will have a positive interlock (e.g., key) which will prevent the inadvertent firing of the system when removed.
- The test engineer will keep the key/shorting device in their possession at all times.
- No duplicate keys or shorting devices will be allowed on site at any time.
- Laser hazard signs will be placed on the available entry points for BSL prior to arming the laser

Hazardous Waste:

- The use, recovery, collection, transport, and storage of military munitions for Research, Development, Testing and Evaluation (RDT&E) (e.g. safety, developmental testing, surveillance function testing, static fire, or quality control or assurance testing) is considered use for intended purpose and not subject to regulation under Resource Conservation and Recovery Act (RCRA). (Military Munitions Rule (MMR) paragraph 3.B.2.b.)
- As long as all excess energetic material is destroyed on site, and not removed from the test range, it is not considered waste and does not fall under RCRA. (MMR paragraph 10.C.3.)
- Any spilled loose material will be completely gathered up and determined if the material is still usable.
- If the material is still usable, it is not considered waste and should be used or stored as applicable.
- Spilled material deemed unusable will be properly containerized, labeled and stored for later disposal in accordance with local policies and procedures.

Misfire Procedures:

- If there are no indications that the detonator, ignitor, etc., initiated, all connections will be checked (in the bunker or personnel shelter only) to ensure they are connected correctly. If instrumentation does not need to be reset, then another attempt to fire may be made. The engineer/test manager will be consulted prior to attempting to fire again.
- If there is still no indication that the detonator or ignitor initiated, begin the applicable wait time as stated below:
    - All electric misfires will include a 15-minute wait time before personnel are permitted to approach the test article, unless determined to be otherwise.
    - All non-electric misfires will include a 30-minute wait time before personnel are permitted to approach the test article, unless determined to be otherwise.

- During the wait time, the engineer/test manager and the ordnance technician will contact the Ordnance Supervisor, Safety Officer and the Associate Director or their designated representatives, to inform them of the misfire and to discuss troubleshooting options.

Emergency Procedures:

- Lightning: (reference procedures in SOP 104)
- Fire:
  - If there is a fire on or near the test pad, all personnel will evacuate to the personnel shelter immediately (or further depending on the severity of the fire) and the safety office will be notified.

WARNING
Personnel WILL NOT fight a fire that could have any remote possibility of involving explosives.

WARNING
Personnel WILL NOT fight a fire that is located off the test pad. There is a strong possibility of unexploded ordnance being present off the test pad.

- Unexpected Explosion:
  - All personnel will immediately assemble at the personnel shelter (or other previously identified location) and all personnel accounted for;
  - All personnel will be checked for possible injuries, first aid applied as needed, and the area inspected for remaining hazards by ordnance personnel;
  - Emergency Medical Services will be called for assistance, if needed;
  - The safety office will then be notified immediately.

WARNING
If an explosion involves the Ordnance Technician (or any other personnel) on the test pad, personnel in the personnel shelter must make a determination whether or not it is safe to attempt to treat or assist the individual on the test pad.

Personnel and AA&E Limits:

- Limit exposure to a minimum number of personnel, for a minimum amount of time, to the minimum amount of the hazardous material consistent with safe and efficient operations.
- Personnel Limits – All non-essential personnel will be located in the personnel shelter during all operation involving the handling of energetic material unless prior approval has been granted from the Safety Office.
- Explosive Limits – Only explosives needed for a single test will be allowed on the test pad at any one time.

Indicators for Identifying Abnormal Process Conditions: (applies only to in-process operations)

- Bad grounds
- Bad system check

Attachment 3

Site Closure Map

Figure 4: Site closure map.

Enclosure Details:

- A cable gate and Z-sign will block the road into the Torres and BSL complex.
- The gate to East and West lab will be closed.
  - Non test personnel are allowed to work at East and West labs.
- A Z-sign will block the steps from Torres Labs.
  - Non test personnel are allowed to work at Torres Labs.
- All doors into the BSL will contain caution signs (excluding the Bay doors).
  - The Bay doors will be closed and locked.
- All personnel working at West, East and Torres labs will be briefed on the appropriate procedures for entering and exiting the site clearance zone.
  - Personnel must get the OK to enter the clearance from either the test engineer or Ordnance
  - Personnel must inform the test engineer or Ordnance that they have left the clearance
- Prior to site closure the alarm will be sounded for 1 min to warn others about the closure and the explosive testing warning light will be turned on and will remain on the duration of the test.

- Area will remain enclosed until the explosives have been removed from the testing location.

Attachment 4

Test Checklist

START OF DAY TEST SHEET FOR Multi-Point Explosion Visualization

1.1. Testing Conditions and Safety:

1.1.1. Test Engineer: _____

1.1.2. Ordnance: _____

1.1.3. Operator Safety: _____

1.1.4. Personnel present: _____

1.1.5. Total persons present: _____

1.1.6. Note date/time: _____

1.1.7. Sound the alarm for 1 minute and turn on the explosive test warning light

1.1.8. Clear the testing range as outlined in Attachment 3

1.1.9. Check the Torres Main Building, West and East lab. If non-test related personnel are to be present in the Torres Main Building, inform them of testing to be performed in the BSL and brief them appropriately for entering and exiting the clearance.

1.1.10. Barometric pressure (inHg):_____

1.1.11. BSL inside temperature:_____

1.1.12. Number of planned tests:_____

1.2. Safety Briefing:

1.2.1. Review hazards present on site during testing and required personnel protective equipment (PPE) as specified by the PPE survey and JHA

1.2.2. Distribute PPE (at a minimum hearing protection and safety glasses) to all personnel to be present during testing

1.3. Signatures of Responsible Parties:

1.3.1. Test Engineer: _____

1.3.2. Ordnance: _____

1.3.3. Operator Safety: _____

2. PRETEST PROCEDURES

Prior to testing day, a full walk through of all steps will be performed with Dr. Michael Hargather or his designated representative.

(If already completed and start of new test go to the appropriate test steps)

2.1. Start of Day

2.1.1. Ensure Start of Day Pretest Sheet has been properly filled out.

2.1.2. Calculate the pressure needed in gauge PSI/ Ton to reach desired stress. Write the calculate pressure value in on steps 2.4.28 and 3.3.27.

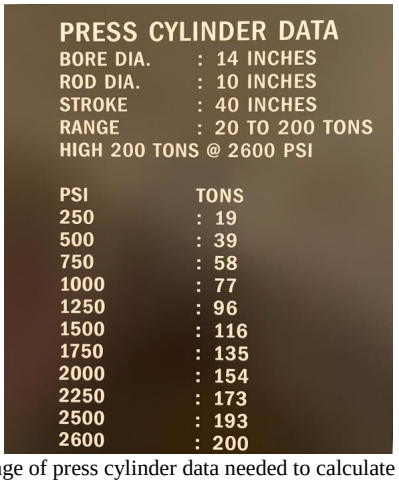

Figure 5: Image of press cylinder data needed to calculate the desired pressure.

2.1.3. Place the diffuse reflector on the PMMA sample where the PDV measurements will be made.

2.1.4. Ensure all personnel have been properly briefed on testing hazards and have received proper safety briefing and PPE.

2.1.5. Ensure safety video operating and recording.

2.1.6. Ensure caution signs are posted at BSL entrances.

2.1.7. Perform a walk though of all steps with ordnance and all test personnel.

2.1.8. Verify that laser system is setup properly as outlined in ‘SI-LUX 640 User Guide’ (Attachment 9).

2.2. System Hardware Checkouts (Camera, Laser system, and PDV probes)

2.2.1. Ensure the laser key is removed and the system is disarmed in the software.

2.2.2. Set the Stanford Box to ‘Single shot’ trigger mode.

2.2.3. All personnel without laser safety glasses must be out of the laser radius.

2.2.4. Ensure all remaining personnel have laser safety glasses in place.

2.2.5. Arm the PDV system.

2.2.6. Arm the high-speed cameras.

2.2.7. At the direction of the test engineer, arm the laser in the software and loudly announce that the laser is armed.

2.2.8. Insert the key to the laser safety unit and turn it to the ‘ON’ position. Loudly announce that the key is in and system is on.

2.2.9. Press the ‘EXC’ button on the Stanford box to trigger the camera, laser, and PDV system.

2.2.10. Disarm the PDV system.

2.2.11. Turn the key in the laser safety unit to the ‘OFF’ position and remove the key. Loudly announce that the key is out.

2.2.12. If the laser system did not automatically disarm, disarm the laser in the software and loudly announce that the laser is disarmed.

2.2.13. At this point laser safety glasses may be removed and those without laser safety glasses may return.

2.2.14. Ensure all systems triggered.

2.3. Fire System Checkout (Spark Gap)

2.3.1. Ensure the laser key is removed and the system is disarmed in the software.

2.3.2. Set the Stanford Box to ‘External’ trigger mode.

2.3.3. Place a spark gap in the field of view of the refractive imaging system.

2.3.4. Place a calibration object in the field of view of the imaging system.

2.3.5. Connect the spark gap to the fire system.

2.3.6. All personnel without laser safety glasses must be out of the laser radius.

2.3.7. Ensure all remaining personnel have laser safety glasses in place.

2.3.8. Arm the PDV laser.

2.3.9. Arm the high-speed cameras.

2.3.10. At the direction of the test engineer, arm the laser in the software and loudly announce that the laser is armed.

2.3.11. Insert the key to the laser safety unit and turn it to the 'ON' position. Loudly announce that the key is in and system is on.

2.3.12. Ensure all personnel are separated from the spark gap.

2.3.13. The test engineer will then hand control over to ordnance to fire the spark gap.

2.3.14. Ordnance fires the spark gap.

2.3.15. Disarm PDV laser.

2.3.16. Turn the key in the laser safety unit to the 'OFF' position and remove the key. Loudly announce that the key is out.

2.3.17. If the laser system did not automatically disarm, disarm the laser in the software and loudly announce that the laser is disarmed.

2.3.18. At this point laser safety glasses may be removed and those without laser safety glasses may return.

2.3.19. Verify all systems triggered and the spark can be visualized in high speed images.

2.3.20. Save the calibration image.

2.4. Inert loading of the 200T press main cylinder.
Note: In case of emergency press the E-stop button.

2.4.1. Ensure safety observer has been briefed. Preform a walkthrough of press procedures with safety observer.

2.4.2. Record the starting pressure on the pressure gauge: _____

2.4.3. Ensure the press is clear and there is nothing on the pressing surface (Wood posts should be in place)

2.4.4. Ensure wood posts used for safety when operating in the press are in place. (security for the top cylinder)

2.4.5. Place the bottom tooling in the center of the press.

2.4.6. Align tooling corners with the marks on the press. (center of the press)

2.4.7. Ensure the bottom tooling is in the center of the press.

2.4.8. Place the PMMA test specimen on the tooling.

2.4.9. Reference Figure 6 for full PMMA assembly.

Figure 6: Image of full PMMA assembly.

2.4.10. Align PMMA in the schlieren system using the LED light source while maintain center on the tooling.

2.4.11. Align PDV probes

2.4.12. Ensure all personnel are clear from the press.

2.4.13. Remove the wood posts. Store the wood posts under the press.

2.4.14. Plug the press in.

2.4.15. Place the red water discharge hose outside (for the press heat exchanger).

2.4.16. Turn the water for the supply hose on.

2.4.17. Turn the Press **Main Disconnect** switch into the '**on**' position

2.4.18. Turn the **Control Power** knob into the '**on**' position

2.4.19. At this point the **E-stop reset** button will illuminate.

2.4.20. Pull the **E-stop** button (Red button light off).

2.4.21. Push the **E-stop** reset button. (Blue button light off)

2.4.22. Turn the **Hydraulic Power** knob into the '**on**' position. The knob will start blinking implying the press is in standby mode. The knob will return to center line.

2.4.23. Safety observer will monitor the cylinder as the sample is pressed from the firing booth. Safety observer will communicate to the press operator the movement of the press and when the press has made contact with the sample.

2.4.24. Push the **Side Cylinder Open** button until the limit switch is engaged.

2.4.25. Fully open the **Press Pressure Control** and turn it one and a half turns in the closed direction.

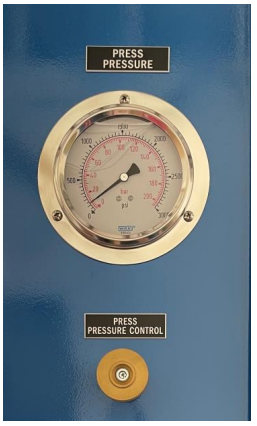

Figure 7: image of the press pressure gauge and the control valve.

NOTE: Step 2.4.25 sets the pressure at which the press registers that the press has latched with the sample.

2.4.26. Set the **Main Cylinder Speed** to the '**slow**' position

NOTE: When closing and opening the press it takes 3 seconds for the press to stop moving once the closing/opening buttons have been released.

2.4.27. Press and hold both **Press Close** buttons. Release the buttons once the **Press HP Latch** light illuminates. Expect the press to take 3 seconds to register the buttons have been released. As the press closes the operator should monitor the **Press HP Latch** light and the pressure gauge. Once the **Press HP Latch** light illuminates release both **Press Close** buttons. If the **Press HP Latch** light does not illuminate:

2.4.27.1. Release both **Press Close** buttons. (Stop closing).

2.4.27.2. Adjust the **Press Pressure Control** by closing it further in half turn increments.

NOTE: Once the press has Latched it will maintain the pressure set on the pressure gauge panel

2.4.28. Slowly adjust the **Press Pressure Control** until the gauge is set to _____ (the calculated gauge pressure)

2.4.29. Check PDV alignment

2.4.30. Check schlieren imaging

2.4.31. Ensure all personnel are clear from the press.

2.4.32. Release the pressure by pressing (do not hold) the **Press Open** button. Once the press is latched the **Press Open** button acts as a 'dead man switch' and will stop the press from maintaining any pressure.

2.4.33. Observe the pressure gauge to see if the pressure has come off and ensure the **Press HP Latch** light no longer illuminates.

2.4.34. Set the **Main Cylinder Speed** to the '**fast**' position.

2.4.35. Fully open the press by pressing and holding the **Press Open** button until the limit switch is engaged. Observer must monitor the press movement and notify the press operator that the top cylinder has engaged the limit switch.

2.4.36. Turn the **Hydraulic Power** knob into the '**off**' position. The knob will no longer illuminate. The knob will return to center line.

2.4.37. Turn the **Control Power** knob into the '**off**' position

2.4.38. Turn the **Main Disconnect** switch into the '**off**' position

2.4.39. Fully close the **Press Pressure Control**

2.4.40. Place and secure the wooden posts using the Velcro straps.

3. STRESSED DETONATOR SAMPLE ASSEMBLY PROCEDURES

3.1. In the event of anything unusable or unexpected during the pressing of explosives the engineer/test manager and the ordnance technician will contact the Ordnance Supervisor and Safety Officer, or their designated representatives, to inform them of the event and to discuss troubleshooting options.

3.2. Setup

3.2.1. Ensure the safety observer is aware of all operations pertaining the explosive event and press operations.

3.2.2. Perform a walk though of all steps with ordnance and all test personnel

3.2.3. Ensure the safety video is recording.

3.2.4. Record the starting pressure on the pressure gauge: _____

3.2.5. Ensure the press is clear and there is nothing on the pressing surface (Wood posts should be in place)

3.2.6. Ensure wood posts used for safety when operating in the press are in place. (security for the top cylinder)

3.2.7. Place the bottom tooling in the center of the press.

3.2.8. Align tooling corners with the marks on the press. (center of the press)

3.2.9. Ensure the bottom tooling is in the center of the press.

3.2.10. Place the PMMA test specimen on the tooling.

3.2.11. Reference Figure 8 for full PMMA assembly.

Figure 8: Image of PMMA assembly.

3.2.12. Ensure the sample is in the field of view using the LED light source.

3.2.13. Ensure the appropriate signal is being output by the PDV system. PDV will be adjusted as necessary.

3.2.14. Switch the light source back to the laser.

3.2.15. All non- Essential personnel will retreat behind the barricades. Non-test personnel will retreat to the loft behind the barricades and the safety observer will retreat to the firing booth.

3.2.16. Ensure all personnel handling explosives are following appropriate static safety procedures (SOP 201, wrist stats, cotton clothing).

3.3. Placing the Explosive Charge into Sample

3.3.1. Ensure all non-essential personnel are behind barricades.

3.3.2. Sound the alarm for 30 seconds.

Only ordnance will carry out steps 3.3.2 - 3.3.6 & 3.3.9-3.3.10

3.3.3. Place the RP - 80 detonator into the milled hole on the PMMA sample.

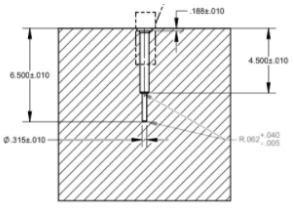

Figure 9: Schematic of 1 ft x 1 ft cube of PMMA.

3.3.4. Secure the detonator in the sample using ordnance approved epoxy. **DO NOT CONNECT DETONATOR TO FIRE SET**

3.3.5. Wait for the epoxy to cure as outlined by the manufacturer.

3.3.6. Fill the borehole with tamp material.

3.3.7. Place the metal stopper into the milled hole in the PMMA cube.

3.3.8. Check schlieren alignment. Verify with the Camera control person (located in the loft) that the schlieren alignment looks good.

3.3.9. Check the PDV system is outputting appropriate signals.

3.3.10. Connect the detonator(s) to the c-cable.

3.3.11. Place the pressure plate on the PMMA sample. Ensure the c-cable is running through the milled hole lined with PEEK (non-conductive plastic).

3.3.12. Remove the wood posts and store under press.

3.3.13. Ordnance and test Engineer retreat back to the firing booth.

3.3.14. Verify the press is plugged in.

3.3.15. Verify that the red water discharge hose is outside (for the press heat exchanger).

3.3.16. Verify the water for the supply hose is on.

3.3.17. Turn the Press **Main Disconnect** switch into the '**on**' position

3.3.18. Turn the **Control Power** knob into the '**on**' position

3.3.19. At this point the **E-stop reset** button will illuminate.

3.3.20. Pull the **E-stop** button (Red button light off).

3.3.21. Push the **E-stop** reset button. (Blue button light off)

3.3.22. Turn the **Hydraulic Power** knob into the '**on**' position. The knob will start blinking implying the press is in standby mode. The knob will return to center line.

3.3.23. Safety observer will monitor the cylinder as the sample is pressed from the firing booth. Safety observer will communicate to the press operator the movement of the press and when the press has made contact with the sample.

3.3.24. Push the **Side Cylinder Open** button until the limit switch is engaged.

3.3.25. Fully open the **Press Pressure Control** and turn it one and a half turns in the closed direction.

NOTE: Step 3.3.24 sets the pressure at which the press registers that the press has latched with the sample.

3.3.26. Set the **Main Cylinder Speed** to the '**slow**' position

NOTE: when closing and opening the press it takes 3 seconds for the press to stop moving once the closing/opening buttons have been released.

3.3.27. Press and hold both **Press Close** buttons. Release the buttons once the **Press HP Latch** light illuminates. Expect the press to take 3 seconds to register the buttons have been released. As the press closes the operator should monitor the **Press HP Latch** light and the pressure gauge. Once the **Press HP Latch** light illuminates release both **Press Close** buttons. If the **Press HP Latch** light does not illuminate:

3.3.27.1. Release both **Press Close** buttons. (Stop closing).

3.3.27.2. Adjust the **Press Pressure Control** by closing it further in half turn increments.

NOTE: Once the press has Latched it will maintain the pressure set on the pressure gauge panel

3.3.28. Slowly adjust the **Press Pressure Control** until the gauge is set to _____ (the calculated gauge pressure)

3.3.29. Check PDV alignment

3.3.30. Check schlieren imaging

3.3.31. Ensure the Stanford Box is set to 'External' trigger mode.

3.3.32. Engineer will announce goggles on (goggles are only required when in the working radius).

Laser safety eye protection is required for all remaining steps for all personnel.

3.3.33. At the direction of the test engineer, arm the laser in the software and loudly announce that the laser is armed.

3.3.34. Insert the key to the laser safety unit and turn it to the 'ON' position. Loudly announce that the key is in and system is on.

3.3.35. Arm the PDV system.

3.3.36. Ensure all personnel are behind barriers.

3.3.37. Ordnance will connect the c-cable to the fire set

3.3.38. Arm the cameras.

Hearing protection is required for all remaining steps for all personnel.

3.3.39. The test engineer will then hand control over to ordnance.

3.3.40. Ordnance will fire the system.

3.3.41. All personnel must remain behind barricades until ordnance gives the all clear.

3.3.42. The test engineer will quickly release the pressure by pressing (do not hold) the **Press Open** button. Once the press is latched the **Press Open** button acts as a 'dead man switch' and will stop the press from maintaining any pressure. Observe the pressure gauge to ensure pressure is released and the **HP Latch** light no longer illuminates.

3.3.43. Set the **Main Cylinder Speed** to the **'fast'** position.

3.3.44. Fully open the press by pressing and holding the **Press Open** button until the limit switch is engaged. Observer must monitor the press movement and notify the press operator that the top cylinder has engaged the limit switch.

3.3.45. Turn the **Hydraulic Power** knob into the '**off**' position. The knob will no longer illuminate. The knob will return to centerline.

3.3.46. Turn the **Control Power** knob into the '**off**' position.

3.3.47. Turn the **Main Disconnect** switch into the **'off'** position.

3.3.48. Fully close the **Press Pressure Control**

3.3.49. Disarm PDV lasers.

Ordnance will carry out steps 3.3.48 - 3.3.50

3.3.50. Ordnance visually clears the press.

3.3.51. Ordnance will place the wood safety post in the press allowing for ordnance to safely work under the press when clearing the range.

3.3.52. Ordnance will clear the range and determine when it is safe for test personnel to exit the barriers.

3.3.53. Turn the key in the laser safety unit to the 'OFF' position and remove the key. Loudly announce that the key is out.

3.3.54. If the laser system did not automatically disarm, disarm the laser in the software and loudly announce that the laser is disarmed.

3.3.55. At this point laser safety glasses may be removed and those without laser safety glasses may return.

3.3.56. Save camera and PDV data

3.3.57. Remove damaged test sample.

4. UNSTRESSED DETONATOR SAMPLE ASSEMBLY PROCEDURES

4.1. In the event of anything unusable or unexpected during the pressing of explosives the engineer/test manager and the ordnance technician will contact the Ordnance Supervisor and Safety Officer, or their designated representatives, to inform them of the event and to discuss troubleshooting options.

4.2. Setup

4.2.1. Ensure the safety observer is aware of all operations pertaining the explosive event.

4.2.2. Perform a walk though of all steps with ordnance and all test personnel

4.2.3. Ensure the safety video is recording.

4.2.4. Ensure the sample has metal tape in place for PDV probes.

4.2.5. Place the PMMA test specimen in the test section.

4.2.6. Ensure the sample is in the field of view using the LED light source.

4.2.7. Align PDV system. Ensure the appropriate signal is being output by the PDV system. PDV will be adjusted as necessary.

4.2.8. Switch the light source back to the laser.

4.2.9. All non- Essential personnel will retreat behind the barricades. Non-test personnel will retreat to the loft behind the barricades and the safety observer will retreat to the firing booth.

4.2.10. Ensure all personnel handling explosives are following appropriate static safety procedures (SOP 201, wrist stats, cotton clothing).

4.3. Placing the Explosive Charge into Sample

4.3.1. Ensure test area is clear of non-test personnel.

Only ordnance will carry out steps 4.3.2 - 4.3.6 & 4.3.9 - 4.3.10

4.3.2. Place the RP - 80 detonator into the milled hole on the PMMA sample.

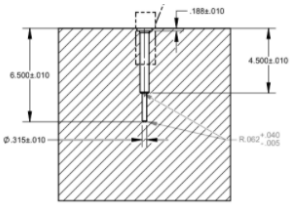

Figure 10: Schematic of 1 ft x 1 ft cube of PMMA.

4.3.3. Secure the detonator in the sample using ordnance approved epoxy. Fill the borehole with tamp material. **DO NOT CONNECT DETONATOR TO FIRE SET**

4.3.4. Wait for the epoxy to cure as outlined by the manufacturer.

4.3.5. Fill the borehole with tamp material.

4.3.6. Place the metal stopper into the milled hole in the PMMA cube.

4.3.7. Check schlieren alignment. Verify with the Camera control person (located in the loft) that the schlieren alignment looks good.

4.3.8. Check the PDV system is outputting appropriate signals.

4.3.9. Connect the detonator(s) to the c-cable.

4.3.10. Place the pressure plate on the PMMA sample. Ensure the c-cable is running through the milled hole lined with PEEK (non-conductive plastic

4.3.11. Both the test engineer and ordnance retreat to the firing booth.

4.4. Arming Cameras and laser systems

4.4.1. Ensure the Stanford Box is set to ‘External’ trigger mode.

4.4.2. Engineer will announce to put laser goggles on (for those within the radius where laser goggles are required)

Laser safety eye protection is required for all remaining steps for all personnel.

4.4.3. At the direction of the test engineer, arm the laser in the software and loudly announce that the laser is armed.

4.4.4. Insert the key to the laser safety unit and turn it to the ‘ON’ position. Loudly announce that the key is in and system is on.

4.4.5. Arm the PDV system.

4.4.6. Ensure all personnel are behind barriers.

4.4.7. Arm the cameras.

Hearing protection is required for all remaining steps for all personnel.

4.4.8. The test engineer will then hand control over to ordnance.

4.4.9. Ordnance will fire the system.

4.4.10. Disarm the PDV laser.

4.4.11. Ordnance will clear the range and determine when it is safe for test personnel to exit the barriers.

4.4.12. Turn the key in the laser safety unit to the 'OFF' position and remove the key. Loudly announce that the key is out.

4.4.13. If the laser system did not automatically disarm, disarm the laser in the software and loudly announce that the laser is disarmed.

4.4.14. At this point laser safety glasses may be removed and those without laser safety glasses may return.

4.4.15. Save camera and PDV data

4.4.16. Remove damaged test sample.

5. END OF DAY PROCEDURES

5.1. Press clean up

5.1.1. Ensure the wood posts are secured in the press

5.1.2. Unplug the press

5.1.3. Turn the water to the heat exchanger off

5.1.4. Bring the discharge hose back inside

5.1.5. Note the pressure remaining on the pressure control gauge: _____

5.2. Shutting off hardware

5.2.1. Ensure all data has been saved

5.2.2. Ensure a calibration image was taken

5.2.3. Turn off cameras

5.2.4. Ensure the PDV lasers are off. Turn off oscilloscope and laser pixie.

5.2.5. Ensure SI-LUX laser is off and the key is removed

5.2.6. Turn Stanford box and laser delay generator box off

5.2.7. Stop the safety video recording and turn the system off.

5.3. Leaving for the day

5.3.1. Remove caution signs from the doors

5.3.2. Remove all z-signs

APPENDIX C

UNCORRECTED FRACTURE RADIUS

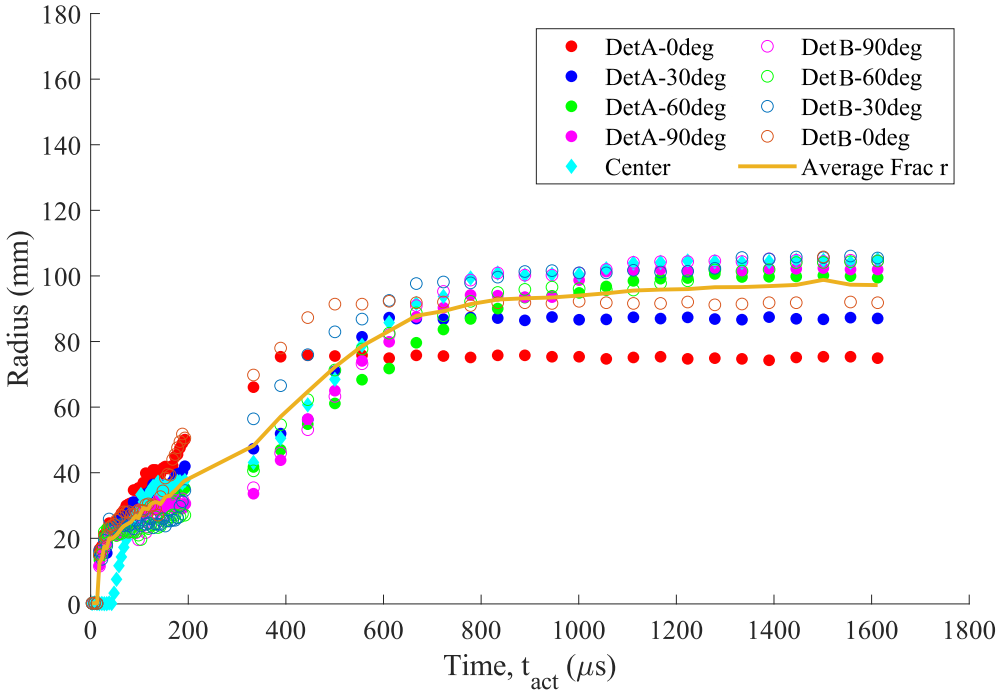

Figure C.1: Uncorrected Fracture radii tracked from the schlieren images for the HS2-2 test.

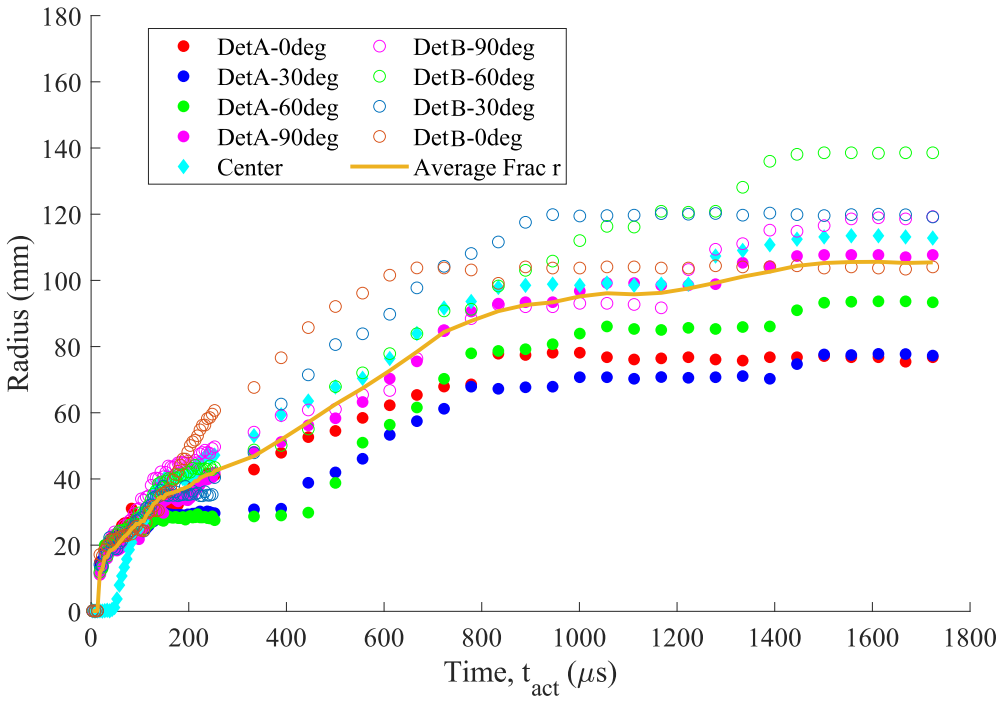

Figure C.2: Uncorrected Fracture radii tracked from the schlieren images for the VS2-2 test.

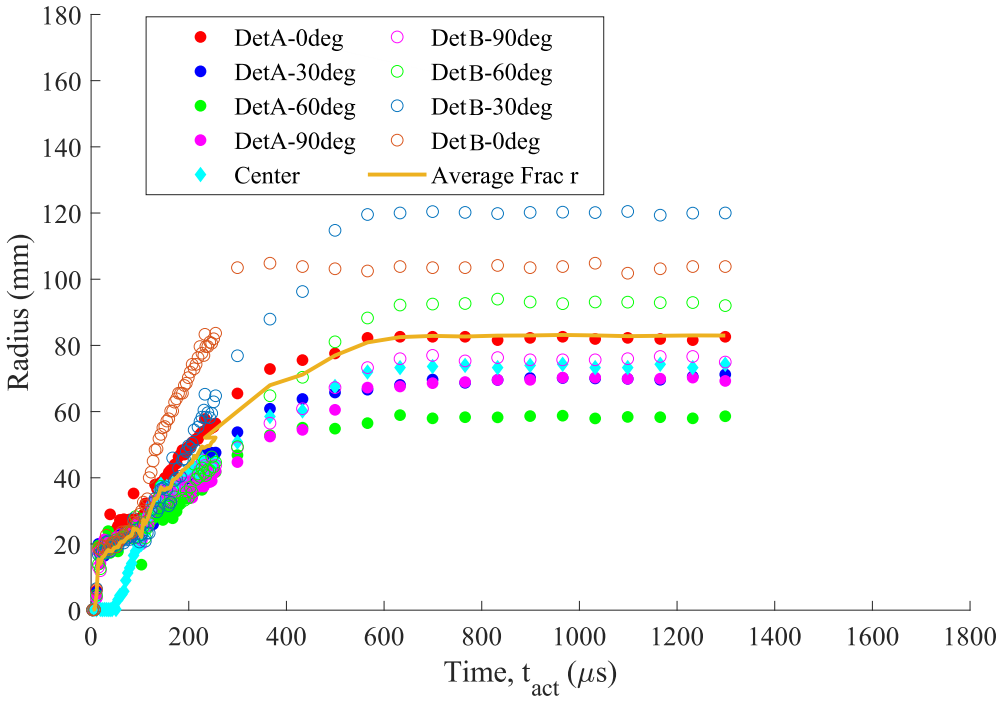

Figure C.3: Uncorrected Fracture radii tracked from the schlieren images for the VS2-20 test.

APPENDIX D

PERMISSIONS

Portions of Chapter 4 and Chapter 5 are reproduced from S. M. Torres, O. Y. Vorobiev, R. E. Robey, and M. J. Hargather. A study of explosive-induced fracture in polymethyl methacrylate (PMMA). Journal of Applied Physics, 134(7), 2023, with the permission of AIP Publishing

Portions of Chapter 3 are reproduced from Torres, S.M., Hargather, M.J., Kimberley, J. et al. Shock Response of Polymethyl Methacrylate (PMMA) Under Explosive Loading. J. dynamic behavior mater. (2024). https://doi.org/10.1007/s40870-024-00415-z

QUANTIFICATION OF POLYMETHYL METHACRYLATE (PMMA) SHOCK, STRESS, AND FRACTURE RESPONSE UNDER EXPLOSIVE LOADING

by

Sivana Mirhai Torres